SCUOLA
NORMALE
SUPERIORE

Classe di Scienze

Corso di perfezionamento in

Metodi e Modelli per le Scienze Molecolari

XXXIII ciclo

Experimental challenges in organic synthesis for the evaluation of molecular structures and for the study of non-covalent interactions

Settore Scientifico Disciplinare **CHIM/06**

Candidato
Simone Potenti

Relatore e Relatrice

Prof. Pier Giorgio Cozzi

Prof.ssa Cristina Puzzarini

Supervisore interno

Prof. Vincenzo Barone

Anno accademico 2021/2022

Alla mia famiglia, a Ottavia, e a Bologna

II

General index

Abstract

In the last decades, the awareness of the importance of organic chemistry has been growing amongst researchers working in the most diverse fields of science. Indeed, much of the current welfare of advanced societies is due to recent huge leaps in the comprehension of the behaviour of matter. In particular, material and life sciences have been undergoing an impressive development, and their academic results keep on having a steady growing impact on our daily routine, albeit most people are not aware of the prompt repercussions of academic research on their own lives. Carbon plays a pivotal role in material and life sciences, hence nowadays both skills and knowledge of organic chemists are fundamental. However, the interpretation of experimental data is often non-trivial, and a theoretical analysis – able to summarize, predict and understand the plethora of experimental data – is important. Hence, computational studies are highly recommended to guide it, since they can (i) anticipate otherwise unpredictable results, (ii) indicate new directions for further investigation, and (iii) readjust misconceptions and false perceptions.

The three main aims of this thesis are:

i. the exploitation of interdisciplinary approaches involving organic chemistry and state-of-the-art computational methods to gain deeper insights into the studied molecular systems, with special attention to molecular structures;

ii. the assessment of the importance of organic chemistry in two apparently unrelated fields, namely astrochemistry and biochemistry;

iii. the evaluation of the effects of non-covalent interactions on molecular geometry, whose detailed study is important for both astrochemical and biochemical purposes, but also in the field of catalysis.

The presentation of the previous goals will be as unitary as possible, since such aims are intimately interconnected with each other.

Finally, some interesting results concerning photocatalysis – a rapidly growing research field of organic chemistry – will be discussed. In the next years, this field is expected to gain unprecedented development with the fruitful interplay between experimental and theoretical chemistry. In particular, the composition of the reaction mixture is known to play a pivotal role in the outcome of the process, due to the reciprocal interactions at the molecular level between the reaction partners. Furthermore, such interactions are also strongly affected by the nature of the solvent.

More specifically, three main projects will be discussed.

Project 1: **Phenylmethanimine**

Abstract

The successful endeavour enabling the generation and characterization of an elusive aromatic imine, i.e. phenylmethanimine (PMI), will be described. PMI was chosen because it is expected to be an astrochemically relevant species.

Project 2: **Fluorothreonine**

A full account concerning synthesis and characterization of the only fluoro amino acid of natural origin discovered so far, namely 4-fluorothreonine, will be reported. Fluorothreonine was chosen as a test case for the evaluation of the effects of fluorination on molecular properties. Indeed, fluorothreonine is expected to feature interesting conformational behaviours due to peculiar non-covalent interactions involving fluorine.

Project 3: **Bismuth-mediated photocatalysis**

A bismuth-mediated photocatalytic reaction in aqueous conditions will be described. Bismuth was chosen as a heavy member of the pnictogens, which are known to be involved in interesting non-covalent interactions.

1. General introduction

In the last decades, huge efforts – experimental and theoretical – have been made to disclose the close connections existing between the molecular structure and the physico-chemical properties of a molecule.[1] In the field of medicinal and pharmaceutical chemistry, this correspondence is commonly referred as structure-activity relationship (SAR).[2] In particular, non-covalent interactions often play a pivotal role in the stabilization of the most representing structures of a molecular species.[3–6] The importance of such interactions was found to be ubiquitous, and the knowledge on the existing relations between chemical composition and noncovalent-related properties is increasing at a rapid pace. Hence, more and more refined ways to control such properties have been recently developed.[7,8] Non-covalent interactions are able to influence molecular properties in all states of matter. In the gas phase, they determine the atomic arrangements of non-covalent complexes,[9–11] such as organic molecules with coordinated water molecules.[12,13] Furthermore, they usually determine the conformational behaviour of flexible molecules.[14] The role of non-covalent interactions becomes even more crucial for molecular systems in the condensed phase,[15] affecting a wide range of properties, from reactivity[16] to biological activity,[17] being involved even in the field of catalysis.[18,19] The aforementioned considerations suggest that a molecular species is expected to show different geometrical properties, depending on whether it is in the gas phase or not.

Rotational spectroscopy is the best technique to study the structure of a molecular system in the gas phase.[20] As a matter of fact, a charge distribution featuring non-superimposed positive and negative charge centres, i.e. with a non-null permanent dipole moment, exhibits the possibility of interaction with electromagnetic radiation in the microwave range. A class of spectrometers in the field of rotational spectroscopy is based on the concept of rotational electric resonance (RER), in analogy with the concept of nuclear magnetic resonance (NMR). The two techniques differ in terms of the frequency range of the electromagnetic radiation (micro- and radio waves, respectively) and the type of transition (involving rotational and nuclear spin states, respectively). The Fourier-Transform Microwave (FTMW) spectrometers, working in the centimetre-wave region, exploit the RER: the gas sample is macroscopically polarized using a resonant pulse radiation, then after the pulse, relaxation occurs and the decay of this polarization with time (Free Induced Decay, FID) is recorded; finally, the FT is applied to the FID and the rotational spectrum in the frequency domain is obtained.

The interaction between microwave radiation and a polar molecule depends on both the dipole moment and the mass distribution of the molecule. While the former only affects the transition intensities, the mass distribution comes into play in the determination of the rotational energy, which is – according to

quantum mechanics – quantized. Conformers and even isotopologues – molecules of the same species, i.e. same molecular formula and bonding arrangement of atoms, but with either different conformation or isotopic composition, respectively – are characterized by different rotational spectra. While conformers feature both different dipole moments and mass distributions, isotopologues show almost negligible differences in terms of the dipole moment, but differ in terms of the mass distribution (Figure 1.1).
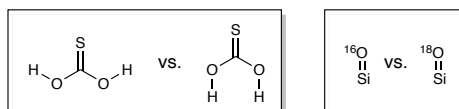

Figure 1.1: Selected examples of conformational and isotopomeric pairs. The left panel shows two conformers of carbonothionic *O,O*-acid, having different dipole moments (computed values: 0.50 D vs. 4.80 D, pointing in the same direction; see Ref. 21) and mass distributions. The right panel shows two isotopomers of SiO, having almost the same dipole moment (about 3.09 D; see Ref. 22) but different mass distributions (^{18}O is heavier than ^{16}O; see Ref. 23).

Two of the main applications of rotational spectroscopy are:

1. Structural "determination" of a known molecule – either used as such[24,25] or generated in situ[26] – in the gas phase. Quotation marks refer to the fact that most molecules are present as a collection of different geometrical species, e.g. conformers (vide supra).

2. Identification of the rotational "fingerprints" of a molecular species.[27,28]

Both applications require preliminary quantum-chemical calculations to guide the spectroscopic analysis and its interpretation.[6,29] Typically, high-level quantum-chemical computations can be used to describe small- to medium-sized molecular systems (often no more than 15 atoms); for larger species, hybrid quantum mechanics/molecular mechanics (QM/MM) approaches and/or Monte Carlo methods can provide a satisfactory preliminary picture.[30] While the first application mainly concerns the investigation of molecular physics, the second one plays a pivotal role in the field of astrochemistry. Indeed, it paves the way toward the exploration of chemical composition and evolution of the interstellar medium (ISM) by means of radioastronomy. An astronomic source usually emits a plethora of rotational transitions belonging to many different species, thus resulting in very crowded spectra. Hence, the identification of unequivocal line patterns (rotational "fingerprints") is often non-trivial. Once the microwave radiation emitted by the chosen astronomic source has been collected with radiotelescopes and analysed, if enough observed transitions are compatible with the rotational spectrum of a known molecule, the latter is present within the studied astronomic source.[31–33] To date, only 25 molecular species with ten or more atoms have been detected in the ISM.[34] In particular, the latter can harbour very exotic molecular species, whose laboratory production and characterization can be very challenging.[35] Indeed, even very unstable molecules can survive long in the interstellar medium (ISM), since the latter typically features very low particle densities and temperatures. Therefore, degradation pathways with non-zero reaction order often have negligible importance. Furthermore, even decomposition mechanisms characterized by very low

activation energies are hampered when occurring within very cold (i.e. less than 10 K) environments.[36]

The interplay between experimental and computational approaches is particularly pivotal when dealing with exotic molecular species. On the one hand, nowadays, even very challenging conditions can be reproduced in an attempt to generate very reactive and/or unstable species just before the spectroscopic acquisition,[37] and organic chemistry can be very helpful for the proper choice of starting materials, reaction conditions and experimental setup.[38,39] On the other hand, *ab initio* quantum chemistry methods are fundamental for a theoretical characterization of the exotic species whose production could not be achieved by means of any available state-of-the-art experimental protocols.[40] In this respect, the ISM can be consider by far the best "laboratory" for the formation of very elusive molecular species.[41] However, very few cases of detection of ISM molecular species based only on *ab initio* calculations have been reported in literature so far.[42–44] Indeed, the detection is considered as confirmed only when experimental data become available and a sufficient number of rotational transitions can be identified within the observed spectrum when compared to the experimental one.

The fruitful combination of organic synthesis and molecular spectroscopy – supported and guided by computational chemistry – for astrochemical purposes and as a multidisciplinary approach to elucidate molecular structures will be discussed in Chapter 2. In particular, the issues concerning the generation and spectroscopic characterization of imine-type species will be presented. Furthermore, the theoretical background of rotational spectroscopy will be introduced. The case of production and rotational spectroscopy of phenylmethanimine (PMI) will be analysed in Section 2.3. In particular, the experimental endeavour will be described in detail.

Despite the strengths of rotational spectroscopy, some important drawbacks must be pointed out:
1. Rotational spectra can be recorded only in the gas phase.
2. The study of large molecular species is very challenging, due to two main issues: (i) they are difficult to be brought in the gas phase by means of mild (i.e. preventing decomposition as much as possible) "gasification" techniques[14,45] and (ii) their moments of inertia are so large that their rotational transitions are often compressed in a narrow spectral range. The spectroscopic acquisition usually generates "crowded" rotational spectra, whose interpretation is becoming more and more feasible thanks to recent instrumental improvements in conjunction with high resolution approaches.[46–49]

Since purely rotational spectroscopy involves the study of isolated molecular systems, it goes without saying that bulk solute-solvent interactions cannot be properly studied using this technique. However, a preliminary picture of such interactions can be obtained if non-covalent complexes are investigated in the gas phase. Several examples have been reported, systematically highlighting the importance of non-

covalent interactions.[5,10,11] Indeed, intermolecular interactions in non-covalent complexes (such as those occurring between an organic molecule and a water molecule in the first shell of solvation)[12,13,50–52] can be accurately described by means of microwave spectroscopy. These types of interactions can be also established at an intramolecular level. If the molecule can be brought in the gas phase, then its conformational behaviour and the effects of intramolecular non-covalent interactions can be investigated with microwave spectroscopy.[25,53–57]

Although preliminary studies in the gas phase are crucial to assess molecular structures, the most interesting behaviours of biologically relevant species are those observed in the condensed phase, especially in aqueous environments.[58–61] Indeed, all terrestrial biochemical processes occur in the presence of water. Hence, other spectroscopic techniques are required to elucidate molecular geometries in aqueous media.[62] The intra- and intermolecular interactions in aqueous media can get even trickier when chiral species are involved. However, such an increase of complexity is precious to get further insights on the conformational behaviour.[63,64] In particular, chiroptical spectroscopies – together with state-of-the-art computational methodologies guiding the interpretation of experimental spectroscopic data[65–69] – can be used to assess molecular structures with unprecedented levels of detail.[70–72]

The spectroscopic characterization of water-soluble organic species is a challenging task. The decoration of such species with peculiar atoms (e.g. fluorine) can represent a further complication for the interpretation of experimental data. Indeed, in the specific case of fluorine, it strongly modifies the stereoelectronic effects, thus strongly altering molecular conformational behaviours in unexpected ways.[73–75] Furthermore, still considering fluorine, its insertion into an organic scaffold is rated among the most demanding synthetic strategies. The importance of fluorinated species, together with the experimental challenges related to their synthesis, will be properly discussed in Chapter 3. Furthermore, the case of 4-fluorothreonine, with particular reference to its synthesis and characterization, will be analysed in detail in Section 3.3.

As far as condensed phases are concerned, aqueous conditions represent the standard for the study of biochemical processes. Until the end of the 20th century, the use of water instead of hazardous organic solvents was considered a challenging target in the field of green and sustainable organic synthetic methodologies, with particular reference to medicinal and pharmaceutical applications.[76–78] Organic synthetic methodologies generally require organic solvents to avoid heterogeneous mixtures and to facilitate chemical reactions, and, in the case of stereoselectivity issues, the organic solvent is accurately chosen to guarantee the desired outcome.[79] Moreover, many catalysts or reaction partners are incompatible/immiscible with water. Nevertheless, water was the preferred solvent in many named reactions developed in the 19th century.[80] However, with the rapid development of organometallic

chemistry, the sensitivity to hydrolysis of the first organometallic reagents led to the replacement of water with volatile organic solvents. Then, in 1980, an accurate study of Diels-Alder reactions reassessed the use of water as a solvent for organic transformations,[81] and by the end of the 1990s water was back on stage due to the definition of "green chemistry" proposed by Anastas and Warner.[82] Since then, an outstanding number of water-compatible organic synthetic methodologies were developed. Such approaches do not only avoid the most common water-related drawbacks, but do rather benefit from the presence of water, due to particular mechanisms occurring in the optimized reactions conditions.[83–85] The complete elucidation of the role of water in such protocols often requires accurate computational studies to guide the interpretation of experimental data. For instance, albeit water is not the best suited solvent to guarantee complete dissolution of slightly polar organic reaction partners, whenever the transition state (i.e. unstable intermediate between reactants and products) is more polarized than the reactants, water may have more stabilizing effects than organic solvents, thus reducing the activation energy (i.e. the energy required for the reaction to occur) and making the reaction faster.[86] Several theoretical investigations revealed that water molecules may be involved in the transition states of many organic reactions when performed in aqueous media,[87–90] and particular attention was devoted to the "reorientation" ability of water, which is particularly relevant nearby the reaction partners.[91] The role of water was investigated in transition-metal catalysed reactions,[92,93] in organocatalytic processes,[94] and also in the case of organic reactions performed in water-oil emulsions.[95] The interplay between theory and experiment in the field of synthetic methodologies is expected to boost the development of different transformations, and to expand their scope, by means of shrewd tuning of the reaction conditions.[96,97]

In particular, metallaphotoredox catalysis – combining photoredox and metal catalysis – is a rapidly growing synthetic methodology,[98,99] but "waterproof" protocols still represent an underexplored area.[100,101] Indeed, metallaphotoredox catalysis relies on the formation of transient nucleophilic organometallic species, most of which undergo rapid hydrolysis in the presence of water.[102–104] The description of metallaphotoredox catalysis will be given in Chapter 4. In particular, an environmentally benign bismuth-mediated photoredox protocol will be described in detail in Section 4.3.

References

(1)   Carey, F. A.; Sundberg, R. J. Structural Effects on Stability and Reactivity. In *Advanced Organic Chemistry*; 2007; pp 253–388. DOI: 10.1007/978-0-387-44899-2_3.

(2)   Ritchie, C. D.; Sager, W. F. An Examination of Structure-Reactivity Relationships. In *Progress in Physical Organic Chemistry*; 2007; Vol. 2, pp 323–400. DOI: 10.1002/9780470171813.ch6.

(3)   Müller-Dethlefs, K.; Hobza, P. Noncovalent Interactions: A Challenge for Experiment and Theory. *Chem. Rev.* **2000**, *100* (1), 143–167. DOI: 10.1021/cr9900331.

(4)   Alessandrini, S.; Barone, V.; Puzzarini, C. Extension of the "cheap" Composite Approach to Noncovalent Interactions: The jun-ChS Scheme. *J. Chem. Theory Comput.* **2020**, *16* (2), 988–1006. DOI: 10.1021/acs.jctc.9b01037.

(5)   Li, W.; Spada, L.; Tasinato, N.; Rampino, S.; Evangelisti, L.; Gualandi, A.; Cozzi, P. G.; Melandri, S.; Barone, V.; Puzzarini, C. Theory Meets Experiment for Noncovalent Complexes: The Puzzling Case of Pnicogen Interactions. *Angew. Chem. Int. Ed.* **2018**, *57* (42), 13853–13857. DOI: 10.1002/anie.201807751.

(6)   Puzzarini, C.; Spada, L.; Alessandrini, S.; Barone, V. The challenge of non-covalent interactions: Theory meets

References

experiment for reconciling accuracy and interpretation. *J. Phys. Condens. Matter* **2020**, *32* (34), 343002. DOI: 10.1088/1361-648X/ab8253.

(7) Guo, X.; Liao, Q.; Manley, E. F.; Wu, Z.; Wang, Y.; Wang, W.; Yang, T.; Shin, Y. E.; Cheng, X.; Liang, Y.; Chen, L. X.; Baeg, K. J.; Marks, T. J.; Guo, X. Materials Design via Optimized Intramolecular Noncovalent Interactions for High-Performance Organic Semiconductors. *Chem. Mater.* **2016**, *28* (7), 2449–2460. DOI: 10.1021/acs.chemmater.6b00850.

(8) Krieg, E.; Rybtchinski, B. Noncovalent water-based materials: Robust yet adaptive. *Chem. Eur. J.* **2011**, *17* (33), 9016–9026. DOI: 10.1002/chem.201100809.

(9) Pietraperzia, G.; Pasquini, M.; Mazzoni, F.; Piani, G.; Becucci, M.; Biczysko, M.; Michalski, D.; Bloino, J.; Barone, V. Noncovalent interactions in the gas phase: The anisole-phenol complex. *J. Phys. Chem. A* **2011**, *115* (34), 9603–9611. DOI: 10.1021/jp200444a.

(10) Spada, L.; Tasinato, N.; Vazart, F.; Barone, V.; Caminati, W.; Puzzarini, C. Noncovalent Interactions and Internal Dynamics in Pyridine–Ammonia: A Combined Quantum-Chemical and Microwave Spectroscopy Study. *Chem. Eur. J.* **2017**, *23* (20), 4876–4883. DOI: 10.1002/chem.201606014.

(11) Obenchain, D. A.; Spada, L.; Alessandrini, S.; Rampino, S.; Herbers, S.; Tasinato, N.; Mendolicchio, M.; Kraus, P.; Gauss, J.; Puzzarini, C.; Grabow, J. U.; Barone, V. Unveiling the Sulfur–Sulfur Bridge: Accurate Structural and Energetic Characterization of a Homochalcogen Intermolecular Bond. *Angew. Chem. Int. Ed.* **2018**, *57* (48), 15822–15826. DOI: 10.1002/anie.201810637.

(12) Wang, J.; Spada, L.; Chen, J.; Gao, S.; Alessandrini, S.; Feng, G.; Puzzarini, C.; Gou, Q.; Grabow, J. U.; Barone, V. The Unexplored World of Cycloalkene–Water Complexes: Primary and Assisting Interactions Unraveled by Experimental and Computational Spectroscopy. *Angew. Chem. Int. Ed.* **2019**, *58* (39), 13935–13941. DOI: 10.1002/anie.201906977.

(13) Lei, J.; Alessandrini, S.; Chen, J.; Zheng, Y.; Spada, L.; Gou, Q.; Puzzarini, C.; Barone, V. Rotational Spectroscopy Meets Quantum Chemistry for Analyzing Substituent Effects on Non-Covalent Interactions: The Case of the Trifluoroacetophenone-Water Complex. *Molecules* **2020**, *25* (21), 4899. DOI: 10.3390/molecules25214899.

(14) Lesarri, A.; Mata, S.; López, J. C.; Alonso, J. L. A laser-ablation molecular-beam Fourier-transform microwave spectrometer: The rotational spectrum of organic solids. *Rev. Sci. Instrum.* **2003**, *74* (11), 4799–4804. DOI: 10.1063/1.1611611.

(15) Aliev, A. E.; Moïse, J.; Motherwell, W. B.; Nič, M.; Courtier-Murias, D.; Tocher, D. A. Probing weak non-covalent interactions in solution and solid states with designed molecules. *Phys. Chem. Chem. Phys.* **2009**, *11* (1), 97–100. DOI: 10.1039/b815906h.

(16) Maharramov, A. M.; Mahmudov, K. T.; Kopylovich, M. N.; Pombeiro, A. J. L. *Non-Covalent Interactions in the Synthesis and Design of New Compounds*; 2016. DOI: 10.1002/9781119113874.

(17) Riley, K. E.; Hobza, P. Noncovalent interactions in biochemistry. *WIREs Comput. Mol. Sci.* **2011**, *1* (1), 3–17. DOI: 10.1002/wcms.8.

(18) Tang, W.; Johnston, S.; Iggo, J. A.; Berry, N. G.; Phelan, M.; Lian, L.; Bacsa, J.; Xiao, J. Cooperative catalysis through noncovalent interactions. *Angew. Chem. Int. Ed.* **2013**, *52* (6), 1668–1672. DOI: 10.1002/anie.201208774.

(19) Wheeler, S. E.; Seguin, T. J.; Guan, Y.; Doney, A. C. Noncovalent Interactions in Organocatalysis and the Prospect of Computational Catalyst Design. *Acc. Chem. Res.* **2016**, *49* (5), 1061–1069. DOI: 10.1021/acs.accounts.6b00096.

(20) Laane, J. *Frontiers of Molecular Spectroscopy*; 2009. DOI: 10.1016/B978-0-444-53175-9.X0001-3.

(21) Alessandrini, S.; Dell'Isola, V.; Spada, L.; Barone, V.; Puzzarini, C. A computational journey in the CH_2O_2S land: an accurate rotational and ro-vibrational analysis of the sulfene molecule and the O,S- and O,O-monothiocarbonic acids. *Mol. Phys.* **2020**, *118* (19–20), e1766707. DOI: 10.1080/00268976.2020.1766707.

(22) Raymonda, J. W.; Muenter, J. S.; Klemperer, W. A. Electric dipole moment of SiO and GeO. *J. Chem. Phys.* **1970**, *52* (7), 3458–3461. DOI: 10.1063/1.1673510.

(23) Müller, H. S. P.; Spezzano, S.; Bizzocchi, L.; Gottlieb, C. A.; Degli Esposti, C.; McCarthy, M. C. Rotational spectroscopy of isotopologues of silicon monoxide, SiO, and spectroscopic parameters from a combined fit of rotational and rovibrational data. *J. Phys. Chem. A* **2013**, *117* (50), 13843–13854. DOI: 10.1021/jp408391f.

(24) Blanco, S.; Sanz, M. E.; López, J. C.; Alonso, J. L. Revealing the multiple structures of serine. *Proc. Natl. Acad. Sci. U. S. A.* **2007**, *104* (51), 20183–20188. DOI: 10.1073/pnas.0705676104.

(25) Alessandrini, S.; Melosso, M.; Jiang, N.; Bizzocchi, L.; Dore, L.; Puzzarini, C. Conformational stability of cyclopropanecarboxaldehyde is ruled by vibrational effects. *Mol. Phys.* **2021**, *119* (21–22), e1955988. DOI: 10.1080/00268976.2021.1955988.

(26) Melli, A.; Potenti, S.; Melosso, M.; Herbers, S.; Spada, L.; Gualandi, A.; Lengsfeld, K. G.; Dore, L.; Buschmann, P.; Cozzi, P. G.; Grabow, J. U.; Barone, V.; Puzzarini, C. A Journey from Thermally Tunable Synthesis to Spectroscopy of Phenylmethanimine in Gas Phase and Solution. *Chem. Eur. J.* **2020**, *26* (65), 15016–15022. DOI: 10.1002/chem.202003270.

(27) Martin-Drumel, M. A.; Baraban, J. H.; Changala, P. B.; Stanton, J. F.; McCarthy, M. C. The Hunt for Elusive Molecules: Insights from Joint Theoretical and Experimental Investigations. *Chem. Eur. J.* **2019**, *25* (30), 7243–7258. DOI: 10.1002/chem.201805986.

(28) Melosso, M.; Bizzocchi, L.; Gazzeh, H.; Tonolo, F.; Guillemin, J. C.; Alessandrini, S.; Rivilla, V. M.; Dore, L.; Barone, V.; Puzzarini, C. Gas-phase identification of (Z)-1,2-ethenediol, a key prebiotic intermediate in the formose reaction. *Chem. Commun.* **2022**, *58* (16), 2750–2753. DOI: 10.1039/d1cc06919e.

(29)   Puzzarini, C. Rotational spectroscopy meets theory. *Phys. Chem. Chem. Phys.* **2013**, *15* (18), 6595–6607. DOI: 10.1039/c3cp44301a.

(30)   Mancini, G.; Fusè, M.; Lazzari, F.; Chandramouli, B.; Barone, V. Unsupervised search of low-lying conformers with spectroscopic accuracy: A two-step algorithm rooted into the island model evolutionary algorithm. *J. Chem. Phys.* **2020**, *153* (12), 124110. DOI: 10.1063/5.0018314.

(31)   McGuire, B. A.; Burkhardt, A. M.; Kalenskii, S.; Shingledecker, C. N.; Remijan, A. J.; Herbst, E.; McCarthy, M. C. Detection of the aromatic molecule benzonitrile (c-C_6H_5CN) in the interstellar medium. *Science* **2018**, *359* (6372), 202–205. DOI: 10.1126/science.aao4890.

(32)   Rivilla, V. M.; Jiménez-Serra, I.; Martín-Pintado, J.; Briones, C.; Rodríguez-Almeida, L. F.; Rico-Villas, F.; Tercero, B.; Zeng, S.; Colzi, L.; De Vicente, P.; Martín, S.; Requena-Torres, M. A. Discovery in space of ethanolamine, the simplest phospholipid head group. *Proc. Natl. Acad. Sci. U. S. A.* **2021**, *118* (22), e2101314118. DOI: 10.1073/pnas.2101314118.

(33)   Rivilla, V. M.; Colzi, L.; Jiménez-Serra, I.; Martín-Pintado, J.; Megías, A.; Melosso, M.; Bizzocchi, L.; López-Gallifa, Á.; Martínez-Henares, A.; Massalkhi, S.; Tercero, B.; de Vicente, P.; Guillemin, J.-C.; García de la Concepción, J.; Rico-Villas, F.; Zeng, S.; Martín, S.; Requena-Torres, M. A.; Tonolo, F.; Alessandrini, S.; Dore, L.; Barone, V.; Puzzarini, C. Precursors of the RNA World in Space: Detection of (Z)-1,2-ethenediol in the Interstellar Medium, a Key Intermediate in Sugar Formation. *Astrophys. J., Lett.* **2022**, *929* (1), L11. DOI: 10.3847/2041-8213/ac6186.

(34)   McGuire, B. A. 2021 Census of Interstellar, Circumstellar, Extragalactic, Protoplanetary Disk, and Exoplanetary Molecules. *Astrophys. J. Suppl. Ser.* **2022**, *259* (2), 30. DOI: 10.3847/1538-4365/ac2a48.

(35)   Green, S. Interstellar Chemistry: Exotic Molecules in Space. *Annu. Rev. Phys. Chem.* **1981**, *32* (1), 103–138. DOI: 10.1146/annurev.pc.32.100181.000535.

(36)   Williams, D. A.; Hartquist, T. W.; Rawlings, J. M. C.; Cecchi-Pestellini, C.; Viti, S. *Dynamical Astrochemistry*; 2017. DOI: 10.1039/9781782629894.

(37)   Grabow, J.-U. Fourier Transform Microwave Spectroscopy Measurement and Instrumentation. In *Handbook of High-resolution Spectroscopy*; 2011. DOI: 10.1002/9780470749593.hrs037.

(38)   Sagan, C. Interstellar organic chemistry. *Nature* **1972**, *238* (5359), 77–80. DOI: 10.1038/238077a0.

(39)   Mccarthy, M. C.; Mcguire, B. A. Aromatics and Cyclic Molecules in Molecular Clouds: A New Dimension of Interstellar Organic Chemistry. *J. Phys. Chem. A* **2021**, *125* (16), 3231–3243. DOI: 10.1021/acs.jpca.1c00129.

(40)   Barone, V.; Alessandrini, S.; Biczysko, M.; Cheeseman, J. R.; Clary, D. C.; McCoy, A. B.; DiRisio, R. J.; Neese, F.; Melosso, M.; Puzzarini, C. Computational molecular spectroscopy. *Nat. Rev. Methods Primers* **2021**, *1* (38). DOI: 10.1038/s43586-021-00034-1.

(41)   Puzzarini, C. Grand Challenges in Astrochemistry. *Front. Astron. Space Sci.* **2020**, *7* (19). DOI: 10.3389/fspas.2020.00019.

(42)   Botschwina, P.; Oswald, R. Carbon chains of type $C_{2n+1}N^-$ (n = 2–6): A theoretical study of potential interstellar anions. *J. Chem. Phys.* **2008**, *129* (4), 044305. DOI: 10.1063/1.2949093.

(43)   Cernicharo, J.; Guélin, M.; Agúndez, M.; McCarthy, M. C.; Thaddeus, P. Detection of C_5N^- and Vibrationally Excited C_6H in IRC+10216. *Astrophys. J.* **2008**, *688* (2), L83–L86. DOI: 10.1086/595583.

(44)   Cernicharo, J.; Marcelino, N.; Pardo, J. R.; Agúndez, M.; Tercero, B.; De Vicente, P.; Cabezas, C.; Bermúdez, C. Interstellar nitrile anions: Detection of C_3N^- and C_5N^- in TMC-1. *Astron. Astrophys.* **2020**, *641*, L9. DOI: 10.1051/0004-6361/202039231.

(45)   Caminati, W.; Grabow, J. U. Microwave Spectroscopy: Molecular Systems. In *Frontiers of Molecular Spectroscopy*; 2009; pp 455–552. DOI: 10.1016/B978-0-444-53175-9.00015-5.

(46)   Neill, J. L.; Douglass, K. O.; Pate, B. H.; Pratt, D. W. Next generation techniques in the high resolution spectroscopy of biologically relevant molecules. *Phys. Chem. Chem. Phys.* **2011**, *13* (16), 7253–7262. DOI: 10.1039/c0cp01573c.

(47)   Pratt, D. W. High Resolution Spectroscopy in the Gas Phase: Even Large Molecules Have Well-Defined Shapes. *Annu. Rev. Phys. Chem.* **1998**, *49* (1), 481–530. DOI: 10.1146/annurev.physchem.49.1.481.

(48)   Shipman, S. T.; Pate, B. H. New Techniques in Microwave Spectroscopy. In *Handbook of High-resolution Spectroscopy*; 2011; pp 801–828. DOI: 10.1002/9780470749593.hrs036.

(49)   Caminati, W. Microwave Spectroscopy of Large Molecules and Molecular Complexes. In *Handbook of High-resolution Spectroscopy*; 2011; pp 829–852. DOI: 10.1002/9780470749593.hrs035.

(50)   Chen, J.; Zheng, Y.; Melli, A.; Spada, L.; Lu, T.; Feng, G.; Gou, Q.; Barone, V.; Puzzarini, C. Theory meets experiment for elucidating the structure and stability of non-covalent complexes: Water-Amine interaction as a proof of concept. *Phys. Chem. Chem. Phys.* **2020**, *22* (9), 5024–5032. DOI: 10.1039/c9cp06768j.

(51)   Juanes, M.; Li, W.; Spada, L.; Evangelisti, L.; Lesarri, A.; Caminati, W. Internal dynamics of cyclohexanol and the cyclohexanol-water adduct. *Phys. Chem. Chem. Phys.* **2019**, *21* (7), 3676–3682. DOI: 10.1039/c8cp04455d.

(52)   Alonso, J. L.; Cocinero, E. J.; Lesarri, A.; Sanz, M. E.; López, J. C. The glycine-water complex. *Angew. Chem. Int. Ed.* **2006**, *45* (21), 3471–3474. DOI: 10.1002/anie.200600342.

(53)   Alonso, E. R.; León, I.; Alonso, J. L. The role of the intramolecular interactions in the structural behavior of biomolecules: Insights from rotational spectroscopy. In *Intra- and Intermolecular Interactions Between Non-covalently Bonded Species*; 2021; pp 93–141. DOI: 10.1016/b978-0-12-817586-6.00004-9.

(54)   Juanes, M.; Saragi, R. T.; Jin, Y.; Zingsheim, O.; Schlemmer, S.; Lesarri, A. Rotational spectrum and intramolecular hydrogen bonding in 1,2-butanedithiol. *J. Mol. Struct.* **2020**, *1211*, 128080. DOI: 10.1016/j.molstruc.2020.128080.

(55)   Puzzarini, C.; Biczysko, M.; Barone, V.; Largo, L.; Peña, I.; Cabezas, C.; Alonso, J. L. Accurate characterization of the

References

peptide linkage in the gas phase: A joint quantum-chemical and rotational spectroscopy study of the glycine dipeptide analogue. *J. Phys. Chem. Lett.* **2014**, *5* (3), 534–540. DOI: 10.1021/jz402744a.

(56) Loru, D.; Peña, I.; Alonso, J. L.; Eugenia Sanz, M. Intramolecular interactions in the polar headgroup of sphingosine: Serinol. *Chem. Commun.* **2016**, *52* (18), 3615–3618. DOI: 10.1039/c5cc09423b.

(57) Loru, D.; Vigorito, A.; Santos, A. F. M.; Tang, J.; Sanz, M. E. The axial/equatorial conformational landscape and intramolecular dispersion: New insights from the rotational spectra of monoterpenoids. *Phys. Chem. Chem. Phys.* **2019**, *21* (47), 26111–26116. DOI: 10.1039/c9cp05264j.

(58) Bagchi, B. *Water in Biological and Chemical Processes: From Structure and Dynamics to Function*; 2011. DOI: 10.1017/CBO9781139583947.

(59) Tait, M. J.; Franks, F. Water in biological systems. *Nature* **1971**, *230* (5289), 91–94. DOI: 10.1038/230091a0.

(60) Cooke, R.; Kuntz, I. D. The properties of water in biological systems. *Annu. Rev. Biophys. Bioeng.* **1974**, *3*, 95–126. DOI: 10.1146/annurev.bb.03.060174.000523.

(61) Wiggins, P. M. Role of water in some biological processes. *Microbiol. Rev.* **1990**, *54* (4), 432–449. DOI: 10.1128/mmbr.54.4.432-449.1990.

(62) Bakker, H. J.; Skinner, J. L. Vibrational spectroscopy as a probe of structure and dynamics in liquid water. *Chem. Rev.* **2010**, *110* (3), 1498–1517. DOI: 10.1021/cr9001879.

(63) Quesada-Moreno, M. M.; Márquez-García, A. Á.; Avilés-Moreno, J. R.; López-González, J. J. Conformational landscape of L-threonine in neutral, acid and basic solutions from vibrational circular dichroism spectroscopy and quantum chemical calculations. *Tetrahedron: Asymmetry* **2013**, *24* (24), 1537–1547. DOI: 10.1016/j.tetasy.2013.09.025.

(64) Quesada-Moreno, M. M.; Avilés-Moreno, J. R.; Márquez-García, A. Á.; Partal-Ureña, F.; López González, J. J. L-Serine in aqueous solutions at different pH: Conformational preferences and vibrational spectra of cationic, anionic and zwitterionic species. *J. Mol. Struct.* **2013**, *1046*, 136–146. DOI: 10.1016/j.molstruc.2013.04.038.

(65) Barone, V.; Baiardi, A.; Bloino, J. New developments of a multifrequency virtual spectrometer: Stereo-electronic, dynamical, and environmental effects on chiroptical spectra. *Chirality* **2014**, *26* (9), 588–600. DOI: 10.1002/chir.22325.

(66) Bloino, J.; Biczysko, M.; Barone, V. Anharmonic Effects on Vibrational Spectra Intensities: Infrared, Raman, Vibrational Circular Dichroism, and Raman Optical Activity. *J. Phys. Chem. A* **2015**, *119* (49), 11862–11874. DOI: 10.1021/acs.jpca.5b10067.

(67) Fusè, M.; Mazzeo, G.; Longhi, G.; Abbate, S.; Masi, M.; Evidente, A.; Puzzarini, C.; Barone, V. Unbiased Determination of Absolute Configurations by vis-à-vis Comparison of Experimental and Simulated Spectra: The Challenging Case of Diplopyrone. *J. Phys. Chem. B* **2019**, *123* (43), 9230–9237. DOI: 10.1021/acs.jpcb.9b08375.

(68) Paoloni, L.; Mazzeo, G.; Longhi, G.; Abbate, S.; Fusè, M.; Bloino, J.; Barone, V. Toward Fully Unsupervised Anharmonic Computations Complementing Experiment for Robust and Reliable Assignment and Interpretation of IR and VCD Spectra from Mid-IR to NIR: The Case of 2,3-Butanediol and trans-1,2-Cyclohexanediol. *J. Phys. Chem. A* **2020**, *124* (5), 1011–1024. DOI: 10.1021/acs.jpca.9b11025.

(69) Del Galdo, S.; Fusè, M.; Barone, V. The ONIOM/PMM Model for Effective Yet Accurate Simulation of Optical and Chiroptical Spectra in Solution: Camphorquinone in Methanol as a Case Study. *J. Chem. Theory Comput.* **2020**, *16* (5), 3294–3306. DOI: 10.1021/acs.jctc.0c00124.

(70) Berova, N.; Polavarapu, P. L.; Nakanishi, K.; Woody, R. W. *Comprehensive Chiroptical Spectroscopy: Applications in Stereochemical Analysis of Synthetic Compounds, Natural Products, and Biomolecules, Volume 2*; 2012. DOI: 10.1002/9781118120392.

(71) Batista, J. M.; Blanch, E. W.; Da Silva Bolzani, V. Recent advances in the use of vibrational chiroptical spectroscopic methods for stereochemical characterization of natural products. *Nat. Prod. Rep.* **2015**, *32* (9), 1280–1302. DOI: 10.1039/c5np00027k.

(72) Polavarapu, P. L. Determination of the absolute configurations of chiral drugs using chiroptical spectroscopy. *Molecules* **2016**, *21* (8), 1056. DOI: 10.3390/molecules21081056.

(73) Urban, J. J. Computational study of stereoelectronic effects in fluorinated alkylamines. *J. Phys. Org. Chem.* **2005**, *18* (11), 1061–1071. DOI: 10.1002/poc.973.

(74) Shukla, R.; Chopra, D. Crystallographic and computational investigation of intermolecular interactions involving organic fluorine with relevance to the hybridization of the carbon atom. *CrystEngComm* **2015**, *17* (19), 3596–3609. DOI: 10.1039/c4ce02391a.

(75) Wade, A. D.; Rizzi, A.; Wang, Y.; Huggins, D. J. Computational Fluorine Scanning Using Free-Energy Perturbation. *J. Chem. Inf. Model.* **2019**, *59* (6), 2776–2784. DOI: 10.1021/acs.jcim.9b00228.

(76) Li, C. J. Organic reactions in Aqueous media with a focus on carbon-carbon bond formations: A decade update. *Chem. Rev.* **2005**, *105* (8), 3095–3166. DOI: 10.1021/cr030009u.

(77) Li, C. J.; Chen, L. Organic chemistry in water. *Chem. Soc. Rev.* **2006**, *35* (1), 68–82. DOI: 10.1039/b507207g.

(78) Chanda, A.; Fokin, V. V. Organic synthesis "on water." *Chem. Rev.* **2009**, *109* (2), 725–748. DOI: 10.1021/cr800448q.

(79) Cainelli, G.; Galletti, P.; Giacomini, D. Solvent effects on stereoselectivity: More than just an environment. *Chem. Soc. Rev.* **2009**, *38* (4), 990–1001. DOI: 10.1039/b802815j.

(80) Lindström, U. M. Stereoselective organic reactions in water. *Chem. Rev.* **2002**, *102* (8), 2751–2772. DOI: 10.1021/cr010122p.

(81) Rideout, D. C.; Breslow, R. Hydrophobic Acceleration of Diels-Alder Reactions. *J. Am. Chem. Soc.* **1980**, *102* (26), 7816–7817. DOI: 10.1021/ja00546a048.

(82) Anastas, P. T.; Warner, J. C. *Green Chemistry: Theory and Practice*; Oxford University Press: New York, 2000.

14

(83)   Libineau, A.; Auge, J.; Queneau, Y. Water-promoted organic reactions. *Synthesis* **1994**, *1994* (8), 741–760. DOI: 10.1055/s-1994-25562.

(84)   Ameta, C.; Ameta, K. L. Water: A benign solvent for the synthesis of various organic moieties. In *Green Chemistry: Synthesis of Bioactive Heterocycles*; 2014; pp 231–252. DOI: 10.1007/978-81-322-1850-0_8.

(85)   van der Helm, M. P.; Klemm, B.; Eelkema, R. Organocatalysis in aqueous media. *Nat. Rev. Chem.* **2019**, *3* (8), 491–508. DOI: 10.1038/s41570-019-0116-0.

(86)   Chandrasekhar, J.; Shariffskul, S.; Jorgensen, W. L. QM/MM simulations for Diels-Alder reactions in water: Contribution of enhanced hydrogen bonding at the transition state to the solvent effect. *J. Phys. Chem. B* **2002**, *106* (33), 8078–8085. DOI: 10.1021/jp020326p.

(87)   Dickerson, T. J.; Lovell, T.; Meijler, M. M.; Noodleman, L.; Janda, K. D. Nornicotine aqueous aldol reactions: Synthetic and theoretical investigations into the origins of catalysis. *J. Org. Chem.* **2004**, *69* (20), 6603–6609. DOI: 10.1021/jo048894j.

(88)   Kleiner, C. M.; Schreiner, P. R. Hydrophobic amplification of noncovalent organocatalysis. *Chem. Commun.* **2006**, No. 41, 4315–4317. DOI: 10.1039/b605850g.

(89)   Yuan, H.; Zhang, J. Mechanistic insights on DBU catalyzed β-amination of NBS to chalcone driving by water: Multiple roles of water. *J. Comput. Chem.* **2017**, *38* (7), 438–445. DOI: 10.1002/jcc.24700.

(90)   Cao, S.; Yuan, H.; Yang, Y.; Wang, M.; Zhang, X.; Zhang, J. Mechanistic investigation inspired "on water" reaction for hydrobromic acid-catalyzed Friedel-Crafts-type reaction of β-naphthol and formaldehyde. *J. Comput. Chem.* **2017**, *38* (26), 2268–2275. DOI: 10.1002/jcc.24877.

(91)   Laage, D.; Stirnemann, G.; Sterpone, F.; Rey, R.; Hynes, J. T. Reorientation and allied dynamics in water and aqueous solutions. *Annu. Rev. Phys. Chem.* **2011**, *62*, 395–416. DOI: 10.1146/annurev.physchem.012809.103503.

(92)   Shi, F. Q.; Li, X.; Xia, Y.; Zhang, L.; Yu, Z. X. DFT study of the mechanisms of in water Au(I)-catalyzed tandem [3,3]-rearrangement/Nazarov reaction/[1,2]-hydrogen shift of enynyl acetates: A proton-transport catalysis strategy in the water-catalyzed [1,2]-hydrogen shift. *J. Am. Chem. Soc.* **2007**, *129* (50), 15503–15512. DOI: 10.1021/ja071070+.

(93)   Sameera, W. M. C.; Hatanaka, M.; Kitanosono, T.; Kobayashi, S.; Morokuma, K. The Mechanism of Iron(II)-Catalyzed Asymmetric Mukaiyama Aldol Reaction in Aqueous Media: Density Functional Theory and Artificial Force-Induced Reaction Study. *J. Am. Chem. Soc.* **2015**, *137* (34), 11085–11094. DOI: 10.1021/jacs.5b05835.

(94)   Tafida, U. I.; Uzairu, A.; Abechi, S. E. Mechanism and rate constant of proline-catalysed asymmetric aldol reaction of acetone and p-nitrobenzaldehyde in solution medium: Density-functional theory computation. *J. Adv. Res.* **2018**, *12*, 11–19. DOI: 10.1016/j.jare.2018.03.002.

(95)   Jung, Y.; Marcus, R. A. On the theory of organic catalysis "on water." *J. Am. Chem. Soc.* **2007**, *129* (17), 5492–5502. DOI: 10.1021/ja068120f.

(96)   Hatanaka, M.; Morokuma, K. Role of water in Mukaiyama-aldol reaction catalyzed by lanthanide Lewis acid: A computational study. *J. Am. Chem. Soc.* **2013**, *135* (37), 13972–13979. DOI: 10.1021/ja407357c.

(97)   Chang, C. R.; Huang, Z. Q.; Li, J. The promotional role of water in heterogeneous catalysis: mechanism insights from computational modeling. *WIREs Comput. Mol. Sci.* **2016**, *6* (6), 679–693. DOI: 10.1002/wcms.1272.

(98)   Gualandi, A.; Anselmi, M.; Calogero, F.; Potenti, S.; Bassan, E.; Ceroni, P.; Cozzi, P. G. Metallaphotoredox catalysis with organic dyes. *Org. Biomol. Chem.* **2021**, *19* (16), 3527–3550. DOI: 10.1039/d1ob00196e.

(99)   Chan, A. Y.; Perry, I. B.; Bissonnette, N. B.; Buksh, B. F.; Edwards, G. A.; Frye, L. I.; Garry, O. L.; Lavagnino, M. N.; Li, B. X.; Liang, Y.; Mao, E.; Millet, A.; Oakley, J. V.; Reed, N. L.; Sakai, H. A.; Seath, C. P.; MacMillan, D. W. C. Metallaphotoredox: The Merger of Photoredox and Transition Metal Catalysis. *Chem. Rev.* **2022**, *122* (2), 1485–1542. DOI: 10.1021/acs.chemrev.1c00383.

(100)   Kojima, M.; Matsunaga, S. The Merger of Photoredox and Cobalt Catalysis. *Trends Chem.* **2020**, *2* (5), 410–426. DOI: 10.1016/j.trechm.2020.01.004.

(101)   Chilamari, M.; Immel, J. R.; Chen, P.-H.; Alghafli, B. M.; Bloom, S. Flavin Metallaphotoredox Catalysis: Synergistic Synthesis in Water. *ACS Catal.* **2022**, *12* (7), 4175–4181. DOI: 10.1021/acscatal.2c00773.

(102)   Roesky, H. W.; Walawalkar, M. G.; Murugavel, R. Is water a friend or foe in organometallic chemistry? The case of group 13 organometallic compounds. *Acc. Chem. Res.* **2001**, *34* (3), 201–211. DOI: 10.1021/ar0001158.

(103)   Sather, A. C.; Lee, H. G.; Colombe, J. R.; Zhang, A.; Buchwald, S. L. Dosage delivery of sensitive reagents enables glove-box-free synthesis. *Nature* **2015**, *524* (7564), 208–211. DOI: 10.1038/nature14654.

(104)   Zhou, F.; Li, C. J. En route to metal-mediated and metal-catalysed reactions in water. *Chem. Sci.* **2019**, *10* (1), 34–46. DOI: 10.1039/C8SC04271C.

Chapter 2 – Index

2. Exotic molecular species

2.1.   Introduction

2.1.1. *Astrochemistry and molecular spectroscopy*

Astrochemistry is the research field devoted to the study of chemical composition and evolution of ordinary matter in space. In the first half of the 20th century, astrophysicists considered the ISM as too hostile to bear any chemical complexity. During this time, however, they understood that "no absolute vacuum can exist within the galaxy".[1] When radio astronomy took hold in the late 1960s and beginning of the 1970s, the idea of a "chemically hostile" ISM was questioned with the discovery of the first interstellar polyatomic molecules. Over the decades, the chemical complexity has become more and more evident, with lots of molecular species being detected every year.[2] In the meantime, astronomers began questioning about the presence of condensed matter. Its presence was inferred in 1930,[3] but it was mainly considered as an annoying interstellar "fog" hampering accurate astronomical measurements.[4] During the following years, however, an increasing interest was devoted to the physico-chemical properties of what was denoted as cosmic (or interstellar) dust. In particular, the gas condensation scenario – speculating on the formation of water-, ammonia-, and methane-based ices starting from the ISM diffuse gaseous matter – was introduced in the mid 1940s,[5,6] and it represented the base for the so-called "dirty ice" model. The popularity of the latter kept growing until the birth of radioastronomy,[7] but the model was inconsistent with some astronomical observations, and the "silicide condensation core" model (i.e. silicate particles as dust grains for the icy mantle to grow on)[8] was hence proposed. With the detection of silicates in the late 1960s,[9,10] together with the first positive evidence for the presence of an organic dust component (in 1980),[11] mixed models were proposed.[12] In particular, the so-called "cyclic evolutionary model", also involving organics, was developed in the late 1990s.[13] According to this model, interstellar ices evolve chemically and physically in the ISM, and so do the organics (trapped in the icy matrix), in a complex evolutionary picture, involving also the surrounding diffuse gas phase.

For both the gas phase and dust grains, physics and chemistry are intimately interconnected and interdependent: whenever a region of the universe undergoes some physical changes, the latter often enable new chemistry, which in turn can deeply affect further physical evolution.[14] Current state-of-the-art radio telescopes – featuring high sensitivity and resolution, both spectral and spatial – allow a better understanding of interstellar physics, which can be probed by means of rotational line emission, thus enabling the determination of particle density, temperatures, and dynamics of the observed astronomical region.[15] In particular, radio astronomy techniques are responsible for most of new molecule detections (more than 90%). This evident preponderance can be understood by briefly reviewing their characteristics

and their limitations. The main parameter to be considered is the energy required – compared to the available energy in the studied astrophysical environment – to populate molecular energy levels, thus enabling a familiar partition of the electromagnetic spectrum for molecular spectroscopy purposes: radio- and microwaves, infrared radiation, and UV-visible radiation.

The first range spans from centimetre to sub-millimetre wavelengths. The main spectroscopic features observed in such region are those due to the rotational motion of molecules, whose energetics can be understood by considering the simple case of a linear molecule. The energy of the rotational level J (this being the quantum number representing the quantisation of rotational energy) is given by:

$$E_J = BJ(J + 1) \tag{2.1}$$

where B is the rotational constant of the molecule, which is inversely proportional to the molecular moment of inertia, denoted as I:

$$B = \frac{h^2}{8\pi^2 I} \tag{2.2}$$

In turn, I depends on the mass distribution of the molecule. In the approximation of atoms as point masses, once the molecular rotation axis R is identified, the moment of inertia of a linear molecule with N atoms can be defined with respect to this axis as follows:

$$I_R = \sum_{i=1}^{N} m_i \cdot r_{iR}^2 \tag{2.3}$$

where m_i is the mass of the i-th atom, and r_{iR} its distance from the rotation axis R.
Therefore, small molecules have large values of *B*,[16] while large species are characterised by small *B* values.[17] According to Equation 2.1 and to the selection rule for rotational spectroscopy ($\Delta J = \pm 1$, with + sign referring to absorption and – to emission), the observed frequencies of rotational transitions correspond to the difference between energy levels:

$$\Delta E_{J+1,J} = E_{J+1} - E_J = 2B(J + 1) \tag{2.4}$$

Therefore, according to the discussion above, small molecules (large B values and hence widely spaced energy levels) have rotational transitions lying at high frequencies. Larger molecules (small B and thus closely spaced energy levels), on the contrary, have rotational transitions at lower frequencies.
In general, the size range of typical interstellar molecules is compatible with rotational transitions falling between ~500 MHz and ~1 THz, thus making radio telescopes by far the most used facilities for the

observation of pure rotational transitions. The energies involved in these transitions determine how and where they can be observed. The equivalent thermal energy of most rotational levels of interstellar species is typically well below 1000 K. This kind of energy is available in sufficiently dense environment, in which the population distribution is ruled by the collisions between gas particles, and it depends on the kinetic temperature of the medium. Such condition is referred to as local thermodynamic equilibrium. In particular, hot cores and similarly warm regions with sufficient thermal energy (T = 100−500 K), feature a high population distribution: their emitted radiation (due to rotational transitions) is well distinguishable from the background radiation field, and it can be easily detected and analysed.[18] However, even very cold regions (T = 5−10 K) are still characterised by sufficient energy to populate the lowest few rotational energy levels, thus enabling the observation of rotational emission.[19] When even colder regions are studied, there is no more detectable emitted radiation compared to the background radiation field. Nevertheless, molecules can still be detected in absorption if they are located along the sight-line of a suitable background continuum source.[20] All these examples are meant to give a clear picture of the major strength of radio astronomy: it enables the detection of molecules in most of astronomical sources, either in emission (due to the low energy required to populate rotational levels) or in absorption against a background continuum source.

However, some important drawbacks must be pointed out. Completely symmetric molecules (i.e. with null permanent electric dipole moment) cannot be detected, and even the highly symmetric ones are very hard to detect. Furthermore, the more the molecular degrees of freedom (i.e. higher molecular size and complexity), the more the number of accessible energy levels. Hence, population partitioning among these levels results in a tremendous drop in the number of molecules emitting/absorbing at a given frequency. Finally, radio astronomy is completely blind to the molecules trapped in the condensed phase.

The second spectral region is the infrared one. The energy differences between vibrational states are much higher than those involved in pure rotational transitions. Hence, vibrational levels can be populated in presence of radiative pumping mechanisms or at sufficiently high temperatures. Such conditions are not so common from the astrochemical point of view, thus reducing the possibility of observing vibrational transitions in emission. A noteworthy example is represented by polycyclic aromatic hydrocarbons (namely PAHs) which are thought to be responsible for the so-called unidentified infrared emission bands.[21] However, vibrational transitions can still be observed in absorption, but the conditions for such observation – i.e. the presence of a proper sightline-lying background source, lighting up an environment which has to be optically thin enough so that the light coming from the source can go through it – are much rarer than those required for the observation of rotational transitions in absorption. Nevertheless, IR astronomy can fill some pivotal gaps, since it can reveal the presence of highly symmetric molecules, and even those lacking permanent dipole moments. Furthermore, it enables the observation of molecular species in the condensed phase, such as those trapped within interstellar ices.

Indeed, vibrational transitions remain accessible in the case of condensed-phase molecules. Moreover, the properties of the matrix trapping the probed molecules can be studied because they can alter their vibrational frequencies.[22] Since such alterations can also be studied and thus interpreted in the laboratory, IR astronomy is a powerful tool for the study of ISM condensed materials.[23]

Visible and ultraviolet ranges represent a very small niche in terms of spectroscopic relevance in the field of interstellar chemistry. Such radiations are energetic enough to trigger molecular or atomic electronic transitions,[24] which can be observed even for molecular species with no permanent dipole moment, thus giving an important contribution to patch the blindness of radioastronomy. Nevertheless, the required energies are very high, and only few astrochemically relevant environments – such as stellar atmospheres – were found to be sufficiently energetic to display spectroscopically relevant emission features in the UV-Vis range.[25] Furthermore, such conditions do not allow molecular species to survive long: most molecules, whenever formed or brought in such regions, simply dissociate into their constituent atoms. However, fruitful absorption spectroscopic analyses in the UV-Vis range – leading to a few detections so far – are still possible whenever diffuse line-of-sight interstellar clouds are irradiated by the proper continuum background sources. Such conditions are much rarer than those required for IR absorption spectroscopy, since interstellar clouds are characterized by much higher opacities in the UV-Vis range than in the IR.

As well highlighted above, the lower the energy of the molecular levels involved in the chosen spectroscopy, the higher the number of ISM molecular species detected by means of that spectroscopy so far. However, very important reaction pathways – otherwise inaccessible – can be triggered only in sufficiently energetic environments.[26] In particular, when electromagnetic radiations are involved, the higher their energy, the higher the possibility that they can induce relevant chemical transformations. It goes without saying that highly energetic radiations can be fruitful in terms of molecular evolution only whenever the proper equilibrium between photon density, temperature, and particle density is reached, so that photodissociative pathways do not largely outnumber other ones (i.e. leading to complete dissociation of any molecules into their constituent atoms).

This dichotomic importance of electromagnetic radiations depending on their energy can be easily understood in the case of interface chemistry of dust grains in the interstellar medium, where both temperatures and particle densities play pivotal roles.[27] Whenever dust grains are exposed to sufficiently energetic environments, their icy surfaces are heated: photo- and thermal desorption processes (based on highly energetic phenomena) allow complex molecules to escape the outer layers of the grains.[28] Such complex molecules, once in the gas phase, become detectable with radioastronomy (based on much less energetic phenomena). The aforementioned importance of temperatures and particle densities is also

evident: dust grains can be considered as "concentrators" of molecules, thus allowing them to react on their surfaces; furthermore, dust grains can display thermal flywheel effects, i.e. they can "buffer" temperature fluctuations, also those due to non-radiative transitions following absorption of highly energetic radiations.[29] These combined effects, when properly balanced, can trigger interesting chemical transformations even at very low temperatures, also thanks to quantum effects such as quantum tunnelling.[30–35] As a matter of fact, most astrochemical transformations occur at much lower temperatures and pressures compared to those typical of terrestrial laboratories, thus taking place over much longer time scales, up to millions of years.[36] Nonetheless, the understanding of such processes requires laboratory experiments, mainly for the production and spectroscopical characterization of astrochemically relevant species, but also to probe different reaction channels potentially open in the studied astrochemical conditions.[37,38] From this point of view, imines represent an interesting class of organic compounds. Some of them are rather unstable in terrestrial conditions, but have been detected in the ISM, while other imines are bench-stable compounds which have been successfully synthetized using standard laboratory conditions, but they have never been detected in the ISM so far (vide infra). The next section will give a clear picture to explain such dichotomy.

2.1.2. The case of N−H imines

Imines are known to be involved in many chemical processes, from organic chemistry to biochemistry. They are crucial intermediates in organic methodologies for the synthesis of N-bearing organic compounds (Figure 2.1A).[39] Moreover, the imine functional group is extensively present in biologically active molecules (Figure 2.1B).[40–43]
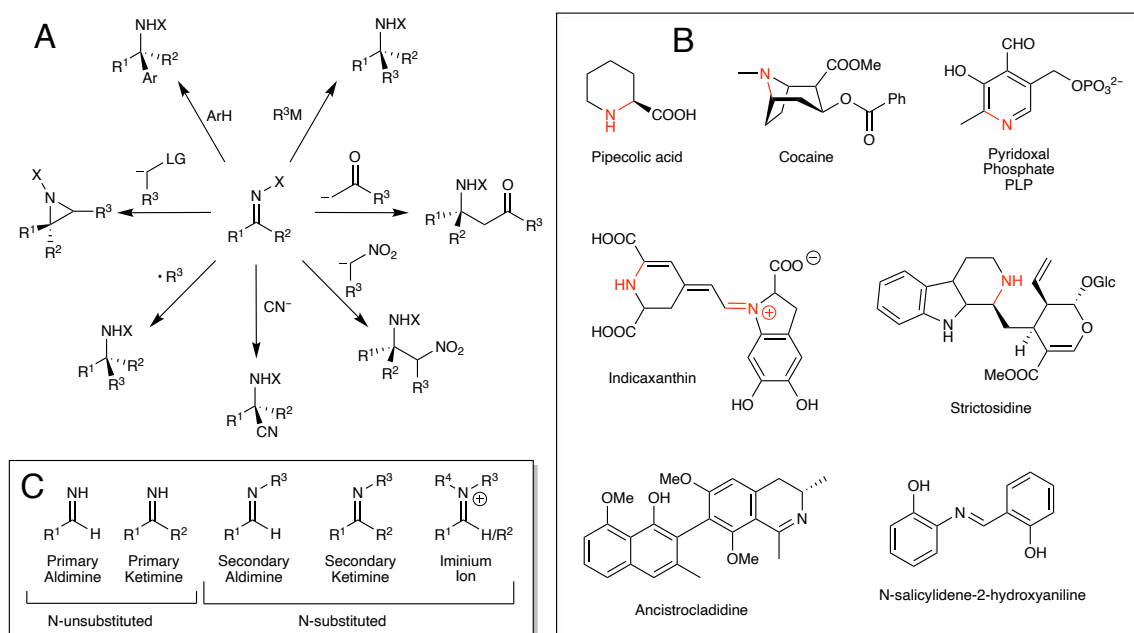
Figure 2.1: (A) Some examples of imine derivatization (mainly additions, see Ref. 39). **(B)** Selected imine-derived natural products (imine-derived C−N bonds depicted in red) and imine-based bioactive molecules (see Refs. 42, 43). **(C)** Imine nomenclature.

The chemistry of vision represents a noteworthy example of imine-based biochemical processes (Figure 2.2). The light-sensitive receptor protein involved in visual phototransduction, namely rhodopsin, is an imine-type macromolecule, resulting from the condensation reaction between an aldehydic cofactor, i.e. 11-*cis*-retinal, and a primary amino group belonging to a protein molecule called opsin.[44–46]
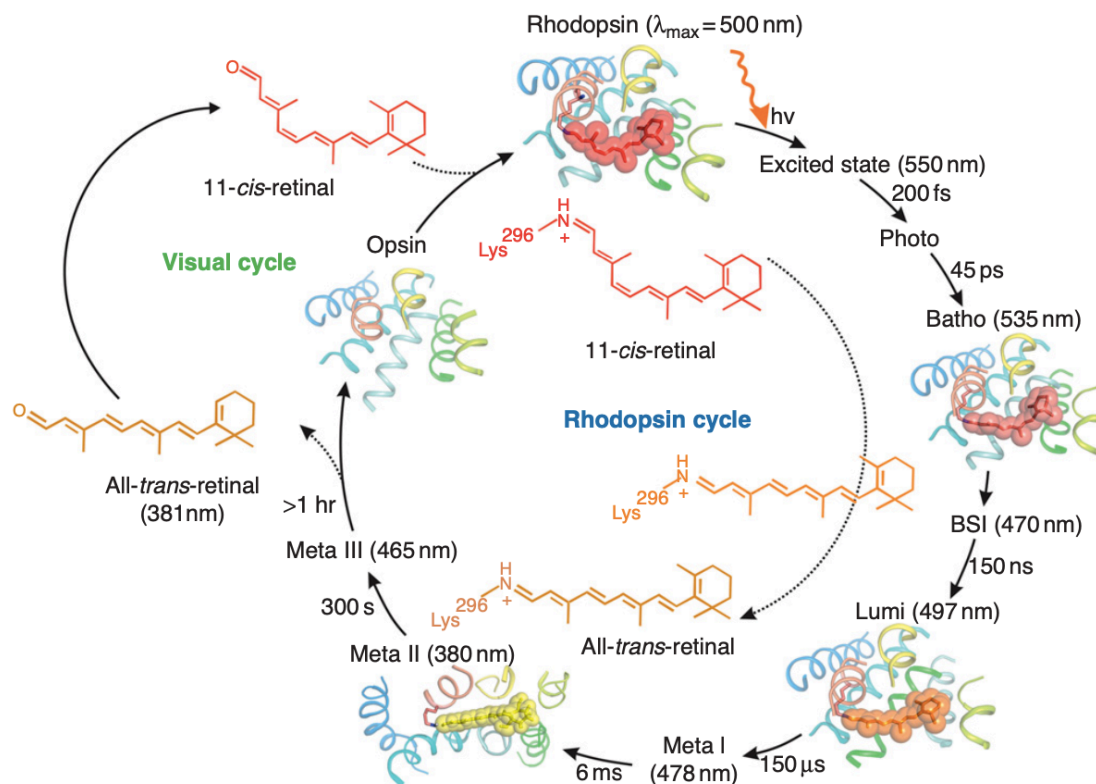
Figure 2.2: Schematic illustration of the rhodopsin cycle (see Ref. 46).

Formally, an imine is the product of the condensation reaction between a carbonyl compound, i.e. an aldehyde or a ketone, and an amine, leading to aldimines or ketimines, respectively. Such condensation reaction is usually performed in the presence of an acid catalyst, with concomitant removal of water, either through azeotropic distillation, or using drying agents, such as molecular sieves or magnesium sulfate (Scheme 2.1A).[47] Depending on the nature of the employed amine, i.e. ammonia or a primary amine, imines can be divided in N−H (also referred to as N-unsubstituted) and N-substituted, respectively (Figure 2.1C). The former are usually much more reactive than the latter.[48] In particular, organic chemists are well aware of the instability of most N−H imine derivatives of aliphatic or aromatic aldehydes. Indeed, only in a few cases they have been successfully isolated or characterized.[49,50] It is worth mentioning the case of some relatively stable primary ketimines with two aromatic substituents: a remarkable example is benzophenone imine ($R^1 = R^2 = Ph$, vide supra), a bench-stable compound which has been extensively used as synthetic equivalent of ammonia in the Buchwald-Hartwig amination reaction.[51] Generally, in the case of N−H imines, a reactivity trend can be observed: the less the number of (aromatic) substituents, the higher the reactivity (and hence the difficulties concerning their isolation). Nevertheless, aromatic aldimines have been identified as important reactive reaction intermediates.[52,53] The labile character of most N−H imines – responsible for the common unfeasibility of their isolation – resulted in the employment of N-substituted imines, i.e. possessing various substituents on the nitrogen atom. Such substituents are used as either activating or protecting groups, depending both on the nature of the imine and on the desired subsequent transformations, and they are usually removed after the synthetic endeavour. The use of N-unsubstituted imines would be ideal to avoid protection and deprotection steps, but the approaches leading to their generation are limited to (often putative) unstable uncharacterized intermediates, whose presence is often strongly debated.[54] In particular, the aforementioned condensation reaction between ammonia and aldehydes is not suited for the synthesis of N−H aldimines. On the one hand, controlled formation of N−H imines can be achieved through peculiar hydrolytic pathways starting from N-metalloimines or silylimines.[55] Even azide precursors can be used to access N−H imines under catalytic conditions, upon loss of N_2 and subsequent migration of hydrogen (Scheme 2.1B).[56–58] Other azide-bearing compounds – such as β-hydroxy azides[59] and α-azidocarboxylic acids[60] – were recently used for the formation of N−H imines in the presence of ruthenium catalysts under photocatalytic conditions.
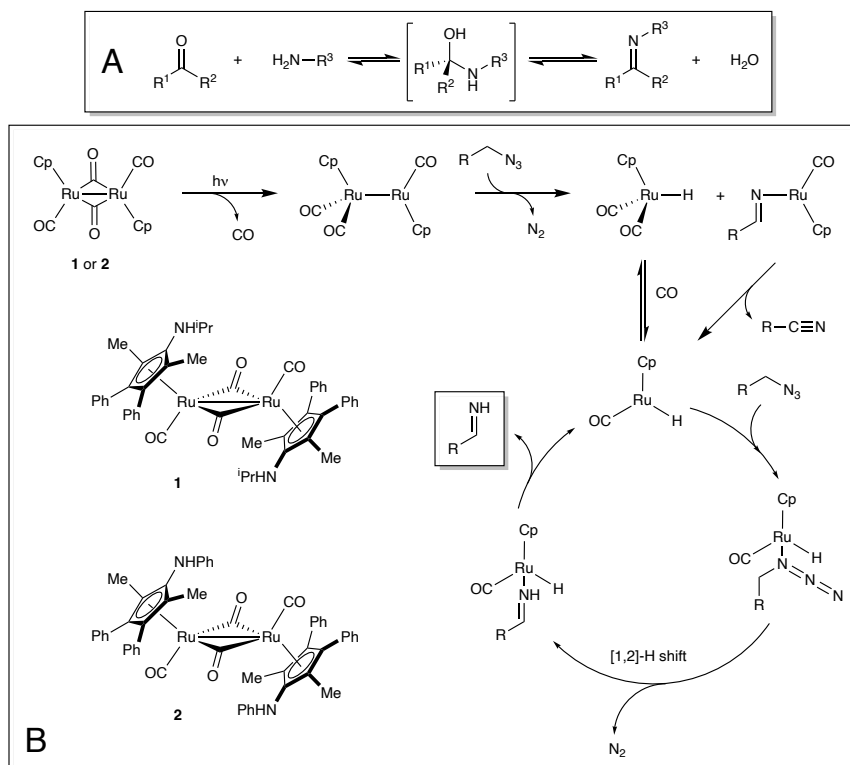
Scheme 2.1: (A) General synthetic approach to imines: condensation reaction between a carbonyl compound and a primary amine (see Ref. 47). **(B)** Selected mechanism for the catalytic generation of imines starting from azides (see Ref. 58).

On the other hand, despite being particularly appealing, hydrogenation protocols starting from the corresponding nitriles are not feasible, due to catalytic conditions which are not compatible with a single hydrogenation process. Indeed, such approaches either directly lead to the saturated derivative, i.e. the corresponding amine, or they afford a mixture of primary-, secondary-, and even tertiary-amines, via cascade pathways – with alternating hydrogenation and nucleophilic addition steps – involving the N−H imine intermediates present in the reaction mixture (Scheme 2.2A).[61–66] Even the other way round, i.e. the oxidation of primary amines, cannot be exploited to synthetize N−H imines. Indeed, once an imine species is generated in the reaction mixture, unless it is further oxidized to the respective nitrile,[67–70] it usually undergoes hydrolysis to give the respective carbonyl compound (reverse reaction of Scheme 2.1A);[71] otherwise, if hydrolysis rates are somehow controlled, the newly-generated imine can either condense with an unreacted amine molecule (with the straightforward elimination of ammonia), or undergo hydrolysis followed by condensation with an unreacted amine molecule (Scheme 2.2B).[72–74]
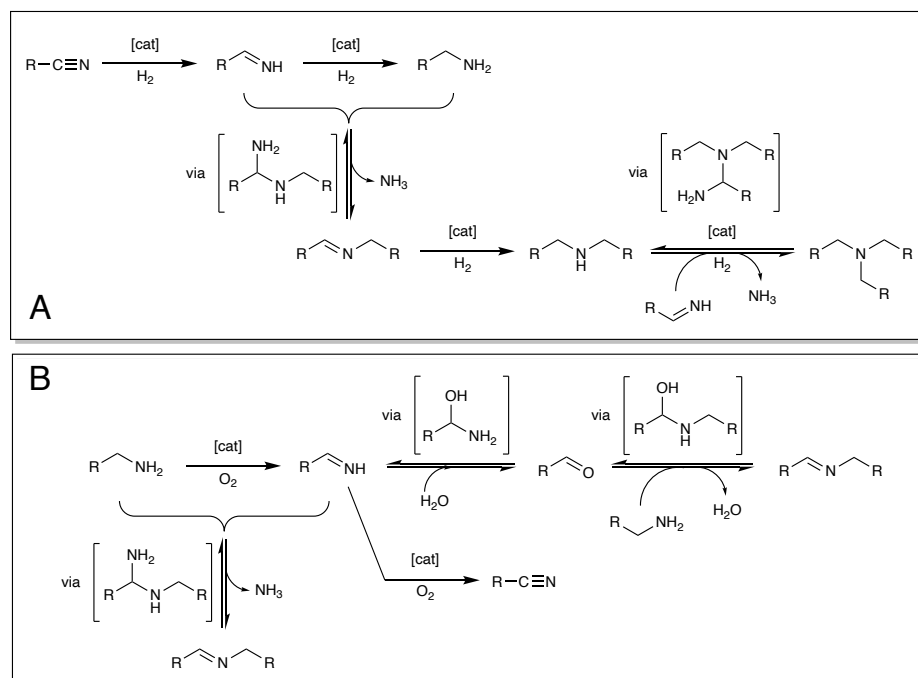
Scheme 2.2: (A) General mechanism for the hydrogenation of nitriles (see Refs. 63, 65, 66). **(B)** General mechanism for the oxidation of amines (see Refs. 72, 73).

All the aforementioned synthetic issues make the characterization of N−H imines a challenging task. The most detrimental feature of classical organic synthetic protocols, hampering the characterization of N-unsubstituted imines, is the nature of the reaction medium: whenever reactive species, such as N−H imines, are generated in the condensed phase, their further transformations are not only unhampered but rather favoured by the close proximity with other species. The best ways to avoid further reactivity are either the use very diluted solutions (but even the solvent molecules can react with sufficiently reactive species), or the generation of the reactive species in the gas phase under low pressure and temperature conditions. In the latter case, the molecules can be considered as non-interacting, due to the very low particle density, and the generated reactive species have no sufficient thermal energy to undergo further chemical evolution on their own. As already mentioned, most detrimental features of "terrestrial" organic procedures do not concern interstellar chemistry. Indeed, the chemical reactivity in the interstellar medium is very different from the terrestrial counterpart. Hence, ISM harbours plenty of reactive and/or unstable species, such as some N−H imines,[75–79] which can survive long in the ISM due to its low temperatures and particle density. The long half-life of such exotic species in the ISM enables their detection by means of radioastronomical observation. However, to confirm such detections, a successful laboratory spectroscopic characterization is mandatory. This dichotomy between the presence of exotic molecular species in the ISM and their very short half-life in "terrestrial" laboratory conditions can be overcome with state-of-the-art instrumental setups, involving the direct generation of labile species inside the spectrometer. The multidisciplinary effort behind the detection of new interstellar species represents one of the most challenging tasks in the field of astrochemistry. The main approaches to generate unstable

species just before spectroscopic analyses are usually based on harsh conditions and rather poorly predictable techniques,[80] such as pyrolysis[81] or electric discharge.[82] However, in some cases, milder conditions – with accurately tuned pressures and temperatures – can be used to generate exotic species with high selectivity, albeit such generation can be very slow, with the desired species being released in the spectrometer in very low amounts, but still sufficient for a complete characterization. In particular, the thermally tuneable formation of imines could be exploited both in the gas phase and in solution for the characterization of phenylmethanimine (PMI).

2.2.   Aim

PMI is an elusive aromatic imine whose characterization is highly desirable for both organic synthesis and astrochemistry. A multidisciplinary strategy has been exploited for the production of PMI in the gas phase and in solution. In particular, the described formation pathway of PMI is based on the thermal decomposition of hydrobenzamide (HBA). A state-of-the-art computational characterization of both isomers of PMI (i.e. *E* and *Z*), in terms of structural and spectroscopic properties, was preliminarily performed to enable its first laboratory observation by means of rotational spectroscopy. This spectroscopic analysis is a preliminary step for future astronomical searches. A further characterization has been carried out using NMR spectroscopy, which enabled the investigation of HBA decomposition in solution. The temperature dependence as well as possible mechanisms of the thermolysis process have been examined.

2.3.   Results and discussion − Phenylmethanimine (PMI)

The detection of benzonitrile (BN) in the Taurus Molecular Cloud (TMC-1) is generally recognized as a milestone in the field of astrochemistry.[83] Such finding was celebrated as the strongest available proof of the presence of benzene in the ISM.[84] Indeed, ground-based astronomical detections of benzene fingerprints are made impossible by two main issues: its infrared vibrational transitions are blocked by atmospheric absorption, and its high molecular symmetry is responsible for its null permanent dipole moment. Thus, no pure-rotational detections are feasible, as already mentioned in Section 2.1.1. Therefore, observations of benzene have been limited to space-based infrared telescopes for the detections of its vibrational transitions. In particular, benzene has only been detected in absorption against few suitable bright sources using the Spitzer Space Telescope and the Infrared Space Observatory.[85–87] Similarly to the case of benzene, the presence of other cyclic and polycyclic aromatic hydrocarbons, such as cyanocyclopentadienes and cyanonaphthalenes, was inferred by other recent detections of nitrile-bearing derivatives.[88–90] The presence of nitrile-bearing unsaturated hydrocarbons serves as a faithful proxy for parent unfunctionalized species.[91] Indeed, reactions of unsaturated hydrocarbons with the ISM-abundant CN radical, are usually exothermic and barrierless, thus being open reaction channels in the ISM.[92–94] In addition to the speculations concerning the possible precursors of nitrile-bearing aromatic hydrocarbons, the detections of such species in the ISM open up new interesting scenarios for the evolution of interstellar organic matter. In particular, polycyclic aromatic nitrogen heterocycles (namely PANHs) are structurally linked to CN-bearing aromatic hydrocarbons, and the presence of the latter in the ISM must be taken into account to understand the origin of PANHs.[95] Finally, the large abundance of hydrogen in the ISM may be responsible of interesting hydrogenation pathways, involving either the cyclic cores or the functional groups at the boundaries.[96,97]

As far as BN is concerned, it can be considered as the precursor of an interesting imine, namely phenylmethanimine (PMI). Hence, the spectroscopic detection of PMI in the ISM (more specifically, starting from the same astronomical sources where BN was detected) is plausible. However, the detection of a molecular species in the ISM requires its experimental spectroscopic characterization, which in turn implies an effective production of the species of interest. Formally, PMI is the imine obtained upon condensation between benzaldehyde (BA) and ammonia, and it exists in two geometric isomers, namely *E* and *Z*, referring to the relative position of the phenyl group with respect to the imine hydrogen (Scheme 2.3, left-hand reaction). However, BA and ammonia, reacting in standard laboratory conditions, generate no PMI at all, but rather a pseudo-trimeric product, namely hydrobenzamide (HBA, Scheme 2.3, right-hand reaction), as white solid.[98–101]
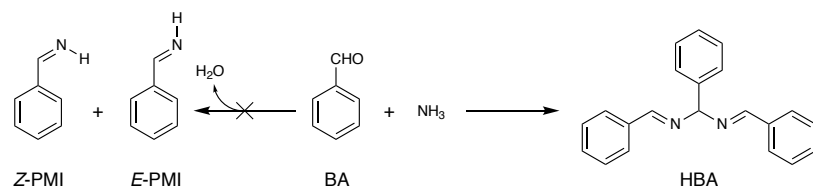
Scheme 2.3: Formal (left) and actual (right) condensation reaction between benzaldehyde (BA) and aqueous ammonia. The products are phenylmethanimine (PMI) and hydrobenzamide (HBA), respectively.

The latter (which can be easily isolated, purified and characterized) can be classified as an aminal, obtained through the formal condensation reaction between BA and two molecules of PMI. The elusiveness of the reactive PMI, hand in hand with the observation of much more stable species (such as HBA, BA, BN, or amines, depending on the reaction conditions), was highlighted many times, and PMI could only be hypothesized as a relevant reaction intermediate.[102–104] Indeed, PMI has never been isolated. There are just a few noteworthy works reporting its NMR identification.[58,59,105] Furthermore, all the reported approaches are not suitable for the generation of PMI in the gas phase (i.e. as required by rotational spectroscopy). Thermally tuneable approaches from simple precursors are desirable alternatives, since they avoid critical issues such as: (i) demanding experimental setups requiring subtle control of reaction conditions; (ii) trapping procedures leading to imine complexes; (iii) use of transition metal catalysis; (iv) unfeasible interface with spectroscopic techniques. Eventually, we were pleased to observe the thermal generation of PMI starting from HBA, both in the gas phase and in solution, thus resorting on rotational and NMR spectroscopy, respectively. This enabled the first complete and accurate spectroscopic characterization of both isomers of PMI by means of rotational spectroscopic techniques, which is prerequisite for its identification in the ISM with radioastronomy. In the following, a full account of such successful endeavour will be reported.

2.3.1. *Rotational spectroscopy of PMI in the gas phase* [†]

The spectroscopic characterization of a molecular species relies on the identification and assignment of its spectroscopic patterns in the recorded rotational spectrum. However, for unstable molecules, directly produced inside the spectrometer cell, such characterization is hampered by the concomitant presence of several different species, whose features contribute to the overall spectrum. To guide the analysis and interpretation of the rotational spectra, a state-of-the-art quantum chemical characterization has been performed. Using the density functional theory (DFT), the potential energy surface of PMI was preliminarily scanned, and its two isomers were located (Figure 2.3). The structures of the latter were accurately computed by means of the so-called "cheap" composite scheme (ChS), which

also provided accurate electronic energies.[106] The analysis revealed that the *E* isomer is 6 kJ mol⁻¹ more stable than the *Z* species. The transition state between the two isomer was identified and properly characterized, revealing a quasi-linear C-N-H geometry.
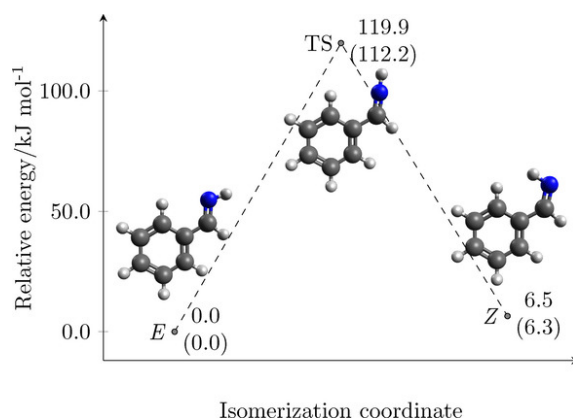

Figure 2.3: Computed energies (ChS level) for the two isomers of PMI (i.e. *E* and *Z*) and the transition state ruling their interconversion. The values in parentheses include harmonic B2PLYP zero-point energy corrections (from Ref. 107, CC BY 4.0).

Indeed, the isomerization process was found to occur in the molecular plane, similarly to what previously determined for other imines, such as ethanimine[108] and C-cyanomethanimine.[109] The interconversion is characterized by an isomerization barrier of 112 kJ mol⁻¹. The geometrical characterization is the starting point for the prediction of the spectroscopic parameters. Indeed, the equilibrium structure of a molecular species straightforwardly provides the equilibrium rotational constants. Even if they contribute to nearly 97-99% of the vibrationally averaged rotational constants (i.e. those corresponding to the vibrational ground state, where the molecules usually lie), the vibrational corrections need to be evaluated and incorporated. Since their evaluation is computationally expensive because it involves anharmonic force-field calculations, DFT (in particular the B3LYP functional) has been used.[110,111] Other properties that are required for predicting the rotational spectrum are centrifugal distortion constants, dipole moment components, and nuclear quadrupole coupling constants. The first parameters account for the fact that the molecule is not a rigid rotor, and the latter ones describe the interaction between the quadrupole moment of the nitrogen atom with the electric field gradient at the nucleus, which is responsible of peculiar features in the rotational spectrum (vide infra). The dipole moment components are instead needed for predicting the intensity of the rotational transitions. All these properties were computed using the double-hybrid B2PLYP functional.[112]

The experimental gas-phase characterization of PMI was performed in the 3−26 GHz range, using the COBRA-type (Coaxially Oriented Beam Resonator Arrangement) Fourier Transform Microwave Spectrometer (FTMW).[113] The reservoir of a nozzle valve was filled with HBA and heated in the 30−100 °C temperature range. The vapours were mixed with neon (backing pressure: 1 bar) and then adiabatically expanded into the cavity of the spectrometer, through a solenoid valve, resulting in a supersonic jet. The

accuracy of the computational prediction allowed an easy interpretation of the rotational spectrum and the unequivocal identification of both PMI isomers.[114] For each isomer, more than one hundred rotational transition frequencies could be identified and assigned. Each transition shows a unique pattern due to the presence of the ^{14}N nucleus, responsible – as mentioned above – for the quadrupole coupling. This interaction leads to the splitting of the rotational energy levels, which in turn determines a splitting of the rotational transitions, the so-called hyperfine structure (see Figure 2.4).[115] Furthermore, all rotational lines appear as doublets because of Doppler effect due to the coaxial alignment of the resonator with respect to the molecular beam. The most stable E isomer was also characterized in the $83-100$ GHz range, using a frequency-modulation millimetre-wave (FM-mmW) spectrometer,[116] and employing a different strategy for the generation of PMI, i.e. flash vacuum pyrolysis (FVP)[117,118] of a sample of α-methylbenzylamine (890 °C). The latter approach will be described in detail in Section 2.3.3.
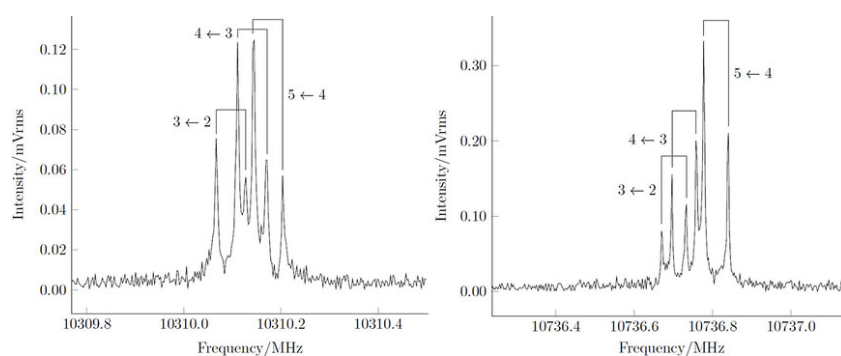
Figure 2.4: Hyperfine structures of selected rotational transitions ($J_{Ka,Kc} \leftarrow J'_{Ka',Kc'}$) of E- and Z-PMI: $4_{1,4} \leftarrow 3_{1,3}$ and $4_{0,4} \leftarrow 3_{0,3}$ respectively. The reported quantum numbers refer to the nuclear quadruple coupling scheme $F \leftarrow F'$, $F = J+I$. The Doppler effect is responsible for the highlighted splitting of each spectral line (from Ref. 107, CC BY 4.0).

The recorded and assigned transition frequencies were analysed using a suitable effective Hamiltonian, thus leading to the derivation of the main spectroscopic parameters. The weighted non-linear fit of the rotational transitions was performed using the Pickett's CALPGM suite of programs.[119] The comparison between experimental and computed values revealed an excellent agreement (for example, for rotational constants, average and maximum errors are 0.03% and <0.05%, respectively). In particular, when such good agreement concerns structure-dependent parameters, the reliability and accuracy of the computed geometries are strongly confirmed.

Figure 2.5 displays the case of a specific rotational transition, recorded for four molecular species, namely BA, BN, and the E and Z isomers of PMI, using the COBRA-FTMW spectrometer and different temperatures. To allow proper thermalization of the sample after the temperature set up, the measurements were performed no sooner than ten minutes after each temperature change. BA was observed at all temperatures, while clearly distinguishable signals of the PMI isomers are observed only above 80 °C. BN lines appear at the same temperature. For both PMI isomers and BN, the higher the temperature, the more intense the transitions. The presence of water was assessed by checking the

12321.0 MHz transition of the water dimer,[120] which was observed for each temperature increment. Hence, water was found to be systematically present in the experimental apparatus, and it very likely played a key role in the investigated hydrolytic process.
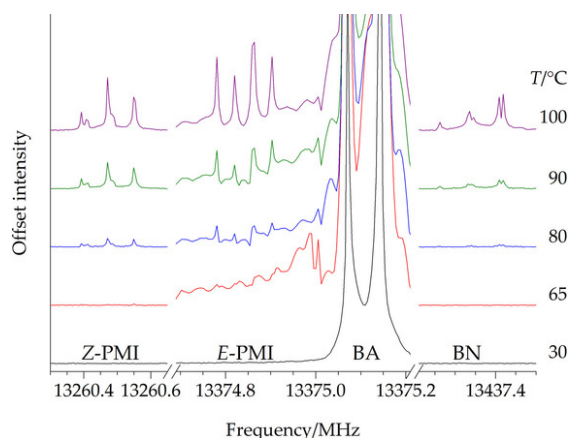

Figure 2.5: Spectral features of the $5_{0,5} \leftarrow 4_{0,4}$ transition for the four investigated molecular species (from Ref. 107, CC BY 4.0).

In principle, the relative populations of the two PMI isomers can be assessed from the spectra of Figure 2.5. Unfortunately, in the case of *E*-PMI, its studied transition lies very close to the strong (out-of-chart) transition of BA: the tail of the BA signal deeply affects the baseline of the *E*-PMI transition, preventing its quantitative comparison with that of *Z*-PMI, and consequently hampering the accurate derivation of the relative populations.

2.3.2. *NMR spectroscopy of PMI in solution*

The mechanism responsible for the generation of PMI vapours starting from HBA was expected to occur through hydrolytic pathways. To support such hypothesis, and to evaluate its extension to the condensed phase (i.e. in solution), even for other N−H imines, the thermal behaviour of HBA in solution has been explored in a similar temperature range (25−110 °C) as gas-phase measurements by ^{1}H-NMR spectroscopy (Figure 2.6, top). Such analyses were performed using 1,1,2,2-tetrachloroethane-d$_2$ (b.p. 147 °C) as the solvent. Quantitative analysis of the diagnostic NMR signals was performed (Figure 2.6, bottom), with particular reference to the temperature dependence of their normalized integral values (with respect to that of the solvent residual peak at 6.0 ppm, arbitrarily fixed to 10).
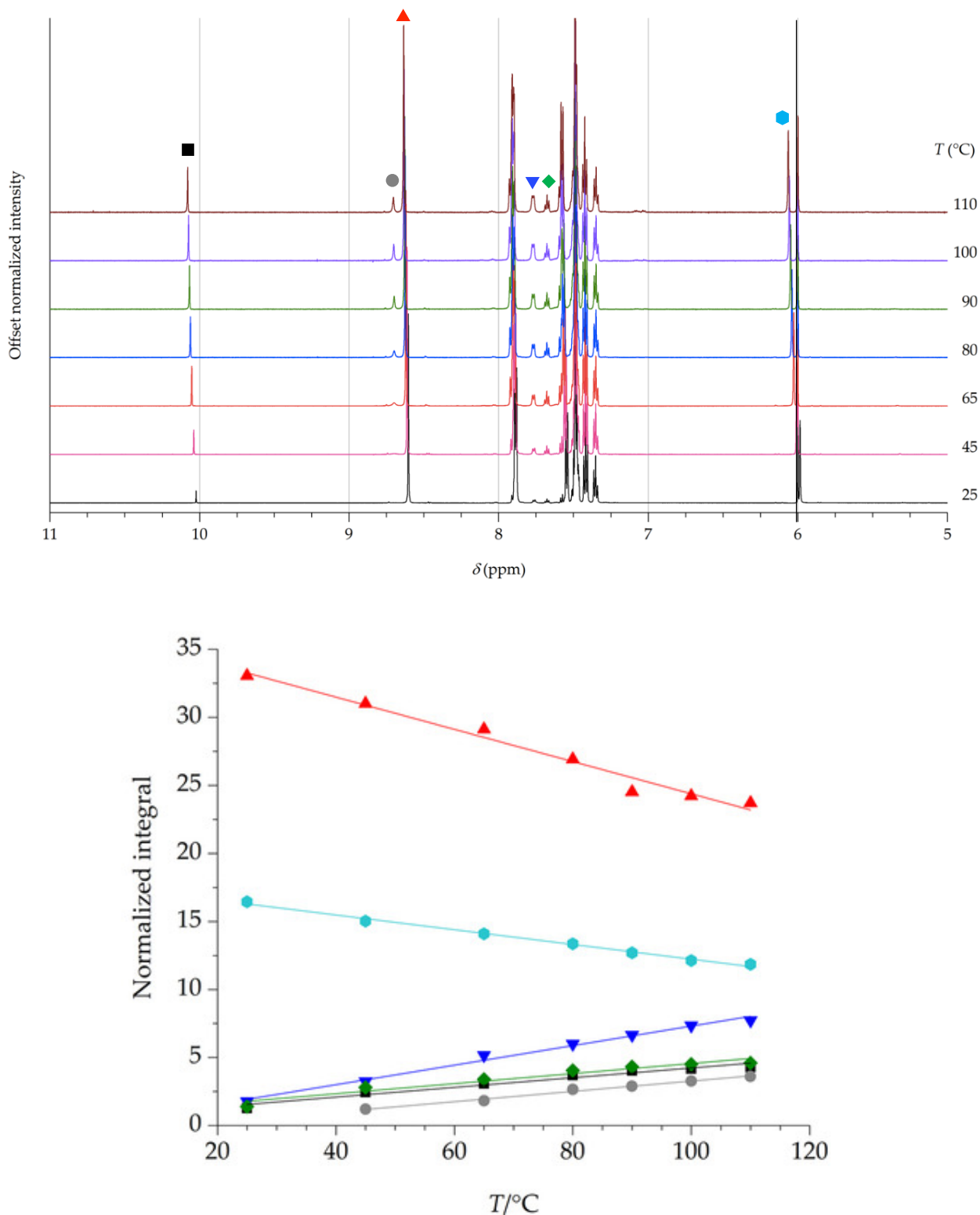
Figure 2.6: Top panel: variable temperature NMR experiments (600 MHz) of an HBA sample dissolved in 1,1,2,2-tetrachloroethane-d$_2$ (C$_2$D$_2$Cl$_4$). The solvent residual peak – highlighted with a vertical black line – was fixed at 6.0 ppm and used as reference signal. The diagnostic NMR signals have been highlighted (vide infra for the assignments). **Bottom panel:** quantitative analysis of variable temperature NMR spectra: temperature-dependence of normalized integral values of NMR signals. Red triangles refer to HBA N=CH (8.63−8.60 ppm), cyan hexagons to HBA aminal (6.06−5.99 ppm), blue triangles to PMI *ortho*-protons (7.77−7.76 ppm), green squares to BA *para*-proton (7.68 ppm), black squares to BA CHO (10.08−10.02 ppm) and grey circles to PMI N=CH (8.70 ppm). (from Ref. 107, CC BY 4.0).

According to the available literature data, since PMI can be present as a mixture of *E* and *Z* isomers, two distinct sets of signals are expected to be present, and the most visible differences can be observed for the C=N protons, which feature different coupling constants depending on the isomer (J_E = 16 Hz, J_Z = 25 Hz).[58] As in the case of the gas-phase experiment, the sample was heated to the desired temperature and the ^{1}H-NMR spectrum was acquired after 10 minutes to avoid thermalization processes during the acquisition. The diagnostic signals of both BA and *E*-PMI were observed with increasing intensities, hand in hand with the increase in temperature. Many signals show a linear dependence with the temperature. In detail, NMR signals corresponding to the precursor (i.e. HBA) are characterized by negative-slope temperature dependences, with the N=CH signals (red triangles) decreasing twice as fast as the single-proton aminal signal. Instead, newly formed species present positive-slope linear regimes. The trends of two signals (i.e. green and black squares) are almost superimposable, in terms of both slope (positive) and normalized integral values. Such overlap occurs either when the respective signals belong to the same species, or if they belong to different species being generated at the same rate. Indeed, these two signals, featuring a 1:1 integration relationship, are compatible with the CHO and *para*-proton (triplet) of BA, respectively. The other two positive-slope signals (i.e. blue triangles and grey circles) feature a 2:1 integration relationship. In particular, the singlet at 8.70 ppm (grey circles) is compatible with an iminic N=CH proton, while the doublet at 7.77 ppm (blue triangles) is compatible with the iminic *ortho*-protons. Furthermore, the trend similarities between the iminic N=CH proton and the aldehydic signals suggest that PMI and BA are generated by putatively interconnected processes. However, BA appears to be produced before PMI, thus suggesting that the involved hydrolytic mechanism proceeds with the initial formation of BA, followed by the formation of PMI starting from other transient species. Noteworthily, neither BN nor *Z*-PMI were detected, even when the top temperature was reached. Nevertheless, the presence of *Z*-PMI could not be unequivocally excluded. The observed differences between the two spectroscopic measurements can be due to either different hydrolytic mechanisms, or the availability of additional pathways in the case of gas-phase measurements. The absence of BN in solution after thermal treatment of HBA was confirmed upon addition of a trace amount of BN to the NMR samples previously heated at 110 °C. The spectrum was again recorded and compared to the one recorded just before BN addition (Figure 2.7). New signals (doublet at 7.68 ppm, overlapping with a BA triplet; doublet at 7.63 ppm; triplet at 7.50 ppm, overlapping with a HBA multiplet) were observed, ascribable to BN and previously absent. The generation of BN in gas-phase experiments may be due to catalytic properties of the metal surfaces, responsible for the fast dehydrogenation of PMI generated in situ.[121–125] The catalytic role of metal surfaces has already been highlighted in other rotational spectroscopy experiments.[126] The complete lack of BN spectroscopic features in the case of NMR experiments in solution, is indeed compatible with the complete absence of metallic surfaces in the NMR tube.
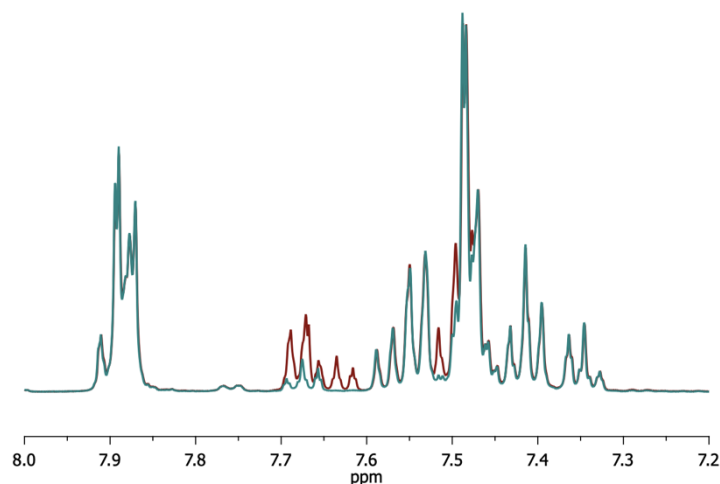
Figure 2.7: ^{1}H-NMR aromatic region (400 MHz, $C_2D_2Cl_4$, 25 °C) of HBA after the thermal gradient, followed by the addition of BN. The teal spectrum is before BN addition, while the red one is after it (from Ref. 107, CC BY 4.0).

2.3.3. Mechanistic hypotheses

Scheme 2.4 depicts a putative hydrolytic pathway in accordance with the observed experimental results.[127–129] In such a general picture, dehydrogenation is supposed to be the main pathway leading to the formation of BN starting from PMI. As already mentioned, such process was found to be active only during COBRA-FTMW measurements. The proposed mechanism, together with the differences between the reported experimental conditions, requires the further analysis of the following key points: (i) the role of water; (ii) the role of metallic surfaces in the COBRA-FTMW spectrometer with respect to the glass surfaces acting in the FM-mmW experiment.
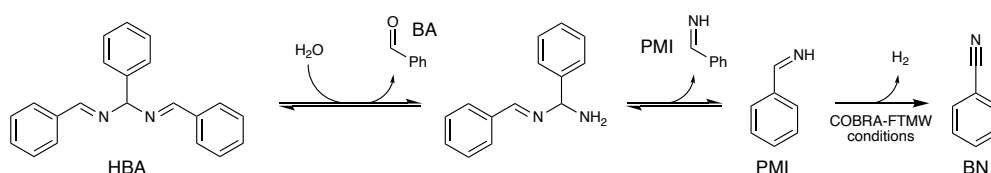
Scheme 2.4: Putative hydrolytic pathway of HBA.

The crucial role of water is self-evident, since the detection of benzaldehyde cannot be justified without oxygen sources. As long as water is available, the hydrolytic pathway can occur. Indeed, both low-temperature experiments, i.e. COBRA-FTMW and NMR, featured the spectroscopically confirmed presence of water (water dimer and residual water of the deuterated solvent, respectively). Its amount is believed to be sufficient to observe the formation of the main species arising from HBA hydrolysis: BA at room temperature and PMI at higher temperatures. The FM-mmW experiment was exploited with the aim of gaining further hints on the hydrolytic mechanism. In analogy with the COBRA-FTMW experiments, a tentative production of PMI in the gas phase by simple thermolysis of HBA was performed. The solid was placed inside a glass tube and heated up to 100 °C. Uniform heating was also ensured along the path to the absorption cell. Based on the data from low-frequency measurements, the

detection of two strong transitions of *E*-PMI was attempted: a portion of the spectrum around 85.5 GHz was scanned as the sample was heated up. However, no signal attributable to PMI (nor BN) was found.

To understand the differences between the experimental evidences from COBRA-FTMW and FM-mmW conditions, a more complete description of the latter is required. Typically, the FM-mmW spectrometer is equipped with a glass cell, in which a continuous gas flux is established by means of the pumping system. Such dynamic conditions are expected to ensure the complete removal of water, although its residual presence cannot be ruled out, as well as of the by-products resulting from the reaction of unstable species such as PMI. Furthermore, contrary to COBRA-FTMW conditions, no metallic surfaces are present in the instrument. Hence, the lack of formation of PMI in the FM-mmW experiment can be explained with two non-mutually exclusive hypothesis: (i) water is not available in a sufficient amount to hydrolyse HBA; (ii) metal catalysis is mandatory to obtain PMI from HBA in the gas phase. Eventually, a different approach (i.e. FVP) enabled the production of PMI, with the aim to extend the spectroscopic investigations at higher frequencies. Two possible precursors were chosen for the pyrolytic generation of PMI: benzylamine and α-methylbenzylamine. These were expected to produce PMI through dehydrogenation or elimination of CH_4, respectively (Scheme 2.5).
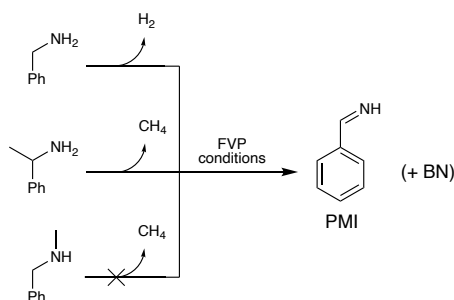
Scheme 2.5: FVP approaches for the generation of PMI.

This approach allowed a small set of 27 transitions (belonging only to *E*-PMI) to be measured. In particular, α-methylbenzylamine led to the best S/N of the spectra. Conversely, its structural isomer *N*-methylbenzylamine, when pyrolyzed, gave no PMI-related signals. Interestingly, BN was detected as a pyrolysis co-product. The PMI signal reached its maximum intensity when the furnace temperature was set to 890 °C, while the intensity of the BN transitions kept increasing up to 1200 °C. Regardless of the mechanism leading to the formation of PMI in FVP conditions, the FM-mmW experiment confirmed COBRA-FTMW measurements and improved their extrapolation at higher frequencies. Still, PMI formation from HBA in the gas phase with no available metallic surfaces remains an unexplored area. The putative absence of *Z*-PMI in both the FVP and NMR conditions is worth of further investigation. The assessment of the causes of such absence may give a clearer general mechanistic picture.

2.4.   Conclusions

The employment of HBA as a bench-stable PMI precursor was found to be suited for the easy and affordable thermal generation of PMI, both in the gas phase and in solution, as confirmed by RER and NMR spectroscopy experiments, respectively. An accurate computational characterization of PMI, in terms of structural, spectroscopic and energetic parameters, has been carried out, thus paving the way for the registration and analysis of the microwave spectrum of both *E*- and *Z*-PMI. This represented their first laboratory identification, a mandatory prerequisite for the astronomical search of these species in the interstellar medium, which indeed relies on accurate rotational rest frequencies. The strong chemical connection between BN and PMI, in conjunction with the reported rotational laboratory identification of PMI, suggested the Taurus Molecular Cloud (TMC-1), where BN was identified, as the region of choice for the first astronomical observation. Unfortunately, no rotational transitions ascribable to PMI have been identified in TMC-1 so far. Indeed, some important differences between BN and PMI may hamper the astronomical detection of the latter. In particular, PMI has a smaller dipole moment than BN and its population is split over two isomers. Nevertheless, the reported spectroscopical characterization will be fundamental for future astronomical searches of PMI, which will also benefit of the steady technological advancement of the more and more numerous astronomical observation facilities.

Finally, the comparison between different generation approaches allowed us to hypothesize a possible mechanism of PMI formation by thermolysis of HBA, in which water is thought to play a crucial role. Further laboratory studies are required to simulate putative astrochemically-relevant pathways for the generation of PMI, since the reported HBA thermolysis was explored as the most straightforward "terrestrial" method for spectroscopic purposes. In particular, hydrogenation studies of benzonitrile performed in astro-mimicking conditions may unveil how PMI can be produced in space.

2.5.   Experimental/computational section

Unless otherwise stated, common chemicals and solvents (HPLC grade or reagent grade) were purchased from commercial sources and used without further purification. NMR spectra (for characterization) were recorded at 25 °C in a 400 MHz spectrometer using the deuterated solvent as an internal deuterium lock. The residual protic signal of the solvent (7.26 ppm, for ^{1}H-NMR), and the [13]CDCl$_3$ signal (77.16 ppm, for ^{13}C-NMR), were used for spectra recorded in CDCl$_3$. Chemical shifts are reported in parts per million (ppm) of the δ scale relative to TMS for ^{1}H and ^{13}C spectra. Coupling constants are in Hertz, and the multiplicity is as follows: s (singlet), d (doublet), t (triplet), q (quartet), m (multiplet), dd (doublet of doublets), dt (doublet of triplets), ddd (doublet of doublet of doublets), br (broad signal). ATR-FTIR spectra were obtained with an ATR-FTIR Bruker Alpha System spectrometer. Gas chromatography-

mass spectrometry (GC-MS) spectra were obtained by EI ionization at 70 eV on a Hewlett-Packard 5971 with GC injection; they are reported as *m/z* (rel. intensity). The gas-phase characterization of PMI has been performed in the 3−26GHz range, using the COBRA-type (Coaxially Aligned Beam Resonator Arrangement) Fourier Transform Microwave Spectrometer (FTMW), described in details elsewhere.[113] Additional spectra were recorded in the 83−100 GHz range using a frequency- modulation millimetre-wave (FM-mmW) spectrometer, described in details elsewhere.[116] Further details on the experimental conditions for rotational spectroscopic measurements are accurately described in Ref. 107. The synthesis of HBA and the experimental conditions for NMR experiments in solution are described in Sections 2.5.2 and 2.5.3, respectively.

2.5.1. *Computational methodology*

A preliminary scan of the potential energy surface (PES) of PMI has been carried out using a cost-effective approach based on density functional theory (DFT). In detail, the B3LYP-D3(BJ)/SNSD level of theory (hereafter referred to as B3 level)[110,111] has been employed for a reliable and fast exploration of the conformational space. The formulation of this hybrid functional includes the treatment of dispersion effects by means of Grimme's DFT-D3 scheme[130] in conjunction with the Becke-Johnson (BJ) damping function.[131] SNSD is double-ζ basis set (available for download at smart.sns.it) derived from the N07D one.[132,133] Subsequently, the double-hybrid B2PLYP-D3(BJ) functional[112] has been employed in conjunction with the maug-cc-pVTZ-dH basis set[134] (hereafter altogether denoted as B2 level), to obtain a more accurate description of the stationary points of the PES. In the basis set above, the "-dH" notation refers to the removal of the d functions on hydrogen atoms from the original maug-cc-pVTZ basis.[135] As mentioned in the main text, this investigation of the PES led to the identification of two isomers: E- and Z-PMI. To allow a straightforward interpretation of their rotational spectrum, the accurate determination of several spectroscopic parameters is mandatory. In this context, the vibrational ground-state rotational constants B_0^i are defined (where i refers to the a, b, c inertial axes) according to vibrational perturbation theory to the second order (VPT2):[136]

$$B_0^i = B_e^i - \frac{1}{2}\sum_r \alpha_r^i \qquad (2.5)$$

where B_e^i are the equilibrium rotational constants and α_r^i are the vibration-rotation interaction constants, the sum running over all r vibrational modes. The B_e^i are straightforwardly derived from the equilibrium structure,[115] while the second term on the right-hand side is the vibrational correction ($\Delta B_{vib} = -\frac{1}{2}\sum_r \alpha_r^i$). If we compare the two terms, B_e^i is significantly larger than ΔB_{vib}.[137,138] Thus, the major computational effort is devoted to the equilibrium geometry optimization. For this purpose, the so-called "cheap" composite scheme (from here on shortly denoted as ChS) was exploited.[106] Despite its denomination, which is explained by the limited computational cost compared to a full coupled-cluster

Computational methodology

(CC) approach, the "cheap" composite scheme leads to accurate results (about $0.001-0.002$ Å for bonds and $0.1-0.2$ Å for angles). To fulfil such an accuracy without steeply raising the computational requirements, composite schemes like the ChS approach rely on the additivity approximation, which states that all contributions required can be evaluated at the best possible level of theory according to the size of the system and combined together. Within this framework, ChS is summarized as follows:

$$r_{ChS} = r(CCSD(T)/VTZ) + \Delta r(MP2/CBS) + \Delta r(MP2/CV) + \Delta r(MP2/AUG) \qquad (2.6)$$

where r denotes a generic structural parameter. On the right-hand side: (i) the first term is r optimized at the fc-CCSD(T)/cc-pVTZ level of theory,[139,140] with "fc-" referring to the frozen-core approximation, and CCSD(T) standing for the CC theory including single and double excitations augmented by a perturbative treatment of triples; (ii) the second term refers to the extrapolation to the complete basis set (CBS) limit, which is carried out using the n^{-3} formula by Helgaker *et al.*[141] applied to Møller-Plesset perturbation theory to second order (MP2),[142] thereby employing fc-MP2/cc-pVTZ and fc-MP2/cc-pVQZ optimized parameters; (iii) the third term is the core-valence (CV) correlation contribution is evaluated as difference between the all-MP2/cc-pCVTZ[143] and fc-MP2/cc-pCVTZ parameters, where "all-" denotes the correlation of all electrons; (iv) the last term introduces the effects of the inclusion of diffuse functions into the basis set, and it is estimated as difference between the fc-MP2/aug-cc-pVTZ[140,144] and fc-MP2/cc-pVTZ optimized parameters.

Subsequently, in order to evaluate the vibrational ground-state rotational constants, as expressed in Equation (2.5), it is necessary to compute the ΔB_{vib} term, which requires expensive anharmonic force-field calculations. However, as anticipated above, the vibrational correction term is significantly smaller (usually $1-3\%$ of the B_0^{α} value),[137,138] thus allowing us to employ a low, cost-effective level of theory. Therefore, anharmonic force fields (one for each isomer) have been computed at the B3 level.

To complete the set of spectroscopic parameters, the (quartic) centrifugal-distortion constants have been obtained from B2 harmonic force-field calculations. At the same level of theory, first-order properties, such as dipole moment and nuclear quadrupole coupling constants, have also been evaluated. While dipole moments are required to have information on the intensity of rotational transitions, the nuclear quadrupole coupling constants have a strong impact on the rotational spectrum.[115] By reformulating Equation (2.6) as follows, the ChS approach can be employed to derive accurate electronic energy of the stationary points on the investigated PES:

$$E_{ChS} = E(CCSD(T)/VTZ) + \Delta E(MP2/CBS) + \Delta E(MP2/CV) \qquad (2.7)$$

For these single-point energy evaluations, the optimized structures at the B2 level have been chosen as reference geometries. Analogously to Equation (2.6), the first term on the right-hand side of Equation (2.7) is the electronic energy evaluated at the fc-CCSD(T)/cc-pVTZ level of theory, while the last term is derived as difference between all-MP2/cc-pCVTZ and fc-MP2/cc-pCVTZ energies. Different is instead the evaluation of the CBS limit term, which is calculated in two steps: (i) the HF energy is extrapolated to the CBS limit by resorting to the three-point formula proposed by Feller[145] and employing the cc-pVTZ, cc-pVQZ and cc-pV5Z basis sets; (ii) the extrapolation to the CBS limit of the MP2 correlation energy is derived according to the formula by Helgaker *et al.*,[141] using the cc-pVTZ and the cc-pVQZ basis sets. To incorporate zero-point energy (ZPE) corrections, ChS energies have been augmented by harmonic ZPE terms obtained from the B2 harmonic force-field calculations mentioned above. Quantum-chemical calculations have been performed using either the Gaussian16 suite (DFT and MP2)[146] or the CFOUR package (coupled cluster).[147]

2.5.2. Synthesis of HBA, 1-phenyl-N,N'-bis(phenylmethylene)methanediamine
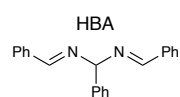
HBA was synthesized following the procedure described in literature.[98–101] Ammonium hydroxide solution (28−30% NH_3 basis, 510 mmol, 33.2 mL) was added to benzaldehyde (BA, 39.4 mmol, 4 mL) and the mixture was stirred at room temperature for three hours. A white precipitate appeared, which was recovered by filtration through a fritted funnel and washed with small portions of cold diethyl ether (3x10 mL). HBA was obtained as spectroscopically pure white solid (2.747g, 9.2mmol, 70%). Spectroscopic data were in agreement with those reported in literature.[148] ^{1}H-NMR (CDCl$_3$, 400 MHz, ppm) δ: 8.60 (2H, s), 7.90−7.84 (4H, m), 7.55−7.50 (2H, m), 7.47−7.41 (6H, m), 7.41−7.35 (2H, m), 7.33−7.27 (1H, m), 5.99 (1H, s). ^{13}C-NMR (CDCl$_3$, 100 MHz, ppm) δ: 160.8 (2C), 141.9, 136.2 (2C), 131.2 (2C), 128.8 (4C), 128.70 (4C), 128.68 (2C), 128.0, 127.4 (2C), 92.8. ATR-FTIR (cm^{-1}) $\tilde{\nu}$: 3059, 3031, 2856, 1638, 1492, 1450, 1578, 1357, 1314, 1296, 1216, 1168, 1075, 1030, 914, 755, 700, 632, 565, 483. MS (EI) *m/z*: 194, 165, 152, 116, 104, 89, 77.

2.5.3. Variable-temperature NMR analysis

Once HBA was obtained with the required level of purity, a sample was placed in an NMR tube and dissolved in 1,1,2,2-tetrachloroethane-d$_2$ (b.p. 146 °C) for variable temperature analysis, using a Varian Inova 600MHz equipped with an ATB Broadband Probe, operating at a field of 14.4 T. The NMR spectra were acquired ten minutes after the chosen temperature was reached, to avoid thermalization processes to occur during the acquisition. Chemical shifts are reported in ppm from TMS with the residual solvent resonance as the internal standard (C$_2$H$_2$Cl$_4$: δ = 6.0 ppm).

2.6.   References

(1)   Thorndike, S. L. Interstellar Matter. *Publ. Astron. Soc. Pac.* **1930**, *42* (246), 99–104. DOI: 10.1086/124007.

(2)   McGuire, B. A. 2021 Census of Interstellar, Circumstellar, Extragalactic, Protoplanetary Disk, and Exoplanetary Molecules. *Astrophys. J. Suppl. Ser.* **2022**, *259* (2), 30. DOI: 10.3847/1538-4365/ac2a48.

(3)   Trumpler, R. J. Absorption of Light in the Galactic System. *Publ. Astron. Soc. Pac.* **1930**, *42*, 214–227. DOI: 10.1086/124039.

(4)   Greenberg, J. M. Interstellar Grains. *Annu. Rev. Astron. Astrophys.* **1963**, *1* (1), 267–290. DOI: 10.1146/annurev.aa.01.090163.001411.

(5)   van de Hulst, H. C. The solid particles in interstellar space. *Recherches Astronomiques de l'Observatoire d'Utrecht* **1946**, *11* (2), 1–50.

(6)   Oort, J. H.; van de Hulst, H. C. Gas and smoke in interstellar space. *Bulletin of the Astronomical Institutes of the Netherlands* **1946**, *10* (376), 187–204.

(7)   Greenberg, J. M.; Yencha, A. J.; Corbett, J. W.; Frisch, H. L. Ultraviolet effects on the chemical composition and optical properties of interstellar grains. *Mémoires Société Royale des Sciences de Liège, 6e série* **1972**, *3* (34), 425–436.

(8)   Kamijo, F. A Theoretical Study on the Long Period Variable Star. III - Formation of Solid or Liquid Particles in the Circumstellar Envelope. *Publ. Astron. Soc. Jpn.* **1963**, *15*, 440–448.

(9)   Woolf, N. J.; Ney, E. P. Circumstellar Infrared Emission from Cool Stars. *Astrophys. J.* **1969**, *155* (3), L181–L184. DOI: 10.1086/180331.

(10)   Knacke, R. F.; Gaustad, J. E.; Gillett, F. C.; Stein, W. A. A Possible Identification of Interstellar Silicate Absorption in the Infrared Spectrum of 119 Tauri. *Astrophys. J.* **1969**, *155* (3), L189–L192. DOI: 10.1086/180333.

(11)   Wickramasinghe, D. T.; Allen, D. A. The 3.4-µm interstellar absorption feature. *Nature* **1980**, *287* (5782), 518–519. DOI: 10.1038/287518a0.

(12)   Duley, W. W.; Jones, A. P.; Williams, D. A. Hydrogenated amorphous carbon-coated silicate particles as a source of interstellar extinction. *Mon. Not. R. Astron. Soc.* **1989**, *236* (4), 709–725. DOI: 10.1093/mnras/236.4.709.

(13)   Greenberg, J. M.; Li, A. Tracking the organic refractory component from interstellar dust to comets. *Adv. Sp. Res.* **1999**, *24* (4), 497–504. DOI: 10.1016/S0273-1177(99)00091-5.

(14)   Tielens, A. G. G. M. *The Physics and Chemistry of the Interstellar Medium*; Cambridge University Press, 2005. DOI: 10.1017/CBO9780511819056.

(15)   Wilson, T. L.; Rohlfs, K.; Hüttemeister, S. *Tools of Radio Astronomy*; Springer, Berlin, Heidelberg, 2009. DOI: 10.1007/978-3-540-85122-6.

(16)   Klaus, T.; Takano, S.; Winnewisser, G. Laboratory measurement of the N = 1 ← 0 rotational transition of NH at 1 THz. *Astron. Astrophys.* **1997**, *322* (2), L1–L4.

(17)   McCarthy, M. C.; Levine, E. S.; Apponi, A. J.; Thaddeus, P. Experimental structures of the carbon chains HC_7N, HC_9N, and $HC_{11}N$ by isotopic substitution. *J. Mol. Spectrosc.* **2000**, *203* (1), 75–81. DOI: 10.1006/jmsp.2000.8149.

(18)   Belloche, A.; Müller, H. S. P.; Menten, K. M.; Schilke, P.; Comito, C. Complex organic molecules in the interstellar medium: IRAM 30 m line survey of Sagittarius B2(N) and (M). *Astron. Astrophys.* **2013**, *559*, A47. DOI: 10.1051/0004-6361/201321096.

(19)   Kaifu, N.; Ohishi, M.; Kawaguchi, K.; Saito, S.; Yamamoto, S.; Miyaji, T.; Miyazawa, K.; Ishikawa, S. I.; Noumaru, C.; Harasawa, S.; Okuda, M.; Suzuki, H. A 8.8-50 GHz Complete Spectral Line Survey Toward TMC-1 I. Survey Data. *Publ. Astron. Soc. Jpn.* **2004**, *56* (1), 69–173. DOI: 10.1093/pasj/56.1.69.

(20)   Neufeld, D. A.; Falgarone, E.; Gerin, M.; Godard, B.; Herbst, E.; Pineau Des Forêts, G.; Vasyunin, A. I.; Güsten, R.; Wiesemeyer, H.; Ricken, O. Discovery of interstellar mercapto radicals (SH) with the GREAT instrument on SOFIA. *Astron. Astrophys.* **2012**, *542*, L6. DOI: 10.1051/0004-6361/201218870.

(21)   Tielens, A. G. G. M. Interstellar polycyclic aromatic hydrocarbon molecules. *Annu. Rev. Astron. Astrophys.* **2008**, *46*, 289–337. DOI: 10.1146/annurev.astro.46.060407.145211.

(22)   Cooke, I. R.; Fayolle, E. C.; Öberg, K. I. CO_2 INFRARED PHONON MODES IN INTERSTELLAR ICE MIXTURES. *Astrophys. J.* **2016**, *832* (1), 5. DOI: 10.3847/0004-637x/832/1/5.

(23)   Potenti, S.; Manini, P.; Fornaro, T.; Poggiali, G.; Crescenzi, O.; Napolitano, A.; Brucato, J. R.; Barone, V.; D'Ischia, M. Solid State Photochemistry of Hydroxylated Naphthalenes on Minerals: Probing Polycyclic Aromatic Hydrocarbon Transformation Pathways under Astrochemically-Relevant Conditions. *ACS Earth Space Chem.* **2018**, *2* (10), 977–1000. DOI: 10.1021/acsearthspacechem.8b00060.

(24)   Lofthus, A.; Krupenie, P. H. The spectrum of molecular nitrogen. *J. Phys. Chem. Ref. Data* **1977**, *6* (1), 113–307. DOI: 10.1063/1.555546.

(25)   Aller, L. H. PHOTOELECTRIC SPECTROPHOTOMETRY OF η CARINAE. *Proc. Natl. Acad. Sci. U. S. A.* **1966**, *55* (4), 671–676. DOI: 10.1073/pnas.55.4.671.

(26)   Burkhardt, A. M.; Dollhopf, N. M.; Corby, J. F.; Carroll, P. B.; Shingledecker, C. N.; Loomis, R. A.; Booth, S. T.; Blake, G. A.; Herbst, E.; Remijan, A. J.; McGuire, B. A. CSO AND CARMA OBSERVATIONS OF L1157. II. CHEMICAL COMPLEXITY IN THE SHOCKED OUTFLOW. *Astrophys. J.* **2016**, *827* (1), 21. DOI: 10.3847/0004-637x/827/1/21.

(27)   Hocuk, S.; Szucs, L.; Caselli, P.; Cazaux, S.; Spaans, M.; Esplugues, G. B. Parameterizing the interstellar dust temperature. *Astron. Astrophys.* **2017**, *604*, A58. DOI: 10.1051/0004-6361/201629944.

(28)   Silsbee, K.; Caselli, P.; Ivlev, A. V. Ice mantles on dust grains: Dramatic variation of thickness with grain size. *Mon.*

Not. R. Astron. Soc. **2021**, *507* (4), 6205–6214. DOI: 10.1093/mnras/stab2546.

(29) Esplugues, G.; Cazaux, S.; Caselli, P.; Hocuk, S.; Spaans, M. Dust temperature and time-dependent effects in the chemistry of photodissociation regions. *Mon. Not. R. Astron. Soc.* **2019**, *486* (2), 1853–1874. DOI: 10.1093/mnras/stz1009.

(30) Sims, I. R. Low-Temperature Reactions: Tunnelling in Space. *Nat. Chem.* **2013**, *5* (9), 734–736. DOI: 10.1038/nchem.1736.

(31) Trixler, F. Quantum Tunnelling to the Origin and Evolution of Life. *Curr. Org. Chem.* **2013**, *17* (16), 1758–1770. DOI: 10.2174/13852728113179990083.

(32) Lamberts, T.; Samanta, P. K.; Köhn, A.; Kästner, J. Quantum tunneling during interstellar surface-catalyzed formation of water: The reaction H + H$_2$O$_2$ → H$_2$O + OH. *Phys. Chem. Chem. Phys.* **2016**, *18* (48), 33021–33030. DOI: 10.1039/C6CP06457D.

(33) Lamberts, T.; Fedoseev, G.; Kästner, J.; Ioppolo, S.; Linnartz, H. Importance of tunneling in H-abstraction reactions by OH radicals: The case of CH$_4$ + OH studied through isotope-substituted analogs. *Astron. Astrophys.* **2017**, *599*, A132. DOI: 10.1051/0004-6361/201629845.

(34) Molpeceres, G.; Rimola, A.; Ceccarelli, C.; Kästner, J.; Ugliengo, P.; Maté, B. Silicate-mediated interstellar water formation: A theoretical study. *Mon. Not. R. Astron. Soc.* **2019**, *482* (4), 5389–5400. DOI: 10.1093/mnras/sty3024.

(35) Zamirri, L.; Ugliengo, P.; Ceccarelli, C.; Rimola, A. Quantum Mechanical Investigations on the Formation of Complex Organic Molecules on Interstellar Ice Mantles. Review and Perspectives. *ACS Earth Space Chem.* **2019**, *3* (8), 1499–1523. DOI: 10.1021/acsearthspacechem.9b00082.

(36) Millar, T. J. Astrochemistry. *Plasma Sources Sci. Technol.* **2015**, *24* (4), 043001. DOI: 10.1088/0963-0252/24/4/043001.

(37) Potapov, A.; McCoustra, M. Physics and chemistry on the surface of cosmic dust grains: a laboratory view. *Int. Rev. Phys. Chem.* **2021**, *40* (2), 299–364. DOI: 10.1080/0144235X.2021.1918498.

(38) Smith, I. W. M. Laboratory astrochemistry: Gas-phase processes. *Annu. Rev. Astron. Astrophys.* **2011**, *49*, 29–66. DOI: 10.1146/annurev-astro-081710-102533.

(39) Friestad, G. K.; Mathies, A. K. Recent developments in asymmetric catalytic addition to C=N bonds. *Tetrahedron* **2007**, *63* (12), 2541–2569. DOI: 10.1016/j.tet.2006.11.076.

(40) Bhat, S. V.; Nagasampagi, B. A.; Sivakumar, M. *Chemistry of Natural Products*, 1st ed.; Springer: Berlin, 2005.

(41) Mann, J.; Davidson, R. S.; Hobbs, J. B.; Banthorpe, D. V.; Harborne, J. B. *Natural Products: Their Chemistry and Biological Significance*, 1st ed.; Addison Wesley Longman Limited: London, 1994.

(42) Torrens-Spence, M. P.; Glinkerman, C. M.; Günther, J.; Weng, J. K. Imine chemistry in plant metabolism. *Curr. Opin. Plant Biol.* **2021**, *60*, 101999. DOI: 10.1016/j.pbi.2020.101999.

(43) Altamimi, M. A.; Hussain, A.; Alshehri, S.; Imam, S. S.; Alnami, A.; Bari, A. Novel hemocompatible imine compounds as alternatives for antimicrobial therapy in pharmaceutical application. *Processes* **2020**, *8* (11), 1476. DOI: 10.3390/pr8111476.

(44) Bownds, D.; Wald, G. Reaction of the rhodopsin chromophore with sodium borohydride. *Nature* **1965**, *205* (4968), 254–257. DOI: 10.1038/205254a0.

(45) Bownds, D. Site of attachment of retinal in rhodopsin. *Nature* **1967**, *216* (5121), 1178–1181. DOI: 10.1038/2161178a0.

(46) Pulagam, L. P.; Palczewski, K. Phototransduction: Rhodopsin. In *Encyclopedia of the Eye*; 2010; pp 403–412. DOI: 10.1016/B978-0-12-374203-2.00183-4.

(47) Layer, R. W. The chemistry of imines. *Chem. Rev.* **1963**, *63* (5), 489–510. DOI: 10.1021/cr60225a003.

(48) Sprung, M. M. A summary of the reactions of aldehydes with amines. *Chem. Rev.* **1940**, *26* (3), 297–338. DOI: 10.1021/cr60085a001.

(49) R. Boyd, D.; Hamilton, R.; T. Thompson, N.; E. Stubbs, M. Base catalysed decomposition of oxaziridines to yield N-unsubstituted aldimines. *Tetrahedron Lett.* **1979**, *20* (34), 3201–3204. DOI: 10.1016/S0040-4039(01)95362-6.

(50) Bergman, Y.; Perlmutter, P.; Thienthong, N. Solvent-free preparation of primary imines from (2-hydroxyaryl)ketones. *Green Chem.* **2004**, *6* (11), 539–540. DOI: 10.1039/b412192a.

(51) Wolfe, J. P.; Åhman, J.; Sadighi, J. P.; Singer, R. A.; Buchwald, S. L. An ammonia equivalent for the palladium-catalyzed amination of aryl halides and triflates. *Tetrahedron Lett.* **1997**, *38* (36), 6367–6370. DOI: 10.1016/S0040-4039(97)01465-2.

(52) Chen, G. M.; Ramachandran, P. V.; Brown, H. C. The critical importance of water in the asymmetric allylboration of N-trimethylsilylbenzaldimines with B-allyldiisopinocampheylborane. *Angew. Chem. Int. Ed.* **1999**, *38* (6), 825–826. DOI: 10.1002/(SICI)1521-3773(19990315)38:6<825::AID-ANIE825>3.0.CO;2-V.

(53) Sugiura, M.; Hirano, K.; Kobayashi, S. α-aminoallylation of aldehydes with ammonia: Stereoselective synthesis of homoallylic primary amines. *J. Am. Chem. Soc.* **2004**, *126* (23), 7182–7183. DOI: 10.1021/ja049689o.

(54) Chen, G. M.; Brown, H. C. An efficient synthesis of N-unsubstituted imines as organoborane adducts stable at room temperature: New promising intermediates for synthesis. *J. Am. Chem. Soc.* **2000**, *122* (17), 4217–4218. DOI: 10.1021/ja993965v.

(55) Itsuno, S.; Watanabe, K.; Matsumoto, T.; Kuroda, S.; Yokoi, A.; El-Shehawy, A. Enantioselective synthesis of optically active homoallylamines by nucleophilic addition of chirally modified allylboranes to N-silylimines. *J. Chem. Soc., Perkin Trans. 1* **1999**, No. 14, 2011–2016. DOI: 10.1039/a902635e.

(56) Kyba, E. P.; Abramovitch, R. A. Photolysis of Alkyl Azides. Evidence for a Nonnitrene Mechanism. *J. Am. Chem. Soc.* **1980**, *102* (2), 735–740. DOI: 10.1021/ja00522a049.

References

(57) Risse, J.; Scopelliti, R.; Severin, K. Beyond click-chemistry: Transformation of azides with cyclopentadienyl ruthenium complexes. *Organometallics* **2011**, *30* (12), 3412–3418. DOI: 10.1021/om200295c.

(58) Lee, J. H.; Gupta, S.; Jeong, W.; Rhee, Y. H.; Park, J. Characterization and utility of N-unsubstituted imines synthesized from alkyl azides by ruthenium catalysis. *Angew. Chem. Int. Ed.* **2012**, *51* (43), 10851–10855. DOI: 10.1002/anie.201204483.

(59) Lee, J. M.; Bae, D. Y.; Park, J. Y.; Jo, H. Y.; Lee, E.; Rhee, Y. H.; Park, J. Concurrent Formation of N-H Imines and Carbonyl Compounds by Ruthenium-Catalyzed C-C Bond Cleavage of β-Hydroxy Azides. *Org. Lett.* **2020**, *22* (12), 4608–4613. DOI: 10.1021/acs.orglett.0c01145.

(60) Jo, H. Y.; Lee, J. M.; Pietrasiak, E.; Lee, E.; Rhee, Y. H.; Park, J. Generation of N-H Imines from α-Azidocarboxylic Acids through Ru-Catalyzed Decarboxylation. *J. Org. Chem.* **2021**, *86* (23), 17409–17417. DOI: 10.1021/acs.joc.1c01841.

(61) Heinen, A. W.; Peters, J. A.; Van Bekkum, H. The reductive amination of benzaldehyde over Pd/C catalysts: Mechanism and effect of carbon modifications on the selectivity. *Eur. J. Org. Chem.* **2000**, No. 13, 2501–2506. DOI: 10.1002/1099-0690(200007)2000:13<2501::AID-EJOC2501>3.0.CO;2-S.

(62) Chakraborty, S.; Milstein, D. Selective Hydrogenation of Nitriles to Secondary Imines Catalyzed by an Iron Pincer Complex. *ACS Catal.* **2017**, *7* (6), 3968–3972. DOI: 10.1021/acscatal.7b00906.

(63) Reguillo, R.; Grellier, M.; Vautravers, N.; Vendier, L.; Sabo-Etienne, S. Ruthenium-catalyzed hydrogenation of nitriles: Insights into the mechanism. *J. Am. Chem. Soc.* **2010**, *132* (23), 7854–7855. DOI: 10.1021/ja102759z.

(64) Zerecero-Silva, P.; Jimenez-Solar, I.; Crestani, M. G.; Arévalo, A.; Barrios-Francisco, R.; García, J. J. Catalytic hydrogenation of aromatic nitriles and dinitriles with nickel compounds. *Appl. Catal. A* **2009**, *363* (1–2), 230–234. DOI: 10.1016/j.apcata.2009.05.027.

(65) Shares, J.; Yehl, J.; Kowalsick, A.; Byers, P.; Haaf, M. P. An efficient synthesis of tertiary amines from nitriles in aprotic solvents. *Tetrahedron Lett.* **2012**, *53* (33), 4426–4428. DOI: 10.1016/j.tetlet.2012.06.044.

(66) Monguchi, Y.; Mizuno, M.; Ichikawa, T.; Fujita, Y.; Murakami, E.; Hattori, T.; Maegawa, T.; Sawama, Y.; Sajiki, H. Catalyst-Dependent Selective Hydrogenation of Nitriles: Selective Synthesis of Tertiary and Secondary Amines. *J. Org. Chem.* **2017**, *82* (20), 10939–10944. DOI: 10.1021/acs.joc.7b01823.

(67) Yamaguchi, K.; Mizuno, N. Efficient heterogeneous aerobic oxidation of amines by a supported ruthenium catalyst. *Angew. Chem. Int. Ed.* **2003**, *42* (13), 1480–1483. DOI: 10.1002/anie.200250779.

(68) Yamaguchi, K.; Mizuno, N. Scope, kinetics, and mechanistic aspects of aerobic oxidations catalyzed by ruthenium supported on alumina. *Chem. Eur. J.* **2003**, *9* (18), 4353–4361. DOI: 10.1002/chem.200304916.

(69) Mizuno, N.; Yamaguchi, K. Selective aerobic oxidations by supported ruthenium hydroxide catalysts. *Catal. Today* **2008**, *132* (1–4), 18–26. DOI: 10.1016/j.cattod.2007.12.026.

(70) Schümperli, M. T.; Hammond, C.; Hermans, I. Developments in the aerobic oxidation of amines. *ACS Catal.* **2012**, *2* (6), 1108–1117. DOI: 10.1021/cs300212q.

(71) Capdevielle, P.; Lavigne, A.; Maumy, M. Mechanism of the copper mediated oxidation of primary aliphatic amines by the Cu0/O2/acetic acid system in acetonitrile. *Tetrahedron* **1990**, *46* (8), 2835–2844. DOI: 10.1016/S0040-4020(01)88376-9.

(72) Patil, R. D.; Adimurthy, S. Copper-catalyzed aerobic oxidation of amines to imines under neat conditions with low catalyst loading. *Adv. Synth. Catal.* **2011**, *353* (10), 1695–1700. DOI: 10.1002/adsc.201100100.

(73) Largeron, M. Protocols for the catalytic oxidation of primary amines to imines. *Eur. J. Org. Chem.* **2013**, *2013* (24), 5225–5235. DOI: 10.1002/ejoc.201300315.

(74) Galletti, P.; Funiciello, F.; Soldati, R.; Giacomini, D. Selective oxidation of amines to aldehydes or imines using laccase-mediated bio-oxidation. *Adv. Synth. Catal.* **2015**, *357* (8), 1840–1848. DOI: 10.1002/adsc.201500165.

(75) Godfrey, R. D. J.; Brown, R. D.; Robinson, B. J.; Sinclair, M. W. Discovery of interstellar methanimine (formaldimine). *Astrophys. Lett.* **1973**, *13*, 119–121.

(76) Lovas, F. J.; Hollis, J. M.; Remijan, A. J.; Jewell, P. R. Detection of Ketenimine (CH2CNH) in Sagittarius B2(N) Hot Cores. *Astrophys. J.* **2006**, *645* (2), L137–L140. DOI: 10.1086/506324.

(77) Zaleski, D. P.; Seifert, N. A.; Steber, A. L.; Muckle, M. T.; Loomis, R. A.; Corby, J. F.; Martinez, O.; Crabtree, K. N.; Jewell, P. R.; Hollis, J. M.; Lovas, F. J.; Vasquez, D.; Nyiramahirwe, J.; Sciortino, N.; Johnson, K.; McCarthy, M. C.; Remijan, A. J.; Pate, B. H. DETECTION OF E-CYANOMETHANIMINE TOWARD SAGITTARIUS B2(N) IN THE GREEN BANK TELESCOPE PRIMOS SURVEY. *Astrophys. J., Lett.* **2013**, *765* (1), L10. DOI: 10.1088/2041-8205/765/1/L10.

(78) Loomis, R. A.; Zaleski, D. P.; Steber, A. L.; Neill, J. L.; Muckle, M. T.; Harris, B. J.; Hollis, J. M.; Jewell, P. R.; Lattanzi, V.; Lovas, F. J.; Martinez, O.; McCarthy, M. C.; Remijan, A. J.; Pate, B. H.; Corby, J. F. THE DETECTION OF INTERSTELLAR ETHANIMINE (CH3CHNH) FROM OBSERVATIONS TAKEN DURING THE GBT PRIMOS SURVEY. *Astrophys. J., Lett.* **2013**, *765* (1), L9. DOI: 10.1088/2041-8205/765/1/L9.

(79) Rivilla, V. M.; Martín-Pintado, J.; Jiménez-Serra, I.; Zeng, S.; Martín, S.; Armijos-Abendaño, J.; Requena-Torres, M. A.; Aladro, R.; Riquelme, D. Abundant Z-cyanomethanimine in the interstellar medium: Paving the way to the synthesis of adenine. *Mon. Not. R. Astron. Soc.: Lett.* **2019**, *483* (1), L114–L119. DOI: 10.1093/mnrasl/sly228.

(80) Zaleski, D. P.; Stephens, S. L.; Walker, N. R. A perspective on chemistry in transient plasma from broadband rotational spectroscopy. *Phys. Chem. Chem. Phys.* **2014**, *16* (46), 25221–25228. DOI: 10.1039/c4cp04108a.

(81) Wentrup, C. Flash Vacuum Pyrolysis: Techniques and Reactions. *Angew. Chem. Int. Ed.* **2017**, *56* (47), 14808–14835. DOI: 10.1002/anie.201705118.

(82) McCarthy, M. C.; Chen, W.; Travers, M. J.; Thaddeus, P. Microwave Spectra of 11 Polyyne Carbon Chains. *Astrophys. J. Suppl. Ser.* **2000**, *129* (2), 611–623. DOI: 10.1086/313428.

(83) McGuire, B. A.; Burkhardt, A. M.; Kalenskii, S.; Shingledecker, C. N.; Remijan, A. J.; Herbst, E.; McCarthy, M. C. Detection of the aromatic molecule benzonitrile (c-C_6H_5CN) in the interstellar medium. *Science* **2018**, *359* (6372), 202–205. DOI: 10.1126/science.aao4890.

(84) Lee, K. L. K.; McGuire, B. A.; McCarthy, M. C. Gas-phase synthetic pathways to benzene and benzonitrile: A combined microwave and thermochemical investigation. *Phys. Chem. Chem. Phys.* **2019**, *21* (6), 2946–2956. DOI: 10.1039/c8cp06070c.

(85) Cernicharo, J.; Heras, A. M.; Tielens, A. G. G. M.; Pardo, J. R.; Herpin, F.; Guélin, M.; Waters, L. B. F. M. Infrared Space Observatory's Discovery of C_4H_2, C_6H_2, and Benzene in CRL 618. *Astrophys. J.* **2001**, *546* (2), L123–L126. DOI: 10.1086/318871.

(86) Kraemer, K. E.; Sloan, G. C.; Bernard-Salas, J.; Price, S. D.; Egan, M. P.; Wood, P. R. A Post-AGB Star in the Small Magellanic Cloud Observed with the Spitzer Infrared Spectrograph. *Astrophys. J.* **2006**, *652* (1), L25–L28. DOI: 10.1086/509778.

(87) Malek, S. E.; Cami, J.; Bernard-Salas, J. The rich circumstellar chemistry of SMP LMC 11. *Astrophys. J.* **2012**, *744* (1), 16. DOI: 10.1088/0004-637X/744/1/16.

(88) McCarthy, M. C.; Lee, K. L. K.; Loomis, R. A.; Burkhardt, A. M.; Shingledecker, C. N.; Charnley, S. B.; Cordiner, M. A.; Herbst, E.; Kalenskii, S.; Willis, E. R.; Xue, C.; Remijan, A. J.; McGuire, B. A. Interstellar detection of the highly polar five-membered ring cyanocyclopentadiene. *Nat. Astron.* **2021**, *5* (2), 176–180. DOI: 10.1038/s41550-020-01213-y.

(89) Kelvin Lee, K. L.; Changala, P. B.; Loomis, R. A.; Burkhardt, A. M.; Xue, C.; Cordiner, M. A.; Charnley, S. B.; McCarthy, M. C.; McGuire, B. A. Interstellar Detection of 2-cyanocyclopentadiene, C_5H_5CN, a Second Five-membered Ring toward TMC-1. *Astrophys. J., Lett.* **2021**, *910* (1), L2. DOI: 10.3847/2041-8213/abe764.

(90) McGuire, B. A.; Loomis, R. A.; Burkhardt, A. M.; Lee, K. L. K.; Shingledecker, C. N.; Charnley, S. B.; Cooke, I. R.; Cordiner, M. A.; Herbst, E.; Kalenskii, S.; Siebert, M. A.; Willis, E. R.; Xue, C.; Remijan, A. J.; McCarthy, M. C. Detection of two interstellar polycyclic aromatic hydrocarbons via spectral matched filtering. *Science* **2021**, *371* (6535), 1265–1269. DOI: 10.1126/science.abb7535.

(91) Mccarthy, M. C.; Mcguire, B. A. Aromatics and Cyclic Molecules in Molecular Clouds: A New Dimension of Interstellar Organic Chemistry. *J. Phys. Chem. A* **2021**, *125* (16), 3231–3243. DOI: 10.1021/acs.jpca.1c00129.

(92) Sayah, N.; Li, X.; Caballero, J. F.; Jackson, W. M. Laser induced fluorescence studies of CN reactions with alkanes, alkenes and substituted aliphatic species. *J. Photochem. Photobiol. A Chem.* **1988**, *45* (2), 177–194. DOI: 10.1016/1010-6030(88)80127-8.

(93) Bennett, C. J.; Morales, S. B.; Le Picard, S. D.; Canosa, A.; Sims, I. R.; Shih, Y. H.; Chang, A. H. H.; Gu, X.; Zhang, F.; Kaiser, R. I. A chemical dynamics, kinetics, and theoretical study on the reaction of the cyano radical (CN; $X^2\Sigma^+$) with phenylacetylene (C_6H_5CCH; X^1A_1). *Phys. Chem. Chem. Phys.* **2010**, *12* (31), 8737–8749. DOI: 10.1039/b925072g.

(94) Cooke, I. R.; Gupta, D.; Messinger, J. P.; Sims, I. R. Benzonitrile as a Proxy for Benzene in the Cold ISM: Low-temperature Rate Coefficients for CN + C_6H_6. *Astrophys. J.* **2020**, *891* (2), L41. DOI: 10.3847/2041-8213/ab7a9c.

(95) Yang, Y.; Hu, X.; Zhang, D.; Zhang, W.; Liu, G.; Zhen, J. Laboratory formation and photochemistry of covalently bonded polycyclic aromatic nitrogen heterocycle (PANH) clusters in the gas phase. *Mon. Not. R. Astron. Soc.* **2020**, *498* (1), 1–11. DOI: 10.1093/mnras/staa2212.

(96) Miksch, A. M.; Riffelt, A.; Oliveira, R.; Kästner, J.; Molpeceres, G. Hydrogenation of small aromatic heterocycles at low temperatures. *Mon. Not. R. Astron. Soc.* **2021**, *505* (3), 3157–3164. DOI: 10.1093/mnras/stab1514.

(97) Nguyen, T.; Fourré, I.; Favre, C.; Barois, C.; Congiu, E.; Baouche, S.; Guillemin, J. C.; Ellinger, Y.; Dulieu, F. Formation of amines: Hydrogenation of nitrile and isonitrile as selective routes in the interstellar medium. *Astron. Astrophys.* **2019**, *628*, A15. DOI: 10.1051/0004-6361/201935127.

(98) Hunter, D. H.; Sim, S. K. 2,4-Diazapentadienes. I. Prototropy, Cyclization, and Addition–Elimination. *Can. J. Chem.* **1972**, *50* (5), 669–677. DOI: 10.1139/v72-104.

(99) Kupfer, R.; Brinker, U. H. A novel synthesis of aromatic N-chloro aldimines. *J. Org. Chem.* **1996**, *61* (12), 4185–4186. DOI: 10.1021/jo960171f.

(100) Mlynarz, P.; Ptak, T.; Czernicka, A.; Pankiewicz, R.; Gluza, K.; Zarzeczańska, D. Bis{phenyl[di(methoxyethyloxy)phosphoryl]methyl}amine as a new ligand for metal ions and cationic organic molecules. *J. Mol. Struct.* **2011**, *991* (1–3), 18–23. DOI: 10.1016/j.molstruc.2011.01.016.

(101) Pecnikaj, I.; Foschi, F.; Bucci, R.; Gelmi, M. L.; Castellano, C.; Meneghetti, F.; Penso, M. Stereoselective Synthesis of α,α'-Dihydroxy-β,β'-diaryl-β-amino Acids by Mannich-Like Condensation of Hydroarylamides. *Eur. J. Org. Chem.* **2019**, *2019* (39), 6707–6713. DOI: 10.1002/ejoc.201901325.

(102) Boyd, D. R.; Coulter, P. B.; Hamilton, R.; Thompson, N. T.; Sharma, N. D.; Stubbs, M. E. The synthesis of NH aldimines and derivatives by spontaneous and base-catalysed decomposition of oxaziridines. *J. Chem. Soc. Perkin Trans. 1* **1985**, 2123–2127. DOI: 10.1039/p19850002123.

(103) Gomez, S.; Peters, J. A.; Van der Waal, J. C.; Van den Brink, P. J.; Maschmeyer, T. The rationalization of catalyst behaviour in the reductive amination of benzaldehyde with ammonia using a simple computer model. *Appl. Catal. A Gen.* **2004**, *261* (1), 119–125. DOI: 10.1016/j.apcata.2003.10.037.

(104) Fang, C.; Li, M.; Hu, X.; Mo, W.; Hu, B.; Sun, N.; Jin, L.; Shen, Z. A practical iodine-catalyzed oxidative conversion of aldehydes to nitriles. *RSC Adv.* **2017**, *7* (3), 1484–1489. DOI: 10.1039/c6ra26435b.

References

(105) Zars, E.; Gravogl, L.; Gau, M.; Carroll, P. J.; Meyer, K.; Mindiola, D. J. Iron(II) Mediated Deazotation of Benzyl Azide: Trapping and Subsequent Transformations of the Benzaldimine Fragment. *Inorg. Chem.* **2022**, *61* (2), 1079–1090. DOI: 10.1021/acs.inorgchem.1c03243.

(106) Puzzarini, C.; Barone, V. Extending the molecular size in accurate quantum-chemical calculations: The equilibrium structure and spectroscopic properties of uracil. *Phys. Chem. Chem. Phys.* **2011**, *13* (15), 7189–7197. DOI: 10.1039/c0cp02636k.

(107) Melli, A.; Potenti, S.; Melosso, M.; Herbers, S.; Spada, L.; Gualandi, A.; Lengsfeld, K. G.; Dore, L.; Buschmann, P.; Cozzi, P. G.; Grabow, J. U.; Barone, V.; Puzzarini, C. A Journey from Thermally Tunable Synthesis to Spectroscopy of Phenylmethanimine in Gas Phase and Solution. *Chem. Eur. J.* **2020**, *26* (65), 15016–15022. DOI: 10.1002/chem.202003270.

(108) Melli, A.; Melosso, M.; Tasinato, N.; Bosi, G.; Spada, L.; Bloino, J.; Mendolicchio, M.; Dore, L.; Barone, V.; Puzzarini, C. Rotational and Infrared Spectroscopy of Ethanimine: A Route toward Its Astrophysical and Planetary Detection. *Astrophys. J.* **2018**, *855* (2), 123. DOI: 10.3847/1538-4357/aaa899.

(109) Puzzarini, C. Isomerism of Cyanomethanimine: Accurate Structural, Energetic, and Spectroscopic Characterization. *J. Phys. Chem. A* **2015**, *119* (47), 11614–11622. DOI: 10.1021/acs.jpca.5b09489.

(110) Becke, A. D. Density-functional exchange-energy approximation with correct asymptotic behavior. *Phys. Rev. A* **1988**, *38* (6), 3098–3100. DOI: 10.1103/PhysRevA.38.3098.

(111) Lee, C.; Yang, W.; Parr, R. G. Development of the Colle-Salvetti correlation-energy formula into a functional of the electron density. *Phys. Rev. B* **1988**, *37* (2), 785–789. DOI: 10.1103/PhysRevB.37.785.

(112) Grimme, S. Semiempirical hybrid density functional with perturbative second-order correlation. *J. Chem. Phys.* **2006**, *124* (3), 034108. DOI: 10.1063/1.2148954.

(113) Grabow, J. U.; Stahl, W.; Dreizler, H. A multioctave coaxially oriented beam-resonator arrangement Fourier-transform microwave spectrometer. *Rev. Sci. Instrum.* **1996**, *67* (12), 4072–4084. DOI: 10.1063/1.1147553.

(114) Melosso, M.; Melli, A.; Spada, L.; Zheng, Y.; Chen, J.; Li, M.; Lu, T.; Feng, G.; Gou, Q.; Dore, L.; Barone, V.; Puzzarini, C. Rich Collection of n-Propylamine and Isopropylamine Conformers: Rotational Fingerprints and State-of-the-Art Quantum Chemical Investigation. *J. Phys. Chem. A* **2020**, *124* (7), 1372–1381. DOI: 10.1021/acs.jpca.9b11767.

(115) Gordy, W.; Cook, R. L. *Microwave Molecular Spectra*; Wiley, 1984.

(116) Melosso, M.; Achilli, A.; Tamassia, F.; Canè, E.; Pietropolli Charmet, A.; Stoppa, P.; Dore, L. High-resolution millimeter-wave spectroscopy of CH₂DCl: Paving the way for future astronomical observations of chloromethane isotopologues. *J. Quant. Spectrosc. Radiat. Transf.* **2020**, *248*, 106982. DOI: 10.1016/j.jqsrt.2020.106982.

(117) Melosso, M.; McGuire, B. A.; Tamassia, F.; Degli Esposti, C.; Dore, L. Astronomical Search of Vinyl Alcohol Assisted by Submillimeter Spectroscopy. *ACS Earth Space Chem.* **2019**, *3* (7), 1189–1195. DOI: 10.1021/acsearthspacechem.9b00055.

(118) Degli Esposti, C.; Melosso, M.; Bizzocchi, L.; Tamassia, F.; Dore, L. Determination of a semi-experimental equilibrium structure of 1-phosphapropyne from millimeter-wave spectroscopy of CH₃CP and CD₃CP. *J. Mol. Struct.* **2020**, *1203*, 127429. DOI: 10.1016/j.molstruc.2019.127429.

(119) Pickett, H. M. The fitting and prediction of vibration-rotation spectra with spin interactions. *J. Mol. Spectrosc.* **1991**, *148* (2), 371–377. DOI: 10.1016/0022-2852(91)90393-O.

(120) Coudert, L. H.; Lovas, F. J.; Suenram, R. D.; Hougen, J. T. New measurements of microwave transitions in the water dimer. *J. Chem. Phys.* **1987**, *87* (11), 6290–6299. DOI: 10.1063/1.453458.

(121) Ditlevsen, P. D.; Gardin, D. E.; Van Hove, M. A.; Somorjai, G. A. Molecular Modeling of Amine Dehydrogenation on Ni(111). *Langmuir* **1993**, *9* (6), 1500–1503. DOI: 10.1021/la00030a013.

(122) Krupka, J.; Pasek, J. Nitrile Hydrogenation on Solid Catalysts – New Insights into the Reaction Mechanism. *Curr. Org. Chem.* **2012**, *16* (8), 988–1004. DOI: 10.2174/138527212800194692.

(123) Tseng, K. N. T.; Rizzi, A. M.; Szymczak, N. K. Oxidant-free conversion of primary amines to nitriles. *J. Am. Chem. Soc.* **2013**, *135* (44), 16352–16355. DOI: 10.1021/ja409223a.

(124) Krupka, J.; Dluhoš, L.; Mrózek, L. Evaluation of Benzylamine Production via Reductive Amination of Benzaldehyde in a Slurry Reactor. *Chem. Eng. Technol.* **2017**, *40* (5), 870–877. DOI: 10.1002/ceat.201600538.

(125) Achard, T.; Egly, J.; Sigrist, M.; Maisse-François, A.; Bellemin-Laponnaz, S. Easy Ruthenium-Catalysed Oxidation of Primary Amines to Nitriles under Oxidant-Free Conditions. *Chem. Eur. J.* **2019**, *25* (58), 13271–13274. DOI: 10.1002/chem.201902557.

(126) Nava, M.; Martin-Drumel, M. A.; Lopez, C. A.; Crabtree, K. N.; Womack, C. C.; Nguyen, T. L.; Thorwirth, S.; Cummins, C. C.; Stanton, J. F.; McCarthy, M. C. Spontaneous and Selective Formation of HSNO, a Crucial Intermediate Linking H₂S and Nitroso Chemistries. *J. Am. Chem. Soc.* **2016**, *138* (36), 11441–11444. DOI: 10.1021/jacs.6b05886.

(127) Crowell, T. I.; McLeod, R. K. Kinetics of Hydrobenzamide Formation from p-Dimethylaminobenzaldehyde and Ammonia. Role of the Imine. *J. Org. Chem.* **1967**, *32* (12), 4030–4033. DOI: 10.1021/jo01287a067.

(128) Huang, J. M.; Zhang, J. F.; Dong, Y.; Gong, W. An effective method to prepare imines from aldehyde, bromide/epoxide, and aqueous ammonia. *J. Org. Chem.* **2011**, *76* (9), 3511–3514. DOI: 10.1021/jo102455q.

(129) van Schijndel, J.; Molendijk, D.; Spakman, H.; Knaven, E.; Canalle, L. A.; Meuldijk, J. Mechanistic considerations and characterization of ammonia-based catalytic active intermediates of the green Knoevenagel reaction of various benzaldehydes. *Green Chem. Lett. Rev.* **2019**, *12* (3), 323–331. DOI: 10.1080/17518253.2019.1643931.

(130)   Grimme, S.; Antony, J.; Ehrlich, S.; Krieg, H. A consistent and accurate ab initio parametrization of density functional dispersion correction (DFT-D) for the 94 elements H-Pu. *J. Chem. Phys.* **2010**, *132* (15), 154104. DOI: 10.1063/1.3382344.

(131)   Grimme, S.; Ehrlich, S.; Goerigk, L. Effect of the damping function in dispersion corrected density functional theory. *J. Comput. Chem.* **2011**, *32* (7), 1456–1465. DOI: 10.1002/jcc.21759.

(132)   Barone, V.; Cimino, P. Accurate and feasible computations of structural and magnetic properties of large free radicals: The PBE0/N07D model. *Chem. Phys. Lett.* **2008**, *454* (1–3), 139–143. DOI: 10.1016/j.cplett.2008.01.080.

(133)   Barone, V.; Cimino, P.; Stendardo, E. Development and validation of the B3LYP/N07D computational model for structural parameter and magnetic tensors of large free radicals. *J. Chem. Theory Comput.* **2008**, *4* (5), 751–764. DOI: 10.1021/ct800034c.

(134)   Fornaro, T.; Biczysko, M.; Bloino, J.; Barone, V. Reliable vibrational wavenumbers for C=O and N-H stretchings of isolated and hydrogen-bonded nucleic acid bases. *Phys. Chem. Chem. Phys.* **2016**, *18* (12), 8479–8490. DOI: 10.1039/c5cp07386c.

(135)   Papajak, E.; Leverentz, H. R.; Zheng, J.; Truhlar, D. G. Efficient diffuse basis sets: cc-pVxZ+ and maug-cc-pVxZ. *J. Chem. Theory Comput.* **2009**, *5* (5), 1197–1202. DOI: 10.1021/ct800575z.

(136)   Mills, I. M. Vibration–Rotation Structure in Asymmetric- and Symmetric-Top Molecules. In *Molecular Spectroscopy*; Rao, K. N., Matthews, C. W., Eds.; Academic Press, 1972; pp 115–140. DOI: 10.1016/b978-0-12-580640-4.50013-3.

(137)   Puzzarini, C.; Heckert, M.; Gauss, J. The accuracy of rotational constants predicted by high-level quantum-chemical calculations. I. molecules containing first-row atoms. *J. Chem. Phys.* **2008**, *128* (19), 194108. DOI: 10.1063/1.2912941.

(138)   Barone, V.; Biczysko, M.; Puzzarini, C. Quantum chemistry meets spectroscopy for astrochemistry: Increasing complexity toward prebiotic molecules. *Acc. Chem. Res.* **2015**, *48* (5), 1413–1422. DOI: 10.1021/ar5003285.

(139)   Raghavachari, K.; Trucks, G. W.; Pople, J. A.; Head-Gordon, M. A fifth-order perturbation comparison of electron correlation theories. *Chem. Phys. Lett.* **1989**, *157* (6), 479–483. DOI: 10.1016/S0009-2614(89)87395-6.

(140)   Dunning, T. H. Gaussian basis sets for use in correlated molecular calculations. I. The atoms boron through neon and hydrogen. *J. Chem. Phys.* **1989**, *90* (2), 1007–1023. DOI: 10.1063/1.456153.

(141)   Helgaker, T.; Klopper, W.; Koch, H.; Noga, J. Basis-set convergence of correlated calculations on water. *J. Chem. Phys.* **1997**, *106* (23), 9639–9646. DOI: 10.1063/1.473863.

(142)   Møller, C.; Plesset, M. S. Note on an approximation treatment for many-electron systems. *Phys. Rev.* **1934**, *46* (7), 618–622. DOI: 10.1103/PhysRev.46.618.

(143)   Woon, D. E.; Dunning, T. H. Gaussian basis sets for use in correlated molecular calculations. V. Core-valence basis sets for boron through neon. *J. Chem. Phys.* **1995**, *103* (11), 4572–4585. DOI: 10.1063/1.470645.

(144)   Kendall, R. A.; Dunning, T. H.; Harrison, R. J. Electron affinities of the first-row atoms revisited. Systematic basis sets and wave functions. *J. Chem. Phys.* **1992**, *96* (9), 6796–6806. DOI: 10.1063/1.462569.

(145)   Feller, D. The use of systematic sequences of wave functions for estimating the complete basis set, full configuration interaction limit in water. *J. Chem. Phys.* **1993**, *98* (9), 7059–7071. DOI: 10.1063/1.464749.

(146)   Frisch, M. J.; Trucks, G. W.; Schlegel, H. B.; Scuseria, G. E.; Robb, M. A.; Cheeseman, J. R.; Scalmani, G.; Barone, V.; Petersson, G. A.; Nakatsuji, H.; Li, X.; Caricato, M.; Marenich, A. V.; Bloino, J.; Janesko, B. G.; Gomperts, R.; Mennucci, B.; Hratchian, H. P.; Ortiz, J. V.; Izmaylov, A. F.; Sonnenberg, J. L.; Williams-Young, D.; Ding, F.; Lipparini, F.; Egidi, F.; Goings, J.; Peng, B.; Petrone, A.; Henderson, T.; Ranasinghe, D.; Zakrzewski, V. G.; Gao, J.; Rega, N.; Zheng, G.; Liang, W.; Hada, M.; Ehara, M.; Toyota, K.; Fukuda, R.; Hasegawa, J.; Ishida, M.; Nakajima, T.; Honda, Y.; Kitao, O.; Nakai, H.; Vreven, T.; Throssell, K.; Montgomery, J. A., J.; Peralta, J. E.; Ogliaro, F.; Bearpark, M. J.; Heyd, J. J.; Brothers, E. N.; Kudin, K. N.; Staroverov, V. N.; Keith, T. A.; Kobayashi, R.; Normand, J.; Raghavachari, K.; Rendell, A. P.; Burant, J. C.; Iyengar, S. S.; Tomasi, J.; Cossi, M.; Millam, J. M.; Klene, M.; Adamo, C.; Cammi, R.; Ochterski, J. W.; Martin, R. L.; Morokuma, K.; Farkas, O.; Foresman, J. B.; Fox, D. J. Gaussian 16, Rev. C.01. *Gaussian, Inc., Wallingford, CT* **2016**.

(147)   Matthews, D. A.; Cheng, L.; Harding, M. E.; Lipparini, F.; Stopkowicz, S.; Jagau, T. C.; Szalay, P. G.; Gauss, J.; Stanton, J. F. Coupled-cluster techniques for computational chemistry: The CFOUR program package. *J. Chem. Phys.* **2020**, *152* (21), 214108. DOI: 10.1063/5.0004837.

(148)   Chou, C. H.; Chu, L. T.; Chiu, S. J.; Lee, C. F.; She, Y. T. Synthesis of N,N-di(arylmethylidene)arylmethanediamines by flash vacuum pyrolysis of arylmethylazides. *Tetrahedron* **2004**, *60* (31), 6581–6584. DOI: 10.1016/j.tet.2004.06.082.

Chapter 3 – Index

3. Fluorinated organic species

3.1.   Introduction

3.1.1. Importance and occurrence

Fluorinated molecules have a wide range of applications.[1] In particular, fluorine is the second most used heteroelement in life sciences after nitrogen.[2–5] Approximately 20% of marketed drugs and 50% of agrochemicals registered in the last two decades are estimated to contain one or more fluorine atoms (Figures 3.1A and 3.1B, respectively).[6–8]
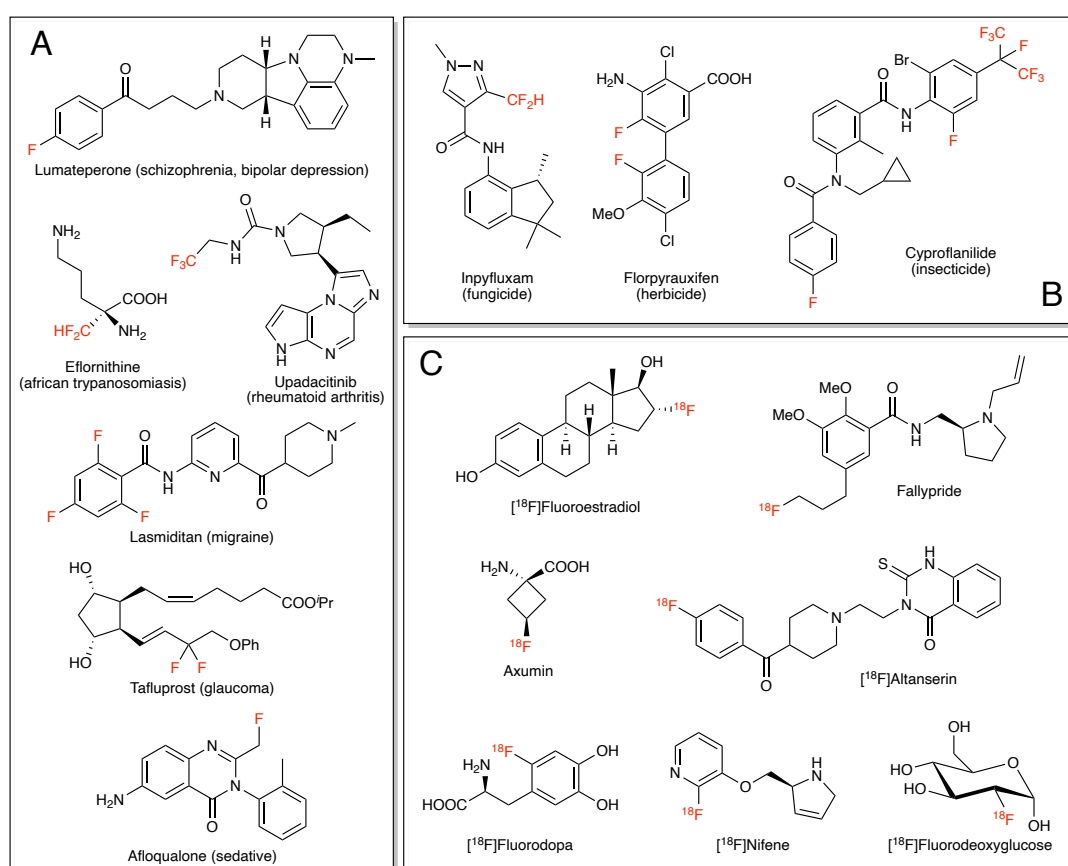

Figure 3.1: Some examples of synthetic organofluorine compounds used in life sciences: **(A)** drugs (selected from Refs. 9, 10), **(B)** agrochemicals (selected from Ref. 8), **(C)** PET imaging agents (selected from Ref. 11).

In particular, the key role of fluorine in medicinal chemistry[12–14] is also witnessed its increasing importance in biological studies by extensive use of ^{18}F-labeled molecules in positron emission tomography (Figure 3.1C).[15,16] Indeed, the incorporation of fluorine in key positions of a molecular system can affect its conformational stability (see, e.g., the "gauche effect"),[17] membrane permeability, metabolic stability, and binding affinity,[18,19] thus representing a very useful and versatile tool for drug design.[20,21] These distinctive features are related to the intrinsic properties of the C−F bond (a highly polarized covalent bond with a large dipole moment and bond strength greater than that of C−H), which is able to establish interactions

of charge/dipole nature with the environment, also showing hyperconjugative effects related to the presence of a low-energy C−F sigma antibonding orbital.[22] The importance of fluorine and, especially, organofluorine compounds, has stimulated the development of a large number of interesting methodologies for fluorine incorporation,[23–26] with fluorinated amino acids being particularly significant targets since their introduction in specific domains of proteins can improve their stability and folding[27–31] as well as their biological activity.[32,33] Indeed, the incorporation of fluoro amino acids, such as fluorinated proline,[34] phenylalanine,[35] and tyrosine[36,37] in specific proteins, has been analysed in detail. Fluorinated amino acids can also be introduced in peptides by chemical synthesis,[38] ribosomal translation,[39] or chemical ligation.[40] It is from this perspective that the increasing importance of fluorination for pharmaceutical applications has been put forward.[41]

3.1.2. *Methodologies for fluorine incorporation into organic molecules*

Fluorination and fluoroalkylation are the major strategies used for the formation of carbon-fluorine bonds and fluorinated carbon-carbon bonds, respectively. The past two decades have witnessed a rapid growth in fluorination and fluoroalkylation methods thanks to the development of new reagents and catalysts.[42] Nevertheless, although inorganic fluorides – such as CaF_2, a mineral also called fluorite or fluorspar – are abundant on Earth, their physical properties and lack of reactivity make them unsuited for most synthetic organic chemistry. Furthermore, the organofluorine compounds typically required for the synthesis of pharmaceuticals are extremely rare in nature.[43,44] As a result, almost all of the organofluorine compounds and materials used in industry and academia are synthetic. The source of fluorine for all fluorination and fluoroalkylation reactions is HF, which is prepared from the reaction of CaF_2 mineral with sulfuric acid.[45] Unfortunately, HF is not a process friendly reagent in a typical laboratory setting, as it has the ability to dissolve glass by reacting with silicon. It must be handled carefully due to its corrosive nature, since it can penetrate the skin, causing severe burns and toxicity as the fluoride ion reacts with calcium in the body.[46] However, suitably equipped industrial plants can efficiently and safely use HF to produce most of the available fluorination reagents. Eventually, the increasing knowledge of the properties and behaviours of chemical bonds involving fluorine enabled the production of greener, milder, safer, cheaper, more efficient and more selective fluorinating reagents.[47–49] Recently, huge efforts have been devoted to the development of catalytic methodologies for the incorporation of single fluorine atoms or fluorinated groups into organic molecules. In particular, the optimization of reactivity and selectivity can be achieved combining astute selection of fluorination/fluoroalkylation reagents with new catalyst designs.[50,51] Fluorination protocols may seem the most straightforward methods for the introduction of a fluorine atom. Actually, the displacement of a leaving group with a simple fluoride source is a difficult reaction, since the fluoride anion tends to act more as a base than a nucleophile, unless aided by hydrogen bonding.[52] Hence, fluorine is usually introduced into organic

scaffolds as part of polyatomic fluorine-bearing groups, mainly by means of fluoroalkylation protocols, such as trifluoromethylation, difluoromethylation or monofluoromethylation. Before analysing in detail the most common fluorination protocols, a brief summary of the main fluoroalkylation strategies will be given in the following.

Trifluoromethylation protocols are very widespread as fruitful strategies for the introduction of fluorinated functional groups. Indeed, such methodologies can be efficiently exploited thanks to a plethora of trifluoromethylation reagents – whose properties and reactivity depend on their electronic properties – stimulating the development of various trifluoromethylation methods, including electrophilic, nucleophilic, radical and transition-metal catalysed or mediated reactions (Figure 3.2).[53]
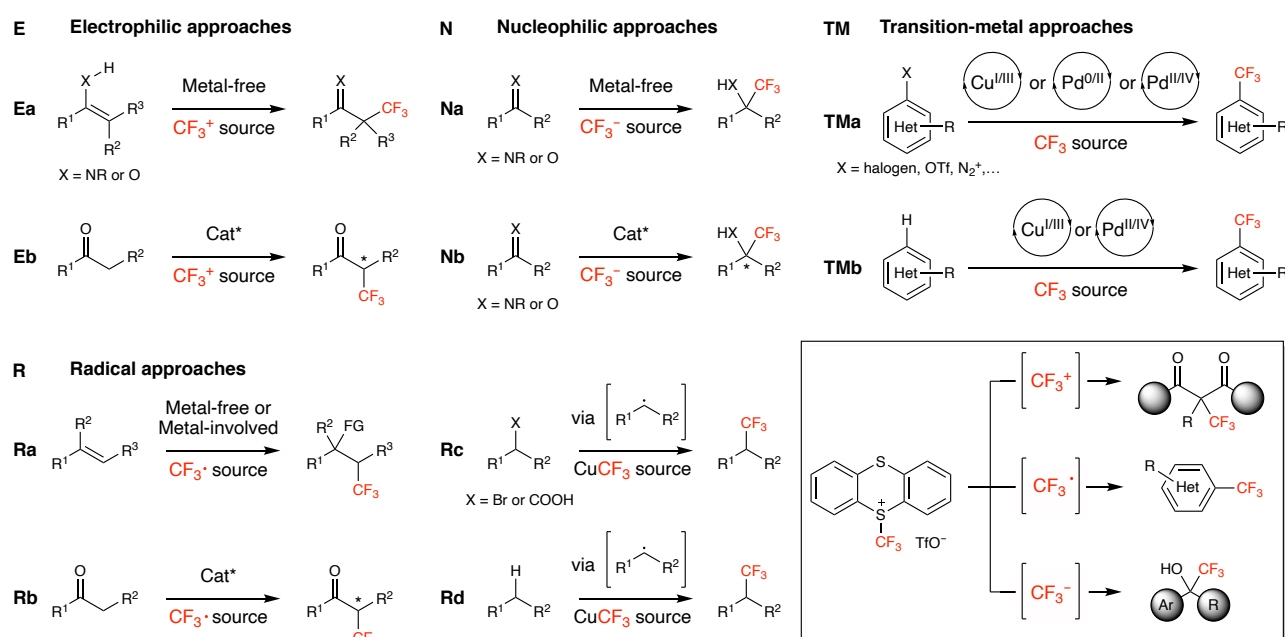
Figure 3.2: General account of trifluoromethylation methods. Electrophilic methods (**E**): addition to electron-rich alkenes (**Ea**), asymmetric α-trifluoromethylation of carbonyl compounds (**Eb**). Nucleophilic methods (**N**): uncatalyzed (**Na**) and catalyzed (**Nb**, asymmetric) addition to carbonyls/imines. Radical methods: addition to alkenes (**Ra**), asymmetric α-trifluoromethylation of carbonyl compounds (**Rb**), trifluoromethylation of alkyl bromides/carboxylic acids (**Rc**), trifluoromethylation through C−H activation (**Rd**). Transition-metal methods (**TM**): cross-coupling with aryl electrophiles (**TMa**), aryl C−H trifluoromethylation (**TMb**). Inset: trifluoromethyl thianthrenium triflate, an example of versatile trifluoromethylating reagent (Ref. 54).

Due to the high electronegativity of fluorine, nucleophilic trifluoromethylation reagents, i.e. having a partial negative charge on the active trifluoromethyl donor group,[55] are more common than electrophilic ones. Indeed, only few trifluoromethylation reagents have a partial positive charge on the fluorinated group.[56] Particular trifluoromethylation reagents can behave as nucleophilic, electrophilic or radical sources of trifluoromethyl groups, depending on reaction partners and conditions (Figure 3.2, inset).[54] Contrary to trifluoromethylation protocols, difluoromethylation and monofluoromethylation methodologies are much less versatile in terms of the electronic properties of the active fluorinated donor group.[57] Some examples of tri-, di-, and mono-fluoromethylating reagents are reported in Figure 3.3.
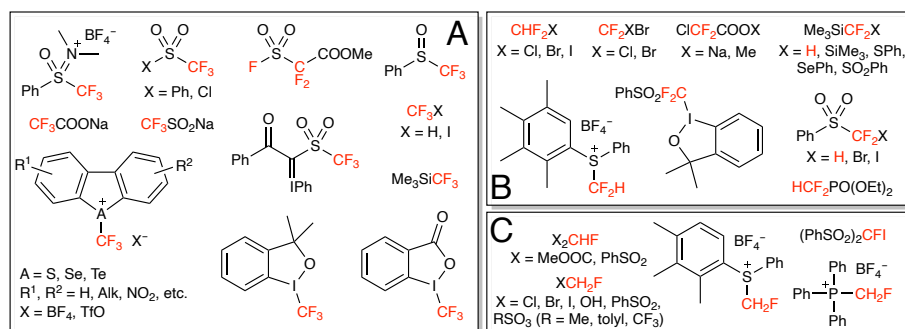
Figure 3.3: Selected examples of tri-, di-, and mono-fluoromethylating reagents (**A**, **B**, and **C**, respectively).

Albeit the aforementioned strategies and reagents can be used to solve most synthetic issues related to fluorine incorporation into organic molecules, some of them can only be overcome by inserting single fluorine atoms. Due to the high electronegativity of fluorine, nucleophilic reagents are the most prominent (Figure 3.4A).
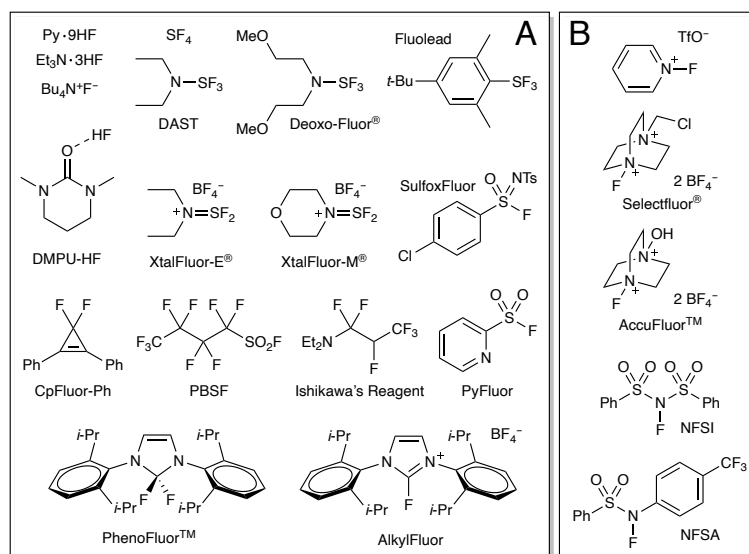
Figure 3.4: Most common nucleophilic and electrophilic fluorinating reagents (**A** and **B**, respectively).

In particular, well-known HF derivatives include HF-pyridine (Py·9HF, Olah's reagent),[58] triethylamine trihydrofluoride (Et₃N·3HF)[59] and HF complexed with 1,3-dimethyl-3,4,5,6-tetrahydro-2-pyrimidinone (DMPU-HF).[60] Gradual release fluoride sources – such as diethylaminosulfur trifluoride (DAST), Deoxo-Fluor®, PhenoFluor™ and PyFluor – are usually referred as deoxyfluorinating reagents, since they merge high oxophilicity with the ability to release fluoride in solution.[61] The rationale behind the use of tetrabutylammonium fluoride (TBAF) as a fluoride source, is often controversial, mainly because of the difficulties in establishing its hydration degree.[62,63] Nevertheless, it can be employed in the form of hydrogen-bonded complexes – such as TBAF(*t*-BuOH)₄ and TBAF(pin)₂ – with tuneable nucleophilic properties.[64,65] Moving to electrophilic fluorinating reagents such as Selectfluor® and N-fluorobenzenesulfonimide (NFSI), the partial positive charge on the electronegative fluorine makes them useful as powerful oxidants (Figure 3.4B).[66] As far as transition metal catalysis is concerned, reductive

elimination is usually the most relevant issue in the case of C−F bond formation. Accurate mechanistic studies revealed that reductive elimination – whenever Pd(0)/Pd(II) catalytic cycles are involved – is feasible with a bulky ancillary ligand, forcing C−F bond formation from a 14-electron Pd(II) complex.[67] However, high oxidation metal complexes, such as those involved in Pd(II)/Pd(IV) and Cu(I)/Cu(III) catalytic cycles, were found to ease the reductive elimination step,[68,69] together with the introduction of properly designed novel ligands or assisting/directing groups.[70] Promising decarboxylative fluorination protocols have recently emerged amongst photoredox catalysis approaches.[71,72] The challenge of controlled stereoselectivity can be tackled with the use of electrophilic fluorination reagents and transition metal catalysis,[73] or by means of organocatalytic approaches, such as enamine catalysis[74] or cationic/anionic phase transfer catalysis.[75,76] Recent biomimetic studies, focused on the fluorinase enzyme, ended up with alternative bioinspired strategies merging hydrogen bonding and phase transfer catalysis to use alkali metal fluorides as fluorine sources in asymmetric catalysis.[77–79] However, most of the aforementioned approaches require pre-functionalized substrates, lowering the atom economy of the transformations. This drawback can be overcome by means of fluorination protocols through C−H activation,[80] allowing selective functionalization at late synthetic stages, a fairly common occurrence when preparing novel drugs and chemical libraries.[81] Even in this case, electrophilic fluorination reagents dominate, due to their ability to act as both fluorine sources and oxidants. Nevertheless, shrewd combinations with suitable external oxidants have recently enabled the use of nucleophilic fluorination reagents.[70,82] Depending on the activation mode operating in C−H fluorination approaches, they can be divided into two classes: transition metal-catalysed protocols, involving a metal centre in the C−H activation step, and radical-based methodologies, involving carbon-centred radicals.[80]

3.1.3. *Fluorine in the biosphere: such a rarity*

The abundance of laboratory strategies for the incorporation of fluorine into organic molecules is not matched with a wide range of natural approaches. Although fluorine is the 24th most abundant element in the universe, and the 13th most common element in the Earth's crust (0.059% by weight),[83] the biosphere appears as almost "impermeable" to the involvement of fluorine in most biochemical processes.[84] The first obstacle preventing fluorine to flow from abiotic inorganic matter to the biosphere is the low water solubilities of the most common natural inorganic sources of fluorine, i.e. the minerals fluorspar (CaF_2), fluorapatite [$Ca_5(PO_4)_3F$] and cryolite (Na_3AlF_6).[85] For the sake of comparison, the bioavailability of fluoride in seawater is four orders of magnitude lower than that of chloride (1.3 mg L^{-1} and 19 g L^{-1}, respectively). Besides, the electronic properties of fluorine (in particular its electronegativity) make its redox chemistry virtually inaccessible for most of the known enzymatic kits. Indeed, fluorine redox potential ($F_2/2F^-$ = +2.87 V) is much higher with respect to other halogens, hampering the formation of fluorine analogues of hypohalites or other electrophilic halogen species involved in

enzymatic halogenation processes.[86] Finally, fluoride ion has a very high hydration energy (490 kJ mol^{-1}) and is therefore a rather poor nucleophile in aqueous/biological media. Hence, the formation of organic C$-$F bonds via typical nucleophilic substitution pathways involving fluoride ion can hardly occur in such environments, unless peculiar enzymatic systems come into play.[87] Therefore, fluoride ion (the most common fluorine species in nature)[88] is usually considered a xenobiotic, contrarily to the other halides, albeit fluorine is by far the most common halogen on Earth (chlorine, bromine, and iodine rank 19th, 49th, and 62nd, respectively). Despite the aforementioned difficulties, eventually some organisms managed to develop enzymatic kits for the synthesis of fluorinated organic compounds (Figure 3.5).[89]
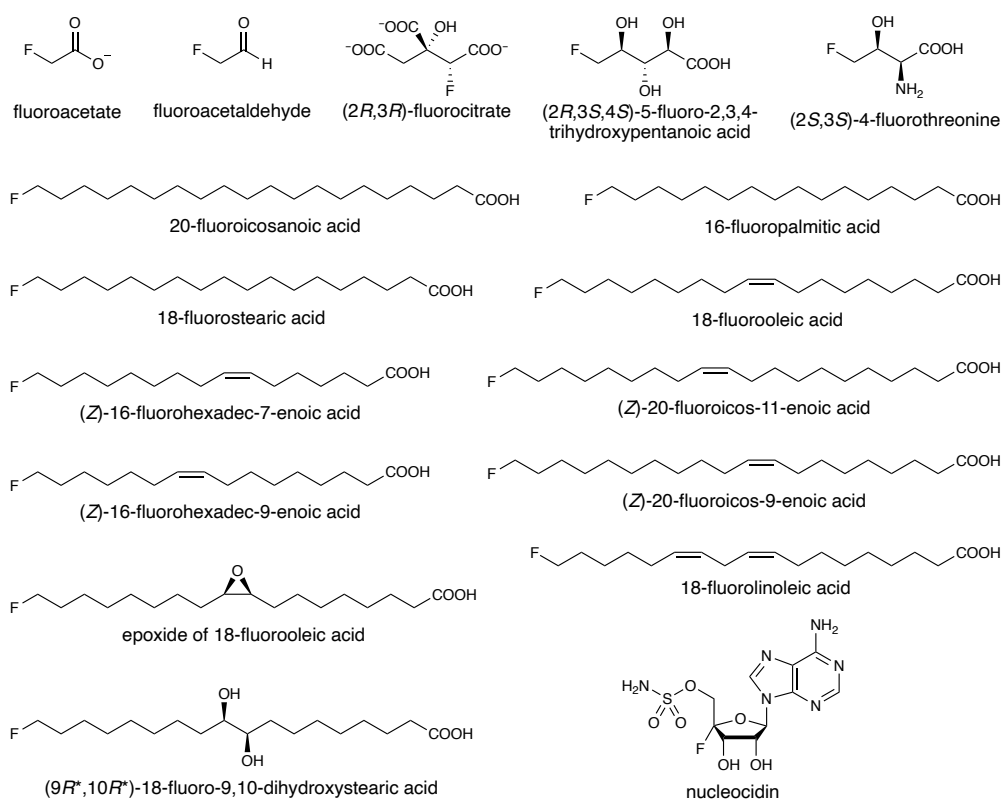
Figure 3.5: Selected naturally occurring fluorinated organic species.

In the following, a brief account of the main fluorinated organic species of biogenic origin discovered so far, is reported:

1. Fluoroacetate is produced by numerous plant species. Even some edible plants – e.g. tea leaves, soy beans, oatmeal – were found to contain nontoxic levels of fluoroacetate. The mechanism of fluoroacetate biosynthesis in plants is still unknown.[90] Some microorganisms also produce fluoroacetate. In the case of *Streptomyces cattleya*, its whole biosynthetic pathway was uncovered. More specifically, the mechanism of the fluorination step – catalysed by the fluorinase enzyme – was fully elucidated.[91,92] Furthermore, the metabolism of fluoroacetate was identified as the main cause of its high toxicity.[93] Fluoroacetate-producing organisms developed proper strategies to

avoid self-poisoning. High fluoroacetate resistance was also observed in the case of herbivores living in areas harbouring fluoroacetate-producing plants.

2. (2*R*,3*R*)-Fluorocitrate is a metabolite of fluoroacetate, formed whenever the latter enters the citric acid cycle.[94]

3. Fluoroacetaldehyde is a metabolic precursor of fluoroacetate in *Streptomyces cattleya*.[95]

4. (2*R*,3*S*,4*S*)-5-Fluoro-2,3,4-trihydroxypentanoic acid is a side fluorometabolite of the fluorinase pathway.[96]

5. Nucleocidin is a fluorinated nucleoside produced by *Streptomyces calvus*.[97]

6. ω-Fluorinated fatty acids were discovered in the seed oil of *Dichapetalum toxicarium*, a West African plant.[98–100] They are toxic because their metabolism generates fluoroacetate. Contrarily to the latter, they are very lipophilic and can be directly absorbed through the skin. Their ratios are similar to those observed for the parent nonfluorinated fatty acids, thus suggesting a common biosynthetic origin.

7. (2*S*,3*S*)-4-Fluorothreonine (4F-Thr) is the only naturally occurring fluorinated amino acid discovered so far. It is coproduced with fluoroacetate by *Streptomyces cattleya*.[101] It acts as an antibiotic agent towards several bacteria.[102] It probably exerts its action when it replaces parent nonfluorinated threonine (Thr) in primary metabolic pathways, thus resulting in the production of other toxic fluorinated species.[103]

3.2.   Aim

4F-Thr has been examined as a fluorinated analogue of Thr, aiming at a deeper understanding of the effects of fluorine insertion into organic molecules.[19] This task requires special computational methodologies to evaluate structural and physicochemical properties. Indeed, flexible molecules in aqueous media need to be described in terms of an ensemble of low-lying conformers experiencing local fluctuations. The conformational ensemble must be as exhaustive as possible to avoid unsatisfactory description and modelling. Such "completeness" can be achieved by combining quantum chemistry and machine learning. This strategy enables an effective exploration of the "flat" conformational space, which means a detailed analysis of conformational changes involving small energy variations. Indeed, 4F-Thr represents an ideal compromise – between the need for compounds with non-trivial PES as test cases, and the need to keep complexity low enough to avoid excessively demanding computational analyses – to test and validate the proposed strategy. Although enantioenriched samples enable comparative studies between calculated and experimental chiroptical properties, direct diastereoselective approaches allow the production of racemic samples, which are still very useful to assess a wide range of relevant properties. Indeed, this is the case for the acid dissociation constants of 4F-Thr, which were determined through accurate titration experiments. From the synthetic point of view, the main aim of this project was the development of new synthetic approaches to obtain sufficient amount of 4F-Thr for its characterization.[104] Moreover, gas-phase measurements – by means of laser-ablation techniques – are currently ongoing (the racemic sample is suited for this purpose), with the aim of measuring the rotational spectrum of 4F-Thr to determine its conformational population in the gas phase. Even in this case, preliminary computational studies are necessary to guide the interpretation of the experimental data.

3.3.　Results and discussion − 4-Fluorothreonine (4F-Thr)

An effective comparison between theoretical investigations and observed physicochemical properties requires enough 4F-Thr, depending on the experimental measurement. Detailed studies and advancements in possible applications of 4F-Thr have been suffering from the lack of available materials due to difficult or tedious syntheses, while drug design applications might be hampered by the lack of structural and physicochemical characterization. To date, according to the best of our knowledge, only five synthetic routes have been reported for 4F-Thr (Scheme 3.1).[105–109]
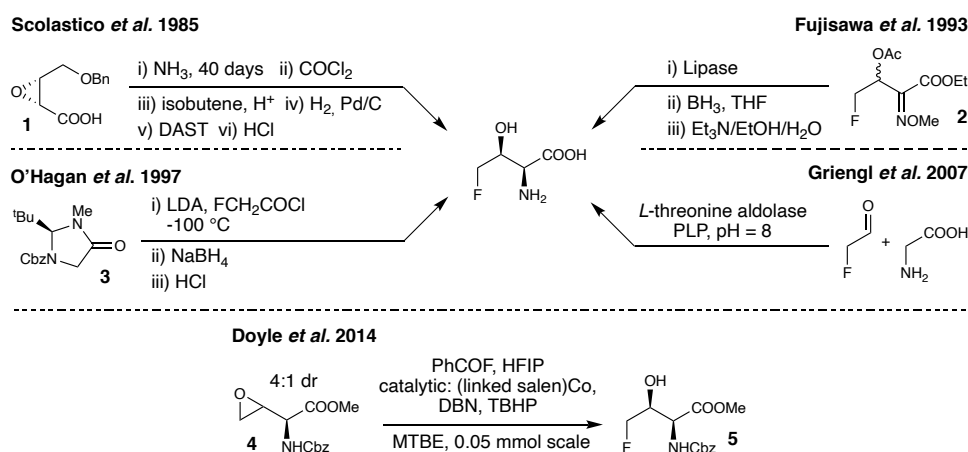
Scheme 3.1: Previous literature synthetic routes for 4F-Thr.

In the following, a brief account of these strategies is reported, with particular emphasis on the main drawbacks:

1. In 1985, Scolastico *et al.*[105] reported an enantioselective approach starting from the known (2S,3R)-3-benzyloxymethyl-2-(hydroxymethyl)-oxirane, affording 4F-Thr in 7 steps. Ruthenium-catalysed oxidation with sodium metaperiodate led to the corresponding carboxylic acid **1**. The latter was treated with concentrated ammonia for 40 days (prolonged reaction time, first relevant drawback), undergoing a ring-opening (R-O) reaction on the epoxide moiety. The latter afforded a regioisomeric amino acid mixture in favour of the desired product (r.r. 9:1). Such mixture was resolved by conversion into the corresponding oxazolidinecarboxylic acids (with phosgene, second drawback), followed by esterification with isobutene (gas, third drawback), leading to the corresponding *t*-butyl esters. These were separated by flash chromatography. The desired isomer was hydrogenated to remove the benzyl protection, affording a primary alcohol, which was treated with DAST at low temperature (deoxyfluorination reaction). The obtained fluorinated compound was hydrolysed (HCl 6M), and (2*S*,3*S*)-4F-Thr was obtained after ion-exchange chromatography.

2. In 1993, Fujisawa *et al.*[106] reported an approach involving enzymatic resolution through lipase-mediate hydrolysis. Starting from ethyl 4-chloro-3-oxobutyrate, 4F-Thr was obtained in 8 steps

(hydroxyimination, methylation, reduction, fluorination, acetylation, enzymatic resolution, reduction, hydrolysis). The main drawback of this approach is the need for enzymatic resolution of the acetylated compound **2**.

3. In 1997, O'Hagan *et al.*[107] developed a synthetic approach through Seebach's imidazolidinone methodology for the synthesis of α-amino-β-hydroxy acids. 4F-Thr was obtained in only 3 steps (acylation, reduction, hydrolysis). Fluorine is already incorporated in the acylating reagent, i.e. fluoroacetyl chloride, obtained by treatment of fluoroacetic acid with thionyl chloride. The main drawback of this approach is the use of fluoroacetyl chloride for the acylation of **3**. This highly toxic chemical must be handled with extreme care.

4. In 2007, Griengl *et al.*[108] reported an enzymatic approach for the synthesis of 4F-Thr. The enzyme *L*-threonine aldolase was able to catalyse the formation of 4F-Thr starting from fluoroacetaldehyde and glycine, in the presence of pyridoxal phosphate (PLP). The use of a non-commercial enzyme represents the main drawback of this strategy. Furthermore, fluoroacetaldehyde is not commercial, and it is usually prepared by oxidation of fluoroethanol.

5. In 2014, Doyle *et al.*[109] reported a R-O reaction leading to vicinal fluoroalcohols starting from epoxides. In particular, starting from the epoxide of protected vinylglycine **4**, protected 4F-Thr **5** could be obtained. This approach requires a non-commercial dimeric (linked-Salen)cobalt catalyst, and benzoyl fluoride as the fluoride source. The synthesis of the cobalt catalyst – having a molecular weight of more than 1000 Da – is very long and tedious,[110] thus representing the main drawback of this approach.

All the above-mentioned papers reported different approaches for the enantioenriched synthesis of 4F-Thr. Recently, some members of the research group of Stereoselective Metal Catalysis and Photoredox Catalysis, led by Cozzi and Gualandi, have explored several synthetic approaches, trying to avoid the main drawbacks of the above-mentioned literature approaches.

3.3.1. *First attempts for the synthesis of enantioenriched 4F-Thr*

First attempts were based on chiral pool approaches starting from commercial amino acids (Scheme 3.2). Such strategies had either an excessively high number of steps, or low-yield and/or unselective steps. In some cases, the pivotal fluorination step did not to occur at all, thus compromising the respective synthetic strategy as a whole.
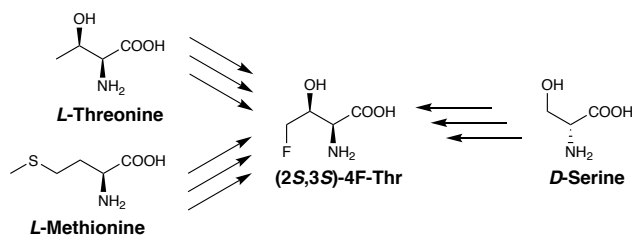
Scheme 3.2: Possible amino acid precursors for chiral pool approaches to 4F-Thr.

First, threonine methyl ester **8** was used as such for a direct photocatalytic electrophilic fluorination methodology reported by Harperin *et al.* in 2015.[111] This C−H activation protocol relies on a hydrogen atom transfer (HAT) step promoted by the excited state of the inorganic photosensitizer, i.e. sodium decatungstate (NaDT). The obtained C-centred radical is then fluorinated by NFSI. Albeit this protocol is suited for the fluorination of branched amino acids, such as valine methyl ester **6**, **8** was unreactive (Scheme 3.3A). Indeed, C-centred radicals in primary positions are very hard to generate. Furthermore, the presence of the hydroxyl group may be detrimental, since it can favour undesired side reactions. Further studies using different protecting groups were also performed. When protected as carbamate (simultaneous protection of hydroxyl and amino groups), the cyclic threonine derivative **10** was unreactive, even using slightly different reaction conditions (Scheme 3.3B).[112] When protected as phthalimide,[113] the threonine derivative **14** was subjected to the photocatalytic conditions reported by Hamashima *et al.*,[114] for the phthalimide-promoted fluorination of aliphatic C−H bonds, using Selectfluor® as the fluorinating agent. Even in this case, although such protocol is suited for the electrophilic fluorination of several phthalimide-protected nonpolar amino acids (such as valine derivative **12**), that was not the case for threonine, whose derivative was found unreactive, probably because of the presence of the free hydroxyl group (Scheme 3.3C).
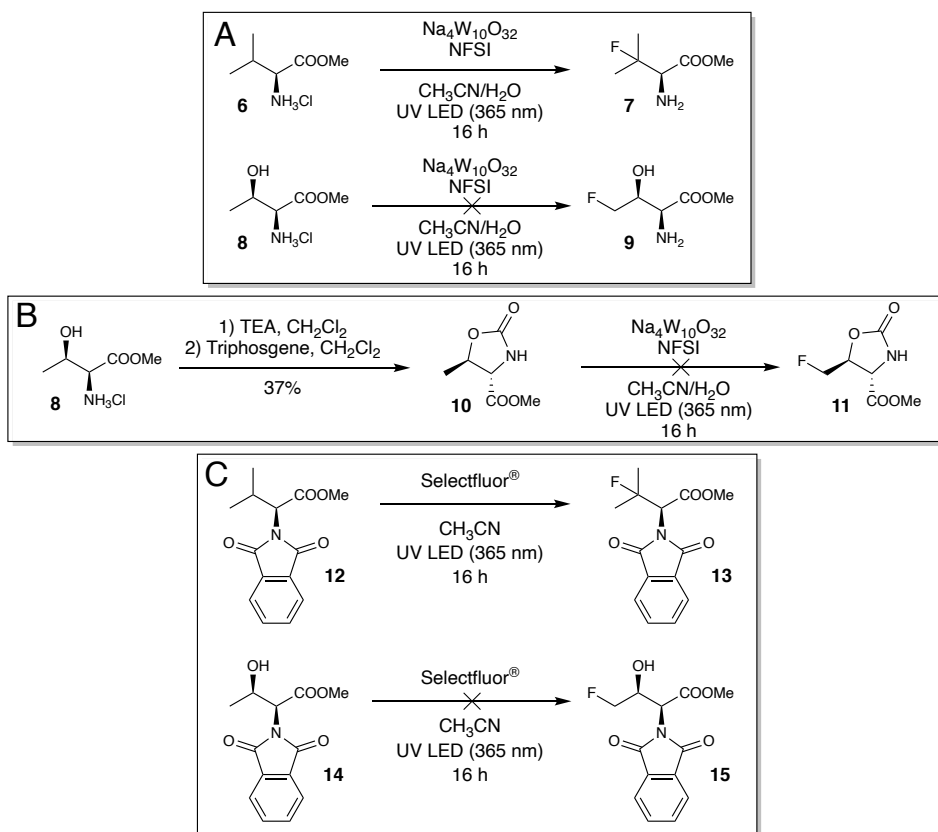
Scheme 3.3: Photocatalytic electrophilic fluorination tests. **(A)** Fluorination of valine and threonine derivatives (**6** and **8**, respectively) with NFSI. **(B)** Synthesis of threonine derivative **10** and successive fluorination with NFSI. Even other four different reaction conditions resulted ineffective: (i) no water; (ii) tetrabutylammonium decatungstate (TBADT) instead of NaDT; (iii) TBADT instead of NaDT, without water; (iv) TBADT instead of NaDT, NaHCO₃ as additive. **(C)** Phthalimide-promoted fluorination of valine and threonine derivatives (**12** and **14**, respectively) with Selectfluor®. **12** was synthetized from *L*-valine in two steps (1. *L*-valine + phthalic anhydride, neat, 140 °C, 72%; 2. SOCl₂, MeOH, 51%), while **14** was synthetized from **8** (phthalic anhydride, Et₃N, toluene, 10%).

Based on these unsatisfactory results, electrophilic fluorination methodologies were abandoned, in favour of nucleophilic ones. First, compound **10** was subjected to nucleophilic fluorination protocol via C−H activation, using the system AgF/TBAF as the fluorinating agent, and SalenMnCl as the metal catalyst.[115] This strategy resulted unsuccessful for the fluorination of the primary position of threonine oxazolidinone derivative. Indeed, this system can promote the fluorination of sufficiently activated C−H bonds, such as benzylic ones (Scheme 3.4).

Scheme 3.4: SalenMnCl-catalysed nucleophilic fluorination test using **10** as starting material.

Nucleophilic fluorination protocols via epoxide R-O reaction were then studied, based on a reported methodology for the synthesis of fluorohydrins.[116] In particular, the N-Cbz-protected epoxide of vinylglycine methyl ester **4** – obtained in few steps starting from the commercially available *L*-methionine – was chosen as suitable starting material for R-O reactions (Scheme 3.5).[117]
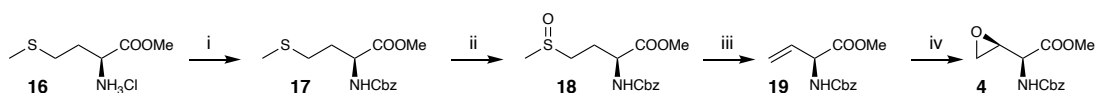
Scheme 3.5: Synthesis of N-Cbz-protected epoxide of vinylglycine methyl ester **4** starting from *L*-methionine methyl ester hydrochloride **16**. (i) CbzCl, K_2CO_3, EtOH/H_2O, 98%. (ii) $NaIO_4$, MeOH/H_2O, 99%. (iii) Elimination by Kugelrohr distillation (240 °C, $6 \cdot 10^{-1}$ mbar), 70%. (iv) MCPBA, CH_2Cl_2, 20h, 37% (70% conv.), single diastereoisomer.

Several strategies for the direct addition of fluoride were explored. First, CsF was used as fluoride source,[118] but no R-O reaction was observed using either *tert*-amyl alcohol (TAA) or trifluoroethanol (TFE) as reaction solvent (Scheme 3.6, top). Treatment with aqueous HBF_4 led to hydrolysis of the methyl ester, together with the formation of the vicinal diol, via epoxide R-O reaction by water, with the formation of compound **20** as the main product (Scheme 3.6, bottom). These observations do not contrast with other literature data reporting HBF_4 as suited fluorinating agent for epoxide R-O reactions. Indeed, in those cases HBF_4 was used as etherate complex in anhydrous conditions.[119]
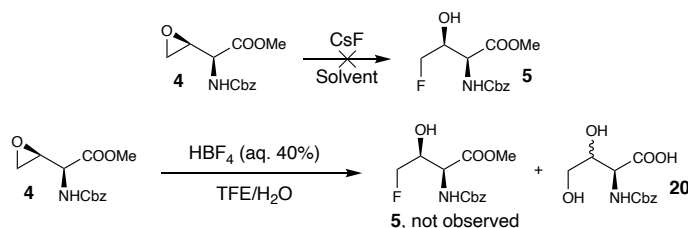
Scheme 3.6: Epoxide R-O reaction tests on **4**, with different fluoride sources. Tested CsF-based conditions: (i) in TAA, 90 °C, 2.5h; (ii) in TFE, r.t., 2.5h.

As a last resort, nucleophilic deoxyfluorination approaches were studied. The main idea was to merge the last part of the synthetic approach of Scolastico, with particular reference to the use of DAST as deoxyfluorinating agent,[105] with the well-known chemistry of epoxides, using suitably protected epoxides of vinylglycine as useful starting materials.[120] In particular, shrewd choices of oxygen nucleophiles can enable useful R-O reactions onto such epoxides. If the nucleophilic attack occurs at the less hindered carbon, the epoxydic oxygen will evolve (upon protonation) to that of the hydroxylic group of 4F-Thr, while the terminal one will be subjected to deoxyfluorination (Scheme 3.7). However, these two hydroxyl groups need to be protected with orthogonal protecting groups, so that the primary one can be selectively deprotected to undergo deoxyfluorination.
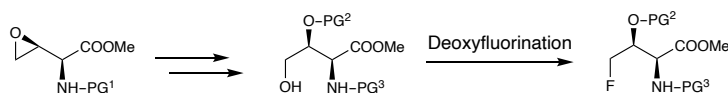
Scheme 3.7: Synthetic strategy starting from protected epoxide of vinylglycine to allow a selective deoxyfluorination step.

Indeed, a good starting point is represented by the oxazolidinone-type primary alcohol **23** obtained upon hydrogenation of **22** in the synthetic approach reported by Scolastico. Hence, the most straightforward way to connect **22** and the protected epoxide of vinylglycine is the epoxide R-O reaction performed with

First attempts for the synthesis of enantioenriched 4F-Thr

benzyl alcohol, followed by deprotection of the amino group to give the amino alcohol **21**, right away reprotected in the form of oxazolidinone **22** (Scheme 3.8).
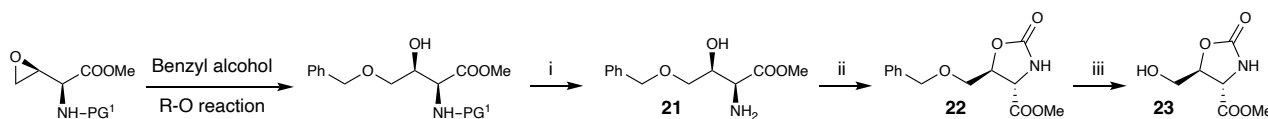
Scheme 3.8: Synthetic strategy to connect protected epoxide of vinylglycine and compound **23**: (i) deprotection conditions depending on the nature of PG[1]; (ii) triphosgene, specific conditions depending on the previous step; (iii) H_2, Pd/C, MeOH.

With this choice, however, the amine-protecting Cbz group must be replaced, since its deprotection is not orthogonal with the deprotection of the benzyl ether moiety obtained after the epoxide R-O reaction. The Boc protection is the best choice, but it cannot be used since the beginning (i.e. in the form of *L*-Boc-methionine), since the elimination step (analogous to the third step of Scheme 3.5) required for the synthesis of Boc-protected vinylglycine proceeds very low yields, due to parasite reactions. Therefore, the protecting group was changed after the epoxidation step (Scheme 3.9).
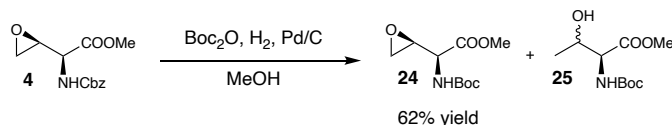
Scheme 3.9: Protecting group exchange from Cbz to Boc.

Unfortunately, Boc-threonine **25** (diastereoisomeric mixture) was obtained as by-product. Compound **24** was successfully subjected to a nucleophilic R-O reaction with freshly distilled benzyl alcohol, employing boron trifluoride etherate as Lewis-acidic catalyst, according to previous literature studies.[121] The formation of the oxazolidinone from **26** was achieved through two steps, performed in a one-pot fashion: Boc deprotection with trifluoroacetic acid (affording the amino alcohol **21**, not isolated), followed by the treatment with triphosgene. **22** was obtained in low yield, probably because of the adopted biphasic conditions. The problem may be solved using exclusively anhydrous conditions for the second step. However, despite the benzyl deprotection proceeded almost quantitatively (Scheme 3.10), the successive deoxyfluorination step resulted very challenging.
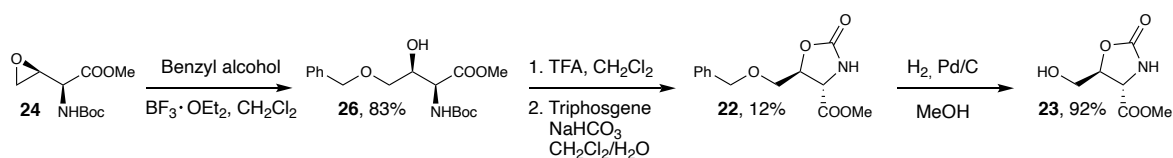
Scheme 3.10: Synthetic approach from epoxide **24** to compound **23**.

In an attempt to avoid the use of DAST, different fluorination conditions ($CsF/ICH_2CH_2I/PPh_3$) were tested,[122] but substrate **23** was unreactive in these conditions (Scheme 3.11, left-hand reaction). Hence, the DAST protocol of Scolastico was performed. The conversion was complete after less than 3 hours,

but only a very small amount of the fluorinated product **11** was recovered by flash chromatography (Scheme 3.11, right-hand reaction).
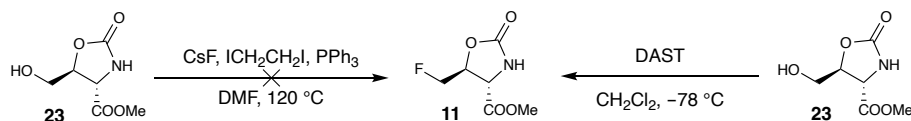
Scheme 3.11: Nucleophilic fluorination tests for the synthesis of **11** starting from **23**. With the DAST-based fluorination protocol reported by Scolastico (right-hand reaction), **11** was obtained in low yield (less than 10%).

Indeed, according to spectroscopic data, extended decomposition was observed. This difference with respect to the observations of Scolastico may be due to the different protection of the carboxyl group: *t*-butyl ester may be much more efficient than methyl ester in hampering undesired decomposition pathways, due to its higher steric hinderance. The change of carboxyl protecting group without undesired racemization pathways is not possible at this synthetic stage. Before starting the whole synthesis with different protections, other strategies were studied.

A completely different approach, involving a monofluoromethylation step, was studied. In particular, *D*-serine **27** was studied as commercially available starting material for this chiral pool approach (the need of *D*-serine instead of *L*-serine will be clarified later). The key compound of this synthetic strategy is the well-known Garner's aldehyde **30**.[123] This compound can be obtained in few steps starting from serine (Scheme 3.12), and has be used as a versatile intermediate in many chiral pool syntheses.[124]
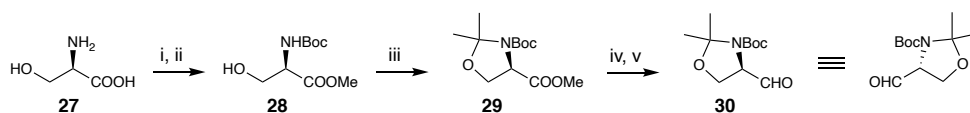
Scheme 3.12: Literature synthesis of Garner's aldehyde **30**: (i) acetyl chloride, MeOH; (ii) Boc$_2$O, Et$_3$N, THF; (iii) 2,2-dimethoxypropane, BF$_3$·OEt$_2$, acetone; (iv) LiAlH$_4$, THF; (v) DMSO, (COCl)$_2$, i-Pr$_2$NEt, CH$_2$Cl$_2$. A different spatial orientation of **30**, useful for the forthcoming discussion, is also reported.

Compound **30** was chosen as the substrate for the monofluoromethylation step. In particular, an exotic lithium fluorocarbenoid (namely LiCH$_2$F, generated is situ from commercially available fluoroiodomethane)[125] was tested as monofluoromethylating reagent for the nucleophilic addition to compound **30** (Scheme 3.13).[‡1]
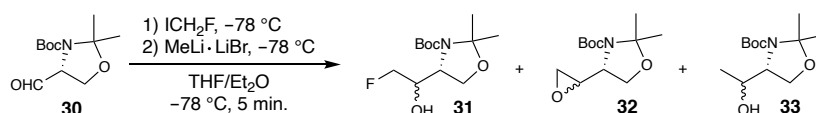
Scheme 3.13: Monofluoromethylation of **30** with LiCH$_2$F. The latter is obtained in situ after the addition of MeLi·LiBr complex (from, ICH$_2$F, upon iodine-lithium exchange).

---

‡ The research group of Prof. R. Luisi (Department of Pharmacy − Drug Sciences, University of Bari "A. Moro") is fully acknowledged for the tests with LiCH$_2$F.

Unfortunately, a mixture of **31**, **32**, and **33** (both diastereoisomers for each compound) was obtained. The formation of **32** is due to the partial carbenoid behaviour of LiCH₂F: elimination of LiF results in the formation of the highly reactive carbene **:CH₂**, followed by its direct insertion into the C=O bond. The formation of **33** is ascribable to the direct addition of MeLi. The extreme reactivity of this monofluoromethylating system, even at very low temperatures, is responsible for its low selectivity. Hence, even this approach was abandoned. However, for the sake of completeness, a brief account of the whole synthetic strategy, leading to 4F-Thr, is reported in Scheme 3.14, also to justify the choice of *D*-serine as commercial starting material.
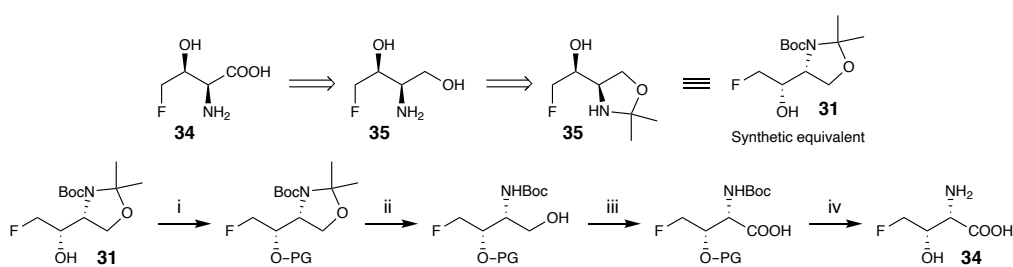
Scheme 3.14: Retrosynthetic analysis from 4F-Thr **34** to compound **31** (top), and relative synthetic strategy (bottom). Steps: (i) protection, (ii) deprotection, (iii) oxidation, (iv) complete deprotection.

3.3.2. *Diastereoselective synthesis of racemic 4F-Thr*

The many difficulties encountered in the development of a high-yielding stereoselective synthesis of 4F-Thr pushed us to focus our attention on a diastereoselective variant. Indeed, such approach should enable the synthesis of enough racemic 4F-Thr to measure its acid-base properties and its rotational spectrum. In particular, the measurement of the latter, even exploiting state-of-the-art laser ablation techniques, requires at least 500-600 mg samples.[126] The unsuccessful efforts of Section 3.3.1, however, paved the way for the development of a new and unprecedented approach. The simultaneous protection of the amino alcohol **21** (see Scheme 3.8) in the form of oxazolidinone **22** served as a cue for other synthetic strategies involving useful cyclic compounds, possibly obtained from simple available precursors, and with the desired relative configurations of their stereocentres. Based on these grounds, a new diastereoselective synthesis of racemic 4F-Thr was developed. The racemic but diastereomerically pure key compound (an oxazoline) was obtained by a copper-mediated cycloaddition, starting from commercially available precursors. The retrosynthetic analysis is reported in Scheme 3.15.
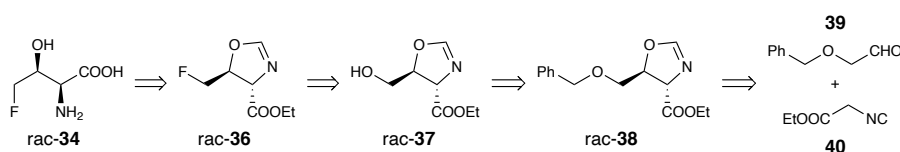
Scheme 3.15: Retrosynthetic analysis for the diastereoselective approach to racemic 4F-Thr.

Recently, the formal [3+2] cycloaddition of α-isocyanoesters with carbonyl compounds has been investigated as a powerful methodology for the synthesis of chiral substituted 2-oxazolines bearing two adjacent stereocentres: both metal catalysis – involving transition metals such as gold,[127] silver,[128–132] platinum,[133–135] palladium,[134,136] copper,[137] and cobalt[138] – and organocatalysis[139–141] were employed to perform this appealing transformation. In particular, the synthesis of *DL*-threonine, through the addition of α-isocyanoacetamides to acetaldehyde as a key step, was reported.[142] A pioneering work by Saegusa *et al.* reported the catalytic use of copper(I) oxide in the addition of isocyanoesters to aldehydes.[143] The copper-mediated cycloaddition was further evaluated for diastereoselective reactions.[144] Noteworthily, aliphatic aldehydes proved to be well-tolerated substates, affording *trans*-oxazolines using simple Cu(I) catalysts. More specifically, the conditions reported by Kirchner *et al.*[145] resulted the best suited for the [3+2] cycloaddition between commercially available or simply prepared benzyloxyacetaldehyde **39** and ethyl isocyanoacetate **40** (Scheme 3.16).
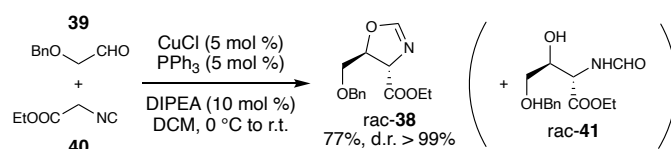
Scheme 3.16: [3+2] cycloaddition between **39** and **40** to give oxazoline rac-**38**.

According to ¹H-NMR analysis of the crude mixture, the *trans* diastereoisomer was obtained as single racemic product (d.r. > 99%). Unfortunately, the oxazoline cannot be used as an effective protective group, since it is very prone to hydrolysis. Indeed, the presence of opened formamide amino alcohol by-product rac-**41** was observed, in variable quantities from batch to batch, and even when no traces of rac-**41** were detected after flash chromatography, air moisture was sufficient to promote the hydrolysis of pure compound rac-**38**. However, even batches with high percentages of rac-**41** can be used: any mixture of rac-**38** and rac-**41** can be hydrolysed with methanolic HCl and then treated with triphosgene to afford the protected oxazolidinone rac-**42** in good yield (Scheme 3.17), thus linking this approach with the one reported by Scolastico. Quantitative debenzylation led to compound rac-**43**.
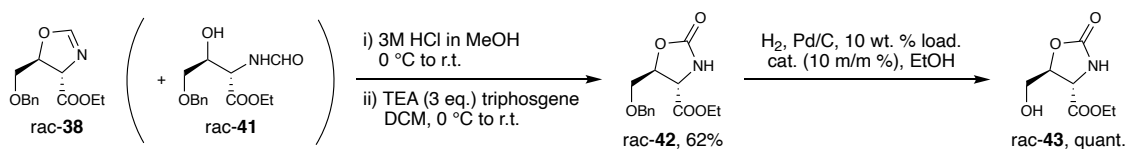
Scheme 3.17: Synthesis of oxazolidinone rac-**42**, followed by debenzylation to give rac-**43**.

Before proceeding with the literature deoxyfluorination conditions reported by Scolastico, several other conditions/reagents were tested, but all attempts, also employing the modern variants of fluorinating agents, gave either extensive decompositions or complex mixtures of products, and in some cases, no reaction was observed at all. Hence, DAST-based conditions were tested. Unfortunately, the protocol

was sensitive to scale up. Its yields were similar or, only in a few cases, slightly better (57%) than those reported by Scolastico. Reaction parameters were accurately studied, and even the quenching conditions proved to be relevant to improve the outcome of the reaction. The best compromise between scale up and satisfactory yield was achieved with 350 mg of starting oxazolidinone rac-**43**, leading to the fluorinated derivative rac-**44** with 32% yield (Scheme 3.18).
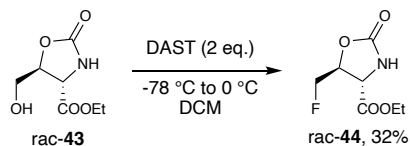
Scheme 3.18: Deoxyfluorination step for the synthesis of rac-**44**.

Racemic 4F-Thr was obtained from rac-**44** in two steps (Scheme 3.19): (i) total deprotection via hydrolysis with aqueous 6M HCl, leading to 4F-Thr hydrochloride, followed by (ii) treatment with an excess of propylene oxide,[146–148] to obtain the neutral form of the amino acid rac-**34** without the use of ion exchange resins. The spectroscopically pure amino acid was isolated upon decantation, with few washings with MeOH, and vacuum-dried as impalpable white powder.
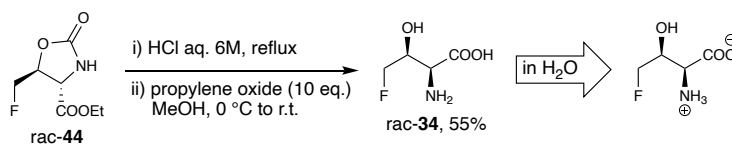
Scheme 3.19: Last two steps in the synthesis of rac-**34**: (i) hydrolysis and (ii) neutralization.

Neutral 4F-Thr is the preferable starting form to study its behaviour in aqueous media. Indeed, in aqueous solution, 4F-Thr is expected to be present in its zwitterionic form (also depicted in Scheme 3.19), like all the canonical proteinogenic amino acids. Albeit this synthetic strategy afforded racemic 4F-Thr, it represented a significant improvement, since it enabled the synthesis of rac-**34** in 7 steps, with an overall yield of 8%. It is worth mentioning that this approach is amenable to a possible enantioselective version using chiral ligands in the first step, i.e. the copper-mediated [3+2] cycloaddition. Even in the worst scenario, i.e. no suitable ligands can be found for whatever copper-mediated cycloaddition, other metals can be tested.

3.3.3. *Successful endeavour in the synthesis of enantioenriched 4F-Thr*

Noteworthily, despite the remaining difficulties concerning scale up and yield, the afore-mentioned deoxyfluorination proved the importance of the carboxyl protecting group. Scolastico deoxyfluorinated the *t*-butyl ester derivative with a 53% yield, the ethyl ester rac-**43** was deoxyfluorinated with a 32% yield, while the methyl ester **23**, in the same conditions, was proved to mainly undergo decomposition pathways, with less than 10% yield of **11**. Therefore, the whole chiral pool strategy starting

from *L*-methionine was studied using different protecting groups. Regarding the protection of the amino group, both Cbz and Boc were proved to be unsuited for this approach. Hence, Fmoc protection was studied, while the carboxyl group was protected as ethyl ester. *L*-Fmoc-methionine **45**, commonly used in peptide synthesis,[149] was used as commercially available starting material (Scheme 3.20).
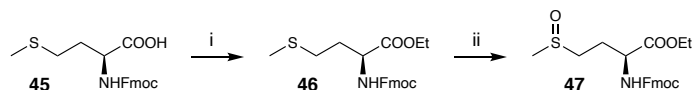

Scheme 3.20: Synthesis of Fmoc-methionine sulfoxide ethyl ester **47** starting from Fmoc-L-methionine **45**: (i) SOCl₂, EtOH, quantitative; (ii) NaIO₄, EtOH/H₂O, 91%.

The synthesis of Fmoc-vinylglycine ethyl ester **48**, occurring from **47** via a pericyclic *syn* elimination (E_i mechanism) involving a 5-membered transition state,[150] required a detailed study of the available literature.[151–153] According to a literature procedure optimized for the methyl ester analogue,[154] 2,4-dichlorotoluene (b.p. 200 °C) proved to be the best suited solvent for this transformation. This choice represented a compromise. Indeed, solvents with lower boiling points – such as chlorobenzene (b.p. 132 °C), xylenes (b.p. 138 °C) and *o*-dichlorobenzene (b.p. 180 °C) – are easier to remove at the end of the reaction. However, the lower the reaction temperature (with the solvent boiling point representing the upper limit), the longer the reaction times and the higher the chances of undesired parasite reactions, e.g. double bond isomerization. In particular, moving from xylenes to 2,4-dichlorotoluene, the reaction time was reduced from 9 days to about 12 hours, and the amount of isomerized by-products was reduced from more than 20% to hardly detectable traces. Moreover, a rather simple procedure enabled the removal of 2,4-dichlorotoluene at relatively low temperatures (less than 50 °C).[155] Compound **48** was epoxidated using MCPBA, according to a literature procedure (Scheme 3.21).[156]
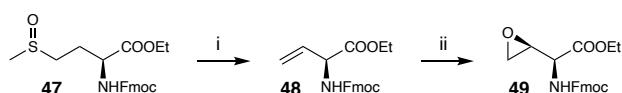
Scheme 3.21: Synthesis of epoxide **49**: (i) 2,4-dichlorotoluene, 190 °C, 72%; (ii) MCPBA, CH₂Cl₂, 0 °C to r.t., 68%, d.r. > 99%.

The epoxide R-O reaction was performed using benzyl alcohol, with the same procedure reported in Scheme 3.10. Fmoc deprotection was performed according to the standard protocol involving the use of piperidine (Scheme 3.22).[157]
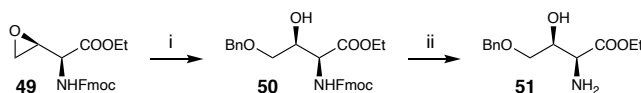
Scheme 3.22: Synthesis of the amino alcohol **51**: (i) benzyl alcohol, BF₃·OEt₂, CH₂Cl₂, 57%; (ii) piperidine in DMF (10% v/v), 78%.

All the subsequent steps were performed similarly to those reported for the methyl ester derivative (Scheme 3.23).
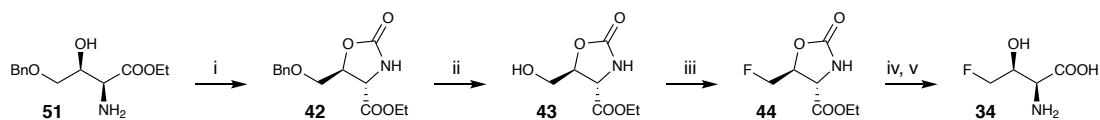
Scheme 3.23: Last steps of the synthesis of **34**: (i) triphosgene, Et₃N, CH₂Cl₂, quant.; (ii) H₂, Pd/C 10 wt. % load. (10% m/m), EtOH, quant.; (iii) DAST, −78 °C to 0 °C, 43%; (iv) 6M HCl, reflux; then (v) propylene oxide, MeOH, 72% (over two steps).

This synthetic approach represented a noteworthy breakthrough with respect to the previously reported total syntheses of enantioenriched 4F-Thr. Indeed, compound **34** was obtained in 11 steps from commercially available Fmoc-*L*-methionine **45**, with an overall yield of 6%. The enantioenriched 4F-Thr sample will be used for VCD and ROA measurements,[158,159] and the results will be reported in due time.

3.3.4. *Conformational analysis* †

As already mentioned, the conformational space of 4F-Thr was explored using a "flat" computational approach, meaning that the relevant structures must lie within 25 kJ mol⁻¹ with respect to the lowest energy minimum (LEM). All the structures fulfilling such constraint were optimized at a high level of theory, also taking into account bulk solvent effects (by means of the polarizable continuum model, PCM). Similarly to what is observed for canonical proteinogenic amino acids, 4F-Thr undergoes multiple acid-base equilibria in aqueous media, hence all the three main amino acid forms – i.e. cationic, zwitterionic, and anionic – were analysed from the conformational point of view. For each form, the conformational analysis was performed using a recently proposed island model evolutionary algorithm,[160] coupled with a two-stage method to evaluate structures.[161] The computational details are reported in Section 3.5.4. In an aqueous solution at neutral pH values, the zwitterionic form is more stable than the corresponding neutral form (see Scheme 3.19).[162] In particular, each amino acid is characterized by a specific pH value, namely the isoelectric point (pI), at which the amino acid is electrically neutral: the most common species is the zwitterion, while the few positively-charged molecules are statistically counterbalanced by the same number of negatively-charged species. Starting from the pI, the zwitterion can undergo either protonation of the negatively-charged carboxylate moiety or deprotonation of the positively-charged ammonium one, by lowering or rising the pH value, respectively. The most prominent low-lying conformers of the three possible protonation states are depicted in Figure 3.6. The transition states ruling the most relevant conformational interconversions are also reported.

---

† Prof. V. Barone, Prof. C. Puzzarini, Dr. L. Spada, Dr. M. Fusè, and Dr. G. Mancini are fully acknowledged for the computational analysis concerning Thr and 4F-Thr.
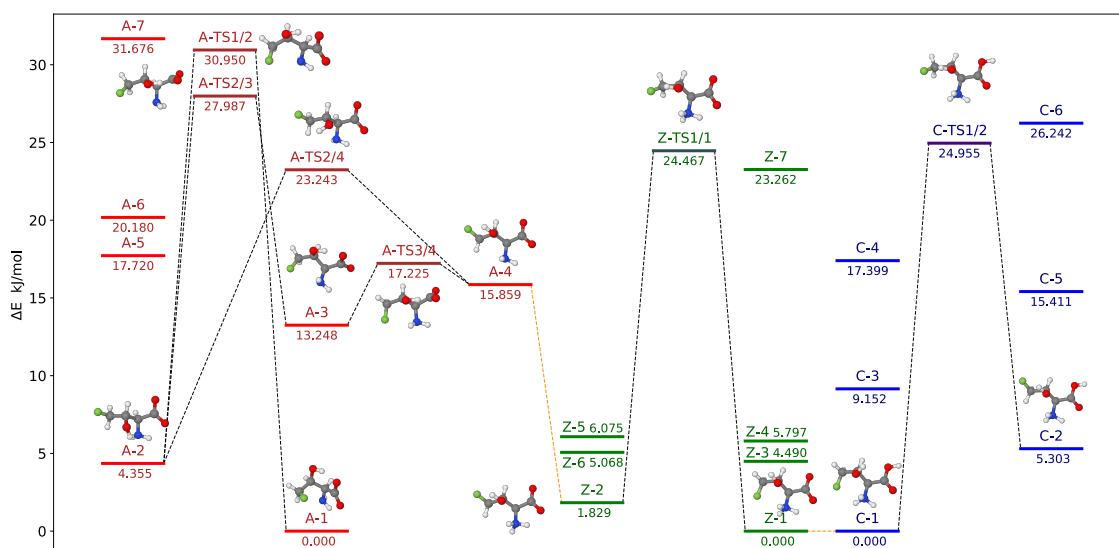
Figure 3.6: Low-lying conformers for the anionic (red), zwitterionic (green) and cation (blue) forms of 4F-Thr. The transition states ruling their interconversion are also shown. For each form, all the considered stationary points are within 32 kJ mol⁻¹ with respect to the respective LEM. The orange dashed lines identify the best conjugate acid-base pairs in terms of conformational similarities: the closest resembling structures moving from anion to zwitterion (red-green match), and the closest resembling ones moving from zwitterion to cation (green-blue match). From Ref. [104] (CC BY-NC-ND 4.0).

As far as the cation is concerned (Figure 3.7, top), its lowest energy minimum (4F-Thr-C-1) is stabilized by a strong interaction between the charged NH_3^+ group and three electronegative atoms, i.e. the non-protonated carboxyl oxygen, the hydroxyl oxygen, and the fluorine atom (N−H⋯O=C, N−H⋯O−H, and N−H⋯F: 2.18, 2.12, and 2.27 Å, respectively). In a second conformer (4F-Thr-C-2), the fluorine atom engages a less stabilizing interaction with the hydroxyl hydrogen (N−H⋯O=C, N−H⋯O−H, and O−H⋯F: 2.06, 2.10, and 2.40 Å, respectively). The interconversion between the two conformers involves the rotation of the monofluoromethyl group (together with a minimal rotation of the hydroxyl group), with the transition state lying about 25 kJ mol⁻¹ above the LEM. A similar behaviour is observed for the zwitterion (Figure 3.7, bottom).
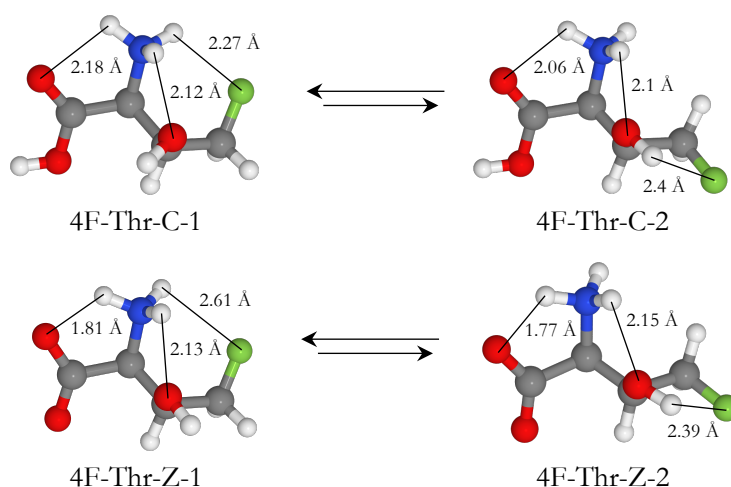
Figure 3.7: Ball-and-stick structures of cationic (top) and zwitterionic (bottom) conformers.

71

Conformational analysis

Indeed, zwitterionic and cationic LEMs differ only for the F-unbound carboxylic oxygen, which is protonated in the cationic species: deprotonation of the carboxylic group occurs without significant conformational rearrangements. The formation of the anion involves the deprotonation of the F-bound ammonium group, hence resulting more complicated in terms of conformational rearrangements: anionic LEM does not show any close resemblance with its zwitterionic counterpart. To understand such strong differences upon deprotonation, the nature of the described interactions needs to be highlighted. Indeed, all the described interactions resemble hydrogen bonds, and are hence ruled by the electronegativities of the involved atoms. Intuitively, protonated sp^3 nitrogen atoms can be considered as more electronegative than the unprotonated ones. In terms of hydrogen bond ability, protonated sp^3 nitrogen atoms are better hydrogen bond donors than unprotonated ones.[163–165] In the case of 4F-Thr, when the charged nitrogen atom becomes neutral upon deprotonation, its hydrogen bond donor ability shrinks, and the higher electronegativity of oxygen with respect to nitrogen leads to a strong hydrogen bond of a carboxylate oxygen with the alcoholic proton (C=O···H−O, 1.70 Å). Therefore, in the case of the anionic LEM (4F-Thr-A-1), the hydroxyl group is no more hydrogen-bonded to the amine one. The latter is hydrogen-bonded to the other carboxylate oxygen (C=O···H−N, 2.12 Å). Therefore, the best conformational match between the zwitterion and the anion involves non-LEM conformers, i.e. 4F-Thr-Z-2 and 4F-Thr-A-4 (Figure 3.8).
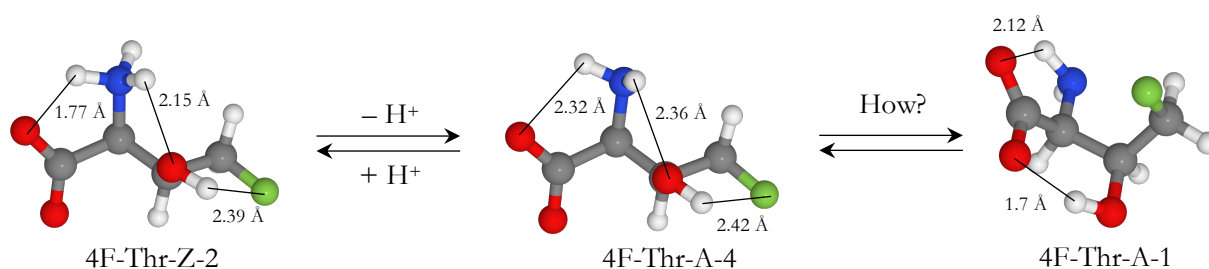
Figure 3.8: Best zwitterion-anion conformational match, represented as an acid-base equilibrium (left-hand side). The anionic LEM is depicted on the right.

Whenever the conformers with the best conformational match are non-LEM species, the possible interconversion paths leading to the respective LEMs must be found. As far as the anion is concerned, 4F-Thr-A-4 and 4F-Thr-A-3 are separated by an almost negligible energy barrier (about 1.5 kJ mol^{-1}). The interconversion mainly involves the rotation of the hydroxyl group, together with minimal rotations of both carboxylate and monofluoromethyl group. A higher barrier connects 4F-Thr-A-4 and 4F-Thr-A-2 (about 7.5 kJ mol^{-1}): the interconversion involves the rotation of both hydroxyl and amine groups, together with a significant change of the H$_2$N−CH−CH−OH dihedral angle. The barrier between 4F-Thr-A-3 and 4F-Thr-A-2 is even higher (nearly 15 kJ mol^{-1}): the interconversion can be described as a hybrid path of the previous two. Eventually, chemical intuition enabled the localization of a direct path connecting 4F-Thr-A-2 to the anionic LEM (Figure 3.9), but the barrier was remarkably high (∼31 kJ mol^{-1}).
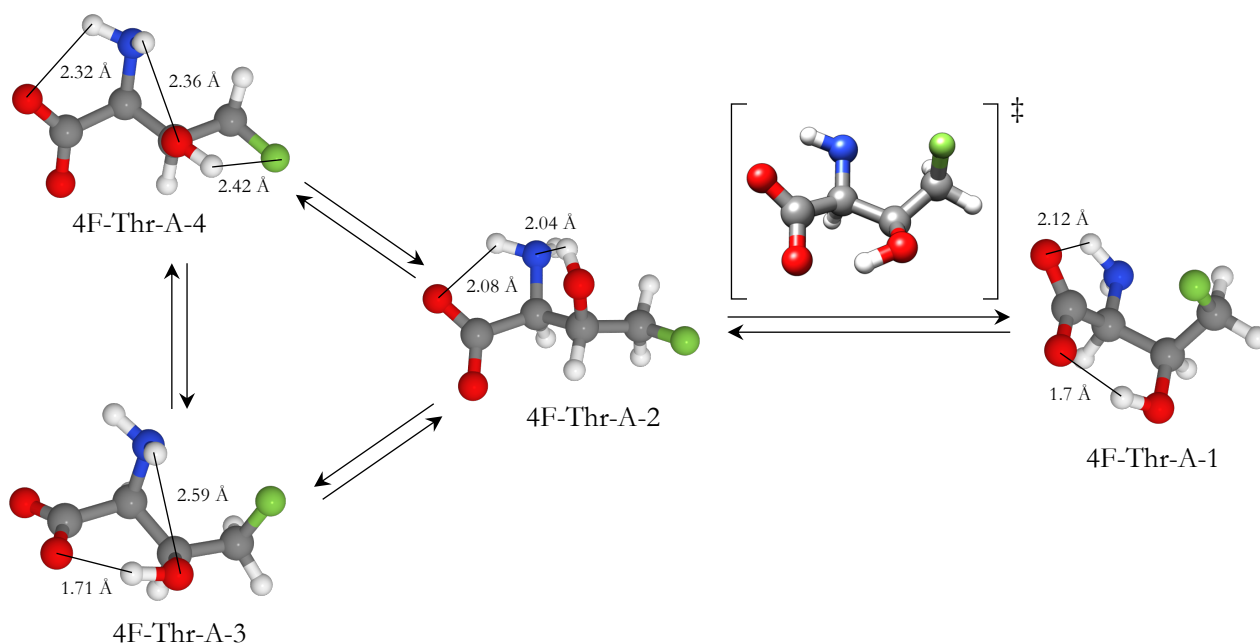
Figure 3.9: Ball-and-stick structures of main anionic conformers. The structural relationships are reported as conformational equilibria.

The interconversion is indeed very tricky: it can be envisioned as a rotation of the hydroxyl group coupled with a marked change of the $H_2N-CH-CH-OH$ dihedral angle. This allows the hydroxyl hydrogen to "slide" from the electron density of the amine group, along the delocalized π-cloud of the carboxylate group, to that of the farthest-from-nitrogen carboxylate oxygen. Moreover, a rotation of the monofluoromethyl group enables a weak interaction between the fluorine atom and the delocalized carboxylate π-cloud.

3.3.5. *Acid-base titrations*

From the experimental point of view, the effect of fluorine can be evaluated by means of comparative titration studies involving 4F-Thr and Thr. The simplest comparison to be performed with titration laboratory data is that between acid dissociation constants (namely pKa), to evaluate how their values are influenced by the presence of fluorine.[14,19] Indeed, fluorine is the most electronegative element and its inclusion in a molecule has a very strong effect on the acidity or basicity of proximal functional groups (increasing the former and reducing the latter).[166–169] This is particularly evident for amphoteric molecules such as amino acids. The fluoro-*L*-alanine series represents a noteworthy example (Table 3.1).[170] Interestingly, almost no difference is observed moving from parent non-fluorinated *L*-alanine to 3-fluoro-*L*-alanine.[171] Nevertheless, for other amino acids, simple monofluorination causes acid dissociation constants to undergo non-negligible shifts, which are particularly evident for the amino group: in the case of *L*-proline, pKa$_2$ shrinks from 10.8 of parent amino acid, to 9.2 of (4*R*)-fluoro-*L*-proline, down to 7.15 of 4,4-difluoro-*L*-proline (Table 3.2).[34] Such differences highlight the importance of the whole molecular structure in the determination of the effects of fluorine insertion.

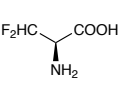**Table 3.1:** Acid dissociation constants for the fluoroalanine series (from Refs. 170, 171).
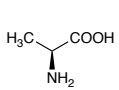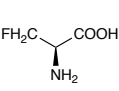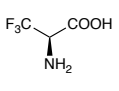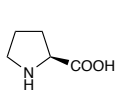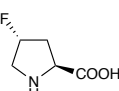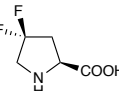
	pKa₁	pKa₂
H_3C—CH(COOH)—NH₂	2.35	9.87
FH_2C—CH(COOH)—NH₂	2.4	9.8
F_2HC—CH(COOH)—NH₂	1.5	8.4
F_3C—CH(COOH)—NH₂	1.2	5.3

Table 3.2: Acid dissociation constants for the fluoroproline series (from Ref. 34).

	pKa₂
proline	10.8
4F-proline (up)	9.2
4F-proline (down)	7.15

Concerning the comparison between Thr and 4F-Thr, their titration curves were recorded three times under the same conditions to allow the calculation of mean values and confidence intervals for the acid dissociation constants (pKa_1, pKa_2) and the isoelectric point (pI). First, pKa_2 was determined as the pH value corresponding to the second half-equivalence point, which coincides with a local maximum of the first derivative of the inverted titration curve. Next, pKa_1 was determined with a graphical method, starting from pKa_2 and taking advantage of both the narrow volume ranges encompassing equivalence zones and the narrow pH ranges encompassing buffer zones. The results were also simulated using the charge balance equation.[172] The value of pI was then evaluated from the pKa_1 and pKa_2 values using the Henderson-Hasselbalch equation (i.e. mean value between pKa_1 and pKa_2). The detailed experimental procedures and setup are reported in the Experimental Section. To better address the role played by fluorination in the behaviour of amino acids, due to the many different literature values reported for Thr, comparative studies were performed considering the experimental and computed differences between the values for 4F-Thr and Thr rather than their absolute values. A good agreement between theory and experiment (Table 3.3) was then observed.

From the theoretical point of view, the role of fluorine in ruling the conformational rearrangements described in Section 3.3.4 can be understood through a comparative study between the conformers of 4F-Thr with the low-lying conformers of the parent non-fluorinated Thr amino acid. Figure 3.10 clearly shows the one-to-one correspondence between the low-lying conformers of 4F-Thr and Thr, either as cations or zwitterions. This is not the case for the LEMs of the anionic forms: this observation is consistent with the particularly significant role of the electronegative fluorine atom in this situation.
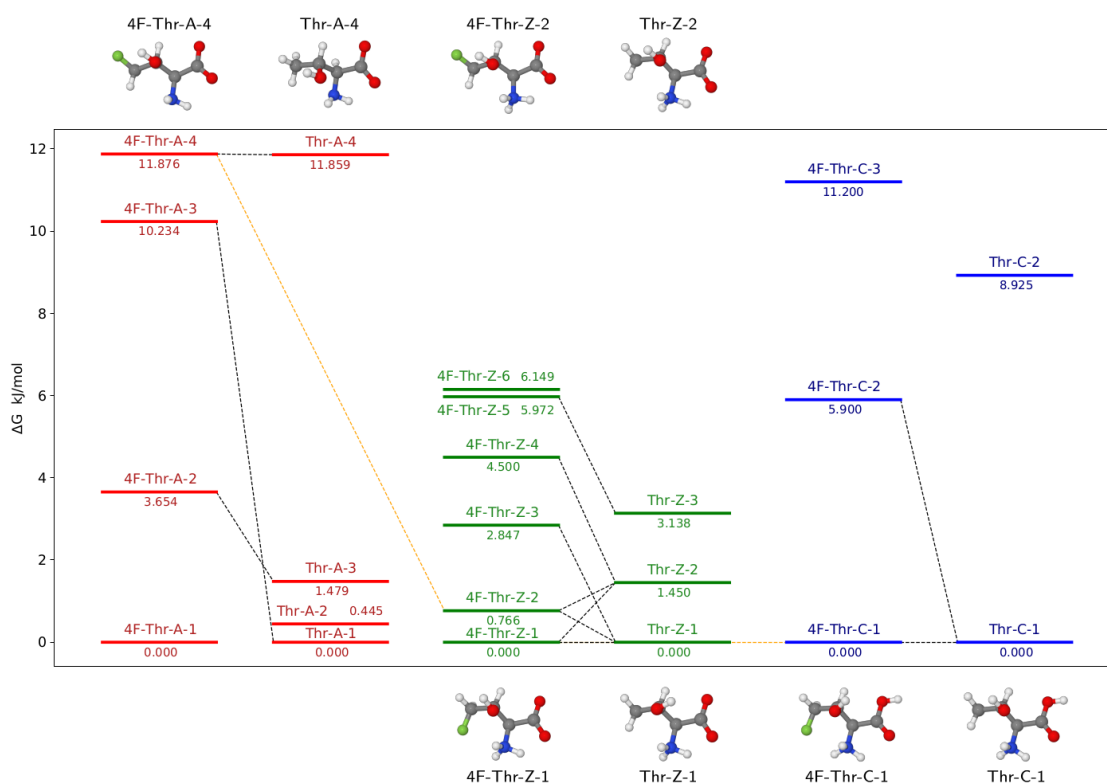
Figure 3.10: Structural correlations between conformers of 4F-Thr and Thr. The top structures were used for the estimation of pKa$_2$, while the bottom ones were used for the estimation of pKa$_1$. From Ref. 104 (CC BY-NC-ND 4.0).

Once the most stable conformers and the possible deprotonation paths of 4F-Thr are known, together with the related Thr structures, the respective acid dissociation constants can be estimated, then addressing the differences between 4F-Thr and Thr. Under the same experimental conditions, the protonation free energies of 4F-Thr are given by:

$$\Delta G_{4FT} = \Delta\Delta G_{4FT,T}^{calc} + \Delta G_T^{exp} \tag{3.1}$$

Where ΔG_T^{exp} is the experimental protonation free energy of Thr and the first term on the right-hand side is evaluated as:

$$\Delta\Delta G_{4FT,T}^{calc} = \left(\Delta G_{4FT}^P - \Delta G_{4FT}^D\right) - \left(\Delta G_T^P - \Delta G_T^D\right) \tag{3.2}$$

This term clearly represents the difference of the computed free energies of the solvated conformers of 4F-Thr and Thr, with D and P denoting the deprotonated and protonated forms, respectively. Concerning the deprotonation of the carboxyl group (pKa$_1$), the reference structures for the calculations were the cationic and zwitterionic LEMs, for both Thr and 4F-Thr. The deprotonation of the ammonium group (pKa$_2$) was evaluated using the close resembling of the 4F-Thr-Z-2 and 4F-Thr-A-4 conformers. As already mentioned, the latter almost freely interconverts to its more stable 4F-Thr-A-3 counterpart. Hence, this form was employed to estimate the ΔG values. A similar behaviour is observed for Thr, with a negligible energy barrier separating the Thr-A-4 and Thr-A-3 conformers. In the attempt to take specific

solvent effects into account, explicit water molecules were included in subsequent computations. Amine and carboxylic groups were considered as the most important to determine the first-solvation shells of 4F-Thr and Thr in different protonation states. For the sake of consistency, once all the first-solvation shells were determined, the maximum number of water molecules found for any species was retained for all of the other ones, ending up with a total of seven water molecules: nearly three close to the amine/ammonium and four close to the carboxyl/carboxylate moieties. The geometries of the clusters were then fully optimized also taking into account bulk solvent effects by means of the PCM (Figure 3.11).
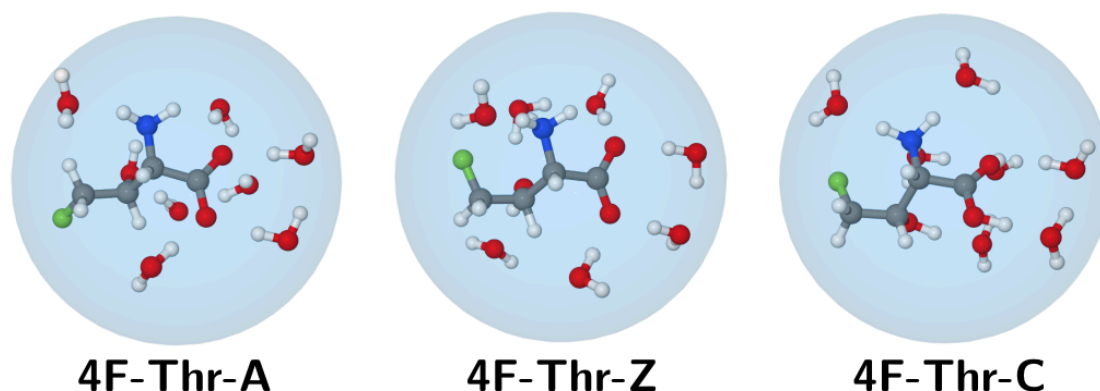
Figure 3.11: 4F-Thr clusters (LEMs) containing the water molecules of the first-solvation shell: anion (left), zwitterion (middle), and cation (right). From Ref. 104 (CC BY-NC-ND 4.0).

These additional tests proved the seven-water clusters to provide converged results, without significant modifications with respect to the results obtained for the bare solutes embedded in a polarizable continuum: albeit slight changes were observed for pKa_1 and pKa_2, the isoelectronic point (pI) and the general trends remained the same. In particular, both deprotonation processes of 4F-Thr are slightly favoured with respect to Thr, in agreement with the presence of the electron-withdrawing fluorine atom (Table 3.3). In particular, similarly to what is reported in literature for other amino acids, the acid dissociation constant of the amino group (pKa_2) is characterized by a higher variation.

Table 3.3: Experimental acid dissociation constants and isoelectric point of Thr and 4F-Thr together with the corresponding (computed and experimental) differences. From Ref. 104 (CC BY-NC-ND 4.0).

	Thr (lit.)[a]	Thr (exp.)	4F-Thr (exp.)	Δ(4F-Thr/Thr) exp.[b]	Δ(4F-Thr/Thr) calc.[c]	Δ(4F-Thr/Thr) calc.[d]
pKa_1	2.20	2.38 ± 0.02	2.26 ± 0.09	−0.12 ± 0.11	−0.16	−0.36
pI	5.60	5.75 ± 0.09	5.43 ± 0.04	−0.32 ± 0.13	−0.40	−0.41
pKa_2	8.96	9.1 ± 0.17	8.61 ± 0.02	−0.49 ± 0.22	−0.64	−0.46

[a] From Ref. 173. **[b]** Differences between experimental values of 4F-Thr and Thr. **[c]** Polarizable continuum model on bare solutes. **[d]** Polarizable continuum model on explicit-water clusters (see Figure 3.11).

3.3.6. *NMR comparative studies*

Finally, NMR spectra of 4F-Thr and Thr (in their zwitterionic form) were recorded under the same experimental conditions.[174] This enabled the evaluation of the effects of fluorine through the

analysis of the observed differences between the chemical shifts of the two species. As expected, the electron-withdrawing properties of fluorine cause the ^{1}H and ^{13}C signals of the monofluoromethyl group to be remarkably shifted towards higher chemical shifts with respect to those of the methyl group in Thr (Figure 3.12).
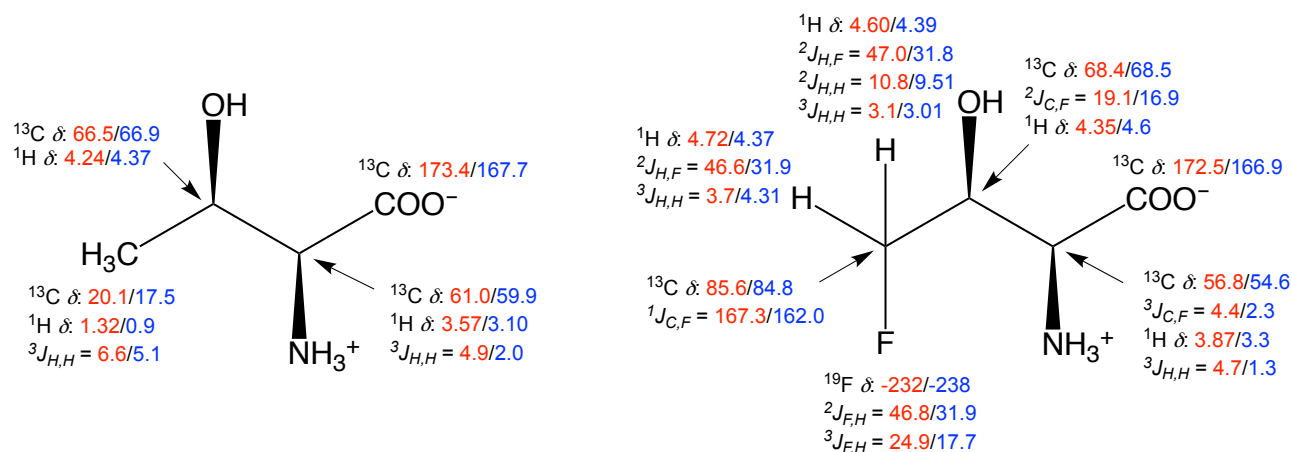

Figure 3.12: Experimental (red values) and simulated (blue values) chemical shifts (δ in ppm) and coupling constants (*J* in Hz) of the zwitterionic form of Thr (left) and 4F-Thr (right) in D$_2$O. Simulated values were computed at the B3/jul-cc-pVDZ (spin-spin) level. Ref. 104 (CC BY-NC-ND 4.0).

Moving away from the monofluoromethyl group, the electron-withdrawing effects decrease, and the chemical shifts of 4F-Thr and Thr get closer to each other. In particular, in the case of ^{1}H signals, the chemical shifts of 4F-Thr are systematically higher than those of Thr. Interestingly, this is not the case for ^{13}C signals. As expected, the signals from exchangeable protons (i.e. belonging to hydroxyl and ammonium groups) were not identified. For 4F-Thr, indirect spin-spin coupling constants lie within the typical range for the C−F interaction. From a computational point of view,[175] the chemical shifts of the low-lying conformations of both molecules are in good agreement with the experimental counterparts (see values in Figure 3.12), thus confirming both the reliability of the conformational search and the inductive nature of the fluorine effect on the active nuclei.

3.4.   Conclusions

Both diastereoselective and enantioselective synthetic strategies to obtain sufficient amounts of 4F-Thr (racemic and enantioenriched, respectively) have been explored. Eventually, two novel routes enabled the synthesis of the only natural fluorinated amino acid: a diastereoselective approach based on a key copper-mediated cycloaddition, and a chiral pool approach starting from commercially available *L*-Fmoc-methionine. Furthermore, an integrated experiment-theory approach for the characterization of 4F-Thr has been reported. The racemic sample of 4F-Thr was employed in acid-base titration experiments to determine the acid dissociation constants and the isoelectric point. In parallel, a comprehensive quantum-chemical investigation at the state of the art shed light on the conformational

behaviours of the cationic, zwitterionic, and anionic forms of 4F-Thr as well as the relationships between them and with the most stable conformers of the parent Thr amino acid. Moreover, the quantum-chemical study led to acid dissociation constants in good agreement with the experimentally-derived ones. The computational analysis of this flexible system has been exploited combining machine learning techniques with a two-stage approach to evaluate geometries and energetics. Further accurate titration studies, using a recently published Microsoft Excel workbook, are highly recommended.[176]

At the same time, the effectiveness of the new synthetic approach allowed us to obtain remarkable quantities of 4F-Thr, thus paving the route toward further spectroscopic investigations. In particular, the enantioenriched sample will be used for VCD and ROA experiments, aiming to give an even clearer picture of the role of fluorine in determining molecular properties. Moreover, further interesting results are expected to be obtained with the ongoing gas-phase experiments. In a more general perspective, the reported strategies offer interesting clues for the study of other systems of biological and/or medicinal relevance.

3.5. Experimental/computational section

Unless otherwise stated, common chemicals and solvents (HPLC grade or reagent grade) were purchased from commercial sources and used without further purification. Solvents are reported with the following abbreviations: cyclohexane (CyH), diethyl ether (Et$_2$O), ethanol (EtOH), ethyl acetate (EtOAc), methanol (MeOH), and tetrahydrofuran (THF). Plastic plates coated with a 0.2 mm thick layer of silica gel 60 F$_{254}$ were used for thin-layer chromatography analyses (TLC), whereas flash column chromatography purification was carried out using silica gel 60 (230−400 mesh). NMR spectra were recorded at 25 °C in a 400 MHz spectrometer using the deuterated solvent as an internal deuterium lock. The residual protic signal of the solvent (7.26 ppm, for ^{1}H-NMR), and the ^{13}CDCl$_3$ signal (77.16 ppm, for ^{13}C-NMR), were used for spectra recorded in CDCl$_3$. For NMR spectra recorded in D$_2$O, a drop of methanol was added, and its signals were used as references for both ^{1}H and ^{13}C spectra (3.34 and 49.50 ppm, respectively). Trifluoroacetic acid signal (−76.55 ppm) was used as a reference for ^{19}F NMR spectra. Chemical shifts are reported in parts per million (ppm) of the δ scale relative to TMS for ^{1}H and ^{13}C spectra and CFCl$_3$ for ^{19}F NMR spectra; coupling constants are in Hertz, and the multiplicity is as follows: s (singlet), d (doublet), t (triplet), q (quartet), m (multiplet), dd (doublet of doublets), dt (doublet of triplets), ddd (doublet of doublet of doublets), br (broad signal). Gas chromatography-mass spectrometry (GC-MS) spectra were obtained by EI ionization at 70 eV on a Hewlett-Packard 5971 with GC injection; they are reported as *m/z* (rel. intensity). High performance liquid chromatography-mass spectrometry (HPLC-MS) analyses were performed on an Agilent Technologies HP1100 instrument coupled with an Agilent Technologies MSD1100 single-quadrupole mass spectrometer using a Phenomenex Gemini C18 3 μm (100 × 3 mm^2) column; mass spectrometric detection was performed in the full-scan mode from
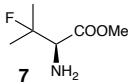
m/z 50 to 2500, a scan time of 0.1 s in the positive ion mode, ESI spray voltage of 4500 V, nitrogen gas of 35 psi, a drying gas flow rate of 11.5 mL min^{-1}, a fragmentor voltage of 30 V.

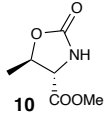### 3.5.1. Synthetic procedures of Section 3.3.1

General procedure for photocatalytic nucleophilic fluorination

All photocatalytic reactions were performed under atmosphere. A 10 mL Schlenk tube, equipped with a Rotaflo® stopcock, magnetic stirring bar and an argon supply tube, was flame-dried under vacuum. Once back to room temperature, the Schlenk tube was refilled with Ar, and charged with all the reagents, followed by the solvent (always under flux). The reaction mixture was subjected to a freeze-pump-thaw procedure (three cycles) and the vessel was then refilled with argon. The reaction mixture was irradiated (UV LED, λ_{max} = 365 nm, 3 cm from the vessel) under vigorous stirring for 36h, with a fan kit to avoid excessive heating.

Methyl (*R*)-2-amino-3-fluoro-3-methylbutanoate (7)

The reaction was performed according to the general procedure for photocatalytic nucleophilic fluorination. The Schlenk tube was charged with **6** (16.8 mg, 0.1 mmol), NFSI (47.3 mg, 0.15 mmol), sodium decatungstate (2.4 mg, 0.001 mmol), acetonitrile (1 mL), water (520 µL). At the end of the irradiation time, the reaction mixture was treated with MeOH (1 mL), and the solvent was evaporated under reduced pressure. The resulting crude was directly analysed by means of NMR spectroscopy, and it was found to be a mixture of NFSI, unreacted **6**, and **7**. Spectroscopic data of **7** are in agreement with those reported in literature.[177]

Methyl (4*S*,5*R*)-5-methyl-2-oxooxazolidine-4-carboxylate (10)

A dry three-neck round-bottom flask, equipped with a pressure-equalizing dropping funnel, was charged with dry CH_2Cl_2 (10 mL) and anhydrous Et_3N (488 µL, 3.5 mmol) under N_2 atmosphere. Then, the vessel was cooled down to 0 °C, and **8** (200 mg, 1.18 mmol) was added. The reaction mixture was stirred for 5 minutes at 0 °C, and for 20 minutes at room temperature. The vessel was again cooled down to 0 °C, and a solution of triphosgene (140 mg, 0.47mmol) in dry CH_2Cl_2 (5 mL) was added dropwise in 15 minutes. The reaction mixture was stirred for 24h at room temperature. The reaction vessel was cooled to 0 °C and saturated aqueous Na_2CO_3 was slowly added under vigorous stirring until the pH was 9−10. Upon separation, the combined organic phase was treated with aqueous 1M HCl until the pH became 1−2. The two phases were separated and the combined organic phase was treated with saturated aqueous $NaHCO_3$ until the pH became 7−8. Upon separation, the combined organic phase was dried on anhydrous Na_2SO_4 and the solvent was removed under reduced pressure.

Synthetic procedures of Section 3.3.1

The crude mixture was chromatographed (silica gel, 20% EtOAc in CyH) to afford 70 mg of **10** (0.44 mmol, yield 37%). Spectroscopic data are in agreement with those reported in literature.[178]

Methyl (*S*)-2-(1,3-dioxoisoindolin-2-yl)-3-methylbutanoate (12)
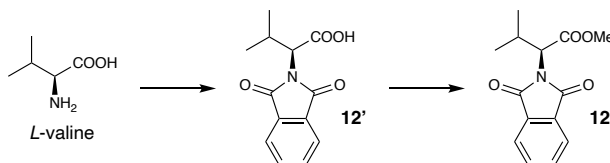
A single-neck round-bottom flask was heated up to 140-145 °C, and was charged with phthalic anhydride (430 mg, 2.92 mmol). The vessel was heated until phthalic anhydride was completely melted. After 5 minutes, *L*-valine (342 mg, 2.92 mmol) was added, and the flask was plugged and the reaction mixture was stirred for 5 minutes. The plug was then removed and then the reaction mixture was stirred for other 5 minutes. Upon cooling back to room temperature, **12'** formed as a white precipitate. Recrystallization from MeOH led to 520 mg of spectroscopically pure **12'** as white crystalline solid (2.1 mmol, yield 72%), which was used as such in the next step. Spectroscopic data are in agreement with those reported in literature.[179]

A single-neck round-bottom flask was charged with MeOH (5 mL) and **12'** (520 mg, 2.1 mmol). The reaction vessel was cooled down to 0 °C, and thionyl chloride (230 μL, 3.15 mmol) was added dropwise. The reaction mixture was stirred 1h at room temperature, and then it was refluxed for 12h. The solvent was evaporated under reduced pressure, and the obtained crude mixture was dissolved in CH_2Cl_2 and washed with saturated aqueous $NaHCO_3$. Upon separation, anhydrification over Na_2SO_4, and solvent evaporation under reduced pressure, the crude mixture was chromatographed (silica gel, 50% EtOAc in CyH) affording 280 mg of **12** as brownish oil (1.07 mmol, yield 51%). Spectroscopic data are in agreement with those reported in literature.[179]

Methyl (*R*)-2-(1,3-dioxoisoindolin-2-yl)-3-fluoro-3-methylbutanoate (13)
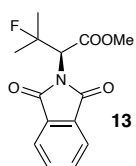
The reaction was performed according to the general procedure for photocatalytic nucleophilic fluorination. The Schlenk tube was charged with **12** (26 mg, 0.1 mmol), Selectfluor® (41 mg, 0.12 mmol), and dry acetonitrile (1 mL). At the end of the irradiation time, the mixture was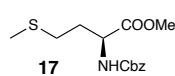 diluted with EtOAc and washed with saturated aqueous $NaHCO_3$. The combined organic phase was dried on anhydrous Na_2SO_4, and the solvent was evaporated under reduced pressure. The resulting crude was directly analysed by means of NMR spectroscopy, and it was found to be a mixture of Selectfluor®, unreacted **12**, and **13**. Spectroscopic data of **13** are in agreement with those reported in literature.[180]

Methyl (2*S*,3*R*)-2-(1,3-dioxoisoindolin-2-yl)-3-hydroxybutanoate (14)
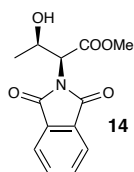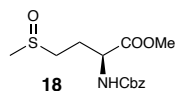
A single-neck round-bottom flask was charged with **8** (200 mg, 1.18 mmol), phthalic anhydride (119 mg, 1.18 mmol), and toluene (2 mL). Then, Et₃N (180 μL, 1.3 mmol) was added. After 2h, the solvent was evaporated under reduced pressure. The crude mixture was dissolved in EtOAc, and sequentially washed with 10% aqueous citric acid (3 mL), water, saturated aqueous NaHCO₃, and brine. The combined organic phase was dried on anhydrous Na₂SO₄, and the solvent was evaporated under reduced pressure. The obtained mixture was chromatographed (silica gel, 30% EtOAc in CyH) affording 33 mg of **14** as colourless oil (0.16 mmol, yield 14%). Spectroscopic data are in agreement with those reported in literature.[181]

Methyl ((benzyloxy)carbonyl)-*L*-methioninate (17)

A single-neck round-bottom flask was charged with Et₂O (33 mL), water (33 mL), and K₂CO₃ (17.3 g, 125 mmol). The vessel was cooled down to 0 °C, and **16** (5 g, 25 mmol) was added to the mixture. Then, CbzCl (3.9 mL, 27.1 mmol) was added dropwise at 0 °C. The reaction mixture was vigorously stirred for 12h at room temperature. The mixture was extracted with Et₂O, the combined organic phase was dried on anhydrous Na₂SO₄, and the solvent was evaporated under reduced pressure, affording 7.3 g of spectroscopically pure **17** as yellowish oil (24.5 mmol, yield 98%), which were used as such in the next step. Spectroscopic data are in agreement with those reported in literature.[151]

Methyl (2*S*)-2-(((benzyloxy)carbonyl)amino)-4-(methylsulfinyl)butanoate (18)

A single-neck round-bottom flask was charged with MeOH (40 mL) and **17** (7.3 g, 24.5 mmol). NaIO₄ (5.8 g, 27.5 mmol) was dissolved in 40 mL of water, and the resulting solution was added dropwise in the reaction vessel at 0 °C. The reaction mixture was vigorously stirred for 48h at room temperature. The resulting mixture was filtered over a celite pad, and the filter cake was washed with CH₂Cl₂ and MeOH. Volatiles were removed under reduced pressure, and the resulting aqueous concentrated mixture was extracted with CH₂Cl₂ (3 × 20 mL). The combined organic phase was dried over anhydrous Na₂SO₄, and the solvent was evaporated under reduced pressure, affording 7.76 g of spectroscopically pure **18** as colourless oil (24.3 mmol, yield 99%), which were used as such in the next step. Spectroscopic data are in agreement with those reported in literature.[151]

### Methyl (*S*)-2-(((benzyloxy)carbonyl)amino)but-3-enoate (19)
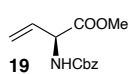
Substrate **18** was Kugelrohr distilled (240 °C, $6.5 \cdot 10^{-1}$ mbar, three-bulb setup). The desired pyrolyzed fraction (yellow oil) was collected in the terminal outside bulb (cooled down to 0 °C). The described distillation was not performed on the whole substrate batch: the latter was split up into relatively small amounts (no more than 1.5 g, 4.8 mmol), and the distillation was repeated as many times as needed. The crude pyrolyzed fraction was chromatographed (silica gel, 20% EtOAc in CyH),

affording **19** as light-yellow oil (maximum yield: 69%). Spectroscopic data are in agreement with those reported in literature.[151]

Methyl (*S*)-2-(((benzyloxy)carbonyl)amino)-2-((*S*)-oxiran-2-yl)acetate (4)
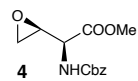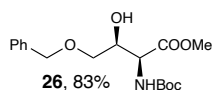
A dry two-neck round-bottom flask was charged with dry CH_2Cl_2 (50 mL) and **19** (2.75 g, 11 mmol) under N_2 atmosphere. The mixture was cooled down to 0 °C, and *m*-chloroperbenzoic acid (MCPBA, 5.7 g, 33 mmol) was slowly added. The reaction mixture was vigorously stirred for 20h at room temperature. The resulting mixture was filtered over a celite pad, and the filtrate was treated with saturated aqueous Na_2SO_3 at 0 °C, until potassium iodide starch paper tested negative for the presence of oxidizing agents. The mixture was again filtered over a celite pad, and the filtrated was sequentially washed with saturated aqueous $NaHCO_3$ (3 × 10 mL) and water (3 × 10 mL). The combined organic phase was dried over anhydrous Na_2SO_4, and the solvent was evaporated under reduced pressure. The crude mixture was chromatographed (silica gel, 30% EtOAc in CyH), affording 1.1 g of **4** (single diastereoisomer) as whitish oil (NMR conversion: 70%; isolated yield: 4.1 mmol, 37%). Spectroscopic data are in agreement with those reported in literature.[117]

Methyl (*S*)-2-((*tert*-butoxycarbonyl)amino)-2-((*S*)-oxiran-2-yl)acetate (24)
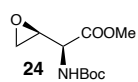
A dry two-neck round-bottom flask was charged with dry MeOH (2.5 mL), **4** (50 mg, 0.19 mmol), Boc_2O (207 mg, 0.95 mmol), and palladium on carbon (Pd/C 10 wt. % loading, 13 mg, 25% m/m). The flask was partially evacuated (until incipient boiling of the solvent), and refilled with H_2 (balloon). The reaction mixture was vigorously stirred for 30 minutes at room temperature. The resulting mixture was filtered over a celite pad, and the filter cake was washed with MeOH. The solvent was evaporated under reduced pressure, and the resulting crude mixture was chromatographed (silica gel, 50% EtOAc in CyH), affording 27 mg of **24** as yellowish oil (0.12 mmol, yield 62%). Spectroscopic data are in agreement with those reported in literature.[182]

Methyl (2*S*,3*S*)-4-(benzyloxy)-2-((*tert*-butoxycarbonyl)amino)-3-hydroxybutanoate (26)
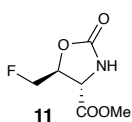
A dry two-neck round-bottom flask was charged with dry CH_2Cl_2 (2 mL), **24** (65 mg, 0.28 mmol), and freshly distilled benzyl alcohol (42 µL, 0.41 mmol) under N_2 atmosphere. The flask was cooled down to 0 °C, and boron trifluoride etherate (7 µL, 0.056 mmol) was added. The reaction mixture was vigorously stirred for 48h at room temperature. The volatiles were accurately evaporated under vacuum affording 95 mg of crude **26** as brownish oil (NMR conversion 83%), which was used as such in the next step. ^{1}H-NMR ($CDCl_3$, 400 MHz, ppm) δ: 1.43 (9H, s), 3.52−3.56 (2H, two merged doublets, *J* = 5.3 Hz), 3.72 (3H, s), 4.12 (1H, dt, *J* = 6.8, 5.3 Hz), 4.57 (1H, d, *J* = 6.8 Hz), 4.55 (1H, s), 7.29-7.47 (5H, m).

Methyl (4*S*,5*S*)-5-((benzyloxy)methyl)-2-oxooxazolidine-4-carboxylate (22)
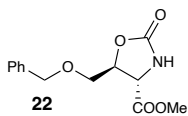
Crude **26** was dissolved in CH_2Cl_2 (10 mL), in a single-neck round-bottom flask, and TFA (3 mL) was added dropwise. The reaction mixture was vigorously stirred for 4h at room temperature. Volatiles were accurately evaporated under vacuum, and the obtained crude mixture was again dissolved in CH_2Cl_2 (15 mL). Saturated aqueous $NaHCO_3$ (15 mL) was added, and the flask was cooled down to 0 °C. Triphosgene (100 mg, 0.34 mmol) was added, and the reaction mixture was vigorously stirred for 12h at room temperature. Upon separation, the aqueous phase was extracted with CH_2Cl_2 (3 × 15 mL), and the combined organic phases were dried over anhydrous Na_2SO_4. The solvent was evaporated under reduced pressure, and the obtained crude mixture was chromatographed (silica gel, 30% EtOAc in CyH), affording 9 mg of **22** as whitish solid (0.03 mmol, yield 12% over two steps). ^{1}H-NMR (CDCl$_3$, 400 MHz, ppm) δ: 2.26 (1H, ddd, J = 13.9, 10.3, 10.0 Hz), 2.14 (1H, ddd, J = 13.9, 4.0, 2.8 Hz), 3.71 (3H, s), 4.02 (1H, dd, J = 10.0, 4.0 Hz), 4.65-4.66 (2H, m), 5.80 (1H, dd, J = 10.3, 2.8 Hz), 7.30-7.47 (5H, m).

Methyl (4*S*,5*S*)-5-(hydroxymethyl)-2-oxooxazolidine-4-carboxylate (23)
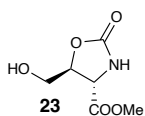
A dry two-neck round-bottom flask was charged with dry MeOH (12 mL), **22** (50 mg, 0.18 mmol), and palladium on carbon (Pd/C 10 wt. % loading, 5 mg, 10% m/m). The flask was partially evacuated (until incipient boiling of the solvent), and refilled with H_2 (balloon). The reaction mixture was vigorously stirred for 12h at room temperature. The resulting mixture was filtered over a celite pad, and the filter cake was washed with MeOH. The solvent was evaporated under reduced pressure, affording 29 mg of spectroscopically pure **23** as yellowish oil (0.17 mmol, yield 92%). ^{1}H-NMR (CDCl$_3$, 400 MHz, ppm) δ: 1.92 (1H, ddd, J = 13.8, 10.3, 10.0 Hz), 2.06 (1H, ddd, J = 13.8, 4.0, 2.8 Hz), 3.71 (3H, s), 3.81−3.84 (2H, two merged doublets, J = 4.7 Hz), 4.02 (1H, dd, J = 10.0, 4.0 Hz), 4.60 (1H, dtd, J = 10.3, 4.7, 2.8 Hz).

Methyl (4*R*,5*S*)-5-(fluoromethyl)-2-oxooxazolidine-4-carboxylate (11)

A dried two-neck round-bottom flask was charged with dry CH_2Cl_2 (0.5 mL) and **23** (10 mg, 0.06 mmol) under N_2 atmosphere. The reaction vessel was placed in a −78 °C bath and diethylaminosulfur trifluoride (DAST, 8 μL, 0.06 mmol) was added. The reaction mixture was stirred at −78 °C for 30 minutes, then allowed to warm up to 0 °C and stirred for 2h. The reaction vessel was cooled down to −78 °C and saturated $NaHCO_3$ (1 mL) was added under vigorous stirring. The mixture was allowed to warm to room temperature under vigorous stirring. Upon separation, the organic phase was dried on anhydrous Na_2SO_4 and the solvent was removed under reduced pressure. A flash column chromatography was performed (silica gel, 50% EtOAc in CyH), affording 1 mg of **10** as

whitish solid (0.006 mmol, yield 10%). H NMR: δ 1.91-2.19 (2H, 2.00 (ddd, J = 13.8, 10.3, 10.0 Hz), 2.13 (ddd, J = 13.8, 4.0, 2.8 Hz)), 3.71 (3H, s), 4.03 (1H, dd, J = 10.0, 4.0 Hz), 4.39-4.43 (2H, 4.41 (d, J = 6.6 Hz), 4.41 (d, J = 6.6 Hz)), 4.71 (1H, dtd, J = 10.3, 6.6, 2.8 Hz19FNMR (CDCl3): δ= -243.16 ppm (dt, JFCH2: 50.8 Hz, J FCH2CH= 25.6 Hz).

Tert-butyl (*R*)-4-formyl-2,2-dimethyloxazolidine-3-carboxylate (30)

Compound **30** was prepared starting from *D*-serine, according to literature procedures.[123]

## 3.5.2. *Synthetic procedures of Section 3.3.2*

2-(Benzyloxy)acetaldehyde (39)

A tube with a bubbler was charged with a solution of allyl benzyl ether (2 mL, 12.9 mmol) in CH_2Cl_2 (20 mL) and cooled at −78 °C. The mixture was fluxed with O_2 for 1 min, then O_3 was fluxed until the mixture became blue, maintaining the reaction temperature at −78 °C. Excess O_3 was removed by fluxing O_2 for 5 min. Dimethyl sulfide (9.5 mL, 129 mmol) was added at −78 °C, and the reaction mixture was slowly warmed at room temperature and stirred overnight. Volatiles were removed under reduced pressure, and the crude aldehyde was purified by flash column chromatography (silica gel, 0−10% EtOAc in CyH), affording 1.15 g (7.7 mmol, 60% yield) of **39** as pale-yellow oil. Spectroscopical data are in agreement with those reported in the literature.[183] TLC: R_f (CyH/EtOAc = 1:1) = 0.25. ^{1}H NMR (400 MHz, CDCl$_3$) δ: 9.73 (1H, s), 7.40−7.30 (5H, m), 4.64 (2H, s), 4.11 (2H, s). ^{13}C NMR (101 MHz, CDCl$_3$) δ: 200.6, 137.0, 128.8 (2C), 128.4, 128.2 (2C), 75.4, 73.8. EI-MS m/z: 107 (M − CH$_2$CHO, 33), 91 (100), 77 (7), 65 (17), 51 (5).

Ethyl (4*S**,5*S**)-5-((benzyloxy)methyl)-4,5-dihydrooxazole-4-carboxylate (rac-38)

A dried three-neck round-bottom flask, equipped with a pressure-equalizing dropping funnel, was charged with CuCl (38 mg, 0.38 mmol), triphenylphosphine (100 mg, 0.38 mmol), and dry CH_2Cl_2 (10 mL) under N_2 atmosphere. The mixture was stirred for 5 min, and then dry diisopropylethylamine (130 μL, 96 mg, 0.76 mmol) was added and the mixture was stirred for further 10 min. A solution of **39** (1.15 g, 7.7 mmol) and **40** (840 μL, 7.7 mmol) in dry CH_2Cl_2 (10 mL) was added dropwise at 0 °C. The dropping funnel was washed with two 5 mL portions of dry CH_2Cl_2 to transfer all of the reagents inside the reaction flask, and the reaction mixture was stirred overnight at room temperature (or until completion by TLC). The solvent was removed under reduced pressure and the crude mixture was chromatographed (silica gel, 0−50% EtOAc in CyH), affording 1.55 g (5.9 mmol, 77% yield) of rac-**38** as pale-yellow oil. TLC: R_f (CyH/Et$_2$O = 1:4) = 0.41. ^{1}H NMR (400 MHz, CDCl$_3$) δ: 7.37−7.28 (5H, m), 6.93 (1H, d, J = 2.0 Hz), 4.85 (1H, ddd, J = 7.8, 5.0, 3.4 Hz), 4.60 (2H, s), 4.57 (1H, dd, J= 7.8, 2.0 Hz), 4.29−4.18 (m, 2H), 3.72 (1H, dd, J = 10.9, 3.4 Hz), 3.60 (1H, dd, J = 10.9, 5.0 Hz), 1.30 (3H, t, J = 7.2 Hz). ^{13}C NMR (101 MHz, CDCl$_3$) δ: 170.7, 156.5, 137.6, 128.6 (2C),

128.0, 127.8 (2C), 80.1, 73.6, 70.2, 69.3, 62.0, 14.3. EI-MS m/z: 190 (M − COOEt, 2), 172 (M − Bn, 2), 157 (8), 91 (100), 84 (35), 77 (5), 70 (6), 65 (13), 56 (8).
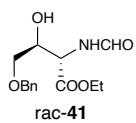
Compound rac-**38** was obtained in a mixture with the corresponding formamide rac-**41** (variable from 0 to 15%, batch dependent), derived from the hydrolysis of the oxazoline ring due to trace of water during the column chromatography process. The mixture of the two compounds could be used directly in the next step without any further purification. In the following, characteristic ^{1}H NMR signals and ESI-MS data for compound rac-**41** are reported. ^{1}H NMR (400 MHz, CDCl$_3$) δ: 8.27 (1H, s), 7.39−7.28 (5H, m), 6.39 (1H, d, J = 8.8 Hz, NH), 4.77 (1H, dd, J = 8.8, 2.6 Hz), 4.54 (2H, s), 4.38 (1H, dddd, J = 7.9, 4.2, 3.9, 2.6 Hz), 4.23 (2H, q, J = 7.1 Hz), 3.59 (1H, dd, J = 9.5, 4.2 Hz), 3.44 (1H, dd, J = 9.5, 7.9 Hz), 2.71 (1H, d, J = 3.9 Hz), 1.28 (3H, t, J = 7.1 Hz). ESI-MS m/z: 282.2 [M + H]$^+$ (100); 304.2 [M + Na]$^+$ (4).

### Ethyl (4S*,5S*)-5-((benzyloxy)methyl)-2-oxooxazolidine-4-carboxylate (rac-42)
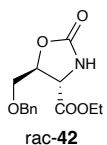
A dried two-neck round-bottom flask was charged with rac-**38** (1.55 g, 5.9 mmol) and dry MeOH (12 mL) under N$_2$ atmosphere. The mixture was cooled to 0 °C and HCl (3 M in MeOH, 12 mL, 36 mmol) was slowly added. The reaction mixture was stirred at 0 °C for 30 minutes and then allowed to warm to room temperature and stirred overnight or until completion (TLC). The solvent was removed under reduced pressure, affording crude ethyl 2-amino-4-(benzyloxy)-3-hydroxybutanoate hydrochloride salt as viscous amber oil, which was used in the next step without purification. The reaction crude was dissolved in dry CH$_2$Cl$_2$ (15 mL) and Et$_3$N (2.67 mL, 19.3 mmol) was added dropwise at 0 °C under N$_2$ atmosphere. The reaction mixture was stirred at 0 °C for 10 min, and then a solution of triphosgene (1.90 g, 6.4 mmol) in dry CH$_2$Cl$_2$ (15 mL) was added dropwise. The reaction mixture was stirred at 0 °C for 30 minutes and then allowed to warm to room temperature and stirred overnight or until completion (TLC). The reaction mixture was cooled to 0 °C, and a saturated Na$_2$CO$_3$ aqueous solution was slowly added under vigorous stirring until basic pH was reached (pH = 9−10). Upon separation, the organic phase was washed with aqueous 1 M HCl and saturated NaHCO$_3$ successively, and then dried on anhydrous Na$_2$SO$_4$. The solvent was removed under reduced pressure. Flash column chromatography of the crude (silica gel, CyH/Et$_2$O = 1:1) afforded 1.02 g (3.7 mmol, 62%) of rac-**42** as pale-yellow oil. TLC: R_f (Et$_2$O) = 0.64. ^{1}H NMR (400 MHz, CDCl$_3$) δ: 7.33−7.22 (5H, m), 6.93 (1H, s), 4.71 (1H, ddd, J = 5.4, 4.4, 3.7 Hz), 4.58 (1H, d, J = 12.1H), 4.56 (1H, d, J = 12.1 Hz), 4.29 (1H, d, J = 5.4 Hz), 4.18 (2H, q, J = 7.1 Hz), 3.71 (1H, dd, J = 11.0, 3.7 Hz), 3.64 (1H, dd, J = 11.0, 4.4 Hz), 1.22 (3H, t, J = 7.1 Hz). ^{13}C NMR (101 MHz, CDCl$_3$) δ: 169.9, 158.4, 137.3, 128.3 (2C), 127.7, 127.5 (2C), 77.4, 73.3, 69.5, 62.0, 55.3, 13.8. EI-MS m/z: 206 (M − COOEt, 2), 173 (7), 130 (3), 107 (7), 100 (20), 91 (100), 86 (14), 77 (5), 65 (14), 56 (17).

*Synthetic procedures of Section 3.3.2*
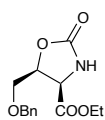
The racemic analytical sample of the *cis* diastereoisomer of rac-**42** was obtained starting from **39** and **40**, through a similar Cu(I)-based experimental procedure (CuCl 5 mol %, Et$_3$N 5 mol %, THF),[184] only partially diastereoselective (*trans/cis* = 85:15), to perform its complete NMR characterization. TLC: R_f (Et$_2$O) = 0.36. ^{1}H NMR (400 MHz, CDCl$_3$) δ: 7.36−7.26 (5H, m), 5.48 (1H, s), 4.94 (1H, dt, J = 9.3, 3.5 Hz), 4.52 (1H, d, J = 12.1 Hz), 4.50 (1H, d, J = 12.1 Hz), 4.48 (1H, d, J = 9.3 Hz), 4.09 (2H, q, J = 7.2 Hz), 3.80−3.78 (2H, m), 1.17 (3H, t, J = 7.2 Hz). ^{13}C NMR (101 MHz, CDCl$_3$) δ: 168.9, 158.4, 137.4, 128.5 (2C), 127.9, 127.7 (2C), 76.9, 73.7, 67.7, 62.2, 55.5, 14.0. EI-MS *m/z* 206 (M − COOEt, 3), 173 (5), 158 (3), 130 (3), 107 (7), 100 (20), 91 (100), 86 (10), 77 (5), 65 (13), 56 (17).

Ethyl (4*S**,5*S**)-5-(hydroxymethyl)-2-oxooxazolidine-4-carboxylate (rac-43)
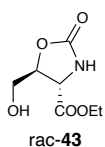
A dried two-neck round-bottom flask was charged with a solution of rac-**42** (830 mg, 2.97 mmol) in EtOH (96%, 30 mL) under N$_2$ atmosphere. Palladium on carbon (Pd/C 10 wt. % loading, 83 mg, 10% m/m) was added to the mixture. The flask was partially evacuated and refilled with H$_2$ (balloon). The mixture was vigorously stirred at room temperature overnight or until completion (TLC). The reaction mixture was filtered over a Celite, washed with CH$_2$Cl$_2$, and the filtrate was evaporated under reduced pressure, affording 562 mg (2.97 mmol, quantitative yield) of spectroscopically pure rac-**43** as colourless oil. The latter solidified upon storage at −20 °C overnight, affording a white sticky solid. TLC: R_f (CyH/EtOAc = 1:4) = 0.22. ^{1}H NMR (400 MHz, CDCl$_3$) δ: 6.19 (1H, bs), 4.70 (1H, ddd, J = 5.6, 3.3, 2.4 Hz), 4.42 (1H, d, J = 5.6 Hz), 4.27 (2H, q, J = 7.1 Hz), 4.01 (1H, dd, J = 12.7, 2.4 Hz), 3.75 (1H, dd, J = 12.9, 3.3 Hz), 2.84 (1H, bs), 1.31 (3H, t, J = 7.1 Hz). ^{13}C NMR (101 MHz, CDCl$_3$) δ: 170.5, 159.1, 79.4, 77.4, 62.3, 55.1, 14.1. EI-MS *m/z* 189 (M$^+$, 2), 173 (7), 130 (3), 107 (7), 100 (20), 91 (100), 86 (14), 77 (5), 65 (14), 56 (17).

Ethyl (4*S**,5*S**)-5-(fluoromethyl)-2-oxooxazolidine-4-carboxylate (rac-44)
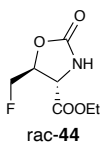
A dried two-neck round-bottom flask was charged with rac-**43** (712 mg, 3.76 mmol) and dry CH$_2$Cl$_2$ (20 mL) under N$_2$ atmosphere. The reaction mixture was cooled at −78 °C and diethylaminosulfur trifluoride (DAST, 990 μL, 7.53 mmol) was added dropwise. The reaction mixture was stirred at −78 °C for 30 min, and then allowed to warm up to 0 °C and stirred 3 h until completion (TLC). The reaction vessel was cooled to −78 °C and a saturated NaHCO$_3$ solution (10 mL) was added under vigorous stirring. The mixture was allowed to warm to room temperature under vigorous stirring. Upon extraction (CH$_2$Cl$_2$, 3 × 10 mL) and separation, the collected organic phases were dried on anhydrous Na$_2$SO$_4$ and the solvent was removed under reduced pressure. Flash column chromatography (silica gel, CyH/Et$_2$O = 1:1) afforded 233 mg (1.2 mmol, 32% yield) of rac-**44** as pale-yellow oil. TLC: R_f (CyH/EtOAc = 1:4) = 0.77. ^{1}H NMR (400 MHz, CDCl$_3$) δ: 5.76 (1H, bs), 4.82 (1H, dddd, J = 23.8, 5.6, 3.2, 2.8 Hz), 4.73 (1H, ddd, J = 47.6, 10.8, 2.8 Hz), 4.58 (1H, ddd, J = 46.1, 10.8, 3.2

Hz), 4.36 (1H, d, J = 5.6 Hz), 4.30 (2H, q, J = 7.2 Hz), 1.33 (3H, t, J = 7.2 Hz). ^{19}F NMR (376.5 Hz, CDCl$_3$) δ: −235 (dt, J = 46.9, 23.8 Hz). ^{13}C NMR (101 MHz, CDCl$_3$) δ: 169.4, 157.6, 81.9 (d, J = 177.7 Hz), 76.7 (d, J = 19.9 Hz), 62.8, 54.5 (d, J = 6.2 Hz), 14.2. EI-MS m/z: 191 (M$^+$, 2), 118 (M − COOEt, 100), 101 (2), 85 (5), 74 (6), 54 (6).

(2S*,3S*)-2-amino-4-fluoro-3-hydroxybutanoic acid, hydrochloride salt (rac-34·HCl)
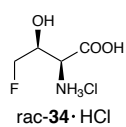
A Schlenk tube was charged with rac-**44** (432 mg, 2.26 mmol) and aqueous HCl (6 M, 4 mL, 24 mmol) under N$_2$ atmosphere. The reaction mixture was refluxed under vigorous stirring for 2 days, until complete conversion (NMR). The solvent was evaporated under reduced pressure, affording 352 mg of crude rac-**34**·HCl (2.03 mmol, 90% yield) as viscous amber oil, which was used as such in the next step. ^{1}H NMR (400 MHz, D$_2$O) δ: 4.76 (1H, ddd, J = 46.2, 10.5, 3.7 Hz), 4.64 (1H, ddd, J = 47.0, 10.5, 3.5 Hz), 4.47 (1H, dddd, J = 24.7, 3.9, 3.7, 3.5 Hz), 4.22 (1H, d, J = 3.9 Hz). ^{19}F NMR (376.5 Hz, D$_2$O) δ: −232 (dt, J = 46.7, 24.8 Hz). ^{13}C NMR (101 MHz, D$_2$O) δ: 170.9, 85.2 (d, J = 168.0 Hz), 67.8 (d, J = 19.2 Hz), 55.7 (d, J = 4.6 Hz). ESI-MS m/z: 138.2 [M − Cl]$^+$ (100); 92.2 [M − (Cl + COOH)]$^+$ (10).

(2S*,3S*)-4-Fluorothreonine; (2S*,3S*)-2-amino-4-fluoro-3-hydroxybutanoic acid (rac-34)
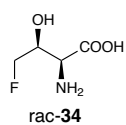
A Schlenk tube was charged with rac-**34**·HCl (352 mg, 2.03 mmol) and dry MeOH (10 mL) under N$_2$ atmosphere. Propylene oxide (1.42 mL, 20.3 mmol) was added to the mixture, which was stirred at room temperature overnight. During this stage, a pale-yellow precipitate formed. The solvent and excess propylene oxide were removed under reduced pressure. Recrystallization from MeOH afforded 171 mg (1.25 mmol, 61% yield) of spectroscopically pure rac-**34** as white powder. Spectroscopical data are in agreement with those reported in the literature.[107] ^{1}H NMR (400 MHz, D$_2$O) δ: 4.72 (1H, ddd, J = 46.6, 10.8, 3.7 Hz), 4.60 (1H, ddd, J = 47.0, 10.8, 3.1 Hz), 4.35 (1H, dddd, J = 24.9, 4.7, 3.7, 3.1 Hz), 3.87 (1H, d, J = 4.7 Hz). ^{19}F NMR (376.5 Hz, D$_2$O) δ: −232 (dt, J = 46.8, 24.9 Hz). ^{13}C NMR (101 MHz, D$_2$O) δ: 172.5, 85.6 (d, J = 167.3 Hz), 68.4 (d, J = 19.1 Hz), 56.8 (d, J = 4.4 Hz). ESI-MS m/z: 138.2 [M + H]$^+$ (100); 92.2 [M − COOH]$^+$ (15).

3.5.3. Synthetic procedures of Section 3.3.3

Ethyl N-(((9H-fluoren-9-yl)methoxy)carbonyl)-L-methioninate (46)
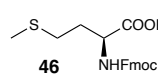
The reported procedure is based on a literature general procedure for the preparation of amino acid esters.[185] A dried two-neck round-bottom flask was charged with **45** (5 g, 13.5 mmol) under N$_2$ atmosphere. EtOH (96 %, 50 mL) was added, and the mixture was cooled down to 0 °C. Thionyl chloride (1.5 mL, 20.7 mmol) was added dropwise under vigorous stirring, and the reaction mixture was stirred at 0 °C for 5 minutes. During this time, the apparatus was isolated from the N$_2$

Schlenk line and equipped with a CaCl$_2$ trap. The reaction mixture was then allowed to warm up to room temperature, and it was stirred for 2 hours. During this time, the initially clear solution coagulated in a hardly stirrable mixture due to the formation of a foamy solid, so EtOH (96%, 20 mL) was added, and the coagulated mass was accurately broken. Once efficient stirring was again achieved (mechanical stirring might be preferable), the reaction mixture was stirred overnight at room temperature. The volatiles were removed under reduced pressure, affording 5.37 g of spectroscopically pure **46** as white solid (13.5 mmol, quantitative). Spectroscopic data were in agreement with those reported in literature.[186] TLC: R_f (CyH/EtOAc = 7:3) = 0.42. m.p. = 120−123 °C. $[\alpha]^{25}_D$ (*c* 1.0, CHCl$_3$) = +13.3°. ^{1}H NMR (400 MHz, CDCl$_3$) δ: 7.77 (2H, d, *J* = 7.5 Hz), 7.63−7.57 (2H, m), 7.41 (2H, t, *J* = 7.5 Hz), 7.32 (2H, t, *J* = 7.3 Hz), 5.41 (1H, d, *J* = 7.8 Hz), 4.54−4.45 (1H, m), 4.42 (2H, d, *J* = 7.3 Hz), 4.29−4.15 (3H, m), 2.59−2.47 (2H, m), 2.23−2.12 (1H, m), 2.11 (3H, s), 2.04−1.92 (1H, m), 1.30 (3H, t, *J* = 7.2 Hz). ^{13}C NMR (101 MHz, CDCl$_3$) δ: 172.1, 156.0, 143.9 and 143.7 (2C, two conformers), 141.3 (2C), 127.7 (2C), 127.1 (2C), 125.1 (2C), 120.0 (2C), 67.0, 61.7, 53.2, 47.2, 32.0, 29.9, 15.5, 14.2.

Ethyl (2*S*)-2-((((9*H*-fluoren-9-yl)methoxy)carbonyl)amino)-4-(methylsulfinyl)butanoate (47)
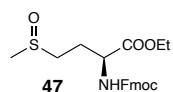
Compound **47** was prepared according to a literature procedure.[156] A round-bottom flask was charged with **46** (5.36 g, 13.4 mmol) in EtOH (96%, 75 mL). The reaction vessel was cooled to 0 °C, and a solution of NaIO$_4$ (3.16 g, 14.8 mmol) in water (60 mL) was slowly added. The reaction mixture was stirred overnight at room temperature. The resulting mixture was filtered over a celite pad, and the filter cake was washed with EtOH followed by CH$_2$Cl$_2$. Volatiles were removed under reduced pressure, and the resulting aqueous concentrated mixture was extracted with CH$_2$Cl$_2$. The organic phase was washed with 1M HCl followed by saturated NaHCO$_3$, and then it was dried on anhydrous Na$_2$SO$_4$. Volatiles were removed under reduced pressure affording crude **47** as yellow viscous oil. Flash chromatography (silica gel, one dead volume of 50% EtOAc in CyH, two dead volumes of EtOAc, then 10% MeOH in EtOAc) afforded 5.07 g of spectroscopically pure **3** as white sticky solid (12.2 mmol, 91% yield, diastereoisomeric mixture, approx. d.r. = 1:1). Spectroscopic data were compatible with those reported in literature for the methyl ester analogue.[156] TLC: R_f (EtOAc/MeOH = 9:1) = 0.38. m.p. (range) = 103−118 °C. $[\alpha]^{25}_D$ (*c* 1.0, CHCl$_3$) = +11.1°. ^{1}H NMR (400 MHz, CDCl$_3$) δ: 7.75 (2H, d, *J* = 7.5 Hz), 7.63−7.56 (2H, m), 7.39 (2H, t, *J* = 7.4 Hz), 7.33−7.27 (2H, m), 5.92 and 5.85 (1H, d, *J* = 7.8 and 8.0 Hz, two diastereoisomers), 4.50−4.35 (3H, m), 4.25−4.17 (3H, m), 2.82−2.65 (2H, m), 2.55 (3H, s), 2.44−2.32 (1H, m), 2.20−2.08 (1H, m), 1.27 (3H, t, *J* = 7.0 Hz). ^{13}C NMR (101 MHz, CDCl$_3$) δ: 171.4, 156.2, 143.9 and 143.7 (2C, two diastereoisomers), 141.4 (2C), 127.8 (2C), 127.1 (2C), 125.1 (2C), 120.1 (2C), 67.1, 62.1, 53.2 and 52.9 (two diastereoisomers), 50.4 and 50.2 (two diastereoisomers), 47.2, 38.6, 26.2 and 25.8 (two diastereoisomers), 14.2.

Ethyl (*S*)-2-(((((9*H*-fluoren-9-yl)methoxy)carbonyl)amino)but-3-enoate (48)
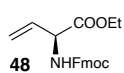
Compound **48** was prepared according to a literature procedure.[154] A dry large Schlenk was charged with **47** (3.08 g, 7.4 mmol) and 2,4-dichlorotoluene (55 mL) under N_2 atmosphere. The reaction mixture was heated (190 °C) under vigorous stirring until completion (TLC). The solvent was evaporated under reduced pressure[155] and the crude mixture was chromatographed (silica gel, two dead volumes of CyH, then 40% Et_2O in CyH. Unreacted starting material can be recovered with 10% MeOH in EtOAc) to afford 1.88 g of pure **48** as white solid (5.35 mmol, yield 72%). Spectroscopic data were compatible with those reported in literature for the methyl ester analogue.[154] TLC: R_f (CyH/Et_2O = 6:4) = 0.38. m.p. = 114−116 °C. $[\alpha]^{25}_D$ (*c* 0.66, CHCl$_3$) = +3.94°. ^{1}H NMR (400 MHz, CDCl$_3$) δ: 7.77 (2H, d, *J* = 7.5 Hz), 7.64−7.57 (2H, m), 7.41 (2H, t, *J* = 7.5 Hz), 7.32 (2H, t, *J* = 7.5 Hz), 5.98−5.87 (1H, m), 5.48 (1H, d, *J* = 7.4 Hz), 5.40−5.25 (2H, m), 4.97−4.89 (1H, m), 4.42 (2H, d, *J* = 7.0 Hz), 4.29−4.19 (3H, m), 1.30 (3H, t, *J* = 7.1 Hz). ^{13}C NMR (101 MHz, CDCl$_3$) δ: 170.5, 155.7, 143.9 (2C), 141.4 (2C), 132.6, 127.8 (2C), 127.2 (2C), 125.2 (2C), 120.1 (2C), 117.7, 67.2, 62.1, 56.3, 47.3, 14.2.

Ethyl (*S*)-2-(((((9*H*-fluoren-9-yl)methoxy)carbonyl)amino)-2-((*S*)-oxiran-2-yl)acetate (49)
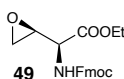
Compound **49** was prepared according to a literature procedure.[156] A dried two-neck round-bottom flask was charged with **48** (1.88 g, 5.35 mmol) and dry CH_2Cl_2 (75 mL). The reaction mixture was cooled to 0 °C and *m*-chloroperbenzoic acid (50-55% MCPBA, 5.89 g, 18.8 mmol) was added under vigorous stirring at 0 °C. The reaction mixture was stirred at room temperature until completion (TLC, with the starting material being completely consumed indicatively after 3 days). The reaction mixture was filtered over a celite pad. The filtrate was cooled to 0 °C, and saturated Na_2SO_3 (32 mL) was added dropwise under vigorous stirring. After 5 minutes, the resulting mixture was filtered over a celite pad and the two phases were separated. The organic phase was washed with saturated Na_2SO_3 (45 mL) followed by saturated $NaHCO_3$ (45 mL). The organic phase was then dried over anhydrous Na_2SO_4 and the solvent was evaporated under reduced pressure. The crude mixture was chromatographed (silica gel, 0−50% EtOAc in CyH) to afford 1.33 g of **49** (single diastereoisomer) as white solid (3.6 mmol, yield 68%). Spectroscopic data were compatible with those reported in literature for the methyl ester analogue.[187] TLC: R_f (CyH/Et_2O = 6:4) = 0.45. m.p. = 141−142 °C. $[\alpha]^{25}_D$ (*c* 1.0, CHCl$_3$) = −7.57°. ^{1}H NMR (400 MHz, CDCl$_3$) δ: 7.77 (2H, d, *J* = 7.5 Hz), 7.62−7.55 (2H, m), 7.41 (2H, t, *J* = 7.5 Hz), 7.36−7.29 (2H, m), 5.32 (1H, d, *J* = 8.6 Hz), 4.73−4.68 (1H, m), 4.42 (2H, d, *J* = 6.9 Hz), 4.29 (2H, q, *J* = 7.1 Hz), 4.22 (1H, t, *J* = 6.9 Hz), 3.50−3.46 (1H, m), 2.80−2.76 (1H, m), 2.64−2.60 (1H, m), 1.32 (3H, t, *J* = 7.1 Hz). ^{13}C NMR (101 MHz, CDCl$_3$) δ: 169.8, 156.2, 143.9 and 143.6 (2C, two conformers), 141.5 (2C), 127.9 (2C), 127.2 (2C), 125.2 (2C), 120.1 (2C), 67.3, 62.3, 53.2, 51.3, 47.2, 43.9, 14.3.

Synthetic procedures of Section 3.3.3

Ethyl (2*S*,3*S*)-2-(((((9*H*-fluoren-9-yl)methoxy)carbonyl)amino)-4-(benzyloxy)-3-hydroxybutanoate (50)
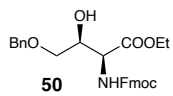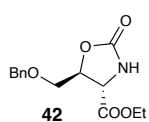

A dried two-neck round-bottom flask was charged with **49** (1.33 g, 3.6 mmol), dry CH_2Cl_2 (24 mL) and dry benzyl alcohol (560 μL, 5.4 mmol). Boron trifluoride etherate (90 μL, 0.73 mmol) was added to the mixture at 0 °C under vigorous stirring. The reaction mixture was stirred overnight at room temperature. The solvent was evaporated under reduced pressure and chromatographed (silica gel, 50% Et_2O in CyH) to afford 980 mg of **50** as white foamy solid (2.1 mmol, yield 57%). TLC: R_f (CyH/Et_2O = 6:4) = 0.32. m.p. = 77−79 °C. $[\alpha]^{25}_D$ (*c* 1.0, CHCl$_3$) = +6.94°. ^{1}H NMR (400 MHz, CDCl$_3$) δ: 7.78 (2H, d, *J* = 7.5 Hz), 7.64 (2H, t, *J* = 7.4 Hz), 7.45−7.38 (2H, m), 7.38−7.27 (7H, m), 5.96−5.82 (1H, br m), 4.55 (2H, s), 4.57−4.50 (1H, m) 4.50−4.34 (3H, m), 4.29−4.19 (3H, m), 3.64−3.58 (1H, m), 3.58−3.49 (1H, m), 1.28 (3H, t, *J* = 7.1 Hz). ^{13}C NMR (101 MHz, CDCl$_3$) δ: 170.8, 156.7, 143.9 and 143.7 (2C, two conformers), 141.3 (2C), 137.5, 128.5 (2C), 128.0, 127.9 (2C), 127.8 (2C), 127.1 (2C), 125.2 (2C), 120.0 (2C), 73.6, 71.2, 70.4, 67.3, 62.0, 55.8, 47.2, 14.2.

Ethyl (2*S*,3*S*)-2-amino-4-(benzyloxy)-3-hydroxybutanoate (51)
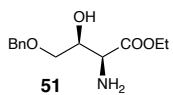
A vial was charged with **50** (980 mg, 2.1 mmol) and dry DMF (2 mL), and piperidine (224 μL, 2.3 mmol) was added. The reaction mixture was stirred overnight. During this time, the initially clear solution coagulated in a viscous milky mixture. The solvent was removed under reduced pressure, and the crude mixture was chromatographed (silica gel, 2% MeOH in EtOAc) to afford 409 mg of **51** as colourless oil (1.6 mmol, yield 78%). Spectroscopic data were compatible with those reported in literature for the methyl ester analogue.[188] TLC: R_f (EtOAc/MeOH = 98:2) = 0.31. $[\alpha]^{25}_D$ (*c* 0.85, CHCl$_3$) = +8.6°. ^{1}H NMR (400 MHz, CDCl$_3$) δ: 7.39−7.26 (5H, m), 4.57 (1H, d, *J* = 11.9 Hz), 4.53 (1H, d, *J* = 11.9 Hz), 4.18 (2H, q, *J* = 7.1 Hz), 4.08 (1H, td, *J* = 5.6, 3.6 Hz), 3.60 (1H, d, *J* = 3.6 Hz), 3.60 (1H, dd, *J* = 9.7, 5.9 Hz), 3.55 (1H, dd, *J* = 9.7, 5.4 Hz), 2.12 (3H, br s), 1.26 (3H, t, *J* = 7.1 Hz). ^{13}C NMR (101 MHz, CDCl$_3$) δ: 174.0, 138.0, 128.6 (2C), 127.93, 127.92 (2C), 73.6, 71.6, 70.7, 61.5, 55.6, 14.3.

Ethyl (4*S*,5*S*)-5-((benzyloxy)methyl)-2-oxooxazolidine-4-carboxylate (42)

A dried two-neck round-bottom flask was charged with **51** (409 mg, 1.6 mmol) and dry CH_2Cl_2 (10 mL). The reaction vessel was cooled down to 0 °C and dry triethylamine (450 μL, 3.2 mmol) was added dropwise, followed by a dropwise addition of a solution of triphosgene (720 mg, 2.4 mmol) in dry CH_2Cl_2 (10 mL). The reaction mixture was then allowed to warm to room temperature and stirred overnight. The reaction vessel was cooled to 0 °C and a saturated Na_2CO_3 aqueous solution was slowly added under vigorous stirring until the pH was 9−10. Upon separation, the organic phase was treated with aqueous 1M HCl until the pH became 1−2. The two phases were separated and the organic was treated with saturated $NaHCO_3$ solution until the pH became

7−8. Upon separation, the organic phase was dried on anhydrous Na_2SO_4 and the solvent was removed under reduced pressure, affording 451 mg of spectroscopically pure **42** as pale-yellow oil (1.6 mmol, quantitative). TLC: R_f (Et$_2$O) = 0.64. $[\alpha]^{25}_D$ (*c* 1, CHCl$_3$) = +40.7°. ^{1}H NMR (400 MHz, CDCl$_3$) *δ*: 7.33−7.22 (5H, m), 6.93 (1H, s), 4.71 (1H, ddd, *J* = 5.4, 4.4, 3.7 Hz), 4.58 (1H, d, *J* = 12.1 Hz), 4.56 (1H, d, *J* = 12.1 Hz), 4.29 (1H, d, *J* = 5.4 Hz), 4.18 (2H, q, *J* = 7.1 Hz), 3.71 (1H, dd, *J* = 11.0, 3.7 Hz), 3.64 (1H, dd, *J* = 11.1, 4.4 Hz), 1.22 (3H, t, *J* = 7.1 Hz). ^{13}C NMR (101 MHz, CDCl$_3$) *δ*: 169.9, 158.4, 137.3, 128.3 (2C), 127.7, 127.5 (2C), 77.4, 73.3, 69.5, 62.0, 55.3, 13.8.

### Ethyl (4*S*,5*S*)-5-(hydroxymethyl)-2-oxooxazolidine-4-carboxylate (43)
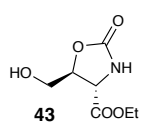
A two-neck round-bottom flask was charged with a solution of **42** (451 mg, 1.6 mmol) in EtOH (96%, 20 mL) under N$_2$ atmosphere. Palladium on carbon (Pd/C 10 wt. % loading, 45 mg, 10% m/m) was added to the mixture. The flask was partially evacuated and refilled with H$_2$ (balloon). The mixture was vigorously stirred at room temperature overnight or until completion (TLC). The reaction mixture was filtered over a celite pad, and the filtrate was evaporated under reduced pressure, affording 305 mg of spectroscopically pure **43** as colourless oil (1.6 mmol, quantitative). TLC: R_f (CyH/EtOAc = 1:4) = 0.22. $[\alpha]^{25}_D$ (*c* 0.5, CHCl$_3$) = +49.0° ^{1}H NMR (400 MHz, CDCl$_3$) *δ*: 6.19 (1H, bs), 4.70 (1H, ddd, *J* = 5.6, 3.3, 2.4 Hz), 4.42 (1H, d, *J* = 5.6 Hz), 4.27 (2H, t, *J* = 7.1 Hz), 4.01 (1H, dd, *J* = 12.7, 2.4 Hz), 3.75 (1H, dd, *J* = 12.9, 3.3 Hz), 2.84 (1H, bs), 1.31 (3H, t, *J* = 7.1 Hz). ^{13}C NMR (101 MHz, CDCl$_3$) *δ*: 170.5, 159.1, 79.4, 77.4, 62.3, 55.1, 14.1.

Ethyl (4*S*,5*S*)-5-(fluoromethyl)-2-oxooxazolidine-4-carboxylate (44)
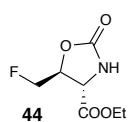
A dried two-neck round-bottom flask was charged with a solution of **43** (305 mg, 1.6 mmol) in CH$_2$Cl$_2$ (10 mL) under N$_2$ atmosphere. The reaction vessel was placed in a −78 °C bath and diethylaminosulfur trifluoride (440 µL, 3.3 mmol) was added dropwise. The reaction mixture was stirred at −78 °C for 30 minutes, then allowed to warm up to 0 °C and stirred until completion (TLC). The reaction vessel was cooled down to −78 °C and saturated NaHCO$_3$ (5 mL) was added under vigorous stirring. The mixture was allowed to warm to room temperature under vigorous stirring. Upon separation, the organic phase was dried on anhydrous Na$_2$SO$_4$ and the solvent was removed under reduced pressure. A flash column chromatography was performed (silica gel, 50% EtOAc in CyH), affording 132 mg of **44** as pale-yellow solid (0.69 mmol, yield 43%). TLC: R_f (CyH/EtOAc = 1:4) = 0.77. m.p. = 58−60 °C. $[\alpha]^{25}_D$ (*c* 1.0, CHCl$_3$) = +31.3°. ^{1}H NMR (400 MHz, CDCl$_3$) *δ*: 5.76 (1H, bs), 4.82 (1H, dddd, *J* = 23.8, 5.6, 3.2, 2.8 Hz), 4.73 (1H, ddd, *J* = 47.6, 10.8, 2.8 Hz), 4.58 (1H, ddd, *J* = 46.1, 10.8, 3.2 Hz), 4.36 (1H, d, *J* = 5.6 Hz), 4.30 (2H, q, *J* = 7.2 Hz), 1.33 (3H, t, *J* = 7.2 Hz). ^{19}F NMR (376.5 Hz, CDCl$_3$) *δ*: −235 (td, *J* = 46.9, 23.8 Hz). ^{13}C NMR (101 MHz, CDCl$_3$) *δ*: 169.4, 157.6, 81.9 (d, *J* = 177.7 Hz), 76.7 (d, *J* = 19.9 Hz), 62.8, 54.5 (d, *J* = 6.2 Hz), 14.2.

(2*S*,3*S*)-2-amino-4-fluoro-3-hydroxybutanoic acid (34)
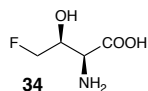
A Schlenk was charged with **44** (132 mg, 0.69 mmol) and aqueous 6M HCl (2 mL) under N$_2$ atmosphere. The reaction mixture was refluxed under vigorous stirring until completion (NMR). The solvent was accurately evaporated under reduced pressure (directly from the Schlenk), and the obtained crude 4-fluoro-*L*-threonine hydrochloride (amber viscous oil) was used as such in the next step. After three vacuum-refill cycles, dry MeOH (3.5 mL) was added under N$_2$ atmosphere. The mixture was vigorously stirred until complete dissolution of crude 4-fluoro-*L*-threonine hydrochloride was achieved. The reaction vessel was cooled down to 0 °C, and propene oxide (480 µL, 6.9 mmol) was added under vigorous stirring. The reaction was stirred for 8 hours at room temperature. During this time, the initially clear solution became opalescent due to a white precipitate. The stirring was stopped and the mixture was allowed to settle overnight. The supernatant clear solution was accurately pipetted away, and the white precipitate was resuspended in fresh MeOH. Volatiles were removed under reduced pressure, affording 68 mg of spectroscopically pure 4-fluoro-*L*-threonine **34** as white powder (0.5 mmol, yield 72%). Spectroscopical data are in agreement with those reported in the literature.[107] m.p. = 178−179 °C (decomposition). ^{1}H NMR (400 MHz, D$_2$O) δ: 4.72 (1H, ddd, J = 46.6, 10.8, 3.7 Hz), 4.60 (1H, ddd, J = 47.0, 10.8, 3.1 Hz), 4.35 (1H, dddd, J = 24.9, 4.7, 3.7, 3.1 Hz), 3.87 (1H, d, J = 4.7 Hz). ^{19}F NMR (376.5 Hz, D$_2$O) δ: −232 (td, J = 46.8, 24.9 Hz). ^{13}C NMR (101 MHz, D$_2$O) δ: 172.5, 85.6 (d, J = 167.3 Hz), 68.4 (d, J = 19.1 Hz), 56.8 (d, J = 4.4 Hz).

3.5.4. *Computational methods of Sections 3.3.4 and 3.3.5*

The conformational space of 4F-Thr (and Thr) was explored using a recently proposed island model evolutionary algorithm (EA),[160] coupled with the two-stage method to evaluate structures.[161] For each form of 4F-Thr, a search using a pool of 30 randomly generated structures was carried out for 70 iterations. At each step, every new structure was evaluated performing a geometry optimization with the semiempirical PM7 method (constraining the dihedral angles, whose values were set up by the EA),[189] followed by a single point energy evaluation at the B3LYP-D3(BJ)/6-31+G(d)level,[190–192] also exploiting the conductor version of the polarizable continuum model (CPCM) to take bulk effects into account (water ε = 78.3553).[193] All structures lying within 25 kJ mol^{-1} above the lowest energy minimum were then reoptimized at a higher level of theory to achieve a better description of the geometry and stability of the 4F-Thr conformer. The double-hybrid B2PLYP functional,[194,195] also including empirical dispersion (D3BJ),[192] in conjunction with the jun-cc-pVTZ basis set,[196] overall shortly denoted as B2, was employed, which is proven to provide reliable results in the characterization of conformers in solution at a limited computational cost.[197,198] Relative free energies were determined by adding CPCM solvent effects together with the zero-point energy and thermal contributions, evaluated within the rigid-rotor harmonic-

oscillator approximation at the B3LYP-D3(BJ)/jul-cc-pVDZ level, to relative electronic energies (ΔE). All quantum-chemical calculations have been performed with the G16.C01 version of the Gaussian suite of programs.[199]

To incorporate the explicit treatment of the first-solvation shells, the solvate structures were obtained from the lowest conformer geometries employing the solvation functionality, as implemented in the Proxima library.[200] Then, only the first seven water molecules directly H-bonded to the solute were kept, and the structures were reoptimized at the B2 level of theory.

3.5.5. *Titration methods of Section 3.3.5*

To determine the main chemical properties (i.e., pKa_1, pKa_2, and pI) of 4F-Thr, a small amount of the racemic amino acid was used to prepare a stock solution to perform acid-base titrations. The approach described below was preliminarily performed with a stock solution of Thr, with the aim of assessing the quality of the experimental procedure. Albeit this method proved to be fully reliable in terms of repeatability, the analysis of titration data were mainly focused on the differences between Thr and 4F-Thr, also in view of the significant spread of the values available in the literature for Thr.

The titration curve of 4F-Thr was recorded three times in the same conditions to allow the calculation of mean values and confidence intervals for pKa_1, pKa_2, and pI. The titration was performed using an aqueous 0.05 M stock solution of 4F-Thr. A test tube equipped with a magnetic stirring bar was charged with 1 mL of such stock solution and a few microliters (thus, a negligible amount with respect to the total volume) of HCl 37% were added under vigorous stirring to lower the pH of the amino acid solution down to 1–2. This ensured that even the first buffer zone (corresponding to pKa_1) could be properly mapped. The pH-meter electrode was inserted in the test tube until its bulb was completely soaked in the stirred solution. A 0.25 M solution of NaOH was used as a titrant. In both the early and late plateau regions of the titration curve (with low slope values), the titrant was added 50 µL at a time, while 10 µL additions were performed in the central part, due to the presence of the two equivalence points, i.e., maximum-slope regions. All of the titrant additions were performed with a 100 µL Hamilton syringe, under proper stirring conditions (Figure 3.13).

Figure 3.13: Depiction of titration experimental setup.

The following semiempirical method was used for the quantitative analyses of titration curves. First, the pKa_2 was determined as the pH value corresponding to the second half-equivalence point. Such specific titration point coincides with a local maximum of the first derivative of the inverted titration curve (i.e., the pH value on the *x*-axis and the titrant volume on the *y*-axis), referred to as the inverted derivative in the following. This approach is applicable only for the determination of pKa values corresponding to buffer zones encompassed between two equivalence points since this situation leads to a single easily identifiable maximum in the inverted derivative. Furthermore, such identification is even easier because buffer zones are usually characterized by a high sampling rate of both pH values and titrant volumes, leading to resolved inverted derivatives. Last but not least, a buffer zone, by definition, is encompassed within a very narrow pH range, thus leading to smaller errors in the determination of the corresponding pKa value. A similar approach could be used for pI, identifiable as the pH value corresponding to the first equivalence point. However, the sampling rate is not sufficiently high to enable easy identification of the equivalence point, even with the analysis of the first and second derivatives of the titration curve, due to their low resolution. Indeed, unlike buffer zones, the region encompassing an equivalence point suffers from tremendous pH changes even when dealing with very small titrant volume variations. Nevertheless, equivalence zones are encompassed within narrow ranges of the titrant volume, thus leading to small errors in volumetric analyses. Therefore, our approach moved to the graphical determination of the pKa_1, starting from pKa_2 and taking advantage of both the narrow volume ranges encompassing equivalence zones and the narrow pH ranges encompassing buffer zones. In particular, the titrant volume difference between the two equivalence points (which is supposed to experience almost negligible fluctuations as a consequence of the unavoidable small discrepancies between the observed and the real equivalence points) is the same observed between the two half-equivalence points.

Such difference was determined graphically, upon identification of five linear-regime zones: three low-slope regions (the early and late titration plateau, and the mid buffer zone corresponding to pKa$_2$) and two high-slope ones (the two equivalence zones). For each zone, the points were interpolated with linear functions and the intersection points between the adjacent linear regressions were determined (four points, overall). Two relevant line segments were then identified: the first one (bounded by the first two points) lies on the first pH jump and its midpoint's abscissa corresponds to the titrant volume at the first equivalence point; the second line segment (bounded by the last two points) lies on the second pH jump and its midpoint's abscissa corresponds to the titrant volume at the second equivalence point. The volume difference between the two equivalence points was hence determined and subtracted to the titrant volume corresponding to pKa$_2$. This new titrant volume is the abscissa of the first half-equivalence point; therefore, the corresponding pH value is pKa$_1$. The value of pI was determined starting from pKa$_1$ and pKa$_2$ using the Henderson-Hasselbalch equation.

3.5.6. *Computational methods of Section 3.3.6*

Indirect J spin-spin coupling constants have been computed at the B3LYP-D3(BJ)/jul-cc-pVDZ level of theory on top of B2PLYP-D3(BJ)/jun-cc-pVTZ reference geometries. Bulk solvent effects were again accounted for using CPCM (see Section 3.5.4). Only conformers within 10 kJ mol^{-1} above the global energy minimum were considered. To compute the ^{1}H and ^{13}C chemical shifts, methanol spectra were simulated at the same level of theory as above and then used as the reference (^{1}H 3.34 ppm and ^{13}C ppm 49.50 ppm). For the ^{19}F nucleus, trifluoroacetic acid (TFA) was used as the reference (-76.55 ppm). Spin–spin coupling constants were simulated with both the one-step (spin–spin) and the two-step (mixed) procedures.[175] All quantum-chemical computations have been performed using the G16.C01 version of the Gaussian suite of programs.[199]

3.6.   References

(1)   Dolbier, W. R. Fluorine chemistry at the millennium. *J. Fluor. Chem.* **2005**, *126* (2), 157–163. DOI: 10.1016/j.jfluchem.2004.09.033.

(2)   Cottet, F.; Marull, M.; Lefebvre, O.; Schlosser, M. Recommendable routes to trifluoromethyl-substituted pyridine- and quinolinecarboxylic acids. *Eur. J. Org. Chem.* **2003**, *2003* (8), 1559–1568. DOI: 10.1002/ejoc.200390215.

(3)   R. Peters (Ed.). *Carbon-Fluorine Compounds: Chemistry, Biochemistry and Biological Activities*; A Ciba Foundation Symposium, Elsevier: Amsterdam, 1972.

(4)   Welch, J. T.; Eswarakrishnan, S. *Fluorine in Bioorganic Chemistry*; Wiley: New York, 1991.

(5)   Kirsch, P. *Modern Fluoroorganic Chemistry: Synthesis, Reactivity, Applications*; Wiley: Weinheim, 2005. DOI: 10.1002/352760393X.

(6)   Wang, J.; Sánchez-Roselló, M.; Aceña, J. L.; Del Pozo, C.; Sorochinsky, A. E.; Fustero, S.; Soloshonok, V. A.; Liu, H. Fluorine in pharmaceutical industry: Fluorine-containing drugs introduced to the market in the last decade (2001-2011). *Chem. Rev.* **2014**, *114* (4), 2432–2506. DOI: 10.1021/cr4002879.

(7)   Zhang, C.; Yan, K.; Fu, C.; Peng, H.; Hawker, C. J.; Whittaker, A. K. Biological Utility of Fluorinated Compounds: From Materials Design to Molecular Imaging, Therapeutics and Environmental Remediation. *Chem. Rev.* **2022**, *122* (1), 167–208. DOI: 10.1021/acs.chemrev.1c00632.

(8)   Ogawa, Y.; Tokunaga, E.; Kobayashi, O.; Hirai, K.; Shibata, N. Current Contributions of Organofluorine Compounds to the Agrochemical Industry. *iScience* **2020**, *23* (9), 101467. DOI: 10.1016/j.isci.2020.101467.

(9)   Inoue, M.; Sumii, Y.; Shibata, N. Contribution of Organofluorine Compounds to Pharmaceuticals. *ACS Omega* **2020**, *5* (19), 10633–10640. DOI: 10.1021/acsomega.0c00830.

References

(10) Caron, S. Where Does the Fluorine Come From? A Review on the Challenges Associated with the Synthesis of Organofluorine Compounds. *Org. Process Res. Dev.* **2020**, *24* (4), 470–480. DOI: 10.1021/acs.oprd.0c00030.

(11) Deng, X.; Rong, J.; Wang, L.; Vasdev, N.; Zhang, L.; Josephson, L.; Liang, S. H. Chemistry for Positron Emission Tomography: Recent Advances in [11]C-, [18]F-, [13]N-, and ^{15}O-Labeling Reactions. *Angew. Chem. Int. Ed.* **2019**, *58* (9), 2580–2605. DOI: 10.1002/anie.201805501.

(12) Böhm, H. J.; Banner, D.; Bendels, S.; Kansy, M.; Kuhn, B.; Müller, K.; Obst-Sander, U.; Stahl, M. Fluorine in medicinal chemistry. *ChemBioChem* **2004**, *5* (5), 637–643. DOI: 10.1002/cbic.200301023.

(13) Bégué, J. P.; Bonnet-Delpon, D. Recent advances (1995-2005) in fluorinated pharmaceuticals based on natural products. *J. Fluor. Chem.* **2006**, *127* (8), 992–1012. DOI: 10.1016/j.jfluchem.2006.05.006.

(14) Purser, S.; Moore, P. R.; Swallow, S.; Gouverneur, V. Fluorine in medicinal chemistry. *Chem. Soc. Rev.* **2008**, *37* (2), 320–330. DOI: 10.1039/b610213c.

(15) Phelps, M. E. Positron emission tomography provides molecular imaging of biological processes. *Proc. Natl. Acad. Sci. U. S. A.* **2000**, *97* (16), 9226–9233. DOI: 10.1073/pnas.97.16.9226.

(16) Ametamey, S. M.; Honer, M.; Schubiger, P. A. Molecular imaging with PET. *Chem. Rev.* **2008**, *108* (5), 1501–1516. DOI: 10.1021/cr0782426.

(17) Wolfe, S. The Gauche Effect. Some Stereochemical Consequences of Adjacent Electron Pairs and Polar Bonds. *Acc. Chem. Res.* **1972**, *5* (3), 102–111. DOI: 10.1021/ar50051a003.

(18) Shah, P.; Westwell, A. D. The role of fluorine in medicinal chemistry. *J. Enzyme Inhib. Med. Chem.* **2007**, *22* (5), 527–540. DOI: 10.1080/14756360701425014.

(19) Gillis, E. P.; Eastman, K. J.; Hill, M. D.; Donnelly, D. J.; Meanwell, N. A. Applications of Fluorine in Medicinal Chemistry. *J. Med. Chem.* **2015**, *58* (21), 8315–8359. DOI: 10.1021/acs.jmedchem.5b00258.

(20) Meanwell, N. A. Fluorine and Fluorinated Motifs in the Design and Application of Bioisosteres for Drug Design. *J. Med. Chem.* **2018**, *61* (14), 5822–5880. DOI: 10.1021/acs.jmedchem.7b01788.

(21) Kirk, K. Selective Fluorination in Drug Design and Development: An Overview of Biochemical Rationales. *Curr. Top. Med. Chem.* **2006**, *6* (14), 1447–1456. DOI: 10.2174/156802606777951073.

(22) O'Hagan, D. Understanding organofluorine chemistry. An introduction to the C–F bond. *Chem. Soc. Rev.* **2008**, *37* (2), 308–319. DOI: 10.1039/b711844a.

(23) Richardson, P. Fluorination methods for drug discovery and development. *Expert Opin. Drug Discov.* **2016**, *11* (10), 983–999. DOI: 10.1080/17460441.2016.1223037.

(24) O'Hagan, D.; Deng, H. Enzymatic fluorination and biotechnological developments of the fluorinase. *Chem. Rev.* **2015**, *115* (2), 634–649. DOI: 10.1021/cr500209t.

(25) Odar, C.; Winkler, M.; Wiltschi, B. Fluoro amino acids: A rarity in nature, yet a prospect for protein engineering. *Biotechnol. J.* **2015**, *10* (3), 427–446. DOI: 10.1002/biot.201400587.

(26) Moschner, J.; Stulberg, V.; Fernandes, R.; Huhmann, S.; Leppkes, J.; Koksch, B. Approaches to Obtaining Fluorinated α-Amino Acids. *Chem. Rev.* **2019**, *119* (18), 10718–10801. DOI: 10.1021/acs.chemrev.9b00024.

(27) Ayyadurai, N.; Prabhu, N. S.; Deepankumar, K.; Kim, A.; Lee, S. G.; Yun, H. Biosynthetic substitution of tyrosine in green fluorescent protein with its surrogate fluorotyrosine in Escherichia coli. *Biotechnol. Lett.* **2011**, *33* (11), 2201–2207. DOI: 10.1007/s10529-011-0679-4.

(28) Baker, P. J.; Montclare, J. K. Enhanced Refoldability and Thermoactivity of Fluorinated Phosphotriesterase. *ChemBioChem* **2011**, *12* (12), 1845–1848. DOI: 10.1002/cbic.201100221.

(29) Steiner, T.; Hess, P.; Bae, J. H.; Wiltschi, B.; Moroder, L.; Budisa, N. Synthetic biology of proteins: Tuning GFPs folding and stability with fluoroproline. *PLoS One* **2008**, *3* (2), e1680. DOI: 10.1371/journal.pone.0001680.

(30) Acevedo-Rocha, C. G.; Hoesl, M. G.; Nehring, S.; Royter, M.; Wolschner, C.; Wiltschi, B.; Antranikian, G.; Budisa, N. Non-canonical amino acids as a useful synthetic biological tool for lipase-catalysed reactions in hostile environments. *Catal. Sci. Technol.* **2013**, *3* (5), 1198–1201. DOI: 10.1039/c3cy20712a.

(31) Deepankumar, K.; Nadarajan, S. P.; Ayyadurai, N.; Yun, H. Enhancing the biophysical properties of mRFP1 through incorporation of fluoroproline. *Biochem. Biophys. Res. Commun.* **2013**, *440* (4), 509–514. DOI: 10.1016/j.bbrc.2013.09.062.

(32) Dominguez Jr., M. A.; Thornton, K. C.; Melendez, M. G.; Dupureur, C. M. Differential effects of isomeric incorporation of fluorophenylalanines into PvuII endonuclease. *Proteins Struct. Funct. Genet.* **2001**, *45* (1), 55–61. DOI: 10.1002/prot.1123.

(33) Parsons, J. F.; Xiao, G.; Gilliland, G. L.; Armstrong, R. N. Enzymes harboring unnatural amino acids: Mechanistic and structural analysis of the enhanced catalytic activity of a glutathione transferase containing 5-flourotryptophan. *Biochemistry* **1998**, *37* (18), 6286–6294. DOI: 10.1021/bi980219e.

(34) Renner, C.; Alefelder, S.; Bae, J. H.; Budisa, N.; Huber, R.; Moroder, L. Fluoroprolines as tools for protein design and engineering. *Angew. Chem. Int. Ed.* **2001**, *40* (5), 923–925. DOI: 10.1002/1521-3773(20010302)40:5<923::aid-anie923>3.0.co;2-%23.

(35) Woll, M. G.; Hadley, E. B.; Mecozzi, S.; Gellman, S. H. Stabilizing and destabilizing effects of phenylalanine → F_5-phenylalanine mutations on the folding of a small protein. *J. Am. Chem. Soc.* **2006**, *128* (50), 15932–15933. DOI: 10.1021/ja0634573.

(36) Minnihan, E. C.; Young, D. D.; Schultz, P. G.; Stubbe, J. Incorporation of fluorotyrosines into ribonucleotide reductase using an evolved, polyspecific aminoacyl-tRNA synthetase. *J. Am. Chem. Soc.* **2011**, *133* (40), 15942–15945. DOI: 10.1021/ja207719f.

(37)   Wilkins, B. J.; Marionni, S.; Young, D. D.; Liu, J.; Wang, Y.; Di Salvo, M. L.; Deiters, A.; Cropp, T. A. Site-specific incorporation of fluorotyrosines into proteins in escherichia coli by photochemical disguise. *Biochemistry* **2010**, *49* (8), 1557–1559. DOI: 10.1021/bi100013s.

(38)   Pandey, A. K.; Naduthambi, D.; Thomas, K. M.; Zondlo, N. J. Proline editing: A general and practical approach to the synthesis of functionally and structurally diverse peptides. Analysis of steric versus stereoelectronic effects of 4-substituted prolines on conformation within peptides. *J. Am. Chem. Soc.* **2013**, *135* (11), 4333–4363. DOI: 10.1021/ja3109664.

(39)   Hoesl, M. G.; Budisa, N. Recent advances in genetic code engineering in Escherichia coli. *Curr. Opin. Biotechnol.* **2012**, *23* (5), 751–757. DOI: 10.1016/j.copbio.2011.12.027.

(40)   Jäckel, C.; Koksch, B. Fluorine in peptide design and protein engineering. *Eur. J. Org. Chem.* **2005**, No. 21, 4483–4503. DOI: 10.1002/ejoc.200500205.

(41)   Johnson, B. M.; Shu, Y. Z.; Zhuo, X.; Meanwell, N. A. Metabolic and Pharmaceutical Aspects of Fluorinated Compounds. *J. Med. Chem.* **2020**, *63* (12), 6315–6386. DOI: 10.1021/acs.jmedchem.9b01877.

(42)   Britton, R.; Gouverneur, V.; Lin, J.-H.; Meanwell, M.; Ni, C.; Pupo, G.; Xiao, J.-C.; Hu, J. Contemporary synthetic strategies in organofluorine chemistry. *Nat. Rev. Methods Primers* **2021**, *1*, 47. DOI: 10.1038/s43586-021-00042-1.

(43)   O'Hagan, D.; Schaffrath, C.; Cobb, S. L.; Hamilton, J. T. G.; Murphy, C. D. Biosynthesis of an organofluorine molecule: A fluorinase enzyme has been discovered that catalyses carbon-fluorine bond formation. *Nature* **2002**, *416* (6878), 279. DOI: 10.1038/416279a.

(44)   Kirk, K. L. Fluorination in medical chemistry: Methods, strategies, and recent development. *Org. Process Res. Dev.* **2008**, *12* (2), 305–321. DOI: 10.1021/op700134j.

(45)   Speight, J. G. *Environmental Inorganic Chemistry for Engineers*; Elsevier, 2017. DOI: 10.1016/c2013-0-16023-0.

(46)   Bertolini, J. C. Hydrofluoric acid: A review of toxicity. *J. Emerg. Med.* **1992**, *10* (2), 163–168. DOI: 10.1016/0736-4679(92)90211-B.

(47)   Tavener, S. J.; Clark, J. H. Can fluorine chemistry be green chemistry? *J. Fluor. Chem.* **2003**, *123* (1), 31–36. DOI: 10.1016/S0022-1139(03)00140-4.

(48)   Yang, L.; Dong, T.; Revankar, H. M.; Zhang, C. P. Recent progress on fluorination in aqueous media. *Green Chem.* **2017**, *19* (17), 3951–3992. DOI: 10.1039/c7gc01566f.

(49)   Harsanyi, A.; Sandford, G. Organofluorine chemistry: Applications, sources and sustainability. *Green Chem.* **2015**, *17* (4), 2081–2086. DOI: 10.1039/c4gc02166e.

(50)   Champagne, P. A.; Desroches, J.; Hamel, J. D.; Vandamme, M.; Paquin, J. F. Monofluorination of Organic Compounds: 10 Years of Innovation. *Chem. Rev.* **2015**, *115* (17), 9073–9174. DOI: 10.1021/cr500706a.

(51)   J.-A. Ma and D. Cahard (Ed.). *Emerging Fluorinated Motifs: Synthesis, Properties and Applications, 2 Volume Set*; Wiley, 2020.

(52)   Liang, S.; Hammond, G. B.; Xu, B. Hydrogen Bonding: Regulator for Nucleophilic Fluorination. *Chem. Eur. J.* **2017**, *23* (71), 17850–17861. DOI: 10.1002/chem.201702664.

(53)   Alonso, C.; Martínez De Marigorta, E.; Rubiales, G.; Palacios, F. Carbon trifluoromethylation reactions of hydrocarbon derivatives and heteroarenes. *Chem. Rev.* **2015**, *115* (4), 1847–1935. DOI: 10.1021/cr500368h.

(54)   Jia, H.; Häring, A. P.; Berger, F.; Zhang, L.; Ritter, T. Trifluoromethyl Thianthrenium Triflate: A Readily Available Trifluoromethylating Reagent with Formal CF$_3^+$, CF$_3$•, and CF$_3^-$ Reactivity. *J. Am. Chem. Soc.* **2021**, *143* (20), 7623–7628. DOI: 10.1021/jacs.1c02606.

(55)   Langlois, B. R.; Billard, T.; Roussel, S. Nucleophilic trifluoromethylation: Some recent reagents and their stereoselective aspects. *J. Fluor. Chem.* **2005**, *126* (2), 173–179. DOI: 10.1016/j.jfluchem.2004.11.007.

(56)   Barata-Vallejo, S.; Lantano, B.; Postigo, A. Recent advances in trifluoromethylation reactions with electrophilic trifluoromethylating reagents. *Chem. Eur. J.* **2014**, *20* (51), 16806–16829. DOI: 10.1002/chem.201404005.

(57)   Hu, J.; Zhang, W.; Wang, F. Selective difluoromethylation and monofluoromethylation reactions. *Chem. Commun.* **2009**, No. 48, 7465–7478. DOI: 10.1039/b916463d.

(58)   Olah, G. A.; Welch, J. T.; Vankar, Y. D.; Nojima, M.; Kerekes, I.; Olah, J. A. Synthetic Methods and Reactions. 63. Pyridinium Poly(hydrogen fluoride)(30% Pyridine-70% Hydrogen Fluoride): A Convenient Reagent for Organic Fluorination Reactions. *J. Org. Chem.* **1979**, *44* (22), 3872–3881. DOI: 10.1021/jo01336a027.

(59)   Haufe, G. Triethylamine trishydrofluoride in synthesis. *J. für Prakt. Chemie - Chem. - Zeitung* **1996**, *338* (2), 99–113. DOI: 10.1002/prac.19963380122.

(60)   Okoromoba, O. E.; Han, J.; Hammond, G. B.; Xu, B. Designer HF-Based fluorination reagent: Highly regioselective synthesis of fluoroalkenes and gem-difluoromethylene compounds from alkynes. *J. Am. Chem. Soc.* **2014**, *136* (41), 14381–14384. DOI: 10.1021/ja508369z.

(61)   Hu, W. L.; Hu, X. G.; Hunter, L. Recent Developments in the Deoxyfluorination of Alcohols and Phenols: New Reagents, Mechanistic Insights, and Applications. *Synthesis* **2017**, *49* (22), 4917–4930. DOI: 10.1055/s-0036-1590881.

(62)   Phillip Cox, D.; Terpinski, J.; Lawrynowicz, W. "Anhydrous" tetrabutylammonium fluoride: A mild but highly efficient source of nucleophilic fluoride ion. *J. Org. Chem.* **1984**, *49* (17), 3216–3219. DOI: 10.1021/jo00191a035.

(63)   Said, M. S.; Khonde, N. S.; Thorat, M. N.; Atapalkar, R. S.; Kulkarni, A. A.; Gajbhiye, J.; Dastager, S. G. A New TBAF Complex, Highly Stable, Facile and Selective Source for Nucleophilic Fluorination: Applications in Batch and Flow Chemistry. *Asian J. Org. Chem.* **2020**, *9* (7), 1022–1026. DOI: 10.1002/ajoc.202000235.

(64)   Kim, D. W.; Jeong, H. J.; Lim, S. T.; Sohn, M. H. Tetrabutylammonium tetra(tert-butyl alcohol)-coordinated fluoride as a facile fluoride source. *Angew. Chem. Int. Ed.* **2008**, *47* (44), 8404–8406. DOI: 10.1002/anie.200803150.

(65)   Engle, K. M.; Pfeifer, L.; Pidgeon, G. W.; Giuffredi, G. T.; Thompson, A. L.; Paton, R. S.; Brown, J. M.; Gouverneur,

References

V. Coordination diversity in hydrogen-bonded homoleptic fluoride-alcohol complexes modulates reactivity. *Chem. Sci.* **2015**, *6* (9), 5293–5302. DOI: 10.1039/c5sc01812a.

(66) Rozatian, N.; Hodgson, D. R. W. Reactivities of electrophilic N–F fluorinating reagents. *Chem. Commun.* **2021**, *57* (6), 683–712. DOI: 10.1039/d0cc06339h.

(67) Watson, D. A.; Su, M.; Teverovskiy, G.; Zhang, Y.; Garcia-Fortanet, J.; Kinzel, T.; Buchwaldf, S. L. Formation of ArF from LPdAr(F): catalytic conversion of aryl triflates to aryl fluorides. *Science* **2009**, *325* (5948), 1661–1664. DOI: 10.1126/science.1178239.

(68) Hull, K. L.; Anani, W. Q.; Sanford, M. S. Palladium-catalyzed fluorination of carbon-hydrogen bonds. *J. Am. Chem. Soc.* **2006**, *128* (22), 7134–7135. DOI: 10.1021/ja061943k.

(69) Casitas, A.; Canta, M.; Solà, M.; Costas, M.; Ribas, X. Nucleophilic aryl fluorination and aryl halide exchange mediated by a Cu^I/Cu^{III} catalytic cycle. *J. Am. Chem. Soc.* **2011**, *133* (48), 19386–19392. DOI: 10.1021/ja2058567.

(70) Truong, T.; Klimovica, K.; Daugulis, O. Copper-catalyzed, directing group-assisted fluorination of arene and heteroarene C-H bonds. *J. Am. Chem. Soc.* **2013**, *135* (25), 9342–9345. DOI: 10.1021/ja4047125.

(71) Rueda-Becerril, M.; Mahé, O.; Drouin, M.; Majewski, M. B.; West, J. G.; Wolf, M. O.; Sammis, G. M.; Paquin, J. F. Direct C-F bond formation using photoredox catalysis. *J. Am. Chem. Soc.* **2014**, *136* (6), 2637–2641. DOI: 10.1021/ja412083f.

(72) Ventre, S.; Petronijevic, F. R.; MacMillan, D. W. C. Decarboxylative fluorination of aliphatic carboxylic acids via photoredox catalysis. *J. Am. Chem. Soc.* **2015**, *137* (17), 5654–5657. DOI: 10.1021/jacs.5b02244.

(73) Yang, X.; Wu, T.; Phipps, R. J.; Toste, F. D. Advances in catalytic enantioselective fluorination, mono-, di-, and trifluoromethylation, and trifluoromethylthiolation reactions. *Chem. Rev.* **2015**, *115* (2), 826–870. DOI: 10.1021/cr500277b.

(74) Beeson, T. D.; MacMillan, D. W. C. Enantioselective organocatalytic α-fluorination of aldehydes. *J. Am. Chem. Soc.* **2005**, *127* (24), 8826–8828. DOI: 10.1021/ja051805f.

(75) Wang, X.; Lan, Q.; Shirakawa, S.; Maruoka, K. Chiral bifunctional phase transfer catalysts for asymmetric fluorination of β-keto esters. *Chem. Commun.* **2010**, *46* (2), 321–323. DOI: 10.1039/b920099a.

(76) Rauniyar, V.; Lackner, A. D.; Hamilton, G. L.; Toste, F. D. Asymmetric electrophilic fluorination using an anionic chiral phase-transfer catalyst. *Science* **2011**, *334* (6063), 1681–1684. DOI: 10.1126/science.1213918.

(77) Pupo, G.; Ibba, F.; Ascough, D. M. H.; Vicini, A. C.; Ricci, P.; Christensen, K. E.; Pfeifer, L.; Morphy, J. R.; Brown, J. M.; Paton, R. S.; Gouverneur, V. Asymmetric nucleophilic fluorination under hydrogen bonding phase-transfer catalysis. *Science* **2018**, *360* (6389), 638–642. DOI: 10.1126/science.aar7941.

(78) Pupo, G.; Vicini, A. C.; Ascough, D. M. H.; Ibba, F.; Christensen, K. E.; Thompson, A. L.; Brown, J. M.; Paton, R. S.; Gouverneur, V. Hydrogen Bonding Phase-Transfer Catalysis with Potassium Fluoride: Enantioselective Synthesis of β-Fluoroamines. *J. Am. Chem. Soc.* **2019**, *141* (7), 2878–2883. DOI: 10.1021/jacs.8b12568.

(79) Roagna, G.; Ascough, D. M. H.; Ibba, F.; Vicini, A. C.; Fontana, A.; Christensen, K. E.; Peschiulli, A.; Oehlrich, D.; Misale, A.; Trabanco, A. A.; Paton, R. S.; Pupo, G.; Gouverneur, V. Hydrogen Bonding Phase-Transfer Catalysis with Ionic Reactants: Enantioselective Synthesis of γ-Fluoroamines. *J. Am. Chem. Soc.* **2020**, *142* (33), 14045–14051. DOI: 10.1021/jacs.0c05131.

(80) Szpera, R.; Moseley, D. F. J.; Smith, L. B.; Sterling, A. J.; Gouverneur, V. The Fluorination of C−H Bonds: Developments and Perspectives. *Angew. Chem. Int. Ed.* **2019**, *58* (42), 14824–14848. DOI: 10.1002/anie.201814457.

(81) Neumann, C. N.; Ritter, T. Late-stage fluorination: Fancy novelty or useful tool? *Angew. Chem. Int. Ed.* **2015**, *54* (11), 3216–3221. DOI: 10.1002/anie.201410288.

(82) McMurtrey, K. B.; Racowski, J. M.; Sanford, M. S. Pd-catalyzed C-H fluorination with nucleophilic fluoride. *Org. Lett.* **2012**, *14* (16), 4094–4097. DOI: 10.1021/ol301739f.

(83) Abundance of Elements in the Earth's Crust and in the Sea. In *CRC Handbook of Chemistry and Physics, 97th Edition*; 2016; p 14.

(84) Carvalho, M. F.; Oliveira, R. S. Natural production of fluorinated compounds and biotechnological prospects of the fluorinase enzyme. *Critical Reviews in Biotechnology*. 2017, pp 880–897. DOI: 10.1080/07388551.2016.1267109.

(85) Harper, D. B.; O'Hagan, D. The Fluorinated Natural Products. *Nat. Prod. Rep.* **1994**, *11*, 123–133. DOI: 10.1039/np9941100123.

(86) Vaillancourt, F. H.; Yeh, E.; Vosburg, D. A.; Garneau-Tsodikova, S.; Walsh, C. T. Nature's inventory of halogenation catalysts: Oxidative strategies predominate. *Chem. Rev.* **2006**, *106* (8), 3364–3378. DOI: 10.1021/cr050313i.

(87) Zechel, D. L.; Reid, S. P.; Nashiru, O.; Mayer, C.; Stoll, D.; Jakeman, D. L.; Warren, R. A. J.; Withers, S. G. Enzymatic synthesis of carbon-fluorine bonds. *J. Am. Chem. Soc.* **2001**, *123* (18), 4350–4351. DOI: 10.1021/ja005855q.

(88) Schmedt Auf Der Günne, J.; Mangstl, M.; Kraus, F. Occurrence of difluorine F_2 in nature - In situ proof and quantification by NMR spectroscopy. *Angew. Chem. Int. Ed.* **2012**, *51* (31), 7847–7849. DOI: 10.1002/anie.201203515.

(89) Cheng, X.; Ma, L. Enzymatic synthesis of fluorinated compounds. *Appl. Microbiol. Biotechnol.* **2021**, *105* (21–22), 8033–8058. DOI: 10.1007/s00253-021-11608-0.

(90) O'Hagan, D.; Harper, D. B. Fluorine-containing natural products. *J. Fluor. Chem.* **1999**, *100* (1–2), 127–133. DOI: 10.1016/S0022-1139(99)00201-8.

(91) Dong, C.; Huang, F.; Deng, H.; Schaffrath, C.; Spencer, J. B.; O'Hagan, D.; Naismith, J. H. Crystal structure and mechanism of a bacterial fluorinating enzyme. *Nature* **2004**, *427* (6974), 561–565. DOI: 10.1038/nature02280.

(92) Cadicamo, C. D.; Courtieu, J.; Deng, H.; Meddour, A.; O'Hagan, D. Enzymatic fluorination in Streptomyces cattleya takes place with an inversion of configuration consistent with an SN2 reaction mechanism. *ChemBioChem* **2004**, *5* (5),

685–690. DOI: 10.1002/cbic.200300839.

(93)   Proudfoot, A. T.; Bradberry, S. M.; Vale, J. A. Sodium fluoroacetate poisoning. *Toxicol. Rev.* **2006**, *25* (4), 213–219. DOI: 10.2165/00139709-200625040-00002.

(94)   Peters, R. A. Croonian Lecture - Lethal synthesis. *Proc. R. Soc. London. Ser. B - Biol. Sci.* **1952**, *139* (895), 143–170. DOI: 10.1098/rspb.1952.0001.

(95)   Moss, S. J.; Murphy, C. D.; Hamilton, J. T. G.; McRobert, W. C.; O'Hagan, D.; Schaffrath, C.; Harper, D. B. Fluoroacetaldehyde: A precursor of both fluoroacetate and 4-fluorothreonine in Streptomyces cattleya. *Chem. Commun.* **2000**, No. 22, 2281–2282. DOI: 10.1039/b007261n.

(96)   Ma, L.; Bartholome, A.; Tong, M. H.; Qin, Z.; Yu, Y.; Shepherd, T.; Kyeremeh, K.; Deng, H.; O'Hagan, D. Identification of a fluorometabolite from Streptomyces sp. MA37: (2R,3S,4S)-5-fluoro-2,3,4-trihydroxypentanoic acid. *Chem. Sci.* **2015**, *6* (2), 1414–1419. DOI: 10.1039/c4sc03540b.

(97)   Bartholomé, A.; Janso, J. E.; Reilly, U.; O'Hagan, D. Fluorometabolite biosynthesis: isotopically labelled glycerol incorporations into the antibiotic nucleocidin in Streptomyces calvus. *Org. Biomol. Chem.* **2017**, *15* (1), 61–64. DOI: 10.1039/c6ob02291j.

(98)   Harper, D. B.; Hamilton, J. T. G.; O' Hagan, D. Identification of threo-18-fluoro-9,10-dihydroxystearic acid: a novel ω-fluorinated fatty acid from Dichapetalum toxicarium seeds. *Tetrahedron Lett.* **1990**, *31* (52), 7661–7662. DOI: 10.1016/S0040-4039(00)97325-8.

(99)   Hamilton, J. T. G.; Harper, D. B. Fluoro fatty acids in seed oil of Dichapetalum toxicarium. *Phytochemistry* **1997**, *44* (6), 1129–1132. DOI: 10.1016/S0031-9422(96)00697-8.

(100)   Christie, W. W.; Hamilton, J. T. G.; Harper, D. B. Mass spectrometry of fluorinated fatty acids in the seed oil of Dichapetalum toxicarium. *Chem. Phys. Lipids* **1998**, *97* (1), 41–47. DOI: 10.1016/S0009-3084(98)00090-5.

(101)   Murphy, C. D.; O'Hagan, D.; Schaffrath, C. Identification of a PLP-dependent threonine transaldolase: A novel enzyme involved in 4-fluorothreonine biosynthesis in Streptomyces cattleya. *Angew. Chem. Int. Ed.* **2001**, *40* (23), 4479–4481. DOI: 10.1002/1521-3773(20011203)40:23<4479::AID-ANIE4479>3.0.CO;2-1.

(102)   Sanada, M.; Miyano, T.; Iwadare, S.; Williamson, J. M.; Arison, B. H.; Smith, J. L.; Douglas, A. W.; Liesch, J. M.; Inamine, E. Biosynthesis of fluorothreonine and fluoroacetic acid by the thienamycin producer, streptomyces cattleya. *J. Antibiot. (Tokyo).* **1986**, *39* (2), 259–265. DOI: 10.7164/antibiotics.39.259.

(103)   Wu, L.; Deng, H. Defluorination of 4-fluorothreonine by threonine deaminase. *Org. Biomol. Chem.* **2020**, *18* (32), 6236–6240. DOI: 10.1039/d0ob01358g.

(104)   Potenti, S.; Spada, L.; Fusè, M.; Mancini, G.; Gualandi, A.; Leonardi, C.; Cozzi, P. G.; Puzzarini, C.; Barone, V. 4-Fluoro-Threonine: From Diastereoselective Synthesis to pH-Dependent Conformational Equilibrium in Aqueous Solution. *ACS Omega* **2021**, *6* (20), 13170–13181. DOI: 10.1021/acsomega.1c01007.

(105)   Scolastico, C.; Conca, E.; Prati, L.; Guanti, G.; Banfi, L.; Berti, A.; Farina, P.; Valcavi, U. Diastereo- And Enantioselective Synthesis of Fluorinated Threonines. *Synthesis* **1985**, *1985* (9), 850–855. DOI: 10.1055/s-1985-31363.

(106)   Shimizu, M.; Yokota, T.; Fujimori, K.; Fujisawa, T. Stereodivergent synthesis of fluorinated threonine derivatives in high optical purity. *Tetrahedron: Asymmetry* **1993**, *4* (5), 835–838. DOI: 10.1016/S0957-4166(00)80121-4.

(107)   Amin, M. R.; Harper, D. B.; Moloney, J. M.; Murphy, C. D.; Howard, J. A. K.; O'Hagan, D. A short highly stereoselective synthesis of the fluorinated natural product (2S,3S)-4-fluorothreonine. *Chem. Commun.* **1997**, No. 15, 1471–1472. DOI: 10.1039/a703121a.

(108)   Steinreiber, J.; Fesko, K.; Mayer, C.; Reisinger, C.; Schürmann, M.; Griengl, H. Synthesis of γ-halogenated and long-chain β-hydroxy-α-amino acids and 2-amino-1,3-diols using threonine aldolases. *Tetrahedron* **2007**, *63* (34), 8088–8093. DOI: 10.1016/j.tet.2007.06.013.

(109)   Graham, T. J. A.; Lambert, R. F.; Ploessl, K.; Kung, H. F.; Doyle, A. G. Enantioselective radiosynthesis of positron emission tomography (PET) tracers containing [18F]fluorohydrins. *J. Am. Chem. Soc.* **2014**, *136* (14), 5291–5294. DOI: 10.1021/ja5025645.

(110)   Kalow, J. A.; Doyle, A. G. Mechanistic investigations of cooperative catalysis in the enantioselective fluorination of epoxides. *J. Am. Chem. Soc.* **2011**, *133* (40), 16001–16012. DOI: 10.1021/ja207256s.

(111)   Halperin, S. D.; Kwon, D.; Holmes, M.; Regalado, E. L.; Campeau, L. C.; Dirocco, D. A.; Britton, R. Development of a Direct Photocatalytic C-H Fluorination for the Preparative Synthesis of Odanacatib. *Org. Lett.* **2015**, *17* (21), 5200–5203. DOI: 10.1021/acs.orglett.5b02532.

(112)   Halperin, S. D.; Fan, H.; Chang, S.; Martin, R. E.; Britton, R. A Convenient Photocatalytic Fluorination of Unactivated C-H Bonds. *Angew. Chemie* **2014**, *126* (18), 4778–4781. DOI: 10.1002/ange.201400420.

(113)   Griesbeck, A. G.; Mauder, H.; Müller, I. Photochemistry of N-Phthaloyl α-Amino Acid Esters: A New Approach to β,γ-Unsaturated α-Amino Acid, Dihydrobenzazepinedione, and Pyrrolizidinone Derivatives. *Chem. Ber.* **1992**, *125* (11), 2467–2475. DOI: 10.1002/cber.19921251119.

(114)   Egami, H.; Masuda, S.; Kawato, Y.; Hamashima, Y. Photofluorination of Aliphatic C-H Bonds Promoted by the Phthalimide Group. *Org. Lett.* **2018**, *20* (5), 1367–1370. DOI: 10.1021/acs.orglett.8b00133.

(115)   Liu, W.; Huang, X.; Placzek, M. S.; Krska, S. W.; McQuade, P.; Hooker, J. M.; Groves, J. T. Site-selective ^{18}F fluorination of unactivated C-H bonds mediated by a manganese porphyrin. *Chem. Sci.* **2018**, *9* (5), 1168–1172. DOI: 10.1039/c7sc04545j.

(116)   Shin, A. P.; Choong, H. L.; Chung, K. H. Epoxide opening with tetrabutylammonium fluoride (TBAF). *Bull. Korean Chem. Soc.* **2007**, *28* (10), 1834–1836. DOI: 10.5012/bkcs.2007.28.10.1834.

(117)   Shaw, K. J.; Luly, J. R.; Rapoport, H. Routes to Mitomycins. Chirospecific Synthesis of Aziridinomitosenes. *J. Org.*

Chem. **1985**, *50* (23), 4515–4523. DOI: 10.1021/jo00223a019.

(118) Kim, D. W.; Jeong, H. J.; Lim, S. T.; Sohn, M. H. Facile nucleophilic fluorination of primary alkyl halides using tetrabutylammonium fluoride in a tert-alcohol medium. *Tetrahedron Lett.* **2010**, *51* (2), 432–434. DOI: 10.1016/j.tetlet.2009.11.058.

(119) Cresswell, A. J.; Davies, S. G.; Lee, J. A.; Morris, M. J.; Roberts, P. M.; Thomson, J. E. Ring-opening hydrofluorination of 2,3- and 3,4-epoxy amines by HBF₄·OEt₂: Application to the asymmetric synthesis of (S,S)-3-deoxy-3-fluorosafingol. *J. Org. Chem.* **2011**, *76* (11), 4617–4627. DOI: 10.1021/jo200517w.

(120) Meffre, P.; Vo-Quang, L.; Vo-Quang, Y.; Le Goffic, F. Unusual α-aminoacids from vinylglycine. *Tetrahedron Lett.* **1990**, *31* (16), 2291–2294. DOI: 10.1016/0040-4039(90)80209-5.

(121) Liu, Y. J.; Chu, T. yi; Engel, R. A synthetically useful regioselective epoxide ring-opening procedure. *Synth. Commun.* **1992**, *22* (16), 2367–2371. DOI: 10.1080/00397919208019093.

(122) Chen, J.; Lin, J. H.; Xiao, J. C. Halogenation through Deoxygenation of Alcohols and Aldehydes. *Org. Lett.* **2018**, *20* (10), 3061–3064. DOI: 10.1021/acs.orglett.8b01058.

(123) Dondoni, A.; Perrone, D. Synthesis of 1,1-Dimethylethyl (S)-4-Formyl-2,2-Dimethyl-3-Oxazolidinecarboxylate by Oxidation of the Alcohol. *Org. Synth.* **2003**, *77*, 64. DOI: 10.1002/0471264180.os077.07.

(124) Passiniemi, M.; Koskinen, A. M. P. Garner's aldehyde as a versatile intermediate in the synthesis of enantiopure natural products. *Beilstein J. Org. Chem.* **2013**, *9*, 2641–2659. DOI: 10.3762/bjoc.9.300.

(125) Parisi, G.; Colella, M.; Monticelli, S.; Romanazzi, G.; Holzer, W.; Langer, T.; Degennaro, L.; Pace, V.; Luisi, R. Exploiting a "beast" in carbenoid chemistry: Development of a straightforward direct nucleophilic fluoromethylation strategy. *J. Am. Chem. Soc.* **2017**, *139* (39), 13648–13651. DOI: 10.1021/jacs.7b07891.

(126) Lesarri, A.; Mata, S.; López, J. C.; Alonso, J. L. A laser-ablation molecular-beam Fourier-transform microwave spectrometer: The rotational spectrum of organic solids. *Rev. Sci. Instrum.* **2003**, *74* (11), 4799–4804. DOI: 10.1063/1.1611611.

(127) Ito, Y.; Sawamura, M.; Hayashi, T. Catalytic Asymmetric Aldol Reaction: Reaction of Aldehydes with Isocyanoacetate Catalyzed by a Chiral Ferrocenylphosphine-Gold(I) Complex. *J. Am. Chem. Soc.* **1986**, *108* (20), 6405–6406. DOI: 10.1021/ja00280a056.

(128) Hayashi, T.; Uozumi, Y.; Yamazaki, A.; Sawamura, M.; Hamashima, H.; Ito, Y. Silver(I)-catalyzed asymmetric aldol reaction of isocyanoacetate. *Tetrahedron Lett.* **1991**, *32* (24), 2799–2802. DOI: 10.1016/0040-4039(91)85090-R.

(129) Sladojevich, F.; Trabocchi, A.; Guarna, A.; Dixon, D. J. A new family of cinchona-derived amino phosphine precatalysts: Application to the highly enantio- and diastereoselective silver-catalyzed isocyanoacetate aldol reaction. *J. Am. Chem. Soc.* **2011**, *133* (6), 1710–1713. DOI: 10.1021/ja110534g.

(130) De La Campa, R.; Ortín, I.; Dixon, D. J. Direct catalytic enantio- and diastereoselective ketone aldol reactions of isocyanoacetates. *Angew. Chem. Int. Ed.* **2015**, *54* (16), 4895–4898. DOI: 10.1002/anie.201411852.

(131) Martínez-Pardo, P.; Blay, G.; Muñoz, M. C.; Pedro, J. R.; Sanz-Marco, A.; Vila, C. Enantioselective synthesis of chiral oxazolines from unactivated ketones and isocyanoacetate esters by synergistic silver/organocatalysis. *Chem. Commun.* **2018**, *54* (23), 2862–2865. DOI: 10.1039/c8cc00856f.

(132) Martínez-Pardo, P.; Blay, G.; Vila, C.; Sanz-Marco, A.; Muñoz, M. C.; Pedro, J. R. Enantioselective Synthesis of 5-Trifluoromethyl-2-oxazolines under Dual Silver/Organocatalysis. *J. Org. Chem.* **2019**, *84* (1), 314–325. DOI: 10.1021/acs.joc.8b02808.

(133) Gorla, F.; Togni, A.; Venanzi, L. M.; Albinati, A.; Lianza, F. Synthesis of an Optically Active Platinum(II) Complex Containing a New Terdentate P-C-P Ligand and Its Catalytic Activity in the Asymmetric Aldol Reaction of Methyl Isocyanoacetate. X-ray Crystal Structure of [2,6-Bis[(1'S,2'S)-1'-(diphenylphosphino)-2',3. *Organometallics* **1994**, *13* (5), 1607–1616. DOI: 10.1021/om00017a018.

(134) Longmire, J. M.; Zhang, X.; Shang, M. Synthesis and X-ray crystal structures of palladium(II) and platinum(II) complexes of the PCP-type chiral tridentate ligand (1R,1'R)-1,3-bis[1-(diphenylphosphino)ethyl]benzene. Use in the asymmetric aldol reaction of methyl isocyanoacetate and aldehydes. *Organometallics* **1998**, *17* (20), 4374–4379. DOI: 10.1021/om980461h.

(135) Yoon, M.-S.; Ryu, D.-W.; Kim, J.-R.; Ramesh, R.; Ahn, K.-H. Cyclometalated platinum(II) complexes derived from a chiral pyridine ligand: Synthesis, structure, and catalytic activity. *Bull. Korean Chem. Soc.* **2007**, *28* (11), 2045–2050. DOI: 10.5012/bkcs.2007.28.11.2045.

(136) Gosiewska, S.; Veld, M. H. in t.; de Pater, J. J. M.; Bruijnincx, P. C. A.; Lutz, M.; Spek, A. L.; van Koten, G.; Klein Gebbink, R. J. M. Novel enantiopure non-C₂-symmetric NCN-pincer palladium complexes with L-proline chiral auxiliaries: mer η³-N,C,N versus square planar η⁴-N,C,N,O coordination. *Tetrahedron Asymmetry* **2006**, *17* (4), 674–686. DOI: 10.1016/j.tetasy.2005.12.040.

(137) Kim, H. Y.; Shih, H. J.; Knabe, W. E.; Oh, K. Reversal of enantioselectivity between the copper(I)- and silver(I)-catalyzed 1,3-dipolar cycloaddition reactions using a brucine-derived amino alcohol ligand. *Angew. Chem. Int. Ed.* **2009**, *48* (40), 7420–7423. DOI: 10.1002/anie.200903479.

(138) Kim, H. Y.; Oh, K. Highly diastereo- and enantioselective aldol reaction of methyl α-isocyanoacetate: A cooperative catalysis approach. *Org. Lett.* **2011**, *13* (6), 1306–1309. DOI: 10.1021/ol103104y.

(139) Xue, M. X.; Guo, C.; Gong, L. Z. Asymmetric synthesis of chiral oxazolines by organocatalytic cyclization of α-aryl isocyanoesters with aldehydes. *Synlett* **2009**, No. 13, 2191–2197. DOI: 10.1055/s-0029-1217549.

(140) Zhao, M. X.; Zhou, H.; Tang, W. H.; Qu, W. S.; Shi, M. Cinchona alkaloid-derived thiourea-catalyzed diastereo- and enantioselective [3+2] cycloaddition reaction of isocyanoacetates to isatins: A facile access to optically active

spirooxindole oxazolines. *Adv. Synth. Catal.* **2013**, *355* (7), 1277–1283. DOI: 10.1002/adsc.201300077.

(141) Wang, F.; Chen, J.; Huang, Y. Synthesis of Optically Active Oxazolines by an Organocatalytic Isocyanoacetate Aldol Reaction with α-Keto Esters. *Synlett* **2017**, *28* (11), 1300–1304. DOI: 10.1055/s-0036-1588718.

(142) Ozaki, Y.; Matsumoto, K.; Miyoshi, M. A useful synthetic method of DL-threonine using α-isocyanoacetamides. *Agric. Biol. Chem.* **1978**, *42* (8), 1565–1569. DOI: 10.1080/00021369.1978.10863205.

(143) Saegusa, T.; Ito, Y.; Kixoshita, H.; Tomita, S. Synthetic Reactions by Complex Catalysts. XIX. Copper-Catalyzed Cycloaddition Reactions of Isocyanides. Novel Synthesis of Δ¹-Pyrroline and Δ²-Oxazoline. *J. Org. Chem.* **1971**, *36* (22), 3316–3323. DOI: 10.1021/jo00821a011.

(144) Aouadi, K.; Lajoix, A. D.; Gross, R.; Praly, J. P. Multi-step synthesis and biological evaluation of analogues of insulin secretagogue (2S,3R,4S)-4-hydroxyisoleucine. *Eur. J. Org. Chem.* **2009**, No. 1, 61–71. DOI: 10.1002/ejoc.200800744.

(145) Benito-Garagorri, D.; Bocokić, V.; Kirchner, K. Copper(I)-catalyzed diastereoselective formation of oxazolines and N-sulfonyl-2-imidazolines. *Tetrahedron Lett.* **2006**, *47* (49), 8641–8644. DOI: 10.1016/j.tetlet.2006.10.040.

(146) Schöllkopf, U.; Hartwig, W.; Pospischil, K. H.; Kehne, H. Asymmetric Synthesis via Heterocyclic Intermediates; VII. Enantioselective Synthesis of (R)-α-Amino Acids using (S)-O,O-Dimethyl-α-methyldopa as Chiral Auxiliary Reagent. *Synthesis* **1981**, *1981* (12), 966–969. DOI: 10.1055/s-1981-29661.

(147) Schöllkopf, U.; Groth, U.; Gull, M. -R; Nozulak, J. Asymmetrische Synthesen über heterocyclische Zwischenstufen, XVIII. Zur enantioselektiven Synthese von (2R)-Serin-methylestern oder (2R)-Serinen ausgehend vom Bislactimether von cyclo-(-L-Val-Gly-). *Liebigs Ann. der Chemie* **1983**, *1983* (7), 1133–1151. DOI: 10.1002/jlac.198319830706.

(148) Ito, Y.; Sawamura, M.; Kobayashi, M.; Hayashi, T. Asymmetric aldol reaction of α-isocyanoacetamides with aldehydes catalyzed by a chiral ferrocenylphosphine-gold(I) complex. *Tetrahedron Lett.* **1988**, *29* (48), 6321–6324. DOI: 10.1016/S0040-4039(00)82336-9.

(149) Hansen, P. R.; Oddo, A. Fmoc solid-phase peptide synthesis. In *Methods in Molecular Biology*; 2015; Vol. 1348, pp 33–50. DOI: 10.1007/978-1-4939-2999-3_5.

(150) Oae, S. Sulfoxides and Sulfilimines. In *Organic Chemistry of Sulfur*; 1977; pp 383–471. DOI: 10.1007/978-1-4684-2049-4_8.

(151) Afzali-Ardakani, A.; Rapoport, H. L-Vinylglycine. *J. Org. Chem.* **1980**, *45* (24), 4817–4820. DOI: 10.1021/jo01312a002.

(152) Meffre, P.; Goffic, F. Le; Vo-Quang, L.; Vo-Quang, Y. N-(Benzyloxycarbonyl)-L-Vinylglycine Methyl Ester from L-Methionine Methyl Ester Hydrochloride. *Synth. Commun.* **1989**, *19* (20), 3457–3468. DOI: 10.1080/00397918908052755.

(153) Patel, S. K.; Long, T. E. Preparation of vinylglycines by thermolysis of homocysteine sulfoxides. *Tetrahedron Lett.* **2009**, *50* (36), 5067–5070. DOI: 10.1016/j.tetlet.2009.06.082.

(154) St-Cyr, D. J.; Jamieson, A. G.; Lubell, W. D. α-Amino-β-hydroxy-γ-lactam for constraining peptide Ser and Tnr residue conformation. *Org. Lett.* **2010**, *12* (8), 1652–1655. DOI: 10.1021/ol1000582.

(155) Kolesnichenko, I. V.; Goloverda, G. Z.; Kolesnichenko, V. L. A Versatile Method of Ambient-Temperature Solvent Removal. *Org. Process Res. Dev.* **2020**, *24* (1), 25–31. DOI: 10.1021/acs.oprd.9b00368.

(156) Sicherl, F.; Cupido, T.; Albericio, F. A novel dipeptidomimetic containing a cyclic threonine. *Chem. Commun.* **2010**, *46* (8), 1266–1268. DOI: 10.1039/b915220b.

(157) Wuts, P. G. M. Protection for the Amino Group. In *Greene's Protective Groups in Organic Synthesis*; Wiley, 2014; pp 895–1193. DOI: 10.1002/9781118905074.ch07.

(158) Dobrowolski, J. C.; Lipinski, P. J. F.; Rode, J. E.; Sadlej, J. α-Amino acids in water: A review of VCD and ROA spectra. In *Optical Spectroscopy and Computational Methods in Biology and Medicine. Challenges and Advances in Computational Chemistry and Physics*; Baranska, M., Ed.; Springer: Dordrecht, 2014; Vol. 14, pp 83–160. DOI: 10.1007/978-94-007-7832-0_5.

(159) Quesada-Moreno, M. M.; Márquez-García, A. Á.; Avilés-Moreno, J. R.; López-González, J. J. Conformational landscape of L-threonine in neutral, acid and basic solutions from vibrational circular dichroism spectroscopy and quantum chemical calculations. *Tetrahedron: Asymmetry* **2013**, *24* (24), 1537–1547. DOI: 10.1016/j.tetasy.2013.09.025.

(160) Mancini, G.; Fusè, M.; Lazzari, F.; Chandramouli, B.; Barone, V. Unsupervised search of low-lying conformers with spectroscopic accuracy: A two-step algorithm rooted into the island model evolutionary algorithm. *J. Chem. Phys.* **2020**, *153* (12), 124110. DOI: 10.1063/5.0018314.

(161) Chandramouli, B.; Del Galdo, S.; Fusè, M.; Barone, V.; Mancini, G. Two-level stochastic search of low-energy conformers for molecular spectroscopy: Implementation and validation of MM and QM models. *Phys. Chem. Chem. Phys.* **2019**, *21* (36), 19921–19934. DOI: 10.1039/c9cp03557e.

(162) Xu, S.; Nilles, J. M.; Bowen, K. H. Zwitterion formation in hydrated amino acid, dipole bound anions: How many water molecules are required? *J. Chem. Phys.* **2003**, *119* (20), 10696–10701. DOI: 10.1063/1.1620501.

(163) Ekimova, M.; Quevedo, W.; Szyc, Ł.; Iannuzzi, M.; Wernet, P.; Odelius, M.; Nibbering, E. T. J. Aqueous Solvation of Ammonia and Ammonium: Probing Hydrogen Bond Motifs with FT-IR and Soft X-ray Spectroscopy. *J. Am. Chem. Soc.* **2017**, *139* (36), 12773–12783. DOI: 10.1021/jacs.7b07207.

(164) Ekimova, M.; Kubin, M.; Ochmann, M.; Ludwig, J.; Huse, N.; Wernet, P.; Odelius, M.; Nibbering, E. T. J. Soft X-ray Spectroscopy of the Amine Group: Hydrogen Bond Motifs in Alkylamine/Alkylammonium Acid-Base Pairs. *J. Phys. Chem. B* **2018**, *122* (31), 7737–7746. DOI: 10.1021/acs.jpcb.8b05424.

(165) Reinholdt, P.; Vidal, M. L.; Kongsted, J.; Iannuzzi, M.; Coriani, S.; Odelius, M. NitrogenK-Edge X-ray Absorption Spectra of Ammonium and Ammonia in Water Solution: Assessing the Performance of Polarizable Embedding Coupled Cluster Methods. *J. Phys. Chem. Lett.* **2021**, *12* (36), 8865–8871. DOI: 10.1021/acs.jpclett.1c02031.

References

(166) Chambers, R. D. *Fluorine in Organic Chemistry*; Blackwell Publishing: Oxford, 2004. DOI: 10.1002/9781444305371.

(167) Morgenthaler, M.; Schweizer, E.; Hoffmann-Röder, A.; Benini, F.; Martin, R. E.; Jaeschke, G.; Wagner, B.; Fischer, H.; Bendels, S.; Zimmerli, D.; Schneider, J.; Diederich, F.; Kansy, M.; Müller, K. Predicting and tuning physicochemical properties in lead optimization: Amine basicities. *ChemMedChem.* 2007, pp 1100–1115. DOI: 10.1002/cmdc.200700059.

(168) Meanwell, N. A.; Eastman, K. J.; Gillis, E. P. Tactical applications of fluorine in drug design and development. In *Fluorine in Heterocyclic Chemistry: Volume 1: 5-Membered Heterocycles and Macrocycles*; Nenajdenko, V., Ed.; Springer International: Cham, Switzerland, 2014; pp 1–54. DOI: 10.1007/978-3-319-04346-3_1.

(169) Alabugin, I. V.; Zeidan, T. A. Stereoelectronic effects and general trends in hyperconjugative acceptor ability of σ bonds. *J. Am. Chem. Soc.* 2002, *124* (12), 3175–3185. DOI: 10.1021/ja012633z.

(170) Kukhar, V. P. Fluorine-containing amino acids. *J. Fluor. Chem.* 1994, *69* (3), 199–205. DOI: 10.1016/0022-1139(94)03131-2.

(171) Humelnicu, I.; Würthwein, E. U.; Haufe, G. The conformers of 3-fluoroalanine. A theoretical study. *Org. Biomol. Chem.* 2012, *10* (10), 2084–2093. DOI: 10.1039/c2ob06492h.

(172) De Levie, R. A General Simulator for Acid-Base Titrations. *J. Chem. Educ.* 1999, *76* (7), 987–991. DOI: 10.1021/ed076p987.

(173) Rumble, J. R. CRC Handbook of Chemistry and Physics, 101 Edition (Internet Version 2020). *CRC Press. Taylor Fr. Boca Rat. FL* 2020.

(174) Roberts, G. C. K.; Jardetzky, O. Nuclear Magnetic Resonance Spectroscopy of Amino Acids, Peptides, and Proteins. *Adv. Protein Chem.* 1970, *24* (C), 447–545. DOI: 10.1016/S0065-3233(08)60246-6.

(175) Deng, W.; Cheeseman, J. R.; Frisch, M. J. Calculation of nuclear spin-spin coupling constants of molecules with first and second row atoms in study of basis set dependence. *J. Chem. Theory Comput.* 2006, *2* (4), 1028–1037. DOI: 10.1021/ct600110u.

(176) Šarac, B.; Hadži, S. Analysis of Protonation Equilibria of Amino Acids in Aqueous Solutions Using Microsoft Excel. *J. Chem. Educ.* 2021, *98* (3), 1001–1007. DOI: 10.1021/acs.jchemed.0c01144.

(177) Groth, U.; Schöllkopf, U. Asymmetric syntheses via heterocyclic intermediates; XIX[1]. On the enantioselective synthesis of β-fluorovaline methyl ester and related α-amino-β-fluorocarboxylic esters. *Synthesis* 1983, *1983* (8), 673–675. DOI: 10.1055/s-1983-30469.

(178) Lemen, G. S.; Wolfe, J. P. Pd-catalyzed carboamination of oxazolidin-2-ones: A stereoselective route to trans-2,5-disubstituted pyrrolidines. *Org. Lett.* 2010, *12* (10), 2322–2325. DOI: 10.1021/ol1006828.

(179) Shendage, D. M.; Fröhlich, R.; Haufe, G. Highly efficient stereoconservative amidation and deamidation of α-amino acids. *Org. Lett.* 2004, *6* (21), 3675–3678. DOI: 10.1021/ol048771l.

(180) Xia, J. B.; Zhu, C.; Chen, C. Visible light-promoted metal-free sp³ C-H fluorination. *Chem. Commun.* 2014, *50* (79), 11701–11704. DOI: 10.1039/c4cc05650g.

(181) Effenberger, F.; Weber, T. Stereoselektive Aromatenalkylierung mit Threonin-trifluormethansulfonaten. *Chem. Ber.* 1988, *121* (3), 421–430. DOI: 10.1002/cber.19881210307.

(182) Van Truong, T.; Rapoport, H. Chirospecific Synthesis of the Tetrahydroimidazodiazepinol Aglycon of Pentostatin and Its Analogues. *J. Org. Chem.* 1993, *58* (22), 6090–6096. DOI: 10.1021/jo00074a041.

(183) Nishizono, N.; Akama, Y.; Agata, M.; Sugo, M.; Yamaguchi, Y.; Oda, K. Synthesis of thietane nucleoside with an anomeric hydroxymethyl group. *Tetrahedron* 2011, *67* (2), 358–363. DOI: 10.1016/j.tet.2010.11.038.

(184) Ito, Y.; Matsuura, T.; Saegusa, T. ZnCl₂ and CuCl promoted aldol reactions of isocyanoacetate with α,β-unsaturated carbonyl compounds. *Tetrahedron Lett.* 1985, *26* (47), 5781–5784. DOI: 10.1016/S0040-4039(00)98925-1.

(185) Ma, C.; Cao, R.; Shi, B.; Li, S.; Chen, Z.; Yi, W.; Peng, W.; Ren, Z.; Song, H. Synthesis and cytotoxic evaluation of N²-benzylated quaternary β-carboline amino acid ester conjugates. *Eur. J. Med. Chem.* 2010, *45* (4), 1515–1523. DOI: 10.1016/j.ejmech.2009.12.060.

(186) Selvaraj, A.; Chen, H. T.; Ya-Ting Huang, A.; Kao, C. L. Expedient on-resin modification of a peptide C-terminus through a benzotriazole linker. *Chem. Sci.* 2018, *9* (2), 345–349. DOI: 10.1039/c7sc03229c.

(187) Chen, J.; Wang, P.; Zhu, J.; Wan, Q.; Danishefsky, S. J. A program for ligation at threonine sites: application to the controlled total synthesis of glycopeptides. *Tetrahedron* 2010, *66* (13), 2277–2283. DOI: 10.1016/j.tet.2010.01.067.

(188) Oida, S.; Yoshida, A.; Ohki, E. Synthesis of Oxapenam Derivatives. *Chem. Pharm. Bull.* 1978, *26* (2), 448–455. DOI: 10.1248/cpb.26.448.

(189) Stewart, J. J. P. Optimization of parameters for semiempirical methods VI: More modifications to the NDDO approximations and re-optimization of parameters. *J. Mol. Model.* 2013, *19* (1), 1–32. DOI: 10.1007/s00894-012-1667-x.

(190) Lee, C.; Yang, W.; Parr, R. G. Development of the Colle-Salvetti correlation-energy formula into a functional of the electron density. *Phys. Rev. B* 1988, *37* (2), 785–789. DOI: 10.1103/PhysRevB.37.785.

(191) Becke, A. D. Density-functional thermochemistry. III. The role of exact exchange. *J. Chem. Phys.* 1993, *98* (7), 5648–5652. DOI: 10.1063/1.464913.

(192) Grimme, S.; Ehrlich, S.; Goerigk, L. Effect of the damping function in dispersion corrected density functional theory. *J. Comput. Chem.* 2011, *32* (7), 1456–1465. DOI: 10.1002/jcc.21759.

(193) Cossi, M.; Rega, N.; Scalmani, G.; Barone, V. Energies, structures, and electronic properties of molecules in solution with the C-PCM solvation model. *J. Comput. Chem.* 2003, *24* (6), 669–681. DOI: 10.1002/jcc.10189.

(194) Grimme, S. Semiempirical hybrid density functional with perturbative second-order correlation. *J. Chem. Phys.* 2006,

124 (3), 034108. DOI: 10.1063/1.2148954.

(195) Biczysko, M.; Panek, P.; Scalmani, G.; Bloino, J.; Barone, V. Harmonic and anharmonic vibrational frequency calculations with the double-hybrid B2PLYP method: Analytic second derivatives and benchmark studies. *J. Chem. Theory Comput.* **2010**, *6* (7), 2115–2125. DOI: 10.1021/ct100212p.

(196) Papajak, E.; Zheng, J.; Xu, X.; Leverentz, H. R.; Truhlar, D. G. Perspectives on basis sets beautiful: Seasonal plantings of diffuse basis functions. *J. Chem. Theory Comput.* **2011**, *7* (10), 3027–3034. DOI: 10.1021/ct200106a.

(197) Fusè, M.; Mazzeo, G.; Longhi, G.; Abbate, S.; Masi, M.; Evidente, A.; Puzzarini, C.; Barone, V. Unbiased Determination of Absolute Configurations by vis-à-vis Comparison of Experimental and Simulated Spectra: The Challenging Case of Diplopyrone. *J. Phys. Chem. B* **2019**, *123* (43), 9230–9237. DOI: 10.1021/acs.jpcb.9b08375.

(198) Paoloni, L.; Mazzeo, G.; Longhi, G.; Abbate, S.; Fusè, M.; Bloino, J.; Barone, V. Toward Fully Unsupervised Anharmonic Computations Complementing Experiment for Robust and Reliable Assignment and Interpretation of IR and VCD Spectra from Mid-IR to NIR: The Case of 2,3-Butanediol and trans-1,2-Cyclohexanediol. *J. Phys. Chem. A* **2020**, *124* (5), 1011–1024. DOI: 10.1021/acs.jpca.9b11025.

(199) Frisch, M. J.; Trucks, G. W.; Schlegel, H. B.; Scuseria, G. E.; Robb, M. A.; Cheeseman, J. R.; Scalmani, G.; Barone, V.; Petersson, G. A.; Nakatsuji, H.; Li, X.; Caricato, M.; Marenich, A. V.; Bloino, J.; Janesko, B. G.; Gomperts, R.; Mennucci, B.; Hratchian, H. P.; Ortiz, J. V.; Izmaylov, A. F.; Sonnenberg, J. L.; Williams-Young, D.; Ding, F.; Lipparini, F.; Egidi, F.; Goings, J.; Peng, B.; Petrone, A.; Henderson, T.; Ranasinghe, D.; Zakrzewski, V. G.; Gao, J.; Rega, N.; Zheng, G.; Liang, W.; Hada, M.; Ehara, M.; Toyota, K.; Fukuda, R.; Hasegawa, J.; Ishida, M.; Nakajima, T.; Honda, Y.; Kitao, O.; Nakai, H.; Vreven, T.; Throssell, K.; Montgomery, J. A., J.; Peralta, J. E.; Ogliaro, F.; Bearpark, M. J.; Heyd, J. J.; Brothers, E. N.; Kudin, K. N.; Staroverov, V. N.; Keith, T. A.; Kobayashi, R.; Normand, J.; Raghavachari, K.; Rendell, A. P.; Burant, J. C.; Iyengar, S. S.; Tomasi, J.; Cossi, M.; Millam, J. M.; Klene, M.; Adamo, C.; Cammi, R.; Ochterski, J. W.; Martin, R. L.; Morokuma, K.; Farkas, O.; Foresman, J. B.; Fox, D. J. Gaussian 16, Rev. C.01. *Gaussian, Inc., Wallingford, CT* **2016**.

(200) Lazzari, F.; Salvadori, A.; Mancini, G.; Barone, V. Molecular Perception for Visualization and Computation: The Proxima Library. *J. Chem. Inf. Model.* **2020**, *60* (6), 2668–2672. DOI: 10.1021/acs.jcim.0c00076.

Chapter 4 – Index

4. Metallaphotoredox catalysis

4.1. Introduction

Nature has been able to convert solar energy to chemical energy since much earlier than human beings: oxygenic photosynthesis – the most widespread biochemical process on Earth – likely first appeared about 2.5 billions years ago or even earlier.[1,2] In particular, through this process, sunlight is "harvested" and used to drive endergonic chemical reactions. Specifically, sunlight photons can excite the pigments – mainly chlorophylls – of photosystem II (PSII). Once in their excited states, they can induce electron transfer phenomena (occurring along the so-called electron transport chain) leading to the formation of highly energetic species.[3] The electron vacancies of PSII are promptly occupied by the electrons arising from the water splitting reaction.[4] This process is mediated by an oxygen-evolving metallo-oxo cluster, containing four manganese ions (in oxidation states ranging from +3 to +4) and one divalent calcium cation.[5,6] However, only recently, laboratories all around the world have taken advantage of light in order to promote new transformations, and photocatalytic organic reactions have been widely investigated in the last decades.[7–9]

4.1.1. Photocatalysis

For a long time, direct excitation of one of the reactants by UV light represented the main approach for the application of photochemistry in organic synthesis.[10] The use of UV light has numerous limitations and drawbacks, and most of them can be hardly overcome. Indeed, this approach is restricted to a limited range of reactions, such as cycloadditions, Norrish-type reactions, sigmatropic rearrangements. Moreover, the high energy of UV radiation is usually non-selective, favouring undesired parasite decomposition pathways. The exploitation of visible light became possible with the advent of photosensitizers, capable of absorbing visible light to promote photoinduced electron or energy transfer processes. Without them, visible radiation usually has no interactions with the reaction partners, unless the latter are decorated with visible-absorbing chromophores. At first, the deliberate use of visible light to promote chemical reactions in a photocatalytic fashion represented a niche approach, with a very slow development. The pioneering work of Kellogg and co-workers (1978) represents a first noteworthy example: it exploited the ability of a ruthenium complex, namely [Ru(bpy)$_3$]Cl$_2$, to act as a photosensitizer in the reduction of phenacyl sulfonium salts using *N*-substituted 1,4-dihydropyridines as the terminal reductant, through mechanisms involving "one electron transfer steps" (vide infra).[11] In the following years, other remarkable (often bioinspired)[12] studies were published.[13] This shift towards less energetic radiations can overcome many issues linked to the use of UV light. First, inexpensive light sources, particularly LEDs or even sunlight, can be employed. Furthermore, the absorption process is much more

selective, with visible light being selectively absorbed by the photosensitizers, avoiding undesired photodegradation pathways of reaction partners. The main benefit of photocatalysis is the easy access to a wide range of otherwise-inaccessible interesting reaction intermediates (such as radical ions, diradicals, excited species), in a sustainable way, with relatively mild reaction conditions. Generally, in the field of traditional ground-state polar chemistry, such intermediates cannot be generated, or require prohibitive conditions in terms of environmental sustainability.[14] A noteworthy example can be found in the field of traditional radical chemistry: for decades, the use of highly toxic tin compounds, such as Bu$_3$SnH, represented a major limitation for a wide application of such chemistry. This drawback was commonly referred to as the so-called "tin tyranny".[15] The recent development in photochemical and photocatalyzed processes enabled the overcoming of such disadvantages. In particular, most of such success depends on the shrewd choice of the photosensitizer, according to the properties of its excited state (energy, lifetime and redox properties). Metal-based photosensitizers, such as Ru(II) and Ir(III) complexes, have long excited-state lifetimes. Furthermore, their oxidized and reduced forms display high chemical stability, contributing to the suitability of such photosensitizers in photoredox catalysis.[16] However, ruthenium and iridium are heavy rare – thus very expensive – elements. The exploitation of photoredox catalysis with metal-based photosensitizers made from Earth-abundant elements[17] was developed to reduce the costs of photocatalytic strategies.[18,19] However, some drawbacks – such as supply (cobalt), efficiency (iron), and toxicity (nickel, chromium) – still remain for some metals, limiting their application in large-scale synthesis of active pharmaceutical ingredients (APIs).[20,21] These limitations can be avoided moving to organic dyes used as photosensitizers. Their properties can be easily tuned by simple modifications of known structures,[22] with the help of state-of-the-art computational analyses.[23,24] A comprehensive and impressive review about organic photosensitizers was recently reported by Nicewicz.[25] According to the aforementioned observations, merging photoredox catalysis with metal-mediated processes can appear as a "devolution" at first glance, especially concerning the use of organic photosensitizers, since the main goal of the change from metal-based photosensitizers to organic dyes was the avoidance of metal-related drawbacks. However, such approach actually enables the generation of transient nucleophilic organometallic species in a much different way from those previously reported in literature (vide infra).[26] The first examples of dual photoredox catalysis involved rare-Earth metal based photosensitizers, coupled to either palladium[27] or nickel.[28,29] Many other metals, such as copper,[30] gold,[31] palladium,[32] rhodium,[33] ruthenium,[34] iron,[35] and titanium,[36] were exploited in innovative dual photoredox catalytic strategies involving metal photosensitizers. Eventually, even organic dyes were investigated to replace expensive metal-based photosensitizers. Fortunately, they proved to be excellent photosensitizers in the field of synergistic photoredox metal catalysis, namely metallaphotoredox catalysis. Such approach has reached nowadays a high level of complexity and broad application. For a clearer general picture to understand the potential of photocatalysis, a preliminary analysis of the physico-chemical properties of

photosensitizers is required. Such general picture is also useful to fully grasp the further evolution towards metallaphotoredox catalysis, which will be analysed in detail in due time.

4.1.2. Photophysics and photochemistry of photosensitizers

Figure 4.1 shows the typical photocatalytic cycle, which has three main phases: (i) the excitation of the photosensitizer, (ii) the interaction between the excited photosensitizer with a substrate, and (iii) the regeneration of the photosensitizer in its ground state. Noteworthily, in some processes, the photosensitizer behaves as a photoinitiator (i.e. it is able, upon light absorption, to initiate a cascade reaction which can proceed without the photoinitiator itself, and even in the absence of light).[37,38] Besides, sometimes the photosensitizer restoration phase is not necessary, since the photosensitizer-substrate interaction already regenerates the photosensitizer in its ground state (e.g. through energy transfer processes, vide infra).[39]
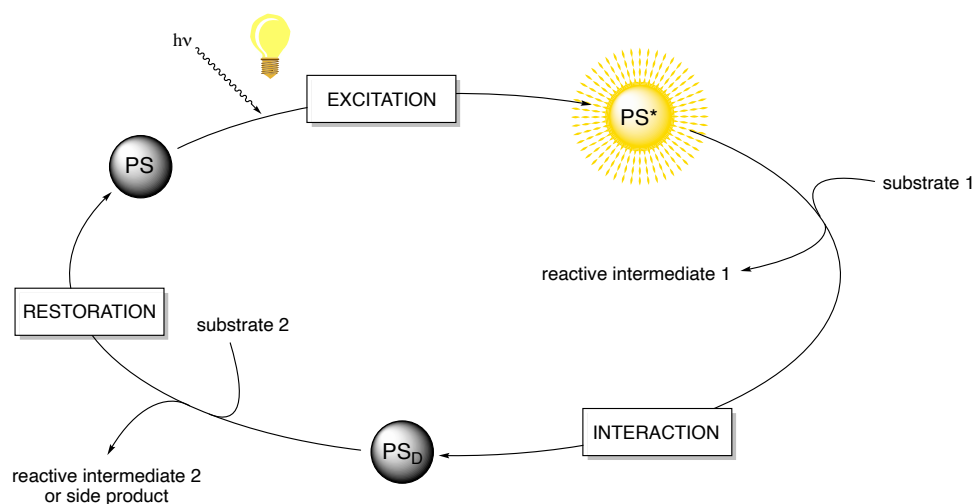
Figure 4.1: General catalytic cycle of a photosensitizer (PS). PS* denotes the photosensitizer excited state, while PS_D denotes a deactivated form of the photosensitizer.

Excitation step

The photoinduced excitation is a photophysical phenomenon occurring whenever a molecule absorbs a sufficiently energetic photon: the irradiated molecule is hence promoted to one of its electronic excited states (Figure 4.2). From now on, the specific case of a photosensitizer will be treated in details.
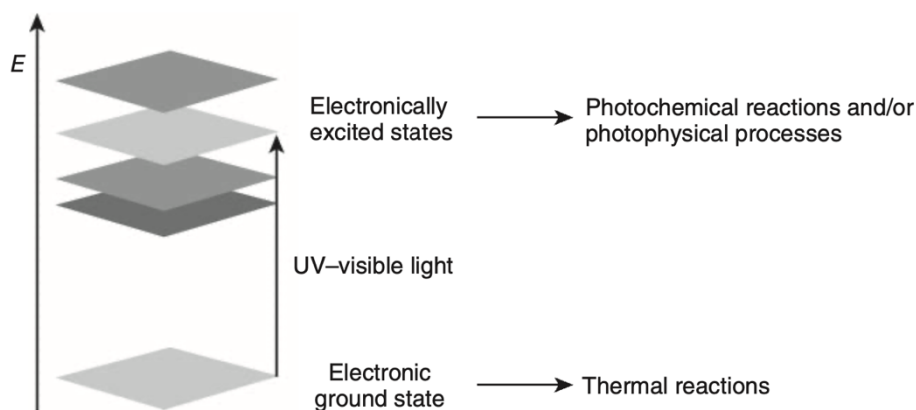
Figure 4.2: Pictorial sketch describing the photoinduced excitation phenomenon (Ref. 10).

The physico-chemical properties of the excited photosensitizer are different with respect to those of the photosensitizer in the ground state. Indeed, the excited state can be engaged in several processes (Figure 4.3): it can react in a photochemical reaction, or it can go back to the ground state, by either radiative processes (such as luminescence) or non-radiative pathways (such as energy degradation to heat).
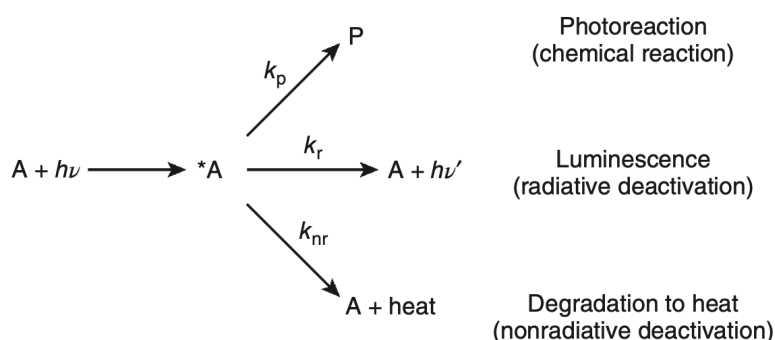
Figure 4.3: Possible downstream processes of a molecule in its excited state (Ref. 10).

The best way to describe the possible downstream events upon photon absorption by a photosensitizer is the Jablonski diagram (Figure 4.4). Generally, the ground state is a singlet state (S_0, closed-shell species) and the photon absorption causes the photosensitizer to be promoted to any of the vibrational levels belonging to any of the excited singlet states. After a few picoseconds, the excited photosensitizer reaches the lowest vibrational level of the lowest singlet excited state (S_1). Then, the range of possibilities widens: the photosensitizer ground state S_0 can be restored either by photon emission (fluorescence) or by non-radiative thermal decay. Otherwise, it can reach any of the vibrational levels belonging to any of the energetically-close triplet excited states through a non-radiative process (namely intersystem crossing, ISC), and then it rapidly relaxes to the lowest vibrational level of the lowest triplet excited state (T_1). From there, the photosensitizer ground state S_0 can be restored according to the aforementioned mechanisms reported in the case of S_1. In this case, however, the radiative decay is called phosphorescence. It is worth mentioning that the transition $T_1 \rightarrow S_0$ is spin-forbidden. Hence, the lifetime of T_1 is much longer than that of S_0 (microseconds vs. nanoseconds, respectively).
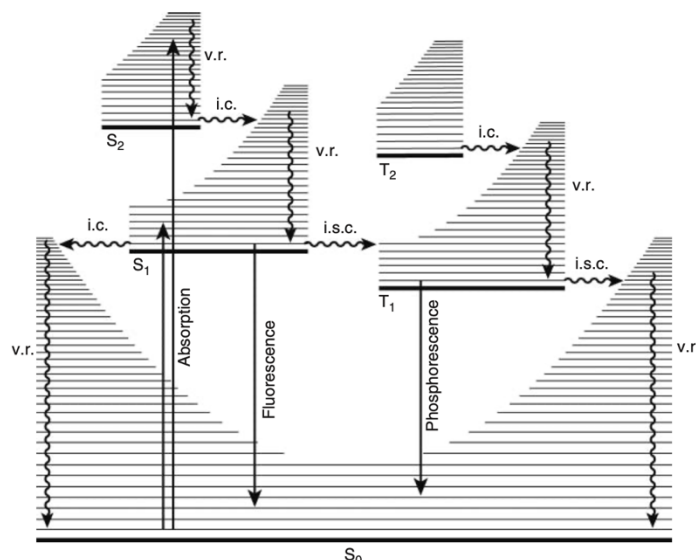
Figure 4.4: Jablonski diagram. The acronyms v.r., i.c., and i.s.c. stand for vibrational relaxation, internal conversion, and intersystem crossing, respectively (Ref. 10).

According to this description, the photocatalytic approach requires the photoreactive process (see Fig. 4.3) to be favoured with respect to the other decay processes. Moreover, in most cases the excited photosensitizer can engage a bimolecular process with a suitable substrate either in its S_1 or T_1 state. Since such bimolecular process is ruled by statistics, the lifetime of the photosensitizer excited state represents a pivotal parameter. It is defined as (cf. Figure 4.3):

$$\tau(^*A) = \frac{1}{k_p + k_r + k_{nr}} = \frac{1}{\sum_j k_j} \tag{4.1}$$

where k_p, k_r, and k_{nr} are photoreaction, radiative, and non-radiative kinetic constants, respectively. The PS lifetime has to be long enough to enable the photosensitizer-substrate interaction. Finally, for each specific downstream event (with respect to the photon absorption phenomenon), the quantum yield Φ_i can be defined as:

$$\Phi_i = \frac{\text{N° of molecules undegoing the process i}}{\text{N° of photons absorbed by the reactant}} \tag{4.2}$$

The two definitions of Equations 4.1 and 4.2 enable the exhaustive description of some important photophysical properties of the photosensitizer, essential to interpret the outcome of a photocatalytic process. The photosensitizer-substrate interaction involves either the PS S_1 state, or the T_1 one. In both cases, the lifetime of the excited state has to be as long as possible, since short-lived excited states (less than 1 ns) cannot undergo photoreactive processes. Assuming that non-radiative processes for the decay of PS* are usually negligible, S_1 lifetime coincides with the fluorescence timescale ($\tau_{S1} \cong \tau_f$), while T_1 lifetime coincides with the phosphorescence timescale ($\tau_{T1} \cong \tau_p$). The ideal photosensitizer involving a S_1-

substrate interaction should have long fluorescence timescales and a high fluorescence quantum yield Φ_f (i.e. as close to unity as possible). Indeed, $\Phi_f \sim 1$ means that almost all the S_1 molecules, with no available substrate, decay back to the ground state radiatively, while $\Phi_f < 1$ means that non-radiative processes compete with fluorescence. The ideal photosensitizer involving a T_1-substrate interaction should have a highly efficient intersystem crossing (high value of k_{ISC}) so that this process can compete with fluorescence.[40] The efficiency of such process is increased when (a) heavy-atom molecules are involved;[41] (b) the involved electronic states are energetically close to each other; (c) the transition involves a change of orbital type (El-Sayed rules).[42] If k_{ISC} is much higher than k_f, the intersystem crossing quantum yield Φ_{ISC} is very close to unity, meaning that almost all the excited PS molecules are in the T_1 state, whose lifetime is usually long enough (up to microseconds, vide supra) to enable the desired photochemical processes. Another important parameter is the radiation wavelength corresponding to the PS absorption maximum, namely λ_{max}^{abs}. The choice of the radiation source depends on this parameter. Indeed, a sufficiently large overlap between the emission spectrum of the radiation source and the PS absorption one is required. Besides, λ_{max}^{abs} is important to evaluate the energy of the PS excited state: the higher λ_{max}^{abs}, the lower the energy of the excited state.

Interaction step

The second phase of the Figure 4.1, namely the interaction step, is a bimolecular PS-substrate process. This represents a pivotal stage, since it rules the reactivity type of the whole photocatalytic reaction. Generally, four different paths are available for the PS-substrate interaction (Figure 4.5): (i) electron transfer (usually by single electron transfer, namely SET), (ii) atom transfer (either a hydrogen or a halogen, namely HAT and XAT, respectively),[43,44] (iii) energy transfer (ET),[39,45] and (iv) proton-coupled electron transfer (PCET).[46]
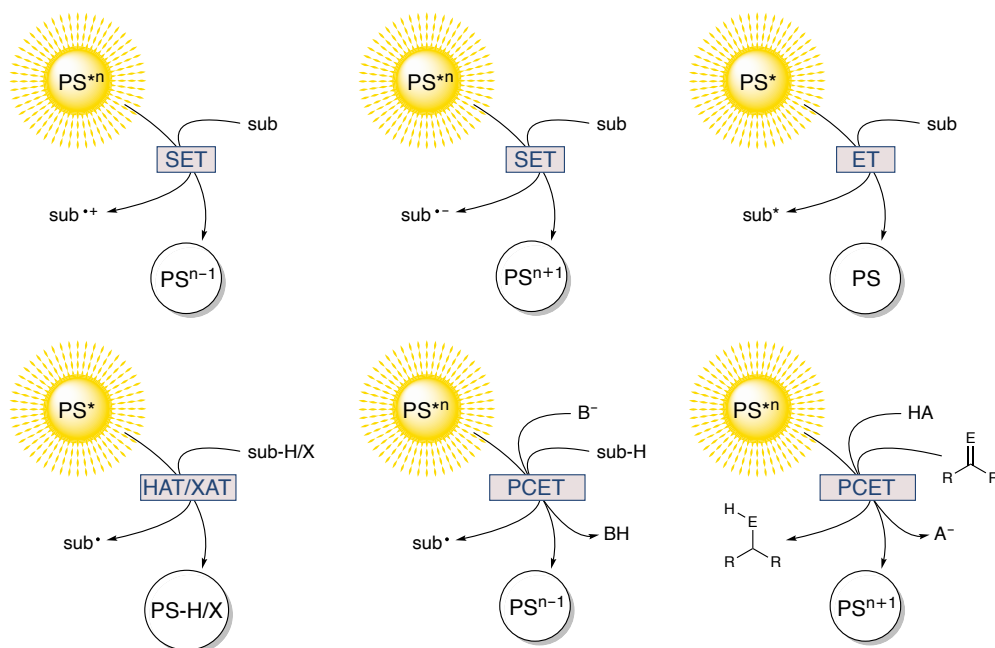
Figure 4.5: Main available paths for PS-substrate interaction.

The experimental studies to assess the involved mechanism are often non-trivial. However, SET mechanism is by far the most common, and photocatalytic processes based on this mechanism belong to the so-called photoredox catalysis. Indeed, PS* is both a better oxidant (i.e. it has a higher electron affinity, EA) and a better reductant (i.e. it has a lower ionization potential, IP) than PS ground state. Hence, the unfeasibility of endergonic transformations can be overcome by adding photons as active "ingredients": absorption processes raise the energy of the system, which can then evolve through a cascade of exergonic transformations. This is clearly depicted in Figure 4.6.
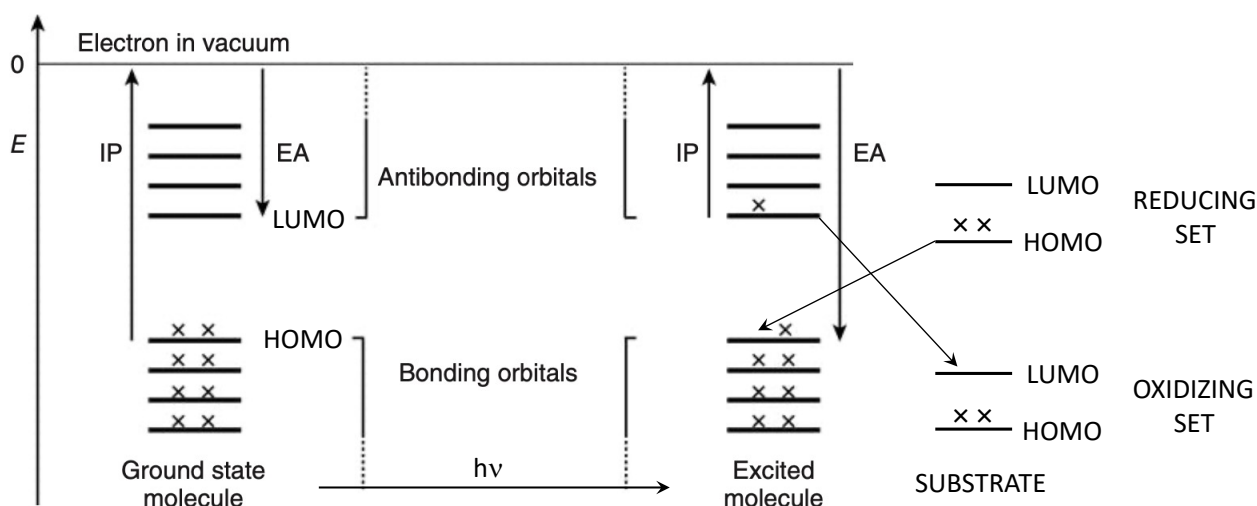
Figure 4.6: Changes of redox properties upon photon absorption.

The knowledge of PS* redox potentials, to be compared to those of the substrate, is a fundamental a-priori thermodynamic base to conceive and develop photocatalytic strategies involving reactive species,

such as radicals, radical anions, and radical anions. Whenever these redox potentials are not available in literature, they can be experimentally determined through specific electrochemical measurements, such as cyclic voltammetry.[47] However, good approximations of PS* redox potentials can be obtained from the ground state redox potentials (which are usually known), using the Rehm-Weller equations, valid when both PS/PS* entropy difference and Coulombic interactions can be neglected.[48]

$$E_{\frac{1}{2}(A^+/A^*)} = E_{\frac{1}{2}(A^+/A)} - E_{00} \tag{4.3}$$

$$E_{\frac{1}{2}(A^*/A^-)} = E_{\frac{1}{2}(A/A^-)} + E_{00} \tag{4.4}$$

where E_{00} refers to the energy difference between the lowest vibrational state of the excited state (either S_1 or T_1) and the lowest vibrational state of the ground state. Starting from the PS absorption spectrum, E_{00} can be roughly estimated as the energy corresponding to the long wavelength tail (λ_{tail}).[10] With a more precise geometrical approach, E_{00} can be determined as the energy corresponding to the intersection point (λ_{geom}) between the x-axis and the line tangent to the spectrum in the long wavelength with 10% of ε_{max}, i.e. the λ_{max}^{abs} molar attenuation coefficient (Figure 4.7).
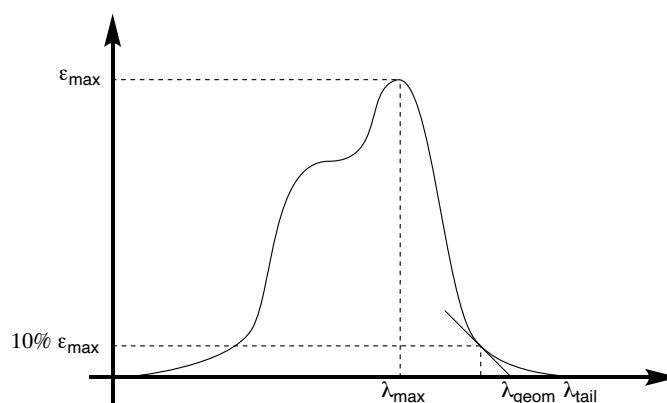
Figure 4.7: Graphic strategies for the evaluation of E_{00} starting from the PS absorption spectrum.

Otherwise, by comparison with the PS emission spectrum, E_{00} can be estimated as the energy corresponding to the midpoint wavelength ($\lambda_{1/2}$) of the Stokes shift (Figure 4.8).
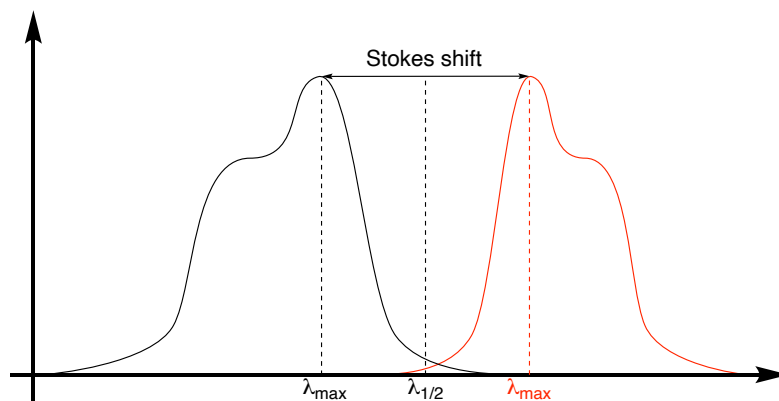
Figure 4.8: Evaluation of E_{00} using the Stokes shift. The absorption spectrum is black, while the emission one is red.

The common nomenclature denotes the PS-substrate interaction process as quenching. The substrate is hence referred to as quencher. Depending on whether the photosensitizers is oxidized or reduced by the quencher, the process is called oxidative quenching or reductive quenching, respectively (Figure 4.9).
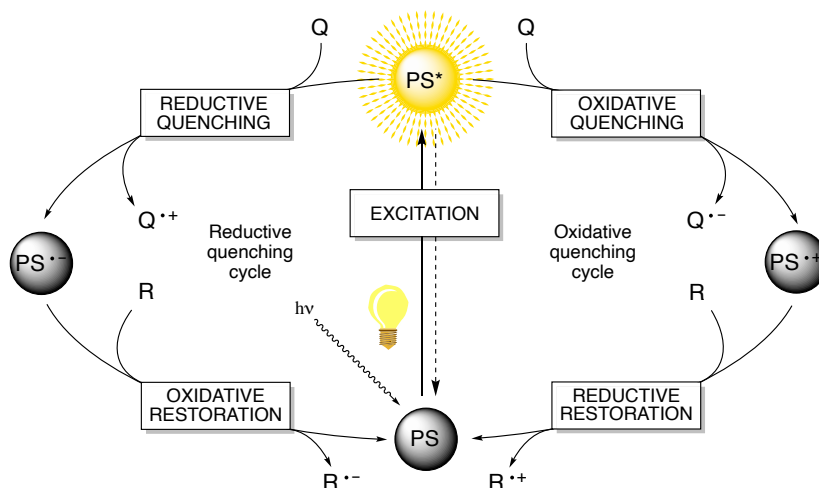
Figure 4.9: General mechanism of photoredox catalytic processes. Q and R stand for quencher and restorer, respectively.

The quenching phenomenon can be analysed through quenching experiments,[49] based on the Stern-Volmer linear relationship:

$$\frac{I_0}{I} = 1 + k_q\tau_0[Q] \tag{4.5}$$

where I_0 is the emission intensity without the quencher, I is the emission intensity in the presence of the quencher, k_q is the quenching constant, τ_0 is the excited state lifetime without the quencher, and [Q] is the concentration of the quencher. During standard Stern-Volmer experiments, the intensity of the emitted radiation is measured at different quencher concentrations, and the data (I/I_0 vs. [Q]) are plotted according to Equation 4.5. The quenching constant is determined starting from the slope of the linear fit. In the case of a photocatalytic reaction, the measurements are repeated for all the reaction partners: that with the highest quenching constant is the best candidate to be the actual quencher in the reaction

conditions. This information is indeed very precious to unveil the overall reaction mechanism. It is worth mentioning that the original Stern-Volmer equation involves lifetimes instead of emission intensities (i.e. the left-hand side of Eq. 4.5 is τ_0/τ). Indeed, some photocatalysts are characterized by non-emissive excited states, thus requiring different experimental techniques, e.g. laser flash photolysis, for the kinetic analysis.[50,51]

Further insights on the involved mechanism can be achieved performing important control experiments. For instance, the possible formation of free radicals during the photocatalytic reaction can be probed adding radical traps (such as TEMPO or PNB) to the reaction mixture. If any radical intermediate is formed during the reaction, it is trapped by such additives and the reaction cannot proceed.

Restoration step

After the PS-quencher interaction (unless it occurred via ET, vide supra), the PS ground state can be restored in several ways.[52] The most common restoration phenomena are the following:

1. Restoration by a reaction intermediate. With reference to Figure 4.9, an oxidative quenching process must be followed by a reductive restoration process, while a reductive quenching must be followed by an oxidative restoration.

2. Restoration by a co-catalyst, e.g. a metal complex or an organocatalyst-derived species.

3. Restoration by a stoichiometric reactant. The latter can be either a sacrificial agent or a reaction intermediate derived from the reaction substrate. Otherwise, the restorer can be another substrate that is involved in the overall reaction.

4. Electrochemical restoration with an electrode.

The restoration step is required to close the photocatalytic cycle, thus ensuring the catalytic turnover. If none of the aforementioned restoration mechanisms occurs, the reaction cannot proceed further. To understand the importance of the restoration step, two remarkable literature examples of photocatalytic cycles are reported in Figure 4.10. These examples are indeed very useful to catch the general picture provided by Figures 4.1 and 4.9. In particular, concerning the aforementioned pioneering work of Kellogg and co-workers for the reduction of phenacyl sulfonium salts (Figure 4.10A),[11] the restoration is guaranteed by a stoichiometric reactant, i.e. the phenacyl sulfonium ion itself. Noteworthily, the proposed quencher is a catalytically generated intermediate that is not present at the start of the reaction. Hence, it must be initially generated via an alternative pathway: a likely route is direct photoexcitation of the terminal reductant – which itself absorb in the visible region, followed by SET to the phenacyl sulfonium. The quenching of the photosensitizer by a catalytically generated intermediate is a feature of many photoredox reactions. On the other hand, in the photoredox organocatalytic protocol reported by Nicewicz and MacMillan (Figure 4.10B),[53] the restorer is a reaction intermediate belonging to the organocatalytic cycle.
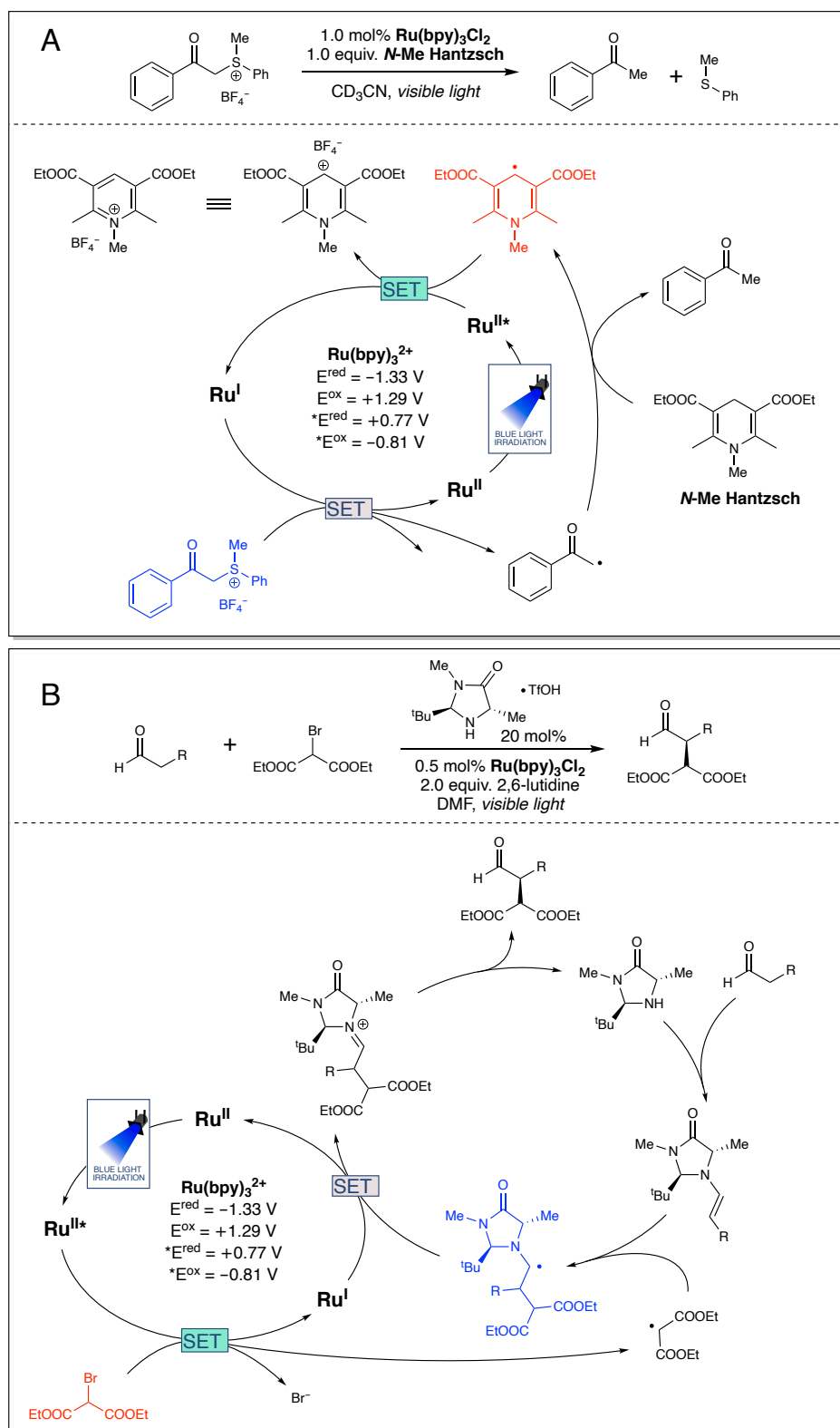
Figure 4.10: (A) Photoredox reduction of phenacyl sulfonium salts (Ref. 11). **(B)** Enantioselective alkylation of aldehydes via photoredox organocatalysis (Ref. 53). The quencher is red, while the restorer is blue. The redox potentials of the photosensitizer are referred to the standard calomel electrode (SCE).

4.1.3. Common photosensitizers

Figure 4.11 lists some common photosensitizers used in photocatalysis. An exhaustive review summarizing the photophysical and electrochemical properties of more than 200 photosensitizers was recently published by Wu and co-workers.[54]
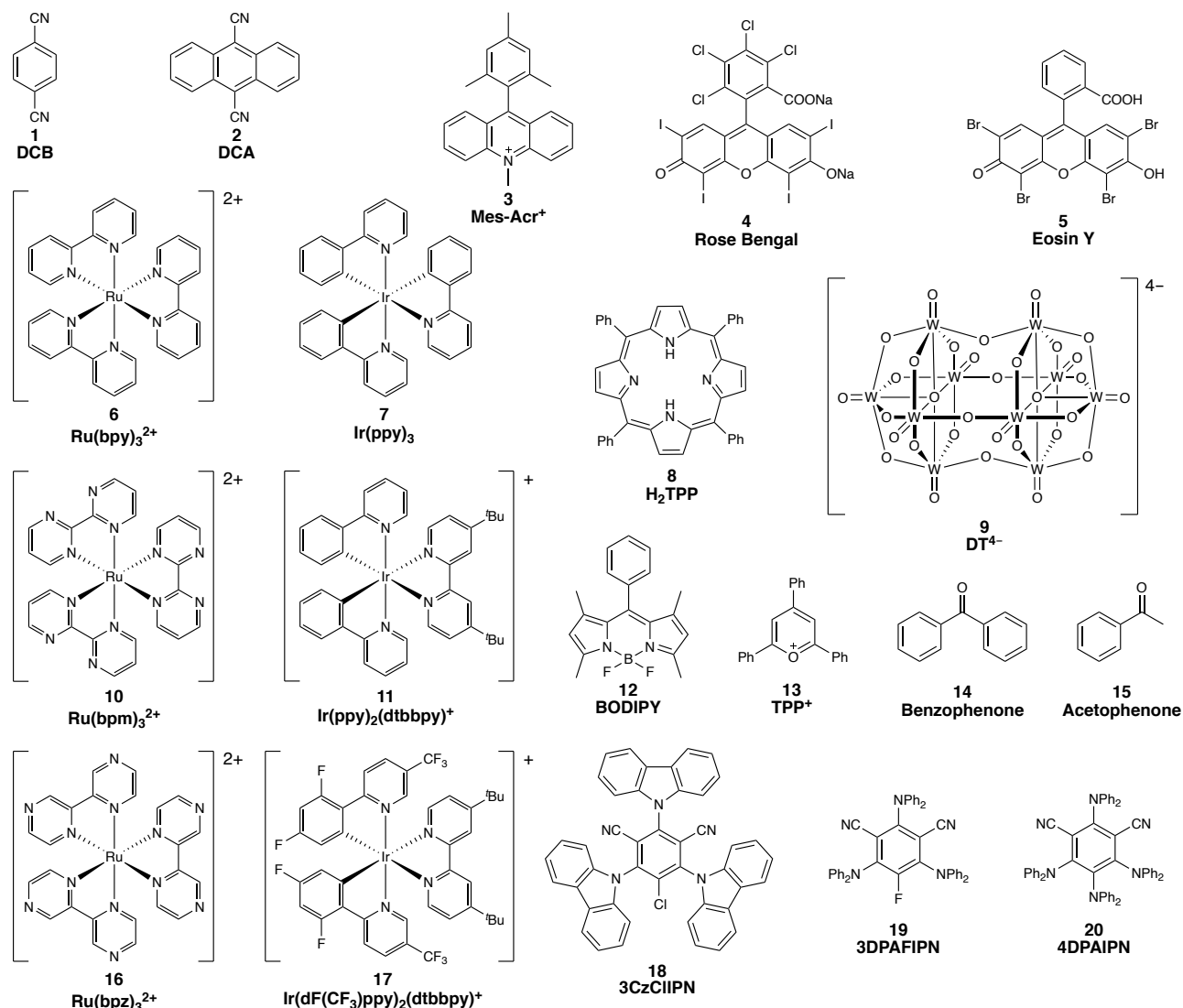
Figure 4.11: Selected photosensitizers.

In particular, since the dawn of organic photoredox catalysis, several classes of organic dyes have been synthesized, studied, and used to promote light-mediated processes. Amongst them, cyanoarenes,[55] flavins,[56] xanthenes,[57] and thiazines,[58] represent noteworthy examples.[59] To date, only some of them have been merged with metal catalysts for metallaphotocatalysis.

4.1.4. Merging photocatalysis and metal catalysis

A short mention to the importance of metal catalysis on its own is appropriate to understand the historical basis for the birth of metallaphotocatalysis. Indeed, in the last decades, broad and accurate

studies have been devoted to metal catalysis, which rapidly became one of the most used synthetic tools in organic synthesis.[60] The catalytic properties of metals (especially transition metals) relies on their capability to shuttle between different oxidation states. In particular, they can engage SET processes.[61] Moreover, as discussed above, some metal complexes display photoredox properties. The previous observations represented strong premises for the possibility of merging photocatalysis and metal catalysis, with the aim of exploring new synthetic tools.[62] It is worth mentioning that, in addition to the common photoinduced electron transfer, energy transfer represents a rather important alternative mechanism ruling the interaction between the photosensitizer catalytic cycle and the one of the metal-based catalyst.[63] Several parameters, correlated to the coulombic or exchange mechanism, can influence the rate of energy transfer.[10,49] Regardless the interaction mechanism, the main prerequisite is that the excited state of the photosensitizer lies at higher energy than the excited state of the metal-based catalyst to be populated. However, metallaphotoredox catalysis specifically deals with photocatalytic processes based on photoinduced electron transfer.[64] In particular, the interplay between photo- and metal catalytic cycles is possible with metals characterized by several stable oxidation states, such as those which have been extensively used in catalytic protocols, and hence have been recognized for their scientific and societal impact.[65–67]

In general, two main interaction mechanisms can be identified (Figure 4.12): (i) the photocatalytic cycle promotes an unfavoured phase of the metal catalytic cycle; (ii) the photocatalytic cycle generates an intermediate which is engaged in the metal catalytic cycle to form the final product.
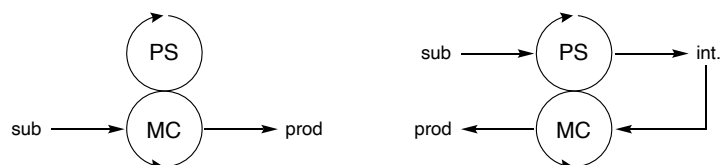
Figure 4.12: Interaction mechanisms between the photocatalytic cycle and the metal catalytic cycle. PS and MC stand for photosensitiser and metal catalyst, respectively.

The catalytic cycle of one of the pioneering works in the field of metallaphotoredox catalysis should give a clear picture of how photo- and metal catalytic cycles can interact with each other. Figure 4.13 depicts the dual palladium-photoredox-catalysed C−H functionalization reaction reported by Sanford and co-workers in 2011.[27]

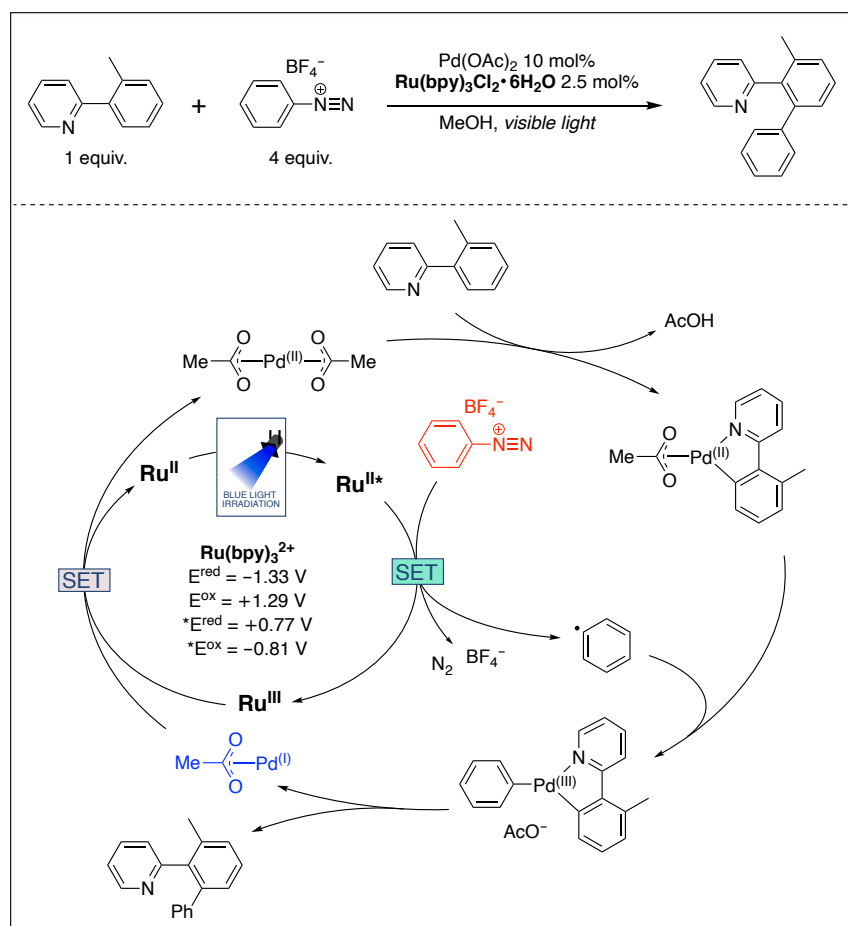# C−C bond formation: the case of carbonyl allylation reactions

Figure 4.13: Dual palladium-photoredox-catalysed C−H functionalization reaction (Ref. 27). In this case, the photosensitizer undergoes oxidative quenching, enabling the formation of an aryl radical starting from the aryldiazonium tetrafluoroborate, acting as the quencher. The palladium catalyst shuttles between three different oxidation states, i.e. Pd[(I)], Pd[(II)], and Pd[(III)].

4.1.5. C−C bond formation: the case of carbonyl allylation reactions

In recent years, photoredox catalysis has proved to be an effective and practical synthetic tool to perform C−C and C−X (X = O, N, S, P) bond-forming reactions.[8,9] Metallaphotoredox catalysis, first pioneered by Sanford,[27] MacMillan-Doyle,[28] and Molander,[29] has enabled a step forward, considerably expanding the repertoire of reactivity and scope, through the development of new, mild, and interesting transformations. In particular, cross-coupling reactions represented a good playground for the application of metallaphotoredox catalysis.[68] An important mechanism of metallaphotoredox catalysed cross-coupling reactions is the so-called radical to polar crossover (RPCO),[69] involving either carbanions[70] or carbenium ions,[71] formed upon reactions between photoredox-generated radicals and metallic species.

Among the plethora of possible reaction partners, carbonyl compounds represent an interesting case in the field of C−C bond-forming reactions. Traditionally, they are used as suitable substrates (electrophiles) for the addition of stoichiometric organometallic reagents (nucleophiles). The carbonyl allylation

reaction, with particular reference to aldehydes as starting materials (for the synthesis of homoallylic alcohols), is an attractive protocol. Indeed, the alcoholic homoallylic moiety can be found in many natural compounds.[72,73] Besides, homoallylic alcohols are valuable intermediates for total syntheses.[74–77] At the beginning of last century, the first developed allylation protocols involved either the stoichiometric use of allylic Grignard reagents, or the in situ generation of allylic nucleophiles via Barbier conditions, i.e. starting from allyl halides and metal overstoichiometric sources. Such strategies are still widespread, but their many drawbacks – such as the large production of metallic waste, low compatibilities with several functional groups, and low stereoselectivity – pushed organic chemists towards alternative methodologies. Eventually, excellent chemo- and enantio-selectivities were achieved by the use of many different metals,[78] ending up with long-sought catalytic approaches.[79] Even in the specific case of catalytic Barbier-type methodologies, however, albeit the nucleophilic organometallic species are generated in a catalytic fashion, stoichiometric sacrificial reductants – usually metals in low oxidation states – are still required to close the catalytic cycle, causing the high production of metallic waste. Moreover, other sacrificial reagents, namely scavengers, are often required to guarantee the turnover of the metal catalyst (Figure 4.14).[80,81]
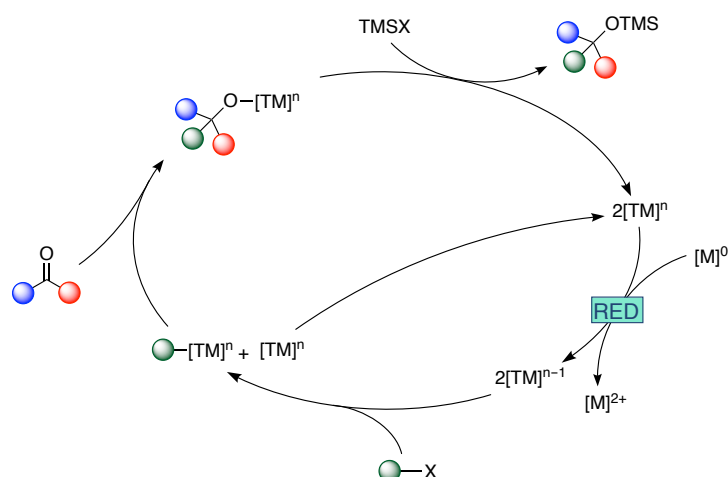
Figure 4.14: *Barbier-type reaction for the generation of transient nucleophilic organometallic species: the general case of nucleophilic addition to carbonyl compounds. In particular, in the case of allylation, the green substituent is an allyl group. Besides the use of a stoichiometric amount of sacrificial reductant, scavengers such as trimethylsilyl chloride (TMSCl) are usually required to guarantee the turnover of the metal catalyst.*

It is worth mentioning some remarkable examples (the allylic source and the employed metal are reported in parenthesis): Nozaki-Hiyama allylation (with allyl halides, stoichiometric in chromium),[82] Hosomi-Sakurai allylation (with allylsilanes, stoichiometric in titanium),[83] Brown allylation (with allylboranes, no metals required),[84] Roush allylation (with allylboronates, no metals required),[85,86] Carreira allylation (with allylsilanes, catalytic in titanium),[87] Keck allylation (with allylstannanes, catalytic in titanium),[88] Krische allylation (with allyl acetate, catalytic in iridium),[89] Leighton allylation (with allylsilanes, no metals required),[90] and Hoveyda allylation (allylation of imines, with allylboronates, catalytic in copper).[91]

C−C bond formation: the case of carbonyl allylation reactions

So far, most allylation protocols involved the classical electrophile-nucleophile reactivity, together with the use of metals. Recently, however, the interest for alternative methodologies involving radical pathways kept growing,[69] aiming at expanding the scope,[92] increasing the functional group tolerance, and developing new synthetic strategies for otherwise-inaccessible compounds (Scheme 4.1).
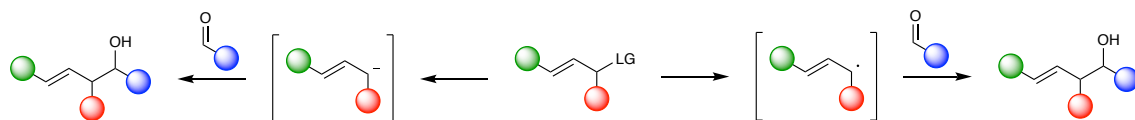
Scheme 4.1: Classical polar approach vs. radical approach for the allylation reaction of aldehydes. LG stands for "leaving group".

Moreover, typical polar chemistry is limited to the use of allylic electrophiles (such as allyl halides), while radical protocols disclose the use of less activated reaction partners, such as those with allylic C−H, allenes, 1,3-dienes. Indeed, first photocatalytic allylation protocols belong to such radical approach.[93] Until a few years ago, two main photochemical strategies have been employed for the activation of carbonyl compounds (Scheme 4.2): (i) ketyl radical formation followed by a radical-radical coupling, (ii) direct radical addition to the carbonyl compound, with the formation of an alkoxy radical.
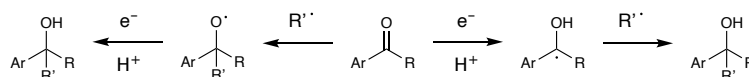
Scheme 4.2: Main radical strategies for the allylation of carbonyl compounds.

The first strategy relies on the relative persistency of aromatic ketyl radicals,[94] which enables their coupling reaction with other transient radicals in solution. Some noteworthy examples were reported by Chen and co-workers in 2016,[95] and by König and co-workers in 2018.[96] The remarkably high reduction potentials of aromatic carbonyl compounds represented a major issue of this strategy: strongly reducing reaction partners (not so easily available) are required, and their high reactivity often promotes undesired parasite reactions. Moreover, the reduction potentials are even higher for aliphatic carbonyl compounds, and the obtained aliphatic ketyl radicals are too reactive to be sufficiently persistent. The second approach has been rarely applied so far. The direct radical addition to a carbonyl is thermodynamically unfavoured and reversible. Indeed, the resulting oxygen radical is highly unstable and rapidly decomposes via C−C β-scission.[97,98] Glorius and co-workers were able to control this decomposition pathway,[99,100] using the so-called electron/hole catalysis.[101] The protonation of carbonyl oxygen favours the radical addition with the formation of the desired product. Unfortunately, any attempts to perform this strategy in a stereocontrolled fashion have failed so far.

The aforementioned RPCO strategy appeared again with the advent of metallaphotoredox catalysis, starting from 2017.[102] Its reductive version (RRPCO) has been successfully employed for decades. Remarkable examples are the samarium-mediated Barbier-type coupling reactions reported by Kagan and Molander.[103,104] This strategy relies on the formation of a carbanion (usually as a nucleophilic organometallic species) through the reduction of a radical intermediate generated in situ (Scheme 4.3).
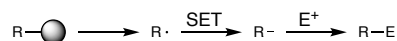
Scheme 4.3: RRPCO strategy. The left-hand species can even be electrophilic, hence this strategy enables the formal reaction between two electrophiles.

Almost simultaneously, starting from 2018, several photocatalytic Barbier-type allylation reactions under RRPCO conditions were described, with the involvement of nickel,[105,106] chromium,[107–109] titanium,[36,110] and cobalt.[111] Stereoselective versions with chromium[109,112] and nickel[113] were also developed. The latter achievements proved that asymmetric approaches can be developed also using photoredox conditions, in the presence of metals. One of the main drawbacks of classical Barbier-type reactions, i.e. the production of large amounts of metallic waste, is avoided using photoredox Barbier conditions, since metal co-reductants (such as Mn or Zn) are no longer required. Depending on the allylic source, sacrificial reducing agents – such as organic molecules, e. g. an amine (DIPEA or TEA) or Hantzsch's ester – may be necessary to ensure the turnover of the photoredox cycle. This is not the case for the reported examples involving chromium: the allylic sources are unfunctionalized alkenes with hydrogen atoms in allylic positions, requiring a C−H activation step, which in turn avoids the need for sacrificial reducing agents (Figure 4.15).
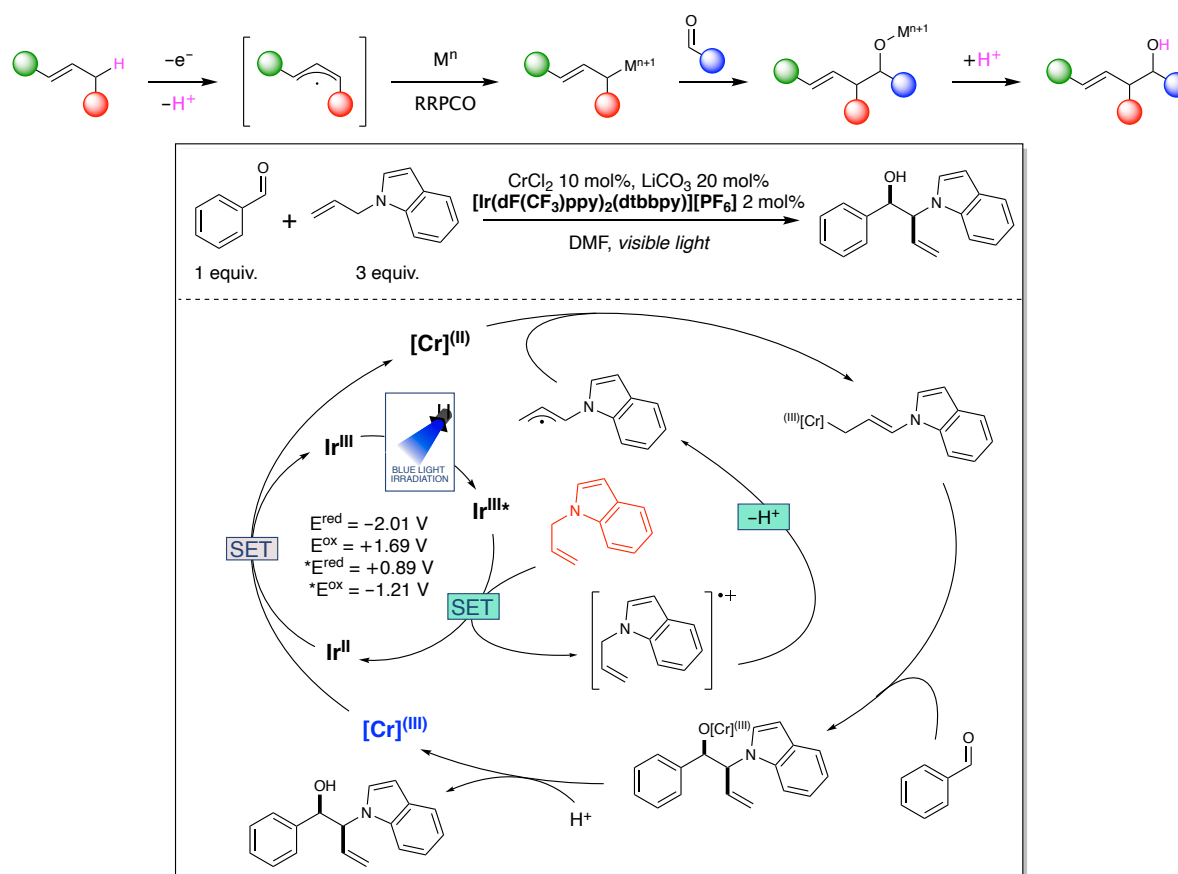
Figure 4.15: Top: general RRPCO strategy via C−H activation for the allylation reaction of aldehydes. The first step (indeed a PCET) ensures – with the mediation of the photosensitizer – the turnover of the metal catalytic cycle, through the restoration of the original M^n oxidation state. No sacrificial reducing agents are thus required. **Bottom:** diastereoselective allylation of aldehydes by dual photoredox and chromium catalysis, reported by Glorius and co-workers in 2018 (Ref. 107).

C−C bond formation: the case of carbonyl allylation reactions

On the contrary, in the case of nickel, cobalt, and titanium, the catalytic cycle is feasible with the use of an organic reducing agent: the allylic sources are allyl halides/acetates, and the missing H is supplied by the reducing agent (Figure 4.16).
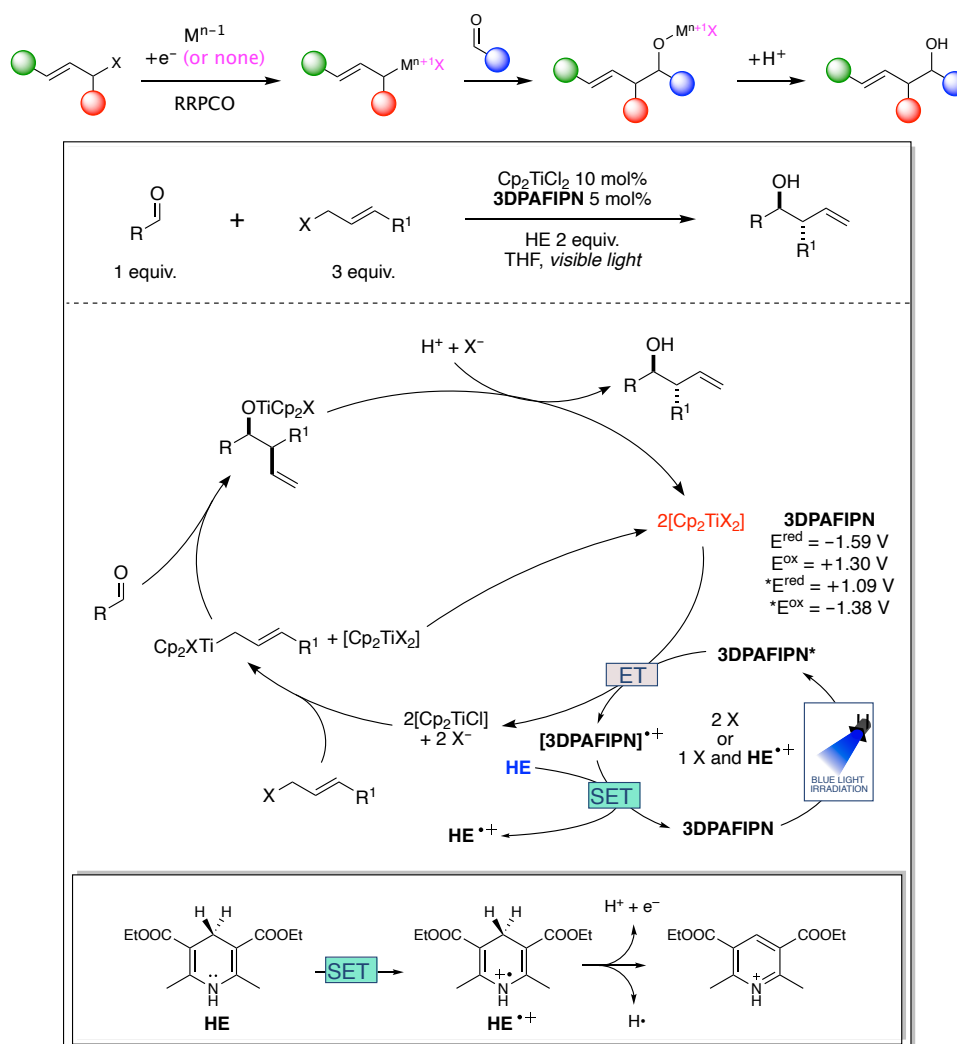

Figure 4.16: Top: general RRPCO strategy via metal insertion into the C−X bond for the allylation reaction of aldehydes. With no SET events during the first step, the insertion is indeed a classical oxidative addition, with the metal oxidation state being increased by two. Regardless this detail, a sacrificial reducing agent (also acting as a proton source for the last step) is required to ensure – with the mediation of the photosensitizer – the turnover of the metal catalytic cycle, through the restoration of the original M^{n-1} oxidation state. **Bottom:** Cp_2TiCl_2-catalysed photoredox allylation of aldehydes, reported by Cozzi and co-workers in 2020 (Ref. 110).

All the reported allylation reactions are performed in the presence of a photosensitizer (either an iridium complex or an organic dye). However, Gansäuer has recently pointed out that titanium complexes themselves can act as photosensitizers and catalyse some reactions under precise conditions (green light irradiation),[114] and similar behaviours were observed with some iron complexes.[115] Even some nickel complexes display photocatalytic properties when irradiated with lower wavelengths.[116] Nevertheless, no photoredox allylation protocols exploiting the use of Ti/Fe/Ni complexes as photosensitizers have been reported so far. Finally, it is worth mentioning that numerous water-compatible non-photocatalytic Barbier-type reactions have been optimized with certain types of metals, such as zinc,[117] indium,[118] bismuth,[119] and gallium,[120] using allyl halides as the allylic source, but even in these circumstances the high

production of metallic waste cannot be avoided, since overstoichiometric metal reductants are still required. As explained before, metallaphotoredox catalysis represent a straightforward strategy to avoid this issue. However, its application in aqueous media is still a largely unexplored area: most of the reported photocatalytic strategies in water have nothing to do with metal catalysis.[121,122]

4.2. Aim

The development of sustainable green methodologies is nowadays the main guideline of modern synthetic organic chemistry. Hence, the replacement of toxic transition metals with easy-to-handle non-toxic ones was studied as a highly desirable goal. As already mentioned, this step forward is appealing also in the specific case of photocatalytic Barbier-type allylation reactions, since they can be performed using metal-free organic photosensitizers. The reported use of non-toxic metals in some non-photocatalytic water-compatible Barbier-type allylation reactions (vide supra) makes water a desirable co-solvent for the optimization of even greener metallaphotoredox strategies.[†] In light of all this, bismuth was chosen as the metallic catalytic partner. Indeed, bismuth-mediated Barbier-type allylation reactions have been already reported, either stoichiometric[123,124] or catalytic in bismuth.[119] When needed, the most common terminal stoichiometric reductants were iron, aluminium, zinc, and $NaBH_4$.[125] In the case of aromatic aldehydes, the undesired pinacol coupling reaction between ketyl radicals (via PCET mechanism, vide supra) represents a possible major drawback of the bismuth-mediated allylation reaction in its photocatalytic version, especially if acidic conditions are required to ensure the turnover of bismuth catalyst. This issue made the reported optimization study even more challenging. Finally, future perspectives concerning other electrophiles as suited substrates will be also discussed.

[†] Some further comments about sustainability can be found in Section 4.4.

4.3. Results and discussion – Photocatalytic Bi-mediated allylation reaction in aqueous media

Bismuth is an Earth-abundant metal, and its only natural isotope, i.e. ^{209}Bi, is considered as the heaviest stable isotope.[126] Contrary to the surrounding elements on the periodic table, bismuth is inexpensive and relatively non-toxic.[127,128] Some bismuth compounds are indeed widely used as valuable drugs.[129,130] These features make bismuth a good candidate for green and sustainable processes, replacing transition metals commonly used in catalysis, such as palladium and nickel.[†] Organobismuth compounds are either trivalent or pentavalent (Figure 4.17), although some examples of tetra- or hexa-coordinated species have been reported, and generally show low toxicities. Gagnon and co-workers have recently published a comprehensive review on the synthesis and reactivity of organobismuth compounds.[131]
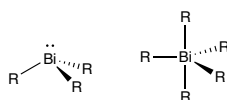
Figure 4.17: General structures of trivalent (left) and pentavalent (right) organobismuth compounds.

In terms of synthetic organic chemistry, organobismuth compounds have been mainly used as arylating agents, starting with the pioneering works of Barton and co-workers in the 1980s (Scheme 4.4).[132]
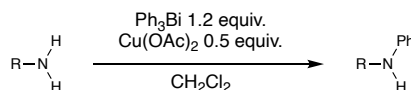
Scheme 4.4: Phenylation of amines by Ph₃Bi and Cu(OAc)₂ (Ref. 132).

Numerous compounds were found to be suited substrates for arylation with organobismuth compounds: diols, alcohols, amines, amides, carbamates, heterocycles with a pyrrolic nitrogen, phenols, and active-methylene compounds were employed to form C−C, C−O, C−S, and C−N bonds.[133] Since the active arylating species is a pentavalent organobismuth species, an external oxidant is required when a trivalent organobismuth compound is used. These arylation reaction can be either acid- or base-catalysed. In some cases, similarly to what is observed for other coupling reactions, e.g. Ullmann and Chan-Lam couplings, catalytic amounts of copper salts are required. In most cases, the involved trivalent organobismuth compound can give away only one of the three substituents, but there are some remarkable exceptions.[134] Recently, the ability of bismuth compounds to shuttle between different oxidation states – bismuth has four easily-accessible oxidation states (+1, +2, +3, +5) – has been extensively studied, with the aim of investigating the possibility of replacing transition metals with bismuth compounds in redox processes.[135] However, the bismuth redox chemistry still remains largely unexplored, and only very few redox cycles

---

[†] Some further comments about sustainability can be found in Section 4.4.

are known and have been investigated with satisfying experimental evidences. In 2018, Coles and co-workers developed an oxidative coupling between TEMPO and phenylsilanes, exploiting a Bi(II)/Bi(III) catalytic cycle, the first accurately-described bismuth-based catalytic cycle.[136] This work represented the first example of dehydrosilylation reaction catalysed by a main-group metal. Besides, it provided an interesting experimental evidence of a Bi(II) species engaging a radical oxidative addition. In 2019, Cornella and co-workers exploited a Bi(I)/Bi(III) cycle to promote a transfer-hydrogenation reaction of azo- and nitro-arenes with ammonia-borane complex.[137] The first examples of Bi(III)/Bi(V) cycles were reported in 2020. Ball and co-workers developed a bismuth-mediated ortho-selective arylation of phenols and naphthols with boronic acids, exploiting a B-to-Bi transmetalation step involving a Bi(III) intermediated.[138] Upon oxidation with an external oxidant, the resulting Bi(V) species can undergo a reductive coupling between ligands to afford the desired product. Cornella and co-workers reported a fluorodeborylation of boronic esters.[139] In this case, the bismuth complex show a similar behaviour to that observed for transition-metal complexes in traditional coupling reactions: transmetalation, oxidative addition, and reductive elimination. Very recently, Cornella and Moon have presented an exhaustive overview on bismuth redox catalysis, highlighting the twofold nature of bismuth, which can be engaged either in low-valent catalysis, involving Bi(II)/Bi(III) or Bi(I)/Bi(III) shuttling, or in high-valent catalysis, involving Bi(III)/Bi(V) cycles.[140]

All the aforementioned features of bismuth, together with its reported use in aqueous media,[141,142] make it an appealing metal to be used as metal catalyst in new metallaphotoredox synthetic approaches, with particular reference to carbonyl allylation reactions.

4.3.1. *First things first: the choice of the photosensitizer*

For a long time, ruthenium and iridium complexes (vide supra) have been by far the most employed photosensitizers in photocatalysis. An outstanding number of Ir- and Ru-based photosensitizers – with different photophysical and electrochemical properties (with particular reference to the redox potentials) – have been prepared and characterized so far.[54] In particular, most of them have strongly reducing excited states. The latter is a highly desirable property for the generation of metallic species in low oxidation states in catalytic Barbier-type conditions. Nevertheless, no sure a priori evaluations can be made, and the suitable photosensitizer can be found only by means of optimization studies, also taking into account the possibility of varying the reaction conditions. However, the exploitation of such photosensitizers clashes with many sustainability principles, such as the need to reduce as much as possible the use of metals, in order to avoid difficult removal processes from the final product. Moreover, Ru and Ir are rare and expensive metals, whose utilization in process and medicinal chemistry increases the prices of the final products. Hence, many efforts have been made to develop new photosensitizers, either changing the metal (Cu-[143] and Fe-based[18] photosensitizers have been reported)

or switching to organic dyes. Until recently, the main drawback of the latter was their hardly tuneable redox potential. However, in 2018, Zeitler and co-workers presented a work describing their attempt to overcome this drawback, through the development of a peculiar class of organic photosensitizers based on either isophthalonitrile- or benzonitrile-type scaffolds,[55] starting from the well-known 4CzIPN described by Adachi in 2012.[41] Shrewd modifications of the substitution pattern enabled the fine modulation of redox properties (Table 4.1): the variations of the electron-acceptor substituents (e.g. halogen atoms and CN) affect the energy of the LUMO, while those of the electron-donor substituents (e.g. carbazolyl and diphenylamino groups) affect the energy of the HOMO (vide supra).
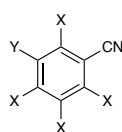
Table 4.1: Redox potentials of the photosensitizers examined by Zeitler and co-workers[55] All the values are reported in V vs SCE (standard calomel electrode). Measurements were performed in MeCN, unless otherwise specified. The general structure is reported above for sake of clarity (see table notes).

Photosensitizer[a]	$E_{1/2}$ (PC·+/PC*)	$E_{1/2}$ (PC*/PC·−)	$E_{1/2}$ (PC·+/PC)	$E_{1/2}$ (PC/PC·−)
4CzIPN[b]	−1.18	+1.43	+1.49	−1.24
3DPAFIPN[c]	−1.38	+1.09	+1.30	−1.59
5CzBN[d]	−1.42	+1.31	+1.41	−1.52
3DPA2FBN[e,f]	−1.60	+0.92	+1.24	−1.92
3CzClIPN[g]	−0.93	+1.56	+1.79	−1.16
3DPAClIPN[h]	−1.34	+1.24	+1.31	−1.41
4MeOCzIPN[i,j]	−1.50	+1.27	+1.11	−1.34
5MeOCzBN[k,f]	−1.79	+1.15	+1.02	−1.66

[a] The numbers reported in the acronyms denote the number of substituents, not their positions, which are instead determined as follows: with reference to the above-reported general structure, the numbering starts from the CN-bearing carbon (numbered as 1) and proceeds counterclockwise. The substitution patterns are accordingly reported in the following. **[b]** X = carbazolyl group (Cz), Y = CN. **[c]** X_2, X_4, X_6 = NPh$_2$, X_5 = F, Y = CN. **[d]** X, Y = Cz. **[e]** X_2, X_4, X_6 = NPh$_2$, X_5, Y = F. **[f]** Measured in CH$_2$Cl$_2$. **[g]** X_2, X_4, X_6 = Cz, X_5 = Cl, Y = CN. **[h]** X_2, X_4, X_6 = NPh$_2$, X_5 = Cl, Y = CN. **[i]** X = 3,6-dimethoxy-Cz, Y = CN. **[j]** Measured in MeCN/CH$_2$Cl$_2$ 5:1 v/v. **[k]** X, Y = 3,6-dimethoxy-Cz.

It is worth mentioning that these photosensitizers can be synthetized with a single step starting from commercially available starting materials, such as tetrachloroisophthalonitrile, tetrafluoroisophthalonitrile and pentafluorobenzonitrile (Scheme 4.5).
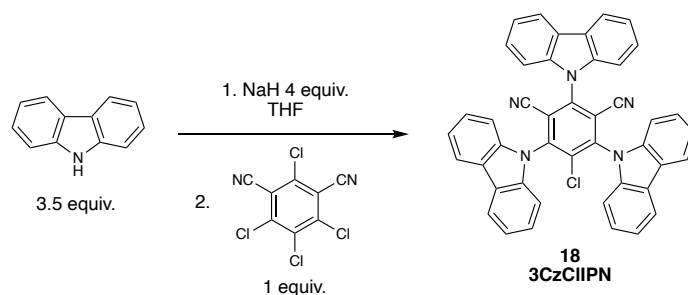
Scheme 4.5: Selected synthesis of an organic dye: 3CzClIPN starting from carbazole and tetrachloroisophthalonitrile.

Some of these photosensitizers have been already used to promote the metallaphotoredox allylation of aldehydes, using allyl bromide as the allylic source (vide supra, Figure 4.16).[110] The general allylation reaction under metallaphotoredox conditions is reported in Scheme 4.6.
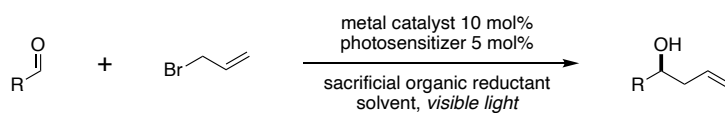
Scheme 4.6: General allylation reaction under metallaphotoredox conditions.

An important drawback of this class of photosensitizers is that, in the presence of aromatic aldehydes, they can promote – in the presence of a suited sacrificial reductant – the uncatalyzed pinacol coupling reaction even in the presence of the metal catalyst. Indeed, a pinacol coupling reaction mediated by 4CzIPN was recently reported.[144] According to this work, the photosensitizer in its reduced formed (generated upon reductive quenching by Hantzsch's ester **21**) is able to promote the formation of the ketyl radical (Figure 4.18). This process is also eased because of the formation of a hydrogen-bonded complex between the aldehyde and the radical cation of **21**. This lowers the reduction potential of the aldehyde, thus favouring the formation of the respective ketyl radical.
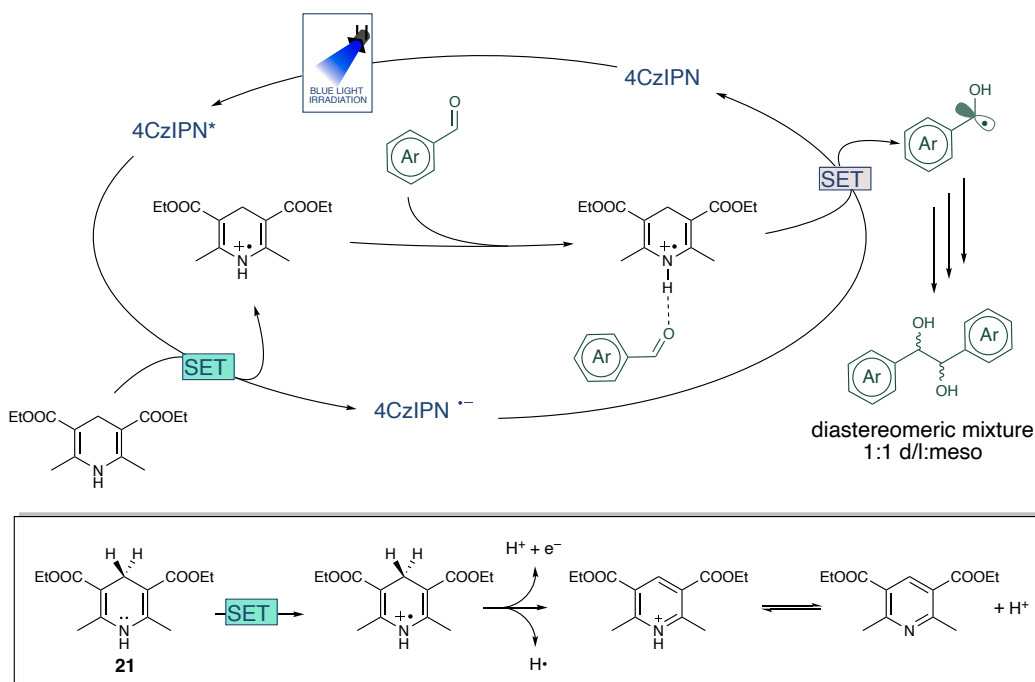
Figure 4.18: Photocatalytic pinacol coupling reaction of aromatic aldehydes mediated by 4CzIPN (Ref. 144).

In order to avoid this undesired reaction, the reducing forms of the photosensitizer (PS* and PC$^{\bullet-}$) must have not excessively high redox potentials compared to those of aromatic aldehydes: both $E_{1/2}$ (PC$^{\bullet+}$/PC*) and $E_{1/2}$ (PC/PC$^{\bullet-}$) should be as low as possible (in absolute value). Among the photosensitizers reported in Table 4.1, 3CzClIPN **18** represents the best choice. It can be easily prepared in a single step from commercially available carbazole and tetrachloroisophthalonitrile (vide supra).

As far as bismuth redox potentials – especially those referring to the reduction of commercially available Bi(III) sources – are concerned, very few literature data are available,[145,146] but they are easily accessible when compared to those of the aforementioned reducing PS forms.

4.3.2. *Optimization of reaction conditions*

The optimization study for the bismuth-mediated allylation protocol (vide supra, Scheme 4.6) was performed using 4-chlorobenzaldehyde as model substrate. The first studied parameter was the reaction solvent (Table 4.2). Water was used as co-solvent according to other reported water-compatible non-photocatalytic bismuth-mediated allylation protocols under Barbier conditions, but also in analogy to what has been observed in the case of a cobalt-mediated metallaphotoredox allylation reaction, reported by Cozzi and co-workers in 2020.[111]

Optimization of reaction conditions

Table 4.2: Screening of reaction solvents.
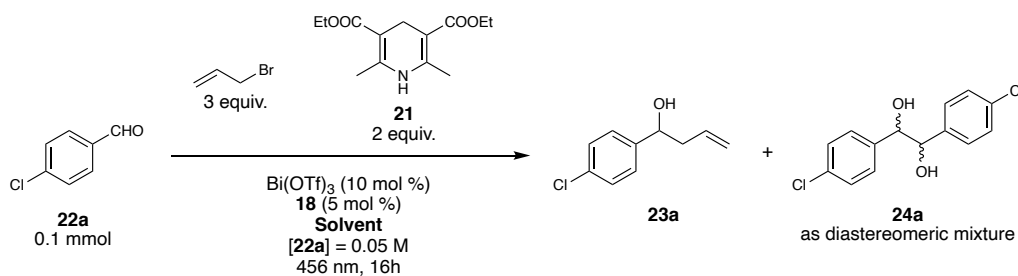
Entry[a]	Solvent	Conv. (%)[b]	23a (%)[b]	23a:24a (%)[b,c]
1	THF/H_2O 9:1	96	30	31:69
2	THF/H_2O 1:1	97	51	52:48
3	DMF/H_2O 1:1	56	48	85:15
4	MeCN/H_2O 1:1	80	45	56:44
5	DMSO/H_2O 1:1	98	66	68:32
6	MeOH/H_2O 1:1	>99	79	79:21
7	EtOH/H_2O 1:1	>99	83(74)[d]	83:17
8	EtOH	90	62	69:31
9	H_2O	92	50	55:45
10[e]	THF/H_2O 9:1	>99	19	19:81

[a] All the reactions were carried out under irradiation with Kessil® 40W blue LED. **[b]** Determined by ^{1}H-NMR. **[c]** The sum of **23a** and **24a** has been normalized to 100. The d.r. for **24a** is ~1:1 for all the reactions. **[d]** Isolated yield after chromatographic purification is reported in parenthesis (0.2 mmol reaction scale). **[e]** **19** instead of **18**. Reaction time: 64h.

Indeed, increasing the amount of water as co-solvent proved to be beneficial for the outcome of the reaction, since the THF/H_2O 1:1 solvent mixture (entry 2) was found to overperform with respect to the THF/H_2O 9:1 mixture (entry 1) in inhibiting the pinacol coupling parasite reaction. Several water-miscible organic solvents were tested (entries 3−7). EtOH represented the best compromise in terms of both conversion and pinacol coupling inhibition (entry 7). Used on their own, both EtOH (96%) and water had worse reaction outcomes (entries 8, 9). The use of a 1:1 EtOH/H_2O solvent mixture represents an important strength in terms of sustainability. EtOH is a green solvent which can be produced starting from biomasses.[147] Besides, it is very inexpensive (40 \$/L) compared to other commonly used green solvents, such as 2-MeTHF (235 \$/L) and ethyl acetate (71 \$/L).[148] As highlighted above, the use of a more reducing photosensitizer proved to be detrimental, and the reaction mainly led to the formation of the pinacol coupling product (entry 10). Table 4.3 reports the reaction outcomes using different allylating reagents.

Table 4.3: Screening of allylating reagents.
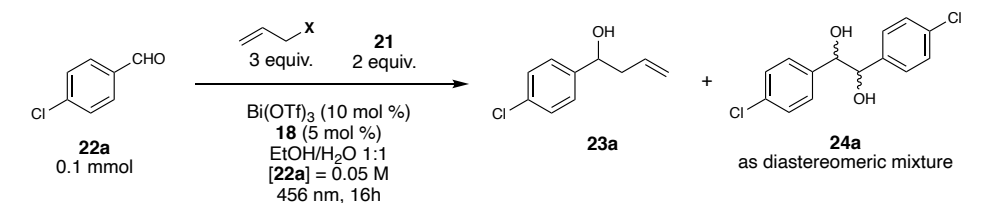
Entry[a]	X	Conv. (%)[b]	23a (%)[b]	23a:24a (%)[b,c]
1	Br	>99	83	83:17
2	Cl	15	7	48:52
3	I	12	12	>99:1
4	OH	97	0	<1:99
5	OAc	>99	0	<1:99

[a] All the reactions were carried out under irradiation with Kessil® 40W blue LED. **[b]** Determined by ^{1}H-NMR. **[c]** The sum of **23a** and **24a** has been normalized to 100. The d.r. for **24a** is ~1:1 for all the reactions.

Allyl bromide is the best allylic source among allyl halides, while no reaction was observed using either allyl alcohol or allyl acetate (entries 4 and 5, respectively). Noteworthily, allyl iodide proved to be the best allyl source in terms of inhibition of the pinacol coupling reaction, but the conversion was unsatisfactory (entry 3). Table 4.4 reports the reaction outcomes using different bismuth sources, and with different catalytic loadings.

Optimization of reaction conditions

Table 4.4: Screening of bismuth salts (counterions and catalytic loadings).
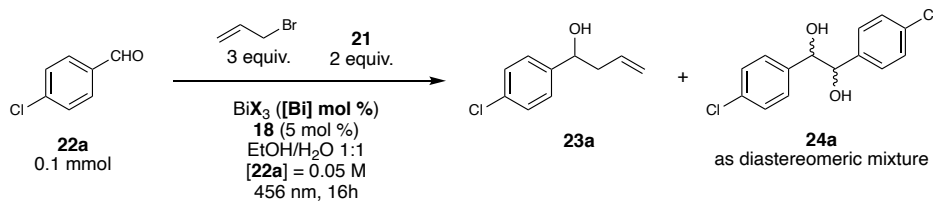
Entry[a]	X	[Bi] mol %	Conv. (%)[b]	23a (%)[b]	23a:24a (%)[b,c]
1	OTf	10	>99	83	83:17
2[d]	OTf	10	>99	79	79:21
3[d]	OTf	5	>99	78	78:22
4[d]	OTf	2	>99	58	58:42
5	Cl	10	50	50	>99:1
6	Br	10	>99	87	87:13
7	Br	5	82	77	87:13
8	Br	2	68	59	79:21

[a] All the reactions were carried out under irradiation with Kessil® 40W blue LED. **[b]** Determined by ^{1}H-NMR. **[c]** The sum of **23a** and **24a** has been normalized to 100. The d.r. for **24a** is ~1:1 for all the reactions. **[d]** MeOH instead of EtOH.

Noteworthily, bismuth bromide was found to be the best tested salt (entry 6). Eventually, bismuth triflate was chosen because it is an easy-to-handle salt, contrary to the highly hygroscopic bismuth bromide. Moreover, the former is less toxic than the latter. Nevertheless, it is worth mentioning that, in the case of bismuth bromide, satisfying results in terms of selectivity can be achieved even with lower catalytic loadings, even if with decreasing conversions (entries 7, 8). Finally, bismuth chloride showed a remarkably lower conversion, but only traces of the pinacol coupling product were detected (entry 5). Finally, Table 4.5 reports the reaction outcomes with different sacrificial reducing agents.

Table 4.5: Screening of sacrificial reductants.
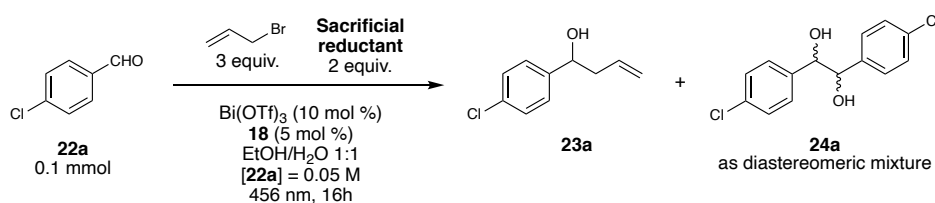
Entry[a]	Sacrificial reductant	Conv. (%)[b]	23a (%)[b]	23a:24a (%)[b,c]
1	**21**	>99	83	83:17
2	TEA	44	44	>99:1

[a] All the reactions were carried out under irradiation with Kessil® 40W blue LED. **[b]** Determined by ^{1}H-NMR. **[c]** The sum of **23a** and **24a** has been normalized to 100. The d.r. for **24a** is ~1:1 for all the reactions.

Triethylamine had a strong inhibition effect against the pinacol coupling reaction, but it underperformed in terms of conversion.
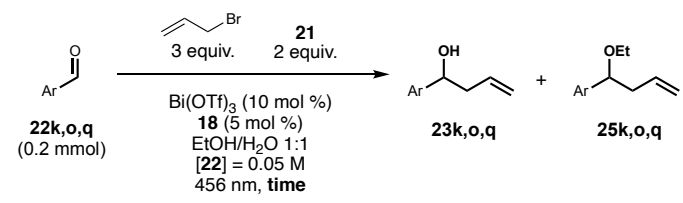
4.3.3. *Reaction scope*

The optimal reaction conditions were explored with a large variety of aromatic and aliphatic aldehydes, and the salient results are reported in Schemes 4.7 and 4.10, respectively.
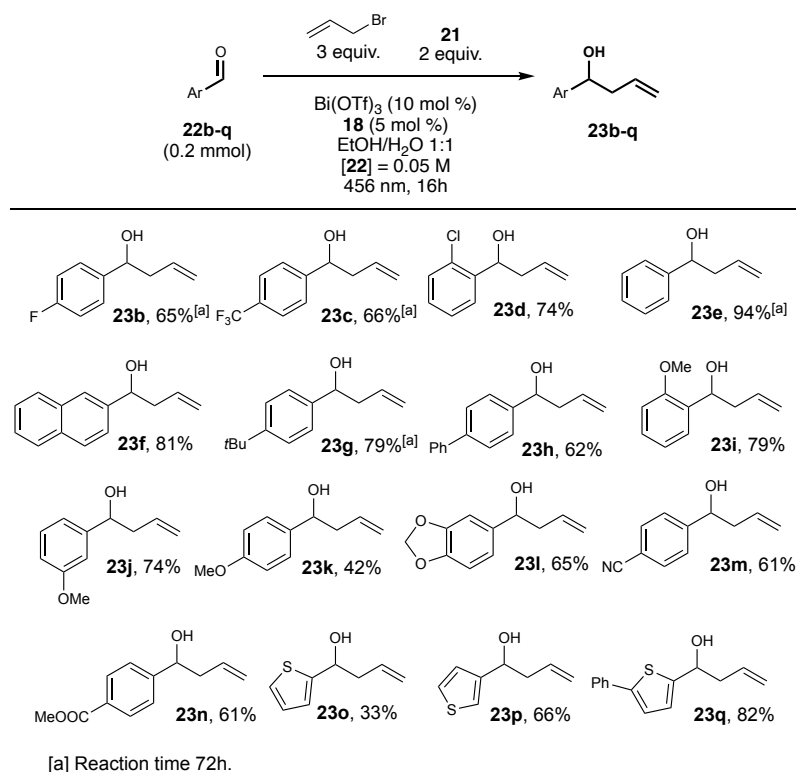
Scheme 4.7: Photoredox allylation of aromatic aldehydes mediated by bismuth.

In general, with aromatic aldehydes, the isolated yields were from moderate to good, with a variety of different functional groups compatible with the reaction conditions. Both electron-rich and -poor aromatic aldehydes are reactive and, in some cases, yields could be improved by an increase of the reaction time to 72h. Sterical hindrance in *ortho* position has no detrimental effects. Heteroaromatic aldehydes can be also employed, with some limitations. Indeed, electron-rich aldehydes bearing pyrrole or indole are unstable during chromatographic purifications due to their attitude to form elimination products. Thiophene is a compatible group, but 2-thiophene carboxaldehyde **22o** was found poorly reactive, probably due to chelation of sulfur to the bismuth active species. The reactivity is restored when 3-thiophene carboxaldehyde **22p** is employed. When long reaction times (72h) were applied to the reactions of the aldehydes **22k**, **22o** and **22q**, by-products were observed (Table 4.6). Noteworthily, the corresponding ethyl ether of the homoallylic alcohols (**23k,o,q**) formed by their reaction with ethanol was detected (and isolated only for **22k**).

Reaction scope

Table 4.6: Screening of reaction times for aldehydes **22k,o,p**.

Aldehyde	Reaction time (h)	Conv. (%)[a]	23:25 (%)[a,b]
22k	16	51	92:8
	72	51	21:79
22o	16	50	>99:1
	72	69	53:47
22q	16	70	86:14
	72	82	<1:99

[a] Determined by ^{1}H-NMR. [b] The sum of **23** and **25** has been normalized to 100.

Although Bi(OTf)$_3$ is described as a catalyst for S$_N$1-type reaction of alcohols,[149] the formation of ethers was determined by the Brønsted acidity of the oxidized Hantzsch's ester (Scheme 4.8).
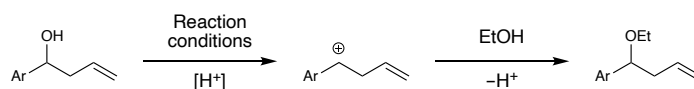
Scheme 4.8: Putative pathway for the formation of **25k,o,q**.

This behaviour was confirmed by dissolving the alcohol **23k** in EtOH in the presence of the pyridinium salt derived from the oxidation of Hantzsch's ester (Scheme 4.9). The formation of these ether by-products was observed only for alcohols bearing an electron-rich aromatic ring.
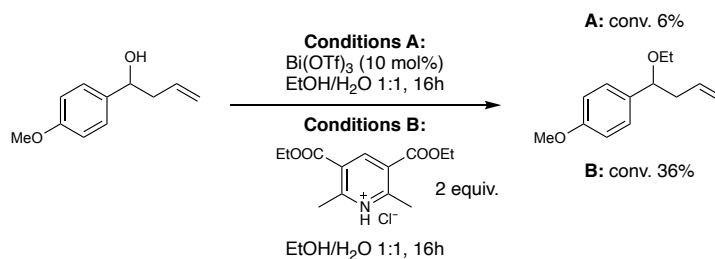
Scheme 4.9: Etherification tests using homoallylic alcohol **23k**. The reported conversions were determined by ^{1}H-NMR. The pyridinium salt (used in conditions B) was obtained by acidic treatment (HCl 1M in Et$_2$O) of oxidized Hantzsch's ester (i.e. its pyridinic form, recovered after chromatographic purifications of compounds **24**), followed by solvent evaporation.
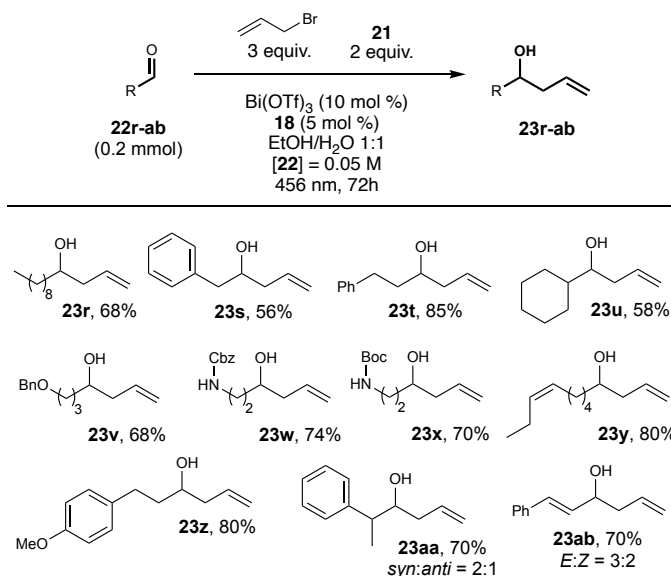
Scheme 4.10: Photoredox allylation of aliphatic aldehydes mediated by bismuth.

Good reaction outcomes were also observed with aliphatic aldehydes **22r–ab**. Several functional groups are tolerated in the reported conditions and the reaction is applicable to linear and branched aldehydes with a reaction time of 72h. Interestingly, cinnamaldehyde (**22ab**) gave a mixture of *E* and *Z* isomer of the corresponding allylated product (**23ab**), probably due to photoisomerization of cinnamaldehyde in presence of light and photosensitizer.[150–152] Concerning the use of substituted allyl bromides, some of them (reported in Figure 4.19) were tested in the reaction with aldehyde **22f** with poor conversions. Whereas prenyl and crotyl bromide (conversions at 72h: 23% and 47%, respectively) led to the exclusive formation of branched products (*syn:anti* = 3:1 in the case of crotylation), cinnamyl bromide gave a complex mixture of products.
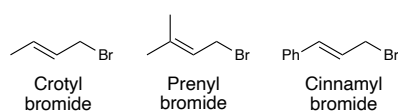
Figure 4.19: Tested substituted allyl bromides.

Other electrophiles (reported in Figure 4.20) were tested with the optimized reaction conditions: epoxides (cyclohexene oxide) and aromatic ketones (acetophenone) were proved unreactive, while traces of allylated products were detected in the case of aliphatic and α,β-unsaturated ketones (cyclohexanone and benzylideneacetone). These results proved that this reaction protocol can be used for the selective allylation of aldehydes in the presence of other electrophilic groups, e.g. epoxides and ketones. Further studies involving imine-type derivatives are currently ongoing. In this case, however, the use of water is detrimental because most imines undergo hydrolysis due to the strongly acidic reaction conditions.

Cyclohexene oxide   Acetophenone   Cyclohexanone   Benzylideneacetone   Imine-type derivative
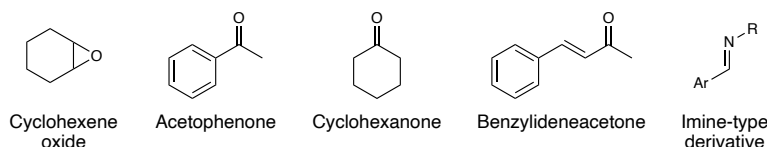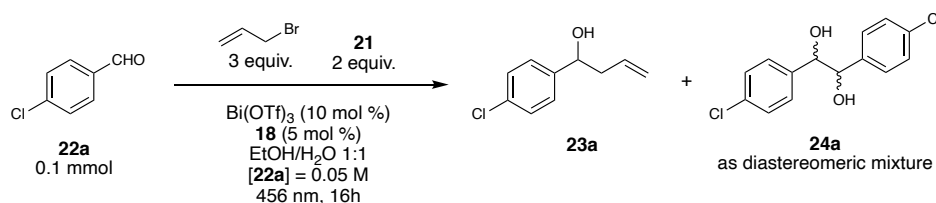
Figure 4.20: Other tested electrophiles.

4.3.4. *Mechanistic studies*

The mechanistic picture was assessed by means of control experiments and photophysical studies. The former are reported in Table 4.7.

Table 4.7: Control experiments for bismuth-mediated photoredox allylation of aldehydes.

Entry[a]	Deviation from standard conditions	Conv. (%)[b]	23a (%)[b]	23a:24a (%)[b,c]
1	–	>99	83(74)[d]	83:17
2	In air	90	70	79:21
3	In the presence of TEMPO (20 mol%)	>99	95	95:5
4	No Bi(OTf)$_3$	>99	16	16:84
5	No **18**	59	59	>99:1
6	No Bi(OTf)$_3$; No **18**	6	0	<1:99
7	No light	0	–	–
8[e]	1 mmol scale	89	85(77)	95:5

[a] All the reactions were carried out under irradiation with Kessil® 40W blue LED. **[b]** Determined by ¹H-NMR. **[c]** The sum of **23a** and **24a** has been normalized to 100. The d.r. for **24a** is ~1:1 for all the reactions. **[d]** Isolated yield after chromatographic purification is reported in parenthesis (0.2 mmol reaction scale). **[e]** The reaction was performed with 8 mol % of Bi(OTf)$_3$ and 3 mol % of **18**. Isolated yield after chromatographic purification is reported in parenthesis.

The reaction does not require strictly de-oxygenated solvents and can be conveniently settled without a freezing-pump thaw procedure to eliminate traces of oxygen (entry 2). The reaction is not sensitive to the presence of radical scavengers like (2,2,6,6-tetramethylpiperidin-1-yl)oxyl (TEMPO, entry 3). Noteworthily, only trace amounts (5%) of **24a** were detected. As a matter of fact, TEMPO behaves as a radical scavenger, hampering radical pathways, including those involved in the generation of **24a** (pinacol coupling via ketyl radical). This control experiments excluded the involvement of radical pathways in the allylation mechanism. In absence of the Bi(OTf)$_3$, but in the presence of **18**, the pinacol coupling of the aldehyde is favoured (entry 4),[23,153] probably according to the mechanism reported in Figure 4.18. If the reaction is carried out without **18**, under irradiation with blue LED (entry 5), a clean allylation reaction is

observed, although with lower conversion. This was probably due to the ability of bismuth to form a reactive allylating agent with the mediation of Hantzsch's ester **21** under light irradiation. In fact, when neither bismuth nor **18** are introduced in the reaction mixture (entry 6), the photoredox properties of the Hantzsch's ester favoured the pinacol coupling.[154] As expected, no reaction is observed in the absence of light (entry 7). The scale-up of the reaction (1 mmol) is possible, with even lower catalytic loadings for both the photosensitizer and the metal catalyst (entry 8).

Concerning the photophysical studies, Stern-Volmer experiments were performed to assess which reaction partner is involved in the quenching interaction with photosensitizer **18**. First, the absorption and emission spectra of **18** were recorded (Figure 4.21).
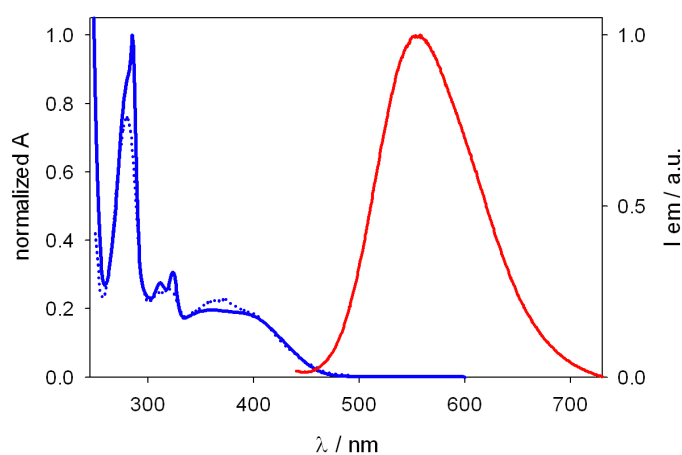
Figure 4.21: Absorption (blue solid line; the blue dotted line refers to high-dilution conditions) and emission spectrum (red line) recorded on a solution of **18** in air-equilibrated ethanol at room temperature.

The emission spectrum has a clear maximum (λ_{em}) at 550 nm. To ensure selective excitation of **18** during the Stern-Volmer experiments (vide infra), the excitation wavelength (λ_{ex}) was placed at 400 nm. Consistently with the reaction outcome of the in-air control experiment (Table 4.7, entry 2), the excited state of **18** is not quenched by oxygen: its lifetime has negligible changes moving from deaerated to air-equilibrated solution. As previously reported in literature,[36,110] isophthalonitrile derivatives represent a class of remarkably visible emitters, which can show long emission lifetimes in specific experimental conditions because of their TADF (thermally activated delayed fluorescence) behaviour.[64,155] Interestingly, **18** displays double deactivation kinetics at λ_{em} = 550 nm even in air-equilibrated ethanol at r.t., most likely due to a TADF-active regime, featuring a delayed component with a lifetime around 150 ns.

In the presence of increasing amounts of Bi(OTf)$_3$ or allyl bromide, no appreciable decrease in the emission intensities of **18** was detected (Figures 4.22 and 4.23, respectively), thus showing that these two reactants are not involved in quenching mechanisms even at high concentrations.
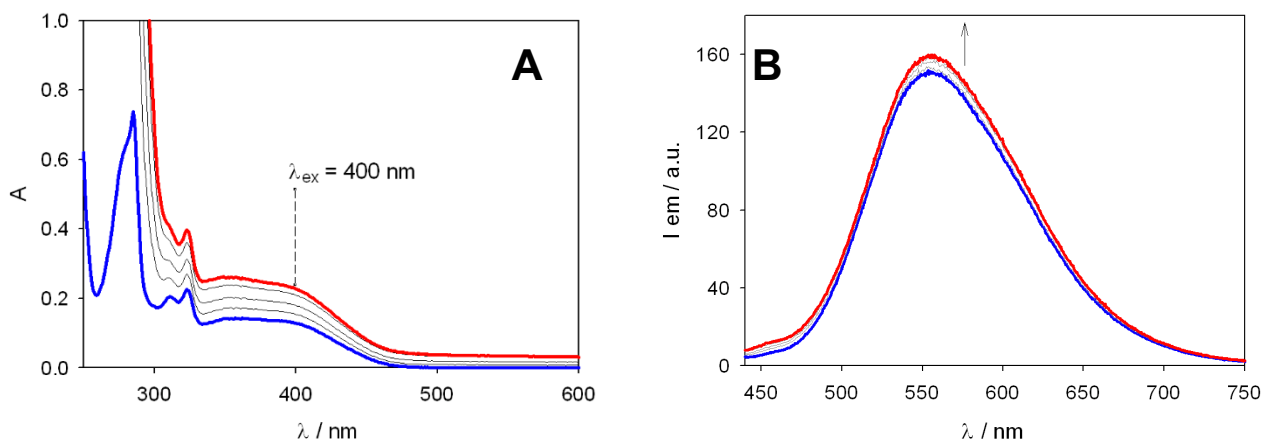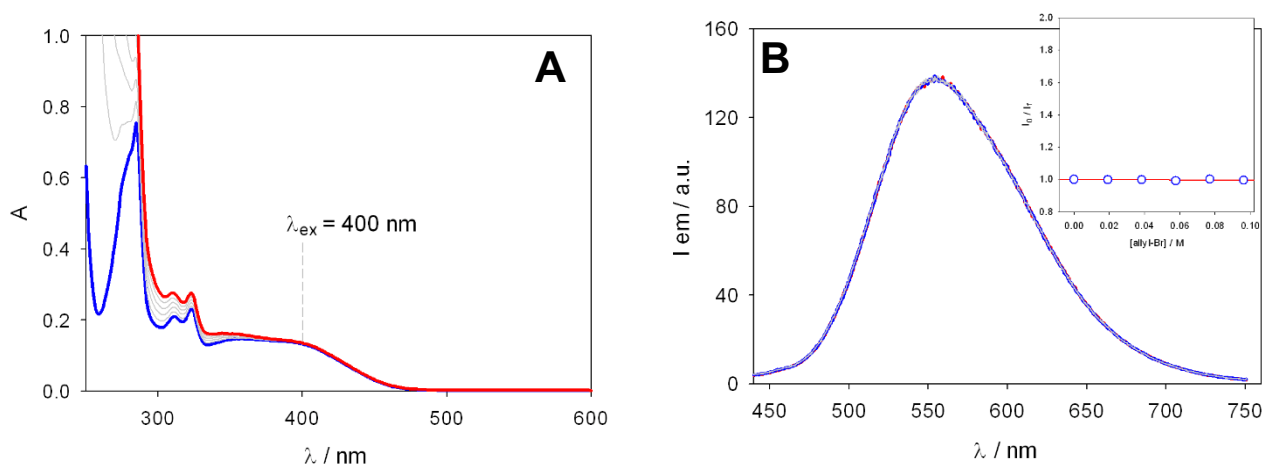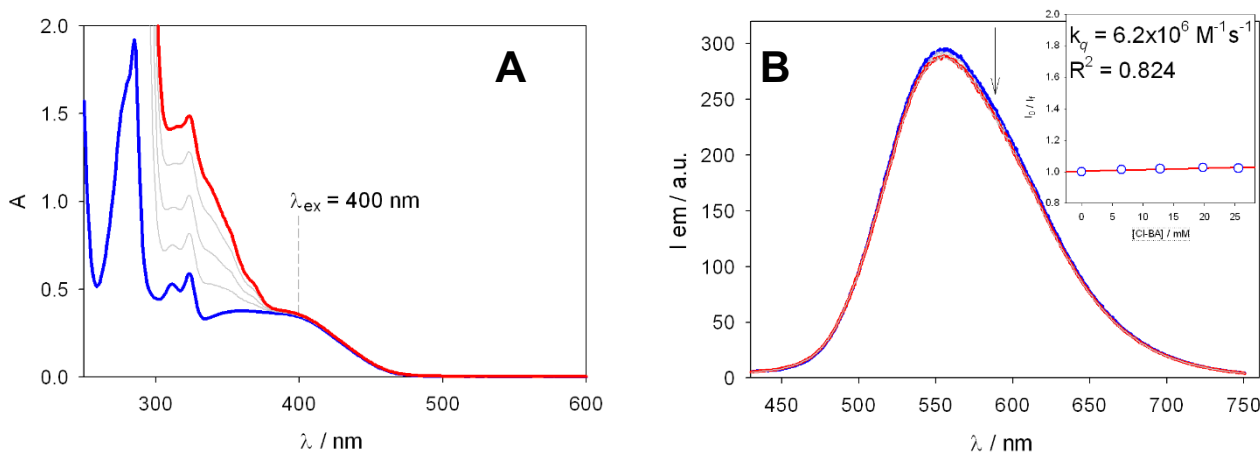
Figure 4.22: (A) Absorption spectra of solutions of **18** in air-equilibrated ethanol (blue line) obtained upon addition of increasing amounts of Bi(OTf)$_3$ (up to ca. 14 mM, red line). **(B)** Fluorescence emission spectra of **18** obtained from the same solutions at λ_{ex} = 400 nm.
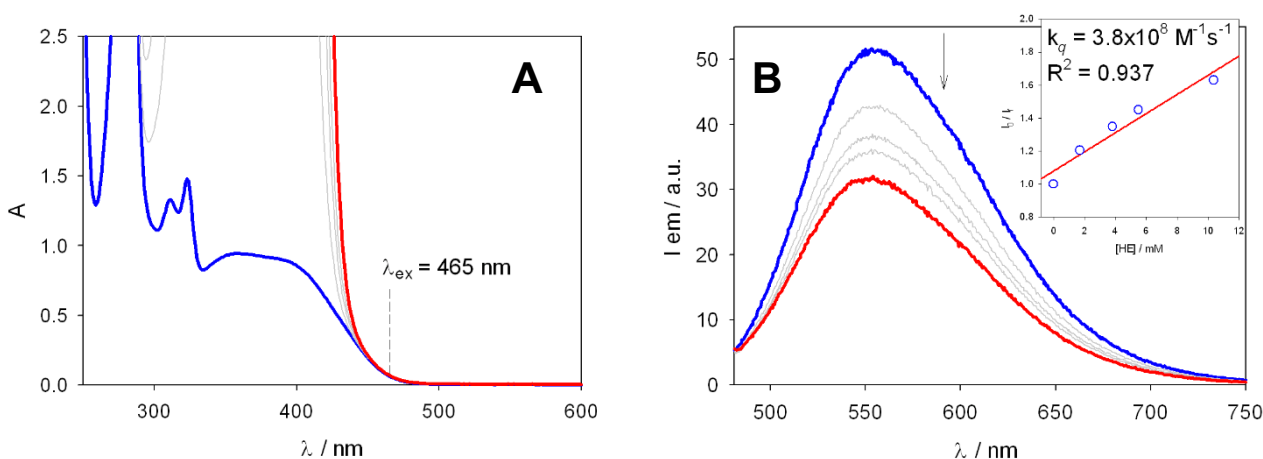

Figure 4.23: (A) Absorption spectra of solutions of **18** in air-equilibrated ethanol (blue line) obtained upon addition of increasing amounts of allyl bromide (up to ca. 95 mM, red line). **(B)** Fluorescence emission spectra of **18** obtained from the same solutions at λ_{ex} = 400 nm. Inset: Stern-Volmer diagram relative to the emission intensities at λ_{em} = 550 nm (since no quenching was detected, the quenching constant was not determined).

The addition of 4-chlorobenzaldehyde **22a** barely decreased the emission intensity of **18** (k_q = 6.2·10^6 M^{-1} s^{-1}), explaining the observed pinacol coupling in absence of Bi(OTf)$_3$ (Figure 4.24).

Figure 4.24: (A) Absorption spectra of solutions of **18** in air-equilibrated ethanol (blue line) obtained upon addition of increasing amounts of 4- chlorobenzaldehyde (**22a**, up to ca. 26 mM, red line). **(B)** Fluorescence emission spectra of **18** obtained from the same solutions at λ_{ex} = 400 nm. Inset: Stern-Volmer diagram relative to the emission intensities at λ_{em} = 550 nm.

A similar behaviour was observed when the Hantzsch's ester **21** is introduced in solutions of **18**, denoting a significantly more efficient quenching (two orders of magnitude) of the emission of the latter(k_q = $3.8 \cdot 10^8$ M^{-1} s^{-1}, Figure 4.25). Indeed, in the presence of both the aldehyde and **21**, the latter is by far the most efficient quencher.

Figure 4.25: (A) Absorption spectra of solutions of **18** in air-equilibrated ethanol (blue line) obtained upon addition of increasing amounts of Hantzsch's ester (**21**, up to ca. 10 mM, red line). **(B)** Fluorescence emission spectra of **18** obtained from the same solutions at λex = 465 nm. Inset: Stern-Volmer diagram relative to the emission intensities at λ_{em} = 550 nm.

It is worth mentioning that the Stern-Volmer experiment with **21** required a higher excitation wavelength (in the tail region of the absorption spectrum of **18**, vide supra) to avoid undesired interferences due to the absorption features of **21** at 400 nm. The effect of the addition of **21** can be easily understood from emission decay profiles (Figure 4.26).
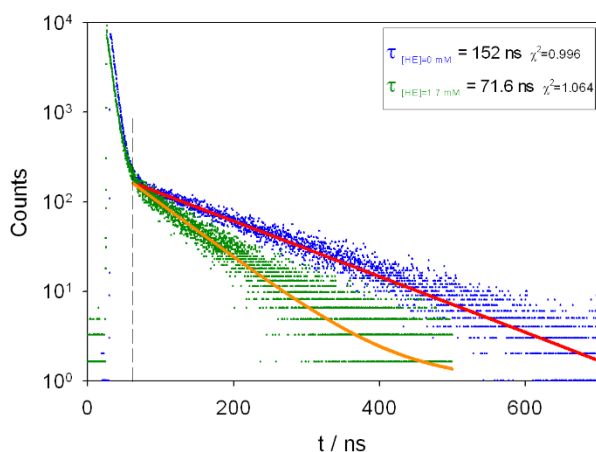
Figure 4.26: Emission decays obtained from **18** in air-equilibrated ethanol (blue dots) and from the same solution upon addition of Hantzsch's ester (**21** or HE, 1.7 mM, green dots). The monoexponential fitting curves are also shown (red and orange lines, respectively).

Based on the results of the photophysical investigation, the quenching step likely occurs via reductive quenching of **18** by **21**, with the formation of **21$^{\bullet+}$**. The thermodynamic feasibility of the photoinduced electron transfer (PET) process relies on the reduction potential of the excited state of **18**, i.e. $E_{1/2}$ (**18***/**18$^{\bullet-}$**) = +1.56 V vs SCE (see Table 4.2), and on the oxidation potential of the Hantzsch's ester **21**, i.e. $E_{1/2}$ (**21$^{\bullet+}$**/**21**) = +1.0 V vs SCE.[156–158] The produced **21$^{\bullet+}$** can participate in further electron transfer events and is a strong reductant: upon proton loss, the obtained radical **[21−H]$^{\bullet}$** has an oxidation potential of −0.76 V vs SCE (see Figure 4.13).[159] Moreover, the obtained radical anion **18$^{\bullet-}$** is also a strong reductant, with $E_{1/2}$ (**18**/**18$^{\bullet-}$**) = −1.16 V vs SCE. The observed high tolerance to oxygen and TEMPO ruled out radical mechanisms, e.g. formation of allylic radicals. No direct unequivocal evidence of the actual reduced bismuth species was observed but, as suggested by the literature, the formation of Bi(0) is likely to occur. Indeed, sometimes the reaction mixture slowly turned black upon irradiation (Figure 4.27).
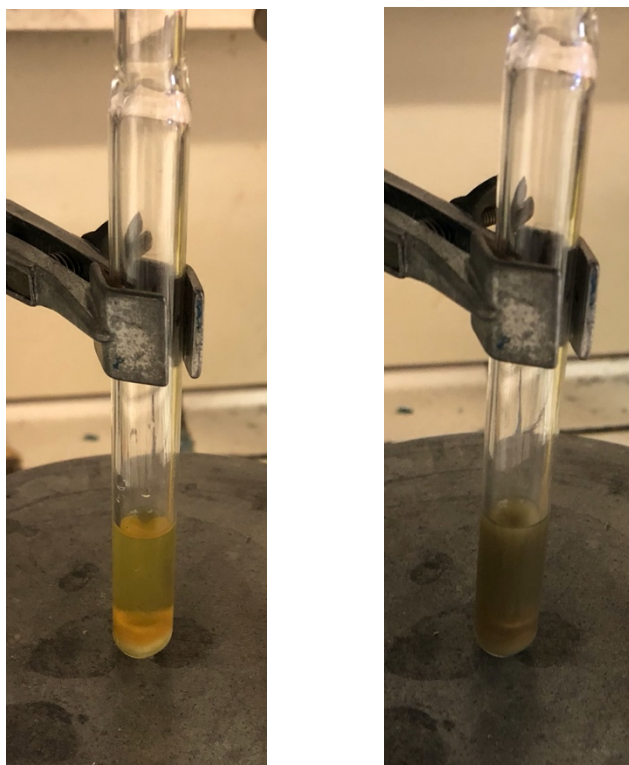
Figure 4.27: Reaction mixture before (left) and after (right) irradiation.

Multiple single electron transfer (SET) events are likely to be responsible for the formation of Bi in low oxidations state from Bi(III) species. Insertion of active bismuth to C−Br bond (see Scheme 4.6) then leads to allylbismuth(III), diallylbismuth(III), and triallylbismuth(III) as the transient nucleophilic organometallic intermediates, that can react with aldehydes to give the corresponding homoallylic alkoxides.[160] The protonated re-aromatized Hantzsch's ester possesses a low pKa and the aqueous conditions enable a facile protonation of the intermediate bismuth alkoxide, allowing the recycle of bismuth salts. Previous studies have shown that such pyridine-type species does not participate in quenching processes.[110] Besides, it can be easily recovered upon flash chromatography and reconverted into the native Hantzsch's ester **21**.[159,161] In light of all this, Figure 4.28 shows a plausible mechanistic picture to describe this photocatalytic bismuth-mediated allylation protocol.
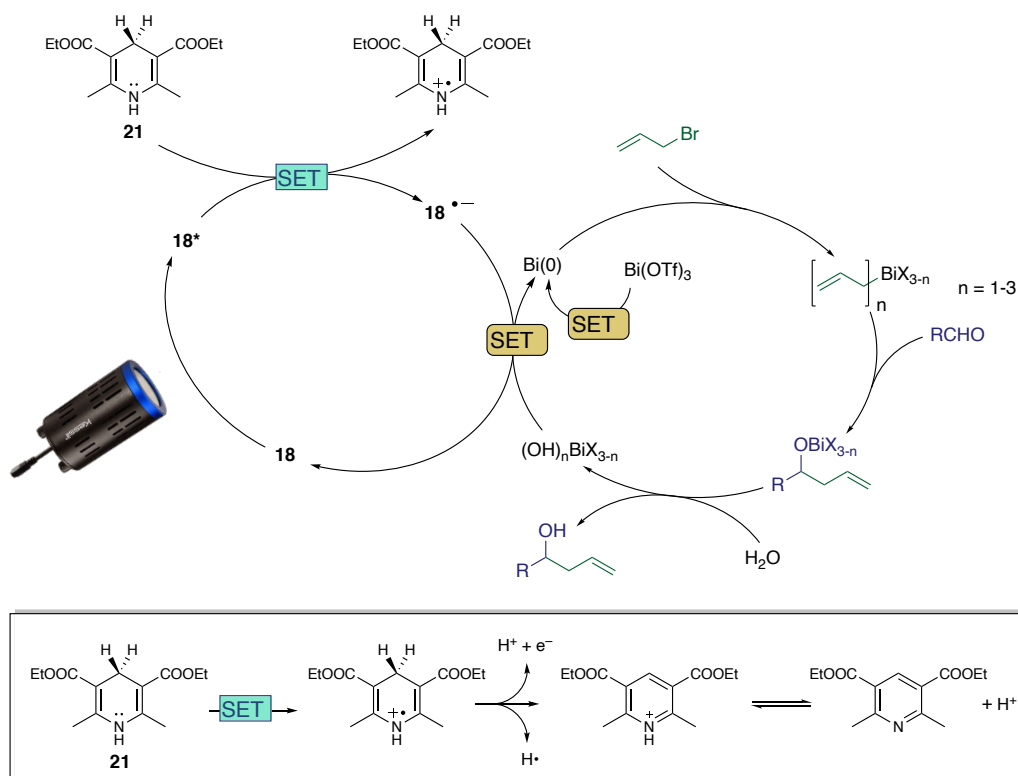
Figure 4.28: Proposed mechanism for the described photoredox bismuth-mediated allylation of aldehydes.

4.4. Conclusions

A new metallaphotoredox protocol for the allylation of aldehydes was developed and implemented.[162] The use of an earth-abundant, inexpensive, and non-toxic metal such as bismuth makes this synthetic methodology particularly appealing if compared to previously described protocols employing toxic metals, e.g. chromium and nickel. However, bismuth also represents a valuable non-toxic replacement for lead in many applications. This is causing the worldwide demand of bismuth to rise. In particular, its price has been keeping rising in the last few years, with China representing the most important supplier in the world.[163] Nevertheless, the sustainability of the whole described process is further increased thanks to the possibility of working in aqueous media, using an inexpensive green organic co-solvent such as ethanol. Even in this case, however, it is worth mentioning that there is no absolutely green solvent, since "green" is a relative term.[164] Expensive and/or toxic metal-based photosensitizers are avoided, and the only used metal species can be easily removed by simple liquid-liquid extraction (bismuth salts are soluble in water). The protocol requires neither strictly deaerated nor anhydrous conditions, and the reaction setup is hence fast and easy (no degassing/drying procedures are required). The scope is wide, with both aromatic and aliphatic aldehydes representing suited substrates. The reaction conditions are mild (ambient temperature), the protocol is amenable of scale-up with even better results, despite lower catalytic loadings, and both the photosensitizer and the oxidized form of the sacrificial reductant can be recovered at the end of the reaction. Further extension to other electrophiles (with particular reference to imine-type substrates) is likely to be achieved. The optimization study for

the allylation of imines – leading to valuable homoallylic amine derivatives – is at the beginning because their intrinsic reactivity and redox properties require much different reaction conditions.

4.5. Experimental section

4.5.1. *General methods and syntheses*

All commercial chemicals and dry solvents were purchased from Sigma Aldrich, Alfa Aesar or TCI Chemicals, and used without further purification, unless otherwise specified. ^{1}H and ^{13}C NMR spectra were recorded on a Varian Inova 400 NMR instrument with a 5 mm probe. All chemical shifts are referenced using deuterated solvent signals. Trifluoroacetic acid signal (-76.55 ppm) was used as a reference for ^{19}F NMR spectra. Coupling constants are in Hertz, and the multiplicity is as follows: s (singlet), d (doublet), t (triplet), q (quartet), m (multiplet), dd (doublet of doublets), dt (doublet of triplets), ddd (doublet of doublet of doublets), br (broad signal). GC-MS spectra were obtained by EI ionization at 70 eV on a Hewlett-Packard 5971 with GC injection; they are reported as: *m/z* (rel. intensity). Flash chromatography purifications were carried out using VWR or Merck silica gel (40-63 μm particle size). Thin-layer chromatography was performed on Merck 60 F$_{254}$ plates. Reaction mixtures were irradiated with Kessil® PR160L@456 nm.† Aldehydes **22l**,[165] **22n**,[166] **22v**,[110] **22w-x**,[167] **22z**,[168–170] photosensitizers **18** and **19**,[55] and Hantzsch's ester **21**[171] were prepared according to literature procedures.

4.5.2. *General procedure for photoredox bismuth-catalysed allylation of aldehydes*
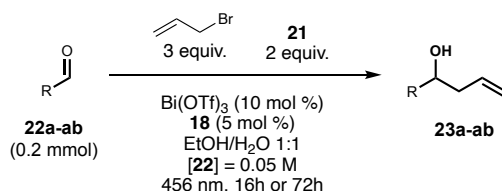
A dry 10 mL Schlenk tube, equipped with a Rotaflo® stopcock, magnetic stirring bar and an argon supply tube, was subjected to three vacuum-argon cycles and then it was first charged with all the solids – i.e. Bi(OTf)$_3$ (0.02 mmol, 13 mg, 10 mol%), **18** (0.01 mmol, 6 mg, 5 mol%), Hantzsch's ester **21** (0.4 mmol, 100 mg, 2 equiv.) and, if solid, the aldehyde (0.2 mmol) – followed by EtOH (2 mL) and water (2 mL). Then, allyl bromide (0.6 mmol, 73 mg, 52 μL, 3 equiv.) and, if liquid, the aldehyde (0.2 mmol) were added. The reaction was irradiated under vigorous stirring for 16 or 72 h. After that, the reaction was quenched with water (approx. 4 mL) and extracted with EtOAc (4 × 5 mL). The combined organic layers were dried over anhydrous Na$_2$SO$_4$ and the solvent was removed under reduced pressure. The crude was subject of flash column chromatography (SiO$_2$) to afford the products **23** in the stated yields.


† https://www.kessil.com/photoreaction/PR160L.php

4.5.3. Preparative scale reaction

The reaction was performed on 1 mmol of aldehyde **22a** (140 mg) following the general procedure irradiating with Kessil® PR160L@456 nm for 72 hours. Reagent amounts: Bi(OTf)$_3$ (0.08 mmol, 52.5 mg, 8 mol%), **18** (0.03 mmol, 20 mg, 3 mol%), Hantzsch's ester **21** (2 mmol, 500 mg, 2 equiv.), allyl bromide (3 mmol, 260 μL, 3 equiv.) in EtOH (7.5 mL) and water (7.5 mL) mixture. Product **23a** was obtained in 77% yield (0.77 mmol, 140 mg) after flash chromatographic purification (CH$_2$Cl$_2$).

4.5.4. Homoallylic alcohols
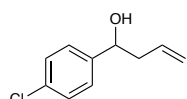
23a: yellowish oil, 74% (0.15 mmol, 27 mg). The general procedure (16 h) was applied using **22a** (0.2 mmol, 28 mg) as aldehyde. The title compound was isolated by flash column chromatography (CH$_2$Cl$_2$). Spectroscopic data were in agreement with those reported in literature.[105]
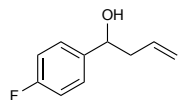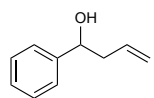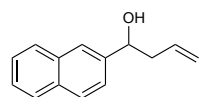

23b: brown oil, 65% (0.13 mmol, 22 mg). The general procedure (72 h) was applied using freshly distilled **22b** (0.2 mmol, 21 μL) as aldehyde. The title compound was isolated by flash column chromatography (CH$_2$Cl$_2$). Spectroscopic data were in agreement with those reported in literature.[172]
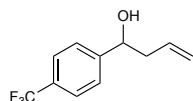
23c: brown oil, 66% (0.13 mmol, 29 mg). The general procedure (72 h) was applied using freshly distilled **22c** (0.2 mmol, 27 μL) as aldehyde. The title compound was isolated by flash column chromatography (CH$_2$Cl$_2$). Spectroscopic data were in agreement with those reported in literature.[105]
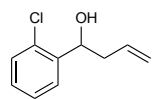
23d: brown oil, 74% (0.15 mmol, 27 mg). The general procedure (16 h) was applied using freshly distilled **22d** (0.2 mmol, 22 μL) as aldehyde. The title compound was isolated by flash column chromatography (CH$_2$Cl$_2$). Spectroscopic data were in agreement with those reported in literature.[105]
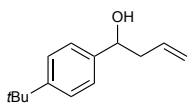

23e: yellowish oil, 94% (0.19 mmol, 28 mg). The general procedure (72 h) was applied using freshly distilled **22e** (0.2 mmol, 20 μL) as aldehyde. The title compound was isolated by flash column chromatography (CH$_2$Cl$_2$). Spectroscopic data were in agreement with those reported in literature.[105]

23f: yellowish oil, 81% (0.16 mmol, 32 mg). The general procedure (16 h) was applied using **22f** (0.2 mmol, 31 mg) as aldehyde. The title compound was isolated by flash

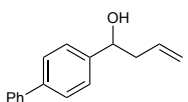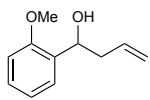column chromatography (CH₂Cl₂). Spectroscopic data were in agreement with those reported in literature.[105]

23g: yellowish oil, 79% (0.16 mmol, 32 mg). The general procedure (72 h) was applied using freshly distilled **22g** (0.2 mmol, 33 μL) as aldehyde. The title compound was isolated by flash column chromatography (CH₂Cl₂). Spectroscopic data were in agreement with those reported in literature.[105]
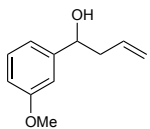
23h: brown oil, 62% (0.12 mmol, 28 mg). The general procedure (16 h) was applied using **22h** (0.2 mmol, 36 mg) as aldehyde. The title compound was isolated by flash column chromatography (CH₂Cl₂). Spectroscopic data were in agreement with those reported in literature.[105]

23i: brown oil, 79% (0.16 mmol, 28 mg). The general procedure (16 h) was applied using freshly distilled **22i** (0.2 mmol, 24 μL) as aldehyde. The title compound was isolated by flash column chromatography (CH₂Cl₂). Spectroscopic data were in agreement with those reported in literature.[173]
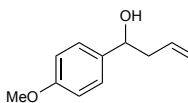
23j: brown oil, 74% (0.15 mmol, 26 mg). The general procedure (16 h) was applied using freshly distilled **22j** (0.2 mmol, 24 μL) as aldehyde. The title compound was isolated by flash column chromatography (CH₂Cl₂). Spectroscopic data were in agreement with those reported in literature.[173]
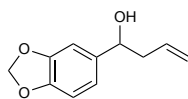
23k: brown oil, 34% (0.07 mmol, 12 mg). The general procedure (16 h) was applied using freshly distilled **22k** (0.2 mmol, 24 μL) as aldehyde. The title compound was isolated by flash column chromatography (CH₂Cl₂). Spectroscopic data were in agreement with those reported in literature.[105]

23l: brown oil, 65% (0.13 mmol, 25 mg). The general procedure (16 h) was applied using previously synthesized **22l** (0.2 mmol, 30 mg) as aldehyde. The title compound was isolated by flash column chromatography (CH₂Cl₂). Spectroscopic data were in agreement with those reported in literature.[105]
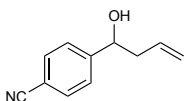
23m: brown oil, 61% (0.12 mmol, 21 mg). The general procedure (16 h) was applied using **22m** (0.2 mmol, 26 mg) as aldehyde. The title compound was isolated by flash

column chromatography (CH$_2$Cl$_2$). Spectroscopic data were in agreement with those reported in literature.[105]
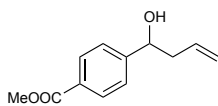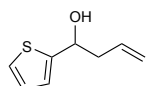
23n: brown oil, 61% (0.12 mmol, 25 mg). The general procedure (16 h) was applied using previously synthesized **22n** (0.2 mmol, 33 mg) as aldehyde. The title compound was isolated by flash column chromatography (CH$_2$Cl$_2$). Spectroscopic data were in agreement with those reported in literature.[105]

23o: yellow oil, 33% (0.07 mmol, 10 mg). The general procedure (16 h) was applied using freshly distilled **22o** (0.2 mmol, 19 µL) as aldehyde. The title compound was isolated by flash column chromatography (CH$_2$Cl$_2$). Spectroscopic data were in agreement with those reported in literature.[173]

23p: brown oil, 66% (0.13 mmol, 20 mg). The general procedure (16 h) was applied using freshly distilled **22p** (0.2 mmol, 18 µL) as aldehyde. The title compound was isolated by flash column chromatography (CH$_2$Cl$_2$). Spectroscopic data were in agreement with those reported in literature.[105]

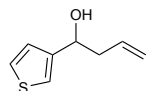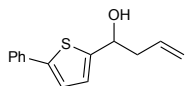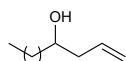**23q:** yellow oil, 60% (0.12 mmol, 28 mg). The general procedure (16 h) was applied using **22q** (0.2 mmol, 38 mg) as aldehyde. The title compound was isolated by flash column chromatography (CH$_2$Cl$_2$). Spectroscopic data were in agreement with those reported in literature.[105]

23r: brown oil, 68% (0.14 mmol, 27 mg). The general procedure (72 h) was applied using freshly distilled **22r** (0.2 mmol, 38 µL) as aldehyde. The title compound was isolated by flash column chromatography (CH$_2$Cl$_2$). Spectroscopic data were in agreement with those reported in literature.[174]
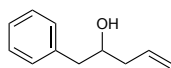
23s: brown oil, 56% (0.11 mmol 18 mg). The general procedure (72 h) was applied using freshly distilled **22s** (0.2 mmol, 23 µL) as aldehyde. The title compound was isolated by flash column chromatography (CH$_2$Cl$_2$). Spectroscopic data were in agreement with those reported in literature.[175]

23t: brown oil, 85% (0.17 mmol, 30 mg). The general procedure (72 h) was applied using freshly distilled **22t** (0.2 mmol, 26 µL) as aldehyde. The title compound was isolated by

flash column chromatography (CH₂Cl₂). Spectroscopic data were in agreement with those reported in literature.[105]

23u: brown oil, 58% (0.12 mmol, 18 mg). The general procedure (72 h) was applied using freshly distilled **22u** (0.2 mmol, 24 μL) as aldehyde. The title compound was isolated by flash column chromatography (CH₂Cl₂). Spectroscopic data were in agreement with those reported in literature.[105]
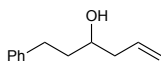
23v: brown oil, 68% (0.14 mmol, 20 mg). The general procedure (72 h) was applied using previously synthesized **22v** (0.2 mmol, 36 mg) as aldehyde. Flash chromatography (0–2 % EtOAc in CH₂Cl₂) afforded a mixture of pyridine-type oxidized Hantzsch's ester and **3v**. Starting from this mixture, the title compound was isolated by flash column chromatography (30 % Et₂O in CyH). Spectroscopic data were in agreement with those reported in literature.[105]

23w: brown oil, 74% (0.15 mmol, 37 mg). The general procedure (72 h) was applied using previously synthesized **22w** (0.2 mmol, 41 mg) as aldehyde. The title compound was isolated by flash column chromatography (0–5 % EtOAc in CH₂Cl₂ until pyridine-type oxidized Hantzsch's ester was recovered, then 2 % MeOH in CH₂Cl₂). Spectroscopic data were in agreement with those reported in literature.[105]
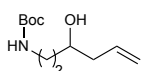
23x: brown oil, 70% (0.14 mmol, 30 mg). The general procedure (72 h) was applied using previously synthesized **22x** (0.2 mmol, 35 mg) as aldehyde. Flash chromatography (0–2 % EtOAc in CH₂Cl₂) afforded a mixture of pyridine-type oxidized Hantzsch's ester and **3x**. Starting from this mixture, the title compound was isolated by flash column chromatography (30–50 % Et₂O in CyH). Spectroscopic data were in agreement with those reported in literature.[105]

23y: brown oil, 80% (0.16 mmol, 29 mg). The general procedure (72 h) was applied using **22y** (0.2 mmol, 33 μL) as aldehyde. The title compound was isolated by flash column chromatography (CH₂Cl₂). Spectroscopic data were in agreement with those reported in literature.[105]
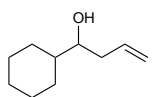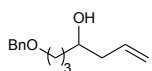
23z: brown oil, 80% (0.16 mmol, 29 mg). The general procedure (72 h) was applied using previously synthesized **22z** (0.2 mmol, 41 mg) as aldehyde. The title compound was isolated by flash column chromatography (CH₂Cl₂). Spectroscopic data were in agreement with those reported in literature.[176]

Homoallylic alcohols

23aa: (*syn*:*anti* d.r. of 2:1) yellow oil, 70% (0.14 mmol, 25 mg). The general procedure (72 h) was applied using freshly distilled **22aa** (0.2 mmol,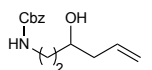 27 µL) as aldehyde. The title compound was isolated by flash column chromatography (CH$_2$Cl$_2$). Spectroscopic data were in agreement with those reported in literature.[105,177]

23ab: the product was isolated as mixture of *E*:*Z* isomers (3:2) as brown oil, 70% (0.14 mmol, 24 mg). The general procedure (72 h) was applied using freshly distilled **22ab** (0.2 mmol, 25 µL) as aldehyde. The title compound was isolated by flash column chromatography (CH$_2$Cl$_2$). Spectroscopic data were in agreement with those reported in literature.[105,178]
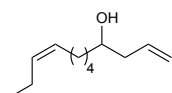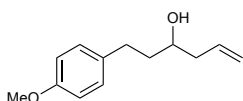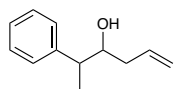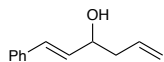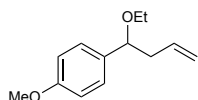
23k: yellow oil, 36% (0.07 mmol, 15 mg). The general procedure (72 h) was applied using freshly distilled **22k** (0.2 mmol, 24 µL) as aldehyde. The title compound was isolated by flash column chromatography (CH$_2$Cl$_2$). ^{1}H-NMR (400 MHz, CDCl$_3$, 25°C): δ = 7.24 – 7.19 (m, 2H), 6.90 – 6.84 (m, 2H), 5.82 – 5.69 (m, 1H), 5.07 – 4.96 (m, 2H), 4.21 (t, *J* = 6.5 Hz, 1H), 3.81 (s, 3H), 3.41 – 3.25 (m, 2H), 2.62 – 2.52 (m, 1H), 2.42 – 2.32 (m, 1H), 1.16 (t, *J* = 6.9 Hz, 3H); ^{13}C-NMR (100 MHz, CDCl$_3$, 25°C): δ = 159.1, 135.3, 134.6, 128.0 (2C), 116.7, 113.8 (2C), 81.5, 64.0, 55.4, 42.7, 15.4. ESI-MS *m/z* = 207.1 [M+H]$^+$.

4.6. References

(1) Lyons, T. W.; Reinhard, C. T.; Planavsky, N. J. The rise of oxygen in Earth's early ocean and atmosphere. *Nature* **2014**, *506*, 307–315. DOI: 10.1038/nature13068.

(2) Cardona, T.; Murray, J. W.; Rutherford, A. W. Origin and evolution of water oxidation before the last common ancestor of the cyanobacteria. *Mol. Biol. Evol.* **2015**, *32* (5), 1310–1328. DOI: 10.1093/molbev/msv024.

(3) Govindjee; Shevela, D.; Björn, L. O. Evolution of the Z-scheme of photosynthesis: a perspective. *Photosynth. Res.* **2017**, *133*, 5–15. DOI: 10.1007/s11120-016-0333-z.

(4) Vinyard, D. J.; Ananyev, G. M.; Charles Dismukes, G. Photosystem II: The reaction center of oxygenic photosynthesis. *Annu. Rev. Biochem.* **2013**, *82*, 577–606. DOI: 10.1146/annurev-biochem-070511-100425.

(5) Vinyard, D. J.; Brudvig, G. W. Progress Toward a Molecular Mechanism of Water Oxidation in Photosystem II. *Annu. Rev. Phys. Chem.* **2017**, *68*, 101–116. DOI: 10.1146/annurev-physchem-052516-044820.

(6) Cox, N.; Pantazis, D. A.; Lubitz, W. Current Understanding of the Mechanism of Water Oxidation in Photosystem II and Its Relation to XFEL Data. *Annu. Rev. Biochem.* **2020**, *89*, 795–820. DOI: 10.1146/annurev-biochem-011520-104801.

(7) Yoon, T. P.; Ischay, M. A.; Du, J. Visible light photocatalysis as a greener approach to photochemical synthesis. *Nat. Chem.* **2010**, *2* (7), 527–532. DOI: 10.1038/nchem.687.

(8) Prier, C. K.; Rankic, D. A.; MacMillan, D. W. C. Visible light photoredox catalysis with transition metal complexes: Applications in organic synthesis. *Chem. Rev.* **2013**, *113* (7), 5322–5363. DOI: 10.1021/cr300503r.

(9) McAtee, R. C.; McClain, E. J.; Stephenson, C. R. J. Illuminating Photoredox Catalysis. *Trends Chem.* **2019**, *1* (1), 111–125. DOI: 10.1016/j.trechm.2019.01.008.

(10) Balzani, V.; Ceroni, P.; Juris, A. *Photochemistry and Photophysics: Concepts, Research, Applications*; Wiley, 2014.

(11) Hedstrand, D. M.; Kruizinga, W. H.; Kellogg, R. M. Light induced and dye accelerated reductions of phenacyl onium salts by 1,4-dihydropyridines. *Tetrahedron Lett.* **1978**, *19* (14), 1255–1258. DOI: 10.1016/S0040-4039(01)94515-0.

(12) Gray, H. B.; Winkler, J. R. Electron transfer in proteins. *Annu. Rev. Biochem.* **1996**, *65*, 537–561. DOI: 10.1146/annurev.bi.65.070196.002541.

(13) Shaw, M. H.; Twilton, J.; MacMillan, D. W. C. Photoredox Catalysis in Organic Chemistry. *J. Org. Chem.* **2016**, *81* (16), 6898–6926. DOI: 10.1021/acs.joc.6b01449.

(14) Crespi, S.; Fagnoni, M. Generation of Alkyl Radicals: From the Tyranny of Tin to the Photon Democracy. *Chem. Rev.* **2020**, *120* (17), 9790–9833. DOI: 10.1021/acs.chemrev.0c00278.

(15) Baguley, P. A.; Walton, J. C. Flight from the tyranny of tin: The quest for practical radical sources free from metal

encumbrances. *Angew. Chem. Int. Ed.* **1998**, *37* (22), 3072–3082. DOI: 10.1002/(sici)1521-3773(19981204)37:22<3072::aid-anie3072>3.0.co;2-9.

(16)   Shon, J. H.; Teets, T. S. Photocatalysis with Transition Metal Based Photosensitizers. *Comments Inorg. Chem.* **2020**, *40* (2), 53–85. DOI: 10.1080/02603594.2019.1694517.

(17)   Larsen, C. B.; Wenger, O. S. Photoredox Catalysis with Metal Complexes Made from Earth-Abundant Elements. *Chem. Eur. J.* **2018**, *24* (9), 2039–2058. DOI: 10.1002/chem.201703602.

(18)   Gualandi, A.; Marchini, M.; Mengozzi, L.; Natali, M.; Lucarini, M.; Ceroni, P.; Cozzi, P. G. Organocatalytic Enantioselective Alkylation of Aldehydes with [Fe(bpy)₃]Br₂ Catalyst and Visible Light. *ACS Catal.* **2015**, *5* (10), 5927–5931. DOI: 10.1021/acscatal.5b01573.

(19)   Gualandi, A.; Marchini, M.; Mengozzi, L.; Kidanu, H. T.; Franc, A.; Ceroni, P.; Cozzi, P. G. Aluminum(III) Salen Complexes as Active Photoredox Catalysts. *Eur. J. Org. Chem.* **2020**, *2020* (10), 1486–1490. DOI: 10.1002/ejoc.201901086.

(20)   Busacca, C. A.; Fandrick, D. R.; Song, J. J.; Senanayake, C. H. The growing impact of catalysis in the pharmaceutical industry. *Adv. Synth. Catal.* **2011**, *353* (11–12), 1825–1864. DOI: 10.1002/adsc.201100488.

(21)   Hayler, J. D.; Leahy, D. K.; Simmons, E. M. A Pharmaceutical Industry Perspective on Sustainable Metal Catalysis. *Organometallics* **2019**, *38* (1), 36–46. DOI: 10.1021/acs.organomet.8b00566.

(22)   Wu, C.; Corrigan, N.; Lim, C. H.; Jung, K.; Zhu, J.; Miyake, G.; Xu, J.; Boyer, C. Guiding the Design of Organic Photocatalyst for PET-RAFT Polymerization: Halogenated Xanthene Dyes. *Macromolecules* **2019**, *52* (1), 236–248. DOI: 10.1021/acs.macromol.8b02517.

(23)   Gualandi, A.; Nenov, A.; Marchini, M.; Rodeghiero, G.; Conti, I.; Paltanin, E.; Balletti, M.; Ceroni, P.; Garavelli, M.; Cozzi, P. G. Tailored Coumarin Dyes for Photoredox Catalysis: Calculation, Synthesis, and Electronic Properties. *ChemCatChem* **2020**, *13* (3), 981–989. DOI: 10.1002/cctc.202001690.

(24)   Sartor, S. M.; Chrisman, C. H.; Pearson, R. M.; Miyake, G. M.; Damrauer, N. H. Designing High-Triplet-Yield Phenothiazine Donor-Acceptor Complexes for Photoredox Catalysis. *J. Phys. Chem. A* **2020**, *124* (5), 817–823. DOI: 10.1021/acs.jpca.9b10400.

(25)   Romero, N. A.; Nicewicz, D. A. Organic Photoredox Catalysis. *Chem. Rev.* **2016**, *116* (17), 10075–10166. DOI: 10.1021/acs.chemrev.6b00057.

(26)   Twilton, J.; Le, C. C.; Zhang, P.; Shaw, M. H.; Evans, R. W.; MacMillan, D. W. C. The merger of transition metal and photocatalysis. *Nat. Rev. Chem.* **2017**, *1*, 0052. DOI: 10.1038/s41570-017-0052.

(27)   Kalyani, D.; McMurtrey, K. B.; Neufeldt, S. R.; Sanford, M. S. Room-temperature C-H arylation: Merger of Pd-catalyzed C-H functionalization and visible-light photocatalysis. *J. Am. Chem. Soc.* **2011**, *133* (46), 18566–18569. DOI: 10.1021/ja208068w.

(28)   Zuo, Z.; Ahneman, D. T.; Chu, L.; Terrett, J. A.; Doyle, A. G.; MacMillan, D. W. C. Merging photoredox with nickel catalysis: Coupling of α-carboxyl sp3-carbons with aryl halides. *Science* **2014**, *345* (6195), 437–440. DOI: 10.1126/science.1255525.

(29)   Tellis, J. C.; Primer, D. N.; Molander, G. A. Single-electron transmetalation in organoboron cross-coupling by photoredox/nickel dual catalysis. *Science* **2014**, *345* (6195), 433–436. DOI: 10.1126/science.1253647.

(30)   Hossain, A.; Bhattacharyya, A.; Reiser, O. Copper's rapid ascent in visible-light photoredox catalysis. *Science* **2019**, *364* (6439), eaav9713. DOI: 10.1126/science.aav9713.

(31)   Hopkinson, M. N.; Tlahuext-Aca, A.; Glorius, F. Merging Visible Light Photoredox and Gold Catalysis. *Acc. Chem. Res.* **2016**, *49* (10), 2261–2272. DOI: 10.1021/acs.accounts.6b00351.

(32)   Zoller, J.; Fabry, D. C.; Ronge, M. A.; Rueping, M. Synthesis of indoles using visible light: Photoredox catalysis for palladium-catalyzed C-H activation. *Angew. Chem. Int. Ed.* **2014**, *53* (48), 13264–13268. DOI: 10.1002/anie.201405478.

(33)   Fabry, D. C.; Zoller, J.; Raja, S.; Rueping, M. Combining rhodium and photoredox catalysis for C-H functionalizations of arenes: Oxidative heck reactions with visible light. *Angew. Chem. Int. Ed.* **2014**, *53* (38), 10228–10231. DOI: 10.1002/anie.201400560.

(34)   Fabry, D. C.; Ronge, M. A.; Zoller, J.; Rueping, M. C-H functionalization of phenols using combined ruthenium and photoredox catalysis: In situ generation of the oxidant. *Angew. Chem. Int. Ed.* **2015**, *54* (9), 2801–2805. DOI: 10.1002/anie.201408891.

(35)   Xu, R.; Cai, C. Three-component difluoroalkylation-thiolation of alkenes by iron-facilitated visible-light photoredox catalysis. *Chem. Commun.* **2019**, *55* (30), 4383–4386. DOI: 10.1039/c9cc00730j.

(36)   Fermi, A.; Gualandi, A.; Bergamini, G.; Cozzi, P. G. Shining Light on Ti^IV Complexes: Exceptional Tools for Metallaphotoredox Catalysis. *Eur. J. Org. Chem.* **2020**, *2020* (45), 6955–6965. DOI: 10.1002/ejoc.202000966.

(37)   Cismesia, M. A.; Yoon, T. P. Characterizing chain processes in visible light photoredox catalysis. *Chem. Sci.* **2015**, *6* (10), 5426–5434. DOI: 10.1039/c5sc02185e.

(38)   Kärkäs, M. D.; Matsuura, B. S.; Stephenson, C. R. J. Enchained by visible light-mediated photoredox catalysis. *Science* **2015**, *349* (6254), 1285–1286. DOI: 10.1126/science.aad0193.

(39)   Strieth-Kalthoff, F.; James, M. J.; Teders, M.; Pitzer, L.; Glorius, F. Energy transfer catalysis mediated by visible light: principles, applications, directions. *Chem. Soc. Rev.* **2018**, *47* (19), 7190–7202. DOI: 10.1039/c8cs00054a.

(40)   Marian, C. M. Spin-orbit coupling and intersystem crossing in molecules. *WIREs Comput. Mol. Sci.* **2012**, *2* (2), 187–203. DOI: 10.1002/wcms.83.

(41)   Uoyama, H.; Goushi, K.; Shizu, K.; Nomura, H.; Adachi, C. Highly efficient organic light-emitting diodes from delayed fluorescence. *Nature* **2012**, *492* (7428), 234–238. DOI: 10.1038/nature11687.

References

(42)   Pokhilko, P.; Krylov, A. I. Quantitative El-Sayed Rules for Many-Body Wave Functions from Spinless Transition Density Matrices. *J. Phys. Chem. Lett.* **2019**, *10* (17), 4857–4862. DOI: 10.1021/acs.jpclett.9b02120.

(43)   Capaldo, L.; Ravelli, D. Hydrogen Atom Transfer (HAT): A Versatile Strategy for Substrate Activation in Photocatalyzed Organic Synthesis. *Eur. J. Org. Chem.* **2017**, *2017* (15), 2056–2071. DOI: 10.1002/ejoc.201601485.

(44)   Juliá, F.; Constantin, T.; Leonori, D. Applications of Halogen-Atom Transfer (XAT) for the Generation of Carbon Radicals in Synthetic Photochemistry and Photocatalysis. *Chem. Rev.* **2022**, *122* (2), 2292–2352. DOI: 10.1021/acs.chemrev.1c00558.

(45)   Strieth-Kalthoff, F.; Glorius, F. Triplet Energy Transfer Photocatalysis: Unlocking the Next Level. *Chem* **2020**, *6* (8), 1888–1903. DOI: 10.1016/j.chempr.2020.07.010.

(46)   Gentry, E. C.; Knowles, R. R. Synthetic Applications of Proton-Coupled Electron Transfer. *Acc. Chem. Res.* **2016**, *49* (8), 1546–1556. DOI: 10.1021/acs.accounts.6b00272.

(47)   Roth, H. G.; Romero, N. A.; Nicewicz, D. A. Experimental and Calculated Electrochemical Potentials of Common Organic Molecules for Applications to Single-Electron Redox Chemistry. *Synlett* **2016**, *27* (5), 714–723. DOI: 10.1055/s-0035-1561297.

(48)   Buzzetti, L.; Crisenza, G. E. M.; Melchiorre, P. Mechanistic Studies in Photocatalysis. *Angew. Chem. Int. Ed.* **2019**, *58* (12), 3730–3747. DOI: 10.1002/anie.201809984.

(49)   Turro, N. J.; Ramamurthy, V.; Scaiano, J. C. *Modern Molecular Photochemistry Of Organic Molecules*; University Science Books: Sausalito, California, 2010.

(50)   Scaiano, J. C. Nanosecond Laser Flash Photolysis: A Tool for Physical Organic Chemistry. In *Reactive Intermediate Chemistry*; Wiley: Hoboken, 2005; pp 847–871. DOI: 10.1002/0471721492.ch18.

(51)   Pitre, S. P.; McTiernan, C. D.; Scaiano, J. C. Understanding the Kinetics and Spectroscopy of Photoredox Catalysis and Transition-Metal-Free Alternatives. *Acc. Chem. Res.* **2016**, *49* (6), 1320–1330. DOI: 10.1021/acs.accounts.6b00012.

(52)   Capaldo, L.; Ravelli, D. The Dark Side of Photocatalysis: One Thousand Ways to Close the Cycle. *Eur. J. Org. Chem.* **2020**, *2020* (19), 2783–2806. DOI: 10.1002/ejoc.202000144.

(53)   Nicewicz, D. A.; MacMillan, D. W. C. Merging photoredox catalysis with organocatalysis: The direct asymmetric alkylation of aldehydes. *Science* **2008**, *322* (5898), 77–80. DOI: 10.1126/science.1161976.

(54)   Wu, Y.; Kim, D.; Teets, T. S. Photophysical Properties and Redox Potentials of Photosensitizers for Organic Photoredox Transformations. *Synlett* **2021**, *32*. DOI: 10.1055/a-1390-9065.

(55)   Speckmeier, E.; Fischer, T. G.; Zeitler, K. A Toolbox Approach to Construct Broadly Applicable Metal-Free Catalysts for Photoredox Chemistry: Deliberate Tuning of Redox Potentials and Importance of Halogens in Donor-Acceptor Cyanoarenes. *J. Am. Chem. Soc.* **2018**, *140* (45), 15353–15365. DOI: 10.1021/jacs.8b08933.

(56)   König, B.; Kümmel, S.; Svobodová, E.; Cibulka, R. Flavin photocatalysis. *Phys. Sci. Rev.* **2018**, *3* (8), 20170168. DOI: 10.1515/psr-2017-0168.

(57)   Srivastava, V.; Singh, P. P. Eosin Y catalysed photoredox synthesis: A review. *RSC Adv.* **2017**, *7* (50), 31377–31392. DOI: 10.1039/c7ra05444k.

(58)   Discekici, E. H.; Treat, N. J.; Poelma, S. O.; Mattson, K. M.; Hudson, Z. M.; Luo, Y.; Hawker, C. J.; De Alaniz, J. R. A highly reducing metal-free photoredox catalyst: Design and application in radical dehalogenations. *Chem. Commun.* **2015**, *51* (58), 11705–11708. DOI: 10.1039/c5cc04677g.

(59)   Lee, Y.; Kwon, M. S. Emerging Organic Photoredox Catalysts for Organic Transformations. *Eur. J. Org. Chem.* **2020**, *2020* (38), 6028–6043. DOI: 10.1002/ejoc.202000720.

(60)   Kim, U. Bin; Jung, D. J.; Jeon, H. J.; Rathwell, K.; Lee, S. G. Synergistic Dual Transition Metal Catalysis. *Chem. Rev.* **2020**, *120* (24), 13382–13433. DOI: 10.1021/acs.chemrev.0c00245.

(61)   Hartwig, J. *Organotransition Metal Chemistry: From Bonding to Catalysis*; University Science Books, 2010.

(62)   Skubi, K. L.; Blum, T. R.; Yoon, T. P. Dual Catalysis Strategies in Photochemical Synthesis. *Chem. Rev.* **2016**, *116* (17), 10035–10074. DOI: 10.1021/acs.chemrev.6b00018.

(63)   Zhou, Q. Q.; Zou, Y. Q.; Lu, L. Q.; Xiao, W. J. Visible-Light-Induced Organic Photochemical Reactions through Energy-Transfer Pathways. *Angew. Chem. Int. Ed.* **2019**, *58* (6), 1586–1604. DOI: 10.1002/anie.201803102.

(64)   Gualandi, A.; Anselmi, M.; Calogero, F.; Potenti, S.; Bassan, E.; Ceroni, P.; Cozzi, P. G. Metallaphotoredox catalysis with organic dyes. *Org. Biomol. Chem.* **2021**, *19* (16), 3527–3550. DOI: 10.1039/d1ob00196e.

(65)   Ault, A. The Nobel Prize in Chemistry for 2001. *J. Chem. Educ.* **2002**, *79* (5), 572–577. DOI: 10.1021/ed079p572.

(66)   Casey, C. P. 2005 Nobel Prize in Chemistry: Development of the Olefin metathesis method in organic synthesis. *J. Chem. Educ.* **2006**, *83* (2), 192–195. DOI: 10.1021/ed083p192.

(67)   Johansson Seechurn, C. C. C.; Kitching, M. O.; Colacot, T. J.; Snieckus, V. Palladium-catalyzed cross-coupling: A historical contextual perspective to the 2010 Nobel Prize. *Angewandte Chemie - International Edition*. 2012, pp 5062–5085. DOI: 10.1002/anie.201107017.

(68)   Milligan, J. A.; Phelan, J. P.; Badir, S. O.; Molander, G. A. Alkyl Carbon–Carbon Bond Formation by Nickel/Photoredox Cross-Coupling. *Angew. Chem. Int. Ed.* **2019**, *58* (19), 6152–6163. DOI: 10.1002/anie.201809431.

(69)   Pitzer, L.; Schwarz, J. L.; Glorius, F. Reductive radical-polar crossover: Traditional electrophiles in modern radical reactions. *Chem. Sci.* **2019**, *10* (36), 8285–8291. DOI: 10.1039/c9sc03359a.

(70)   Donabauer, K.; Maity, M.; Berger, A. L.; Huff, G. S.; Crespi, S.; König, B. Photocatalytic carbanion generation-benzylation of aliphatic aldehydes to secondary alcohols. *Chem. Sci.* **2019**, *10* (19), 5162–5166. DOI: 10.1039/c9sc01356c.

(71)   Webb, E. W.; Park, J. B.; Cole, E. L.; Donnelly, D. J.; Bonacorsi, S. J.; Ewing, W. R.; Doyle, A. G. Nucleophilic

(Radio)Fluorination of Redox-Active Esters via Radical-Polar Crossover Enabled by Photoredox Catalysis. *J. Am. Chem. Soc.* **2020**, *142* (20), 9493–9500. DOI: 10.1021/jacs.0c03125.

(72)   Kang, S. H.; Kang, S. Y.; Kim, C. M.; Choi, H. W.; Jun, H. S.; Lee, B. M.; Park, C. M.; Jeong, J. W. Total Synthesis of Natural (+)-Lasonolide A. *Angew. Chem. Int. Ed.* **2003**, *42* (39), 4779–4782. DOI: 10.1002/anie.200352016.

(73)   Kawamura, S.; Chu, H.; Felding, J.; Baran, P. S. Nineteen-step total synthesis of (+)-phorbol. *Nature* **2016**, *532* (7597), 90–93. DOI: 10.1038/nature17153.

(74)   Gil, A.; Albericio, F.; Álvarez, M. Role of the Nozaki-Hiyama-Takai-Kishi Reaction in the Synthesis of Natural Products. *Chem. Rev.* **2017**, *117* (12), 8420–8446. DOI: 10.1021/acs.chemrev.7b00144.

(75)   Wender, P. A.; Hardman, C. T.; Ho, S.; Jeffreys, M. S.; Maclaren, J. K.; Quiroz, R. V.; Ryckbosch, S. M.; Shimizu, A. J.; Sloane, J. L.; Stevens, M. C. Scalable synthesis of bryostatin 1 and analogs, adjuvant leads against latent HIV. *Science* **2017**, *358* (6360), 218–223. DOI: 10.1126/science.aan7969.

(76)   Nicolaou, K. C.; Rhoades, D.; Kumar, S. M. Total Syntheses of Thailanstatins A-C, Spliceostatin D, and Analogues Thereof. Stereodivergent Synthesis of Tetrasubstituted Dihydro- and Tetrahydropyrans and Design, Synthesis, Biological Evaluation, and Discovery of Potent Antitumor Agents. *J. Am. Chem. Soc.* **2018**, *140* (26), 8303–8320. DOI: 10.1021/jacs.8b04634.

(77)   Lu, Z.; Zhang, X.; Guo, Z.; Chen, Y.; Mu, T.; Li, A. Total Synthesis of Aplysiasecosterol A. *J. Am. Chem. Soc.* **2018**, *140* (29), 9211–9218. DOI: 10.1021/jacs.8b05070.

(78)   Yamamoto, Y.; Asao, N. Selective Reactions Using Allylic Metals. *Chem. Rev.* **1993**, *93* (6), 2207–2293. DOI: 10.1021/cr00022a010.

(79)   Yus, M.; González-Gómez, J. C.; Foubelo, F. Catalytic enantioselective allylation of carbonyl compounds and imines. *Chem. Rev.* **2011**, *111* (12), 7774–7854. DOI: 10.1021/cr1004474.

(80)   Fürstner, A. Carbon-Carbon Bond Formations Involving Organochromium(III) Reagents. *Chem. Rev.* **1999**, *99* (4), 991–1045. DOI: 10.1021/cr9703360.

(81)   Gansäuer, A.; Bluhm, H. Reagent-controlled transition-metal-catalyzed radical reactions. *Chem. Rev.* **2000**, *100* (8), 2771–2788. DOI: 10.1021/cr9902648.

(82)   Okude, Y.; Hirano, S.; Hiyama, T.; Nozaki, H. Grignard-Type Carbonyl Addition of Allyl Halides by Means of Chromous Salt. A Chemospecific Synthesis of Homoallyl Alcohols. *J. Am. Chem. Soc.* **1977**, *99* (9), 3179–3181. DOI: 10.1021/ja00451a061.

(83)   Hosomi, A.; Sakurai, H. Syntheses of γ,δ-unsaturated alcohols from allylsilanes and carbonyl compounds in the presence of titanium tetrachloride. *Tetrahedron Lett.* **1976**, *17* (16), 1295–1298. DOI: 10.1016/S0040-4039(00)78044-0.

(84)   Brown, H. C.; Jadhav, P. K. Asymmetric Carbon-Carbon Bond Formation via B-Allyldiisopinocampheylborane. Simple Synthesis of Secondary Homoallylic Alcohols with Excellent Enantiomeric Purities. *J. Am. Chem. Soc.* **1983**, *105* (7), 2092–2093. DOI: 10.1021/ja00345a085.

(85)   Roush, W. R.; Halterman, R. L. Diisopropyl Tartrate Modified (E)-Crotylboronates: Highly Enantioselective Propionate (E)-Enolate Equivalents. *J. Am. Chem. Soc.* **1986**, *108* (2), 294–296. DOI: 10.1021/ja00262a018.

(86)   Roush, W. R.; Palkowitz, A. D.; Ando, K. Acyclic Diastereoselective Synthesis Using Tartrate Ester Modified Crotylboronates. Double Asymmetric Reactions with α-Methyl Chiral Aldehydes and Synthesis of the C(19)-C(29) Segment of Rifamycin S. *J. Am. Chem. Soc.* **1990**, *112* (17), 6348–6359. DOI: 10.1021/ja00173a024.

(87)   Gauthier, D. R.; Carreira, E. M. Catalytic, enantioselective addition of allylsilanes to aldehydes: Generation of a novel, reactive Ti^{IV} complex from TiF$_4$. *Angew. Chem. Int. Ed.* **1996**, *35* (20), 2363–2365. DOI: 10.1002/anie.199623631.

(88)   Keck, G. E.; Tarbet, K. H.; Geraci, L. S. Catalytic Asymmetric Allylation of Aldehydes. *J. Am. Chem. Soc.* **1993**, *115* (18), 8467–8468. DOI: 10.1021/ja00071a074.

(89)   Kim, I. S.; Ngai, M. Y.; Krische, M. J. Enantioselective iridium-catalyzed carbonyl allylation from the alcohol or aldehyde oxidation level via transfer hydrogenative coupling of allyl acetate: Departure from chirally modified allyl metal reagents in carbonyl addition. *J. Am. Chem. Soc.* **2008**, *130* (44), 14891–14899. DOI: 10.1021/ja805722e.

(90)   Kinnaird, J. W. A.; Ng, P. Y.; Kubota, K.; Wang, X.; Leighton, J. L. Strained silacycles in organic synthesis: A new reagent for the enantioselective allylation of aldehydes. *J. Am. Chem. Soc.* **2002**, *124* (27), 7920–7921. DOI: 10.1021/ja0264908.

(91)   Vieira, E. M.; Snapper, M. L.; Hoveyda, A. H. Enantioselective synthesis of homoallylic amines through reactions of (pinacolato)allylborons with aryl-, heteroaryl-, alkyl-, or alkene-substituted aldimines catalyzed by chiral C$_1$-symmetric NHC-Cu complexes. *J. Am. Chem. Soc.* **2011**, *133* (10), 3332–3335. DOI: 10.1021/ja200311n.

(92)   Studer, A.; Curran, D. P. Catalysis of Radical Reactions: A Radical Chemistry Perspective. *Angew. Chem. Int. Ed.* **2016**, *55* (1), 58–102. DOI: 10.1002/anie.201505090.

(93)   Huang, H. M.; Bellotti, P.; Glorius, F. Transition metal-catalysed allylic functionalization reactions involving radicals. *Chem. Soc. Rev.* **2020**, *49* (17), 6186–6197. DOI: 10.1039/d0cs00262c.

(94)   Leifert, D.; Studer, A. The Persistent Radical Effect in Organic Synthesis. *Angew. Chem. Int. Ed.* **2020**, *59* (1), 74–108. DOI: 10.1002/anie.201903726.

(95)   Qi, L.; Chen, Y. Polarity-Reversed Allylations of Aldehydes, Ketones, and Imines Enabled by Hantzsch Ester in Photoredox Catalysis. *Angew. Chem. Int. Ed.* **2016**, *55* (42), 13312–13315. DOI: 10.1002/anie.201607813.

(96)   Berger, A. L.; Donabauer, K.; König, B. Photocatalytic Barbier reaction-visible-light induced allylation and benzylation of aldehydes and ketones. *Chem. Sci.* **2018**, *9* (36), 7230–7235. DOI: 10.1039/C8SC02038H.

(97)   Hartung, J.; Gottwald, T.; Špehar, K. Selectivity in the chemistry of oxygen-centered radicals - The formation of

carbon-oxygen bonds. *Synthesis* **2002**, No. 11, 1469–1498. DOI: 10.1055/s-2002-33335.

(98) Salamone, M.; Bietti, M. Reaction pathways of alkoxyl radicals. the role of solvent effects on C−C bond fragmentation and hydrogen atom transfer reactions. *Synlett* **2014**, *25* (13), 1803–1816. DOI: 10.1055/s-0033-1341280.

(99) Pitzer, L.; Sandfort, F.; Strieth-Kalthoff, F.; Glorius, F. Intermolecular radical addition to carbonyls enabled by visible light photoredox initiated hole catalysis. *J. Am. Chem. Soc.* **2017**, *139* (39), 13652–13655. DOI: 10.1021/jacs.7b08086.

(100) Pitzer, L.; Sandfort, F.; Strieth-Kalthoff, F.; Glorius, F. Carbonyl–Olefin Cross-Metathesis Through a Visible-Light-Induced 1,3-Diol Formation and Fragmentation Sequence. *Angew. Chem. Int. Ed.* **2018**, *57* (49), 16219–16223. DOI: 10.1002/anie.201810221.

(101) Studer, A.; Curran, D. P. The electron is a catalyst. *Nat. Chem.* **2014**, *6* (9), 765–773. DOI: 10.1038/nchem.2031.

(102) Yatham, V. R.; Shen, Y.; Martin, R. Catalytic Intermolecular Dicarbofunctionalization of Styrenes with CO_2 and Radical Precursors. *Angew. Chem. Int. Ed.* **2017**, *56* (36), 10915–10919. DOI: 10.1002/anie.201706263.

(103) Girard, P.; Namy, J. L.; Kagan, B. Divalent Lanthanide Derivatives in Organic Synthesis. 1. Mild Preparation of SmI_2 and YbI_2 and Their Use as Reducing or Coupling Agents. *J. Am. Chem. Soc.* **1980**, *102* (8), 2693–2698. DOI: 10.1021/ja00528a029.

(104) Molander, G. A.; Kenny, C. Intramolecular Reductive Coupling Reactions Promoted by Samarium Diiodide. *J. Am. Chem. Soc.* **1989**, *111* (21), 8236–8246. DOI: 10.1021/ja00203a027.

(105) Gualandi, A.; Rodeghiero, G.; Faraone, A.; Patuzzo, F.; Marchini, M.; Calogero, F.; Perciaccante, R.; Jansen, T. P.; Ceroni, P.; Cozzi, P. G. Allylation of aldehydes by dual photoredox and nickel catalysis. *Chem. Commun.* **2019**, *55* (48), 6838–6841. DOI: 10.1039/c9cc03344k.

(106) Li, Y. L.; Li, W. D.; Gu, Z. Y.; Chen, J.; Xia, J. B. Photoredox Ni-Catalyzed Branch-Selective Reductive Coupling of Aldehydes with 1,3-Dienes. *ACS Catal.* **2020**, *10* (2), 1528–1534. DOI: 10.1021/acscatal.9b05137.

(107) Schwarz, J. L.; Schäfers, F.; Tlahuext-Aca, A.; Lückemeier, L.; Glorius, F. Diastereoselective Allylation of Aldehydes by Dual Photoredox and Chromium Catalysis. *J. Am. Chem. Soc.* **2018**, *140* (40), 12705–12709. DOI: 10.1021/jacs.8b08052.

(108) Mitsunuma, H.; Tanabe, S.; Fuse, H.; Ohkubo, K.; Kanai, M. Catalytic asymmetric allylation of aldehydes with alkenes through allylic $C(sp^3)$-H functionalization mediated by organophotoredox and chiral chromium hybrid catalysis. *Chem. Sci.* **2019**, *10* (12), 3459–3465. DOI: 10.1039/c8sc05677c.

(109) Schwarz, J. L.; Huang, H. M.; Paulisch, T. O.; Glorius, F. Dialkylation of 1,3-Dienes by Dual Photoredox and Chromium Catalysis. *ACS Catal.* **2020**, *10* (2), 1621–1627. DOI: 10.1021/acscatal.9b04222.

(110) Gualandi, A.; Calogero, F.; Mazzarini, M.; Guazzi, S.; Fermi, A.; Bergamini, G.; Cozzi, P. G. Cp_2TiCl_2-Catalyzed Photoredox Allylation of Aldehydes with Visible Light. *ACS Catal.* **2020**, *10* (6), 3857–3863. DOI: 10.1021/acscatal.0c00348.

(111) Gualandi, A.; Rodeghiero, G.; Perciaccante, R.; Jansen, T. P.; Moreno-Cabrerizo, C.; Foucher, C.; Marchini, M.; Ceroni, P.; Cozzi, P. G. Catalytic Photoredox Allylation of Aldehydes Promoted by a Cobalt Complex. *Adv. Synth. Catal.* **2021**, *363* (4), 1105–1111. DOI: 10.1002/adsc.202001250.

(112) Tanabe, S.; Mitsunuma, H.; Kanai, M. Catalytic Allylation of Aldehydes Using Unactivated Alkenes. *J. Am. Chem. Soc.* **2020**, *142* (28), 12374–12381. DOI: 10.1021/jacs.0c04735.

(113) Calogero, F.; Potenti, S.; Bassan, E.; Fermi, A.; Gualandi, A.; Monaldi, J.; Dereli, B.; Maity, B.; Cavallo, L.; Ceroni, P.; Cozzi, P. G. Nickel-Mediated Enantioselective Photoredox Allylation of Aldehydes with Visible Light. *Angew. Chem. Int. Ed.* **2022**, *61* (11), e202114981. DOI: 10.1002/anie.202114981.

(114) Zhang, Z.; Hilche, T.; Slak, D.; Rietdijk, N. R.; Oloyede, U. N.; Flowers, R. A.; Gansäuer, A. Titanocenes as Photoredox Catalysts Using Green-Light Irradiation. *Angew. Chem. Int. Ed.* **2020**, *59* (24), 9355–9359. DOI: 10.1002/anie.202001508.

(115) Aydogan, A.; Bangle, R. E.; Cadranel, A.; Turlington, M. D.; Conroy, D. T.; Cauët, E.; Singleton, M. L.; Meyer, G. J.; Sampaio, R. N.; Elias, B.; Troian-Gautier, L. Accessing Photoredox Transformations with an Iron(III) Photosensitizer and Green Light. *J. Am. Chem. Soc.* **2021**, *143* (38), 15661–15673. DOI: 10.1021/jacs.1c06081.

(116) Wenger, O. S. Photoactive Nickel Complexes in Cross-Coupling Catalysis. *Chemistry - A European Journal.* 2021, pp 2270–2278. DOI: 10.1002/chem.202003974.

(117) Petrier, C.; Einhorn, J.; Luche, J. L. Selective tin and zinc mediated allylations of carbonyl compounds in aqueous media. *Tetrahedron Lett.* **1985**, *26* (11), 1449–1452. DOI: 10.1016/S0040-4039(00)99068-3.

(118) Loh, T. P.; Tan, K. T.; Yang, J. Y.; Xiang, C. L. Development of a highly α-regioselective indium-mediated allylation reaction in water. *Tetrahedron Lett.* **2001**, *42* (49), 8701–8703. DOI: 10.1016/S0040-4039(01)01883-4.

(119) Wada, M.; Ohki, H.; Akiba, K. A Grignard-Type Addition of Allyl Unit to Aldehydes by Using Bismuth and Bismuth Salt. *Bull. Chem. Soc. Jpn.* **1990**, *63* (6), 1738–1747. DOI: 10.1246/bcsj.63.1738.

(120) Wang, Z.; Yuan, S.; Li, C. J. Gallium-mediated allylation of carbonyl compounds in water. *Tetrahedron Lett.* **2002**, *43* (29), 5097–5099. DOI: 10.1016/S0040-4039(02)00995-4.

(121) Sun, K.; Lv, Q. Y.; Chen, X. L.; Qu, L. B.; Yu, B. Recent advances in visible-light-mediated organic transformations in water. *Green Chem.* **2021**, *23* (1), 232–248. DOI: 10.1039/d0gc03447a.

(122) Barata-Vallejo, S.; Yerien, D. E.; Postigo, A. Advances in Photocatalytic Organic Synthetic Transformations in Water and Aqueous Media. *ACS Sustain. Chem. Eng.* **2021**, *9* (30), 10016–10047. DOI: 10.1021/acssuschemeng.1c03384.

(123) Miyamoto, H.; Daikawa, N.; Tanaka, K. Carbon-carbon bond formation using bismuth in a water medium. *Tetrahedron Lett.* **2003**, *44* (36), 6963–6964. DOI: 10.1016/S0040-4039(03)01649-6.

(124) Smith, K.; Lock, S.; El-Hiti, G. A.; Wada, M.; Miyoshi, N. A convenient procedure for bismuth-mediated Barbier-

type allylation of aldehydes in water containing fluoride ions. *Org. Biomol. Chem.* **2004**, *2* (6), 935–938. DOI: 10.1039/b400179f.

(125) Ping-Da, R.; Shi-Feng, P.; Ting-Wei, D.; Shi-Hui, W. A Barbier type reaction promoted by in situ formed active metal bismuth from NaBH₄ and BiCl₃ in aqueous media. *Chinese J. Chem.* **1996**, *14* (5), 462–466. DOI: 10.1002/cjoc.19960140512.

(126) De Marcillac, P.; Coron, N.; Dambier, G.; Leblanc, J.; Moalic, J. P. Experimental detection of α-particles from the radioactive decay of natural bismuth. *Nature* **2003**, *422* (6934), 876–878. DOI: 10.1038/nature01541.

(127) Bradley, B.; Singleton, M.; Po, A. L. W. Bismuth toxicity - A reassessment. *J. Clin. Pharm. Ther.* **1989**, *14* (6), 423–441. DOI: 10.1111/j.1365-2710.1989.tb00268.x.

(128) Himeno, S.; Fujishiro, H.; Sumi, D. Bismuth. In *Handbook on the Toxicology of Metals - Volume II: Specific Metals*; Nordberg, G. F., Costa, M., Eds.; Academic Press, 2022; pp 121–139. DOI: 10.1016/B978-0-12-822946-0.00005-2.

(129) Sadler, P. J.; Li, H.; Sun, H. Coordination chemistry of metals in medicine: Target sites for bismuth. *Coord. Chem. Rev.* **1999**, *185–186*, 689–709. DOI: 10.1016/s0010-8545(99)00018-1.

(130) Keogan, D. M.; Griffith, D. M. Current and potential applications of bismuth-based drugs. *Molecules* **2014**, *19* (9), 15258–15297. DOI: 10.3390/molecules190915258.

(131) Gagnon, A.; Dansereau, J.; Le Roch, A. Organobismuth Reagents: Synthesis, Properties and Applications in Organic Synthesis. *Synthesis* **2017**, *49* (8), 1707–1745. DOI: 10.1055/s-0036-1589482.

(132) Barton, D. H. R.; Finet, J. P.; Khamsi, J. Copper salts catalysis of N-phenylation of amines by trivalent organobismuth compounds. *Tetrahedron Lett.* **1987**, *28* (8), 887–890. DOI: 10.1016/S0040-4039(01)81015-7.

(133) Finet, J. P. Arylation Reactions with Organobismuth Reagents. *Chem. Rev.* **1989**, *89* (7), 1487–1501. DOI: 10.1021/cr00097a005.

(134) Shimada, S.; Rao, M. L. N. Transition-metal catalyzed C-C bond formation using organobismuth compounds. *Top. Curr. Chem.* **2012**, *311*, 199–228. DOI: 10.1007/128_2011_202.

(135) Ruffell, K.; Ball, L. T. Organobismuth Redox Manifolds: Versatile Tools for Synthesis. *Trends Chem.* **2020**, *2* (10), 867–869. DOI: 10.1016/j.trechm.2020.07.008.

(136) Schwamm, R. J.; Lein, M.; Coles, M. P.; Fitchett, C. M. Catalytic oxidative coupling promoted by bismuth TEMPOxide complexes. *Chem. Commun.* **2018**, *54* (8), 916–919. DOI: 10.1039/c7cc08402a.

(137) Wang, F.; Planas, O.; Cornella, J. Bi(I)-Catalyzed Transfer-Hydrogenation with Ammonia-Borane. *J. Am. Chem. Soc.* **2019**, *141* (10), 4235–4240. DOI: 10.1021/jacs.9b00594.

(138) Jurrat, M.; Maggi, L.; Lewis, W.; Ball, L. T. Modular bismacycles for the selective C–H arylation of phenols and naphthols. *Nat. Chem.* **2020**, *12* (3), 260–269. DOI: 10.1038/s41557-020-0425-4.

(139) Planas, O.; Wang, F.; Leutzsch, M.; Cornella, J. Fluorination of arylboronic esters enabled by bismuth redox catalysis. *Science* **2020**, *367* (6475), 313–317. DOI: 10.1126/science.aaz2258.

(140) Moon, H. W.; Cornella, J. Bismuth Redox Catalysis: An Emerging Main-Group Platform for Organic Synthesis. *ACS Catal.* **2022**, *12* (2), 1382–1393. DOI: 10.1021/acscatal.1c04897.

(141) Li, C. J. Aqueous Barbier-Grignard type reaction: Scope, mechanism, and synthetic applications. *Tetrahedron* **1996**, *52* (16), 5643–5668. DOI: 10.1016/0040-4020(95)01056-4.

(142) Kobayashi, S.; Ueno, M.; Kitanosono, T. Bismuth catalysts in aqueous media. In *Bismuth-Mediated Organic Reactions. Topics in Current Chemistry*; Ollevier, T., Ed.; Springer, Berlin, Heidelberg, 2011; Vol. 311, pp 1–18. DOI: 10.1007/128_2011_174.

(143) Minozzi, C.; Caron, A.; Grenier-Petel, J. C.; Santandrea, J.; Collins, S. K. Heteroleptic Copper(I)-Based Complexes for Photocatalysis: Combinatorial Assembly, Discovery, and Optimization. *Angew. Chem. Int. Ed.* **2018**, *57* (19), 5477–5481. DOI: 10.1002/anie.201800144.

(144) Yedase, G. S.; John, M.; Yatham, V. R. Organophotoredox-Catalyzed Switchable Selective Transformation of Aromatic Aldehydes into Pinacols and Benzyl alcohols. *Asian J. Org. Chem.* **2021**, *10* (11), 2916–2920. DOI: 10.1002/ajoc.202100516.

(145) Kuznetsov, A. M.; Shapnik, M. S.; Masliy, A. N.; Zelenetskaya, K. V. Quantum-chemical calculation of standard redox potentials of half-reactions involving bismuth aquacomplexes. *Russ. J. Electrochem.* **2002**, *38* (7), 669–675. DOI: 10.1023/A:1016362728232.

(146) Lou, Y. Y.; Hapiot, P.; Floner, D.; Fourcade, F.; Amrane, A.; Geneste, F. Efficient Dechlorination of α-Halocarbonyl and α-Haloallyl Pollutants by Electroreduction on Bismuth. *Environ. Sci. Technol.* **2020**, *54* (1), 559–567. DOI: 10.1021/acs.est.9b05732.

(147) Alder, C. M.; Hayler, J. D.; Henderson, R. K.; Redman, A. M.; Shukla, L.; Shuster, L. E.; Sneddon, H. F. Updating and further expanding GSK's solvent sustainability guide. *Green Chem.* **2016**, *18* (13), 3879–3890. DOI: 10.1039/c6gc00611f.

(148) Dalton, T.; Faber, T.; Glorius, F. C-H activation: Toward sustainability and applications. *ACS Cent. Sci.* **2021**, *7* (2), 245–261. DOI: 10.1021/acscentsci.0c01413.

(149) Rueping, M.; Nachtsheim, B. J. Bismuth salts in catalytic alkylation reactions. *Top. Curr. Chem.* **2012**, *311*, 115–141. DOI: 10.1007/128_2011_191.

(150) Metternich, J. B.; Gilmour, R. A Bio-Inspired, Catalytic E→Z Isomerization of Activated Olefins. *J. Am. Chem. Soc.* **2015**, *137* (35), 11254–11257. DOI: 10.1021/jacs.5b07136.

(151) Cai, W.; Fan, H.; Ding, D.; Zhang, Y.; Wang, W. Synthesis of Z-alkenes via visible light promoted photocatalytic E→Z isomerization under metal-free conditions. *Chem. Commun.* **2017**, *53* (96), 12918–12921. DOI:

References

10.1039/c7cc07984b.

(152) Nikitas, N. F.; Triandafillidi, I.; Kokotos, C. G. Photo-organocatalytic synthesis of acetals from aldehydes. *Green Chem.* **2019**, *21* (3), 669–674. DOI: 10.1039/c8gc03605e.

(153) Gualandi, A.; Rodeghiero, G.; Della Rocca, E.; Bertoni, F.; Marchini, M.; Perciaccante, R.; Jansen, T. P.; Ceroni, P.; Cozzi, P. G. Application of coumarin dyes for organic photoredox catalysis. *Chem. Commun.* **2018**, *54* (72), 10044–10047. DOI: 10.1039/C8CC04048F.

(154) Wang, P. Z.; Chen, J. R.; Xiao, W. J. Hantzsch esters: An emerging versatile class of reagents in photoredox catalyzed organic synthesis. *Org. Biomol. Chem.* **2019**, *17* (29), 6936–6951. DOI: 10.1039/c9ob01289c.

(155) Bryden, M. A.; Zysman-Colman, E. Organic thermally activated delayed fluorescence (TADF) compounds used in photocatalysis. *Chem. Soc. Rev.* **2021**, *50* (13), 7587–7680. DOI: 10.1039/d1cs00198a.

(156) Miranda, R.; Aceves, J. M.; Vilchis, M. B.; Garduño, R.; Saloma, M.; Salmón, M. Anodic oxidation of hanizsch esters in acetonitrile. *Heterocycl. Commun.* **1997**, *3* (4), 323–326. DOI: 10.1515/hc.1997.3.4.323.

(157) Zhu, X. Q.; Li, H. R.; Li, Q.; Ai, T.; Lu, J. Y.; Yang, Y.; Cheng, J. P. Determination of the C4-H bond dissociation energies of NADH models and their radical cations in acetonitrile. *Chem. Eur. J.* **2003**, *9* (4), 871–880. DOI: 10.1002/chem.200390108.

(158) Zhang, Z.; Richrath, R. B.; Gansäuer, A. Merging Catalysis in Single Electron Steps with Photoredox Catalysis - Efficient and Sustainable Radical Chemistry. *ACS Catal.* **2019**, *9* (4), 3208–3212. DOI: 10.1021/acscatal.9b00787.

(159) Lee, K. N.; Lei, Z.; Ngai, M. Y. β-Selective Reductive Coupling of Alkenylpyridines with Aldehydes and Imines via Synergistic Lewis Acid/Photoredox Catalysis. *J. Am. Chem. Soc.* **2017**, *139* (14), 5003–5006. DOI: 10.1021/jacs.7b01373.

(160) Jadhav, B. D.; Pardeshi, S. K. Bismuth chloride mediated allylation of carbonyl compounds in aqueous media: A mechanistic investigation. *Tetrahedron Lett.* **2014**, *55* (35), 4948–4952. DOI: 10.1016/j.tetlet.2014.07.031.

(161) Chen, Q. A.; Chen, M. W.; Yu, C. Bin; Shi, L.; Wang, D. S.; Yang, Y.; Zhou, Y. G. Biomimetic asymmetric hydrogenation: In situ regenerable Hantzsch esters for asymmetric hydrogenation of benzoxazinones. *J. Am. Chem. Soc.* **2011**, *133* (41), 16432–16435. DOI: 10.1021/ja208073w.

(162) Potenti, S.; Gualandi, A.; Puggioli, A.; Fermi, A.; Bergamini, G.; Cozzi, P. G. Photoredox Allylation Reactions Mediated by Bismuth in Aqueous Conditions. *Eur. J. Org. Chem.* **2021**. DOI: 10.1002/ejoc.202001640.

(163) Deady, E.; Moon, C.; Moore, K.; Goodenough, K. M.; Shail, R. K. Bismuth: Economic geology and value chains. *Ore Geol. Rev.* **2022**, *143*, 104722. DOI: 10.1016/j.oregeorev.2022.104722.

(164) Häckl, K.; Kunz, W. Some aspects of green solvents. *Comptes Rendus Chim.* **2018**, *21* (6), 572–580. DOI: 10.1016/j.crci.2018.03.010.

(165) Wang, T.; Dong, S.; Chen, X.; Qian, K.; Wang, H.; Quan, H.; Zhang, Z.; Zuo, Y.; Huang, L.; Li, D.; Yang, M.; Yang, S.; Jin, Y.; Wang, Z. Design, synthesis, biological evaluation, homology modeling and docking studies of (E)-3-(benzo[d][1,3]dioxol-5-ylmethylene) pyrrolidin-2-one derivatives as potent anticonvulsant agents. *Bioorganic Med. Chem. Lett.* **2018**, *28* (8), 1324–1329. DOI: 10.1016/j.bmcl.2018.03.015.

(166) Pardin, C.; Keillor, J. W.; Lubell, W. D. Cinnamoyl Inhibitors of Transglutaminase. US008614233B2, 2013.

(167) Jui, N. T.; Garber, J. A. O.; Finelli, F. G.; MacMillan, D. W. C. Enantioselective organo-SOMO cycloadditions: A catalytic approach to complex pyrrolidines from olefins and aldehydes. *J. Am. Chem. Soc.* **2012**, *134* (28), 11400–11403. DOI: 10.1021/ja305076b.

(168) Garayalde, D.; Rusconi, G.; Nevado, C. A Gold- and Brønsted Acid Catalytic Interplay Towards the Synthesis of Highly Substituted Tetrahydrocarbazoles. *Helv. Chim. Acta* **2017**, *100* (3), e1600333. DOI: 10.1002/hlca.201600333.

(169) Brown, T. H.; Blakemore, R. C.; Durant, G. J.; Emmett, J. C.; Ganellin, C. R.; Parsons, M. E.; Rawlings, D. A.; Walker, T. F. Isocytosine H₂-receptor histamine antagonists I. Oxmetidine and related compounds. *Eur. J. Med. Chem.* **1988**, *23* (1), 53–62. DOI: 10.1016/0223-5234(88)90167-5.

(170) Zuckerman, D. S.; Woerpel, K. A. Diastereoselective peroxidation of derivatives of Baylis–Hillman adducts. *Tetrahedron* **2019**, *75* (31), 4118–4129. DOI: 10.1016/j.tet.2019.05.008.

(171) Abdel-Mohsen, H. T.; Conrad, J.; Beifuss, U. Laccase-catalyzed oxidation of Hantzsch 1,4-dihydropyridines to pyridines and a new one pot synthesis of pyridines. *Green Chem.* **2012**, *14* (10), 2686–2690. DOI: 10.1039/c2gc35950b.

(172) Bandini, M.; Cozzi, P. G.; Umani-Ronchi, A. Enantioselective catalytic addition of allyl organometallic reagents to aldehydes promoted by [Cr(Salen)]: The hidden role played by weak Lewis acids in metallo-Salen promoted reactions. *Tetrahedron* **2001**, *57* (5), 835–843. DOI: 10.1016/S0040-4020(00)01047-4.

(173) Wang, T.; Hao, X. Q.; Huang, J. J.; Niu, J. L.; Gong, J. F.; Song, M. P. Chiral bis(imidazolinyl)phenyl NCN pincer rhodium(III) Catalysts for enantioselective allylation of aldehydes and carbonyl-ene reaction of trifluoropyruvates. *J. Org. Chem.* **2013**, *78* (17), 8712–8721. DOI: 10.1021/jo4014194.

(174) Dey, P.; Koli, M.; Goswami, D.; Sharma, A.; Chattopadhyay, S. [Bmim][Br] as an Inexpensive and Efficient Medium for the Barbier-Type Allylation Reaction Using a Catalytic Amount of Indium: Mechanistic Studies. *Eur. J. Org. Chem.* **2018**, *2018* (11), 1333–1341. DOI: 10.1002/ejoc.201800043.

(175) Yin, J. X.; Stark, R. T.; Fallis, I. A.; Browne, D. L. A Mechanochemical Zinc-Mediated Barbier-Type Allylation Reaction under Ball-Milling Conditions. *J. Org. Chem.* **2020**, *85* (4), 2347–2354. DOI: 10.1021/acs.joc.9b02876.

(176) Larouche-Gauthier, R.; Elford, T. G.; Aggarwal, V. K. Ate complexes of secondary boronic esters as chiral organometallic-type nucleophiles for asymmetric synthesis. *J. Am. Chem. Soc.* **2011**, *133* (42), 16794–16797. DOI: 10.1021/ja2077813.

(177) Davis, A. P.; Jaspars, M. Super-acid catalysed addition of allylsilanes to carbonyl compounds; synthetic and

mechanistic aspects. *J. Chem. Soc. Perkin Trans. 1* **1992**, No. 16, 2111–2118. DOI: 10.1039/p19920002111.

(178) Antonsson, T.; Moberg, C.; Tottie, L.; Heumann, A. Palladium-Catalyzed Oxidative Cyclization of 1,5-Dienes. Influence of Different Substitution Patterns on the Regio- and Stereochemistry of the Reaction. *J. Org. Chem.* **1989**, *54* (20), 4914–4929. DOI: 10.1021/jo00281a039.

5.Concluding Remarks

The research projects presented in this thesis are valuable examples of how chemical knowledge can keep growing through the interplay between the many branches of chemistry. Indeed, multidisciplinary approaches represent the only way to support the growth of scientific knowledge at its current rate. In fact, either a single individual or a single discipline cannot deal with such difficult challenges. Nowadays, state-of-the-art theoretical and experimental approaches enable the study of challenging systems/conditions with high fidelity. Besides, even the definition of "challenging" is somehow ambiguous. This was particularly evident in the case of the project concerning exotic molecular species. The multidisciplinary endeavour leading to the generation and spectroscopical characterization of phenylmethanimine represented a noteworthy challenge because we are used to particular reactions conditions, i.e. the terrestrial ones, while those required for the study were designed to mimic putatively common astrochemically relevant conditions. Nevertheless, since there are no possibilities to materially explore distant astronomical environments (and this condition will probably persist for a very long time), the terrestrial "challenge" represents the only available option. This study adds a small piece in the massive puzzle of astrochemistry, which is ultimately aimed at understanding our primordial origins, thus trying to answer to an age-old question. If, and when phenylmethanimine will ever be detected in some astronomical environments by means of its rotational fingerprints, this study will be mentioned in support to the detection.

It is worth mentioning that the methods developed and employed for a particular molecular species can be extended to other systems. This is the case of phenylmethanimine, but it is also evident in the case of 4-fluorothreonine. This molecule was chosen as a case study to evaluate the effects of the insertion of fluorine in a molecular scaffold. Moreover, the available literature lacked high yielding approaches for its total synthesis in sufficiently large amounts for its thorough characterization. Both the theoretical and the synthetic strategies adopted for this specific case will represent useful background information for further studies, even concerning different systems. In particular, the characterization of 4-fluorothreonine by means of rotational spectroscopy in the gas phase (mentioned in Section 3.4) is almost complete, and the results will be published in due time. Hopefully, they will be useful for further studies concerning fluorinated organic species.

Finally, the current energetic crisis – making the transition from fossil fuels to renewable energy sources highly desirable – represents a topical issue to understand the current potential of metallaphotoredox catalysis. Even this research field requires a multidisciplinary approach. Indeed, the use of light to perform challenging chemical transformation can be considered as a bioinspired approach, based on the most common biochemical process on Earth, namely photosynthesis. Bioinspired chemistry is a rapidly growing research field, based on exhaustive studies concerning chemistry, biology, evolution, and many

other disciplines. Even in this case, the interplay between theoretical and experimental strategies is pivotal to understand how Nature was able to optimize its processes. Eventually, taking inspiration from natural phenomena, our energy-intensive societies will evolve to more sustainable ones. In particular, the use of solar light represents the spearhead of sustainability since sunlight has represented the main source of energy since the dawn of life. Noteworthily, both the reported bismuth-mediated photoredox allylation reaction and photosynthesis feature the cooperation between photosensitizers and metal centres: an organic photosensitizer and a bismuth species are involved in the former, while many pigments (such as chlorophylls and carotenoids), together with a metal-based oxygen-evolving complex (containing manganese and calcium), are the main actors of photosynthesis. Many other photocatalytic protocols – even bioinspired ones – have been recently developed, and many more will be explored in the next future, especially under the pressing need to take advantage of sunlight as much as we can.

In conclusion, the research period as a PhD student represented a great opportunity to understand how chemistry – with its many different branches – is involved in almost any process we can think of. Moreover, it was a precious chance to be involved in many different projects, dealing with different people having very different backgrounds. To make a long story short, it was a journey to discover the importance of diversity, and I sincerely hope none of the lessons I learnt will go wasted.